

UNIVERSITAT POLITÈCNICA DE VALÈNCIA

**INSTITUTO INTERUNIVERSITARIO DE INVESTIGACIÓN DE RECONOCIMIENTO
MOLECULAR Y DESARROLLO TECNOLÓGICO**



**New advanced anti-tumor therapies based on hybrid
mesoporous nanodevices**

PhD. THESIS

Submitted by

Elena Lucena Sánchez

PhD. Supervisors:

Prof. Ramón Martínez Máñez

Dra. Alba García Fernández

Valencia, April 2024



UNIVERSITAT
POLITÈCNICA
DE VALÈNCIA

RAMÓN MARTÍNEZ MÁÑEZ, Ph.D. in Chemistry and Professor at the *Universitat Politècnica de València* and ALBA GARCÍA FERNÁNDEZ, Ph.D. in Biotechnology at the *Universitat Politècnica de València*.

CERTIFY:

That the work ***“New advanced anti-tumor therapies based on hybrid mesoporous nanodevices”*** has been developed by Elena Lucena Sánchez under their supervision in the Instituto Interuniversitario de Investigación de Reconocimiento Molecular y Desarrollo Tecnológico (IDM) of the *Universitat Politècnica de València*, forming part of the Unidad Mixta UPV-CIPF de Investigación en Mecanismos de Enfermedades y Nanomedicina, as a Thesis Project in order to obtain the degree of Ph.D. in Chemistry at the *Universitat Politècnica de València*.

Valencia, April 2024

Prof. Ramón Martínez Máñez

Dra. Alba García Fernández

Director

Directora

A mis padres

*“Nada en este mundo debe ser temido...
solo entendido.
Ahora es el momento de comprender más,
para que podamos temer menos.”*
Marie Curie

*“La satisfacción radica en el esfuerzo, no en el logro.
El esfuerzo total es la victoria total.”*
Mahatma Gandhi

Agradecimientos

Acknowledgements

Estos agradecimientos han sido una de las partes más difíciles de escribir pues no soy especialmente buena con las palabras, pero no podía pasar por aquí sin reflejar el cariño que tengo para todos los que me han acompañado durante esta etapa.

En primer lugar, gracias a mis directores de tesis: Ramón y Alba. Gracias, Ramón, por darme la oportunidad de realizar esta tesis y contribuir a mi desarrollo científico y personal. Gracias por tu supervisión y por las oportunidades que me has proporcionado. Gracias por tu exigencia y por darme la libertad que ha permitido que aprendiera tanto por el camino. Alba, más que una directora para mí has sido una más, gracias por tu supervisión y tu ayuda, por tus consejos para lidiar con situaciones complicadas, por saber siempre que decir, por tu eficiencia y por valorar y respetar mi opinión por encima de todo. ¡Te admiro muchísimo!

Gracias también a mis compañeras y compañeros del CIPF, las principesas. Gracias a las que ya no están, Alejandra, Gema y Araceli, por hacerme los comienzos más amenos, vuestros consejos tanto en el laboratorio como en la vida me han enseñado tanto. Sois la definición de la palabra compañerismo, aunque más que compañeras, me llevo amigas.

Gracias a mis chicos, Javi, David A., David B., Juanjo y Xente por estar siempre dispuestos a ayudar, por los momentos compartidos y por tener siempre una sonrisa en la cara. Hacéis que ir a trabajar sea divertido, echaré de menos compartir mi día a día con vosotros. ¡Mucho ánimo que de la tesis también se sale! También gracias a Nelia y Jenni, aunque llegasteis en la etapa final habéis colaborado en que esta tesis sea realidad.

También agradecer al I12: Mar, Mónica Sancho, Ally, Estefi, Paula, Paula Carrascosa, Diego, Iván y Mili. Gracias por integrarme cuando llegué, por transmitir siempre ese buen rollo y por vuestra predisposición para ayudar.

Agradecimientos

Continuo con la que ha sido mi familia en Valencia estos años. Blanca, llegaste cuando estaba en mi peor momento y fuiste luz. No podría imaginar una persona mejor con la que compartir mi tesis. Gracias por tu compañerismo y tu amistad incondicional, por estar siempre disponible, tanto dentro como fuera del laboratorio, no tienes ni idea del apoyo que has sido. Gracias por lo honesta que eres, por ser crítica conmigo y decirme tanto lo bueno como lo malo. Por las tardes merendando y quejándonos de todo, por estar dispuesta siempre a cualquier plan loco que nos hiciera desconectar, y como no, por tantos viajes que, aunque no hayamos cumplido nuestro objetivo por mes han hecho que consiguiera desconectar de todo.

Gracias también a mis chicas de la fe. A Alba y Marina por tantos momentos compartidos, por ofrecernos siempre un lugar en el que juntarnos y charlar de la vida, ¡cualquier excusa era buena para invadir vuestra casa! A Nieves, gracias por ser tan generosa, por no decir nunca que no y estar dispuesta siempre a cualquier plan improvisado. Y cómo no me puedo olvidar de mi gym-sis, Isa, gracias por tantas tardes en el gimnasio, por motivarme siempre, por las confesiones durante el camino y las cervezas de después. Aunque lo que empezó en el gimnasio fue mucho más allá, gracias por acogerme en tu casa, por escucharme como nadie, por ser mi compañera de aventuras y por tener siempre salseo del bueno para reírnos juntas. Mis músculos te lo agradecen, pero yo mucho más. Nuestra rutina es una de las cosas que más voy a echar de menos.

Muchas gracias a mis compañeras y compañeros de química con los que he tenido la oportunidad de coincidir en el laboratorio durante estos años: Andy, Guille, Giovanni, Marcia, Andrea, Elena, Vicente, Serena, Angy... Trabajar directamente con vosotras y compartir momentos ha sido un auténtico placer. Gracias por contribuir a que esta tesis sea posible. Me gustaría dar las gracias de manera especial a Toni por ayudarme tanto en los comienzos. A Paula, por tu implicación y optimismo, por sacar siempre tiempo para atenderme y transmitirme todo tu conocimiento y experiencia. A Javi, gracias por ser mi apoyo químico, por ayudarme a materializar las ideas locas y por tu predisposición. A

Andrea E., por ser tan buena compañera, trabajar contigo ha sido tan fácil. A Gonçalo, por hacer de nosotros tu casa en España y apuntarte siempre a un bombardeo. Y Eva, no me podía olvidar de ti, gracias por todos los momentos compartidos. Que suerte haber coincidido contigo y poder aprender de ti, no conozco a nadie más trabajadora que tú, ¡Eres un ejemplo a seguir!

Gracias a la parte administrativa del IDM por su papel fundamental en esta tesis. Eva Brun por facilitarnos tantos trámites y conseguir que todo esté a tiempo, por tener siempre una sonrisa y tus palabras de ánimo. Gracias a Tania por ser la alegría hecha persona, por ayudarnos tantísimo en las gestiones y tener una paciencia enorme con nosotros.

También quiero agradecer a todo el personal del CIPF que han facilitado mi estancia en él durante estos casi 5 años. En especial a los servicios científicos de microscopía, citometría e histología, Alberto, Ali, Domingo y Mario, gracias por vuestra disponibilidad, vuestra paciencia y por implicaros tanto en cada ensayo. Una parte importante de esta tesis es vuestra.

No puedo olvidarme de agradecer a todas esas personas de fuera del laboratorio, que han contribuido de alguna manera al desarrollo de esta tesis o simplemente a hacer mi vida un poquito más feliz durante esta etapa.

Gracias a la otra parte de mi familia aquí en Valencia, mis chic@s del baile. Julián por estar siempre disponible y apuntarte a cualquier cosa que se me ocurriera, lo mismo nos valía una carrera que unas cervezas. Gracias por ser el más pesado del mundo y ponerme siempre de los nervios, ¡te quiero igual! Al chiquitín, Conver, por ser siempre mi taxista favorito. Gracias por creer en mí más que yo misma y sentirte tan orgulloso, confío en que llegarás muy lejos. A Roberto y Javi por disfrutar compartiendo bailes conmigo y sacarme siempre una sonrisa. Y como no, a mi desastre favorito, Lila, gracias por

Agradecimientos

escucharme y alegrarme siempre, contarme tus locuras y desahogarte conmigo, sabes que siempre tienes una cama en mi casa.

Me gustaría también agradecer a aquellas personas que han formado parte de mi vida desde siempre y que siguen ahí en todos mis éxitos y tropiezos. Gracias a mis amigas del cole, Elvira, Alba y Ana, por sacar siempre tiempo para recargarme de energía cada vez que volvía a casa, no cambio por nada nuestros desayunos juntas. Gracias a mi bailarina favorita, Laura por enseñarme este mundo tan divertido y ser mi cómplice siempre. Gracias a Ali por todo lo que hemos pasado juntas y por la amistad incondicional a pesar de los cambios. Gracias a Ana por no olvidarte nunca de las fiestas y locuras juntas y por contar los días para que volviera a Granada.

Durante mi etapa universitaria también ha habido personas muy importantes de las que no me puedo olvidar. Gracias a mis bioquímicos, en especial a Mercedes, Eli y Luis, hemos compartido tantos momentos juntos, gracias por vuestro apoyo y amistad todos estos años.

Gracias a mis Bioenterprises, Lanchi, Gándara, Andrea, Noelia, Dani, Sara, Rafa y Romera. Gracias por convertir mi año de máster en el mejor de mi etapa universitaria, gracias por tener palabras de apoyo siempre para mí, por tantos momentos juntos, por las noches en casa de Sara, por las casas rurales y por seguir sacando tiempo para los reencuentros por mucho que pasen los años. Toda esta etapa comenzó con vosotros, y no puede acabar de otra forma, sois maravillosos.

Por último, las personas más importantes de mi vida, mi familia. No hay palabras suficientes de agradecimiento para vosotros, gracias a mis tíos y mis primos por confiar más en mí que yo misma y estar siempre tan orgullosos. Gracias a mis padres por vuestro amor y apoyo incondicional, por soportarme que no es nada fácil, y vuestro esfuerzo por darme siempre lo mejor, pero sobre todo por la educación y valores que me habéis dado,

no hay día que no me sienta agradecida. Sin vosotros nunca hubiera llegado tan lejos, os quiero mucho.

A todos y cada uno de vosotros:

Gracias por haber compartido este camino conmigo,

Elena

Resumen

La presente tesis doctoral titulada “New advanced anti-tumor therapies based on hybrid mesoporous nanodevices” se centra en el diseño, síntesis, caracterización y evaluación de nuevos nanodispositivos híbridos orgánico-inorgánicos. En concreto, se han desarrollado nanopartículas de sílice mesoporosas (MSNs) y nanopartículas Janus combinando MSNs con platino y con oro con el objetivo de mejorar los tratamientos anti-tumorales.

El primer capítulo es una introducción general que incluye una visión global del contexto en el que se enmarca la investigación realizada. En particular, se presenta el concepto de nanotecnología y nanomedicina, así como información básica sobre las nanopartículas mesoporosas de sílice, las nanopartículas Janus y sus interacciones con los sistemas biológicos. Finalmente, se describen las características de la enfermedad del cáncer, los tratamientos actuales y la aplicación de los nanomateriales como terapia.

A continuación, en el segundo capítulo, se presentan los objetivos generales de esta tesis doctoral y los objetivos específicos que serán abordados en los siguientes capítulos experimentales.

Los capítulos tercero y cuarto describen dos estrategias terapéuticas basadas en el desarrollo de nanopartículas con movimiento para mejorar la terapia antitumoral. Concretamente, en el primer capítulo experimental se presenta un nanodispositivo autopropulsado para la liberación controlada de fármacos en respuesta al glutatión (GSH) intracelular. Éste se basa en nanopartículas tipo Janus compuestas por sílice mesoporosa y oro, funcionalizadas en la parte del oro con la enzima catalasa, cargadas con doxorubicina y con cadenas de oligo(etilenglicol) (S-S-PEG) unidas por puentes disulfuro en la cara de la sílice. Una vez sintetizado y caracterizado el dispositivo, se confirmó su movimiento gracias a la conversión de peróxido de hidrógeno (fuel) en oxígeno por la enzima catalasa. Por otra parte, se demostró el funcionamiento de la puerta molecular en

presencia de GSH, confirmando de este modo que la liberación de la carga se produce solo en presencia del tripéptido. Finalmente, la internalización celular y la liberación de doxorubicina se estudiaron en la línea celular de cáncer de cérvix Hela, viéndose aumentadas en presencia del fuel.

Motivados por los resultados anteriores, en el cuarto capítulo se describe un nuevo nanomotor diseñado como tratamiento antitumoral y similar al anterior. En este caso, la nanopartícula Janus desarrollada está compuesta por una nanopartícula de sílice mesoporosa junto con una de platino, cargada con doxorubicina y cubierta con S-S-PEG. Al igual que en el trabajo anterior, la descomposición catalítica de bajas concentraciones de peróxido de hidrógeno, por el platino en este caso, consigue la autopropulsión del dispositivo. Además, se obtuvo el perfil cinético de liberación del cargo en respuesta a estímulos y se confirmó su aplicación en un cultivo en monocapa de células THP-1, así como en un dispositivo microchip con el objetivo de simular lo que ocurre en los vasos capilares.

Los capítulos cinco y seis se centran en una estrategia terapéutica nueva que consiste en potenciar la acción del sistema inmune sobre el tumor para conseguir su eliminación. En el primero de estos capítulos experimentales, se utilizaron nanopartículas cargadas con el fármaco JQ-1 y un siRNA frente al factor de crecimiento transformante β (TGF- β) como inmunoterapia. Este nanodispositivo se basa en una MSN cargada con el fármaco JQ-1, funcionalizada con el polímero polietilenimina (PEI) y un siRNA dirigido a TGF- β unido mediante interacciones electrostáticas. Una vez sintetizadas y caracterizadas, se confirmó la capacidad de estas nanopartículas para llevar a cabo el escape endosomal y la liberación en el citosol del siRNA, junto con la disminución en la expresión del ligando 1 de muerte programada (PD-L1) y en la producción de TGF- β . Por último, se confirmó su aplicabilidad al ser capaces de inducir la eliminación específica de las células de melanoma A375 por el sistema inmune.

De acuerdo con el último capítulo experimental, se describe el desarrollo de un nuevo enfoque inmunoterapéutico basado en la comunicación química. En este caso, empleamos una nanopartícula Janus de oro y sílice funcionalizada con un péptido llamado pHLIP en la cara de sílice y el anticuerpo contra el receptor PD-1 unido a la cara de oro (J-pHLIP-PD1). La membrana de la célula tumoral es decorada por este nanodispositivo a través del intercalado del péptido pHLIP, dejando expuesto en su superficie el anticuerpo PD-1. Este anticuerpo fue capaz de atrapar a los linfocitos T circulantes que expresan PD-1 y facilitar la sinapsis y comunicación citotóxicas, desencadenando la eliminación de células tumorales por el sistema inmunitario. Además, estos resultados se confirmaron en un modelo metastásico B16-F10-Luc con una reducción de nódulos metastásicos en los grupos tratados con las nanopartículas J-pHLIP-PD1.

Finalmente, en el capítulo séptimo y octavo, se aborda la discusión general y las conclusiones derivadas de los estudios experimentales presentados en esta tesis doctoral. En conclusión, la preparación de nanopartículas mesoporosas de sílice y su combinación con partículas metálicas y/o grupos orgánicos como puertas moleculares, efectores enzimáticos, modificadores ambientales, mediadores de comunicación y fármacos se presentan en esta tesis como una estrategia con potencial para superar las limitaciones de los tratamientos antitumorales actuales. Esperamos que los resultados obtenidos abran nuevas oportunidades de investigación e inspiren el desarrollo de materiales inteligentes aplicados no solo en el campo de la terapia tumoral, sino también en otras áreas biomédicas para solventar las necesidades de los pacientes.

Resum

Aquesta tesi doctoral titulada “New advanced anti-tumor therapies based on hybrid mesoporous nanodevices” se centra en el disseny, síntesi, caracterització i avaluació de nous nanodispositius híbrids orgànic-inorgànics. En concret, s'han desenvolupat nanopartícules de sílice mesoporoses (MSNs) i nanopartícules Janus combinant MSNs amb platí i amb or per al tractament antitumoral.

El primer capítol és una introducció general que inclou una visió global del context on s'emmarca la recerca realitzada. En particular, es presenta el concepte de nanotecnologia i nanomedicina, així com informació bàsica sobre les nanopartícules de sílice mesoporosa, les nanopartícules Janus i les seves interaccions amb els sistemes biològics. Finalment, es descriuen les característiques de la malaltia del càncer, els tractaments actuals i l'aplicació dels nanomaterials com a teràpia.

A continuació, al segon capítol, es presenten els objectius generals d'aquesta tesi doctoral i els objectius específics que seran abordats en els capítols experimentals següents.

Els capítols tercer i quart descriuen dues estratègies terapèutiques basades en el desenvolupament de nanopartícules amb moviment per aconseguir una millora de la terapia antitumoral. Concretament, al primer capítol experimental es presenta un nanodispositiu autopropulsat per a l'alliberament controlat de fàrmacs en resposta al glutatió (GSH) intracel·lular. Aquest es basa en nanopartícules tipus Janus compostes per sílice mesoporosa i or, funcionalitzades a la part de l'or amb l'enzim catalasa, carregades amb doxorubicina i amb cadenes d'oligo(etilenglicol) (SS-PEG) unides per ponts disulfur a la cara de la sílice. Una vegada sintetitzat i caracteritzat el dispositiu, es va confirmar la seua capacitat de moviment gràcies a la conversió de peròxid d'hidrogen (fuel) en oxigen per l'enzim catalasa. D'altra banda, el funcionament correcte de la porta molecular es va

demostrar en presència de GSH, confirmant així que l'alliberament de la càrrega es produeix només en presència del tripèptid. Finalment, la internalització cel·lular i l'alliberament de doxorubicina es van estudiar a la línia cel·lular de càncer de cèrvix Hela, veient-se augmentades en presència del fuel.

Motivats pels resultats anteriors, al quart capítol es descriu un nanomotor nou dissenyat com a tractament antitumoral i similar a l'anterior. En aquest cas, la nanopartícula Janus desenvolupada està composta per una nanopartícula de sílice mesoporosa juntament amb una de platí, carregada amb doxorubicina i coberta amb S-S-PEG. Igual que en el treball anterior, la descomposició catalítica de baixes concentracions de peròxid d'hidrogen, pel platí en aquest cas, aconsegueix l'autopropulsió del dispositiu. A més, es va obtenir el perfil cinètic d'alliberament del càrrec en resposta a estímuls i se'n va confirmar l'aplicació en un cultiu en monocapa de cèl·lules THP-1, així com en un dispositiu microxip amb l'objectiu d'imitar els vasos capil·lars.

Els capítols cinc i sis se centren en una estratègia terapèutica nova que consisteix a potenciar l'acció del sistema immune sobre el tumor per aconseguir-ne l'eliminació. Al primer d'aquests capítols experimentals, es van utilitzar nanopartícules carregades amb el fàrmac JQ-1 i un siRNA davant el factor de creixement transformant β (TGF- β) com a immunoteràpia. Aquest nanodispositiu es basa en una MSN carregada amb el fàrmac JQ-1, funcionalitzada amb el polímer polietilenimina (PEI) i un siRNA dirigit a TGF- β unit mitjançant interaccions electrostàtiques. Una vegada sintetitzades i caracteritzades, es va confirmar la capacitat d'aquestes nanopartícules per a escapar del compartiment endosomal i l'alliberament al citosol del siRNA, juntament amb la disminució en l'expressió de PD-L1 i en la producció de TGF- β . Finalment, es va confirmar la seua aplicabilitat per induir l'eliminació específica de les cèl·lules de melanoma A375 pel sistema immune.

D'acord amb el darrer capítol experimental, es descriu el desenvolupament d'un enfocament immunoterapèutic nou basat en la comunicació química. En aquest cas, fem servir una nanopartícula Janus d'or i sílice funcionalitzada amb un pèptid anomenat pHLIP a la cara de sílice i l'anticòs PD-1 unit a la cara d'or. La membrana de la cèl·lula tumoral és decorada per aquest nanodispositiu a través de l'intercalat del pèptid pHLIP, deixant exposat a la seua superfície l'anticòs PD-1. Aquest anticòs és capaç d'atrapar els limfòcits T circulants i facilitar la sinapsi i la comunicació citotòxiques, desencadenant l'eliminació de cèl·lules tumorals pel sistema immunitari. A més, aquests resultats es van confirmar en un model metastàtic B16-F10-Luc amb una reducció de nòduls metastàtics als grups tractats amb les nanopartícules J-pHLIP-PD1.

Finalment, al capítol setè i vuitè, s'aborda la discussió general i les conclusions derivades dels estudis experimentals presentats en aquesta tesi doctoral. En conclusió, la preparació de nanopartícules mesoporoses de sílice i la seua combinació amb partícules metàl·liques i/o grups orgànics com portes moleculars, efectors enzimàtics, modificadors ambientals, mediadors de comunicació i fàrmacs es presenten en aquesta tesi com una estratègia amb potencial per superar les limitacions dels tractaments antitumorals actuals. Esperem que els resultats obtinguts obrin noves oportunitats de recerca i inspiren el desenvolupament de materials intel·ligents aplicats no només al camp de la teràpia tumoral, sinó també en altres àrees biomèdiques per resoldre les necessitats dels pacients.

Abstract

The present PhD thesis entitled “New advanced anti-tumor therapies based on hybrid mesoporous nanodevices” focuses on the design, synthesis, characterization, and evaluation of new hybrid organic-inorganic nanodevices. We have developed mesoporous silica nanoparticles (MSNs) and Janus platinum-MSN and gold-MSN nanoparticles for tumor treatment.

The first chapter is a general introduction that includes an overview of the context related to the research developed in this thesis. In particular, the concept of nanotechnology and nanomedicine are presented, as well as basic information about mesoporous silica nanoparticles, janus nanoparticles, and their interactions with biological systems. Finally, cancer disease characteristics, actual treatments, and the application of nanomaterials as therapy are described.

Next, in the second chapter, the general objectives of this Ph.D. thesis and the specific objectives addressed in the following experimental chapters are presented.

The third and fourth chapters describe two nanotechnology-based therapeutic strategies based on the development of nanomotors to improve cancer therapy. Specifically, the first experimental chapter presents a self-moving nanodevice for controlled drug release in response to intracellular glutathione (GSH). It is based on Janus gold-mesoporous silica nanoparticles functionalized with the enzyme catalase in the gold face, loaded with doxorubicin and capped with disulfide-linked oligo(ethylene glycol) (S-S-PEG) chains on the silica face. Once synthesized and characterized, the nanosystem motion capability through hydrogen peroxide (fuel) conversion into oxygen by catalase was confirmed. The proper gating mechanism of the nanodevice was tested in the presence of GSH, thus corroborating that cargo release only occurs in the presence of the

tripeptide. The cellular uptake and doxorubicin release capacity have been demonstrated in the human cervix cell line Hela, being increased in the presence of fuel.

Encouraged by the above results, chapter four describes a similar nanomotor design for antitumor therapy. In this case, the nanoparticle developed is composed of a Janus platinum-mesoporous silica nanoparticle, loaded with doxorubicin, and capped with S-S-PEG. As well as in the previous work, the catalytic decomposition of low concentrations of hydrogen peroxide, in this case by platinum, induced self-propulsion of the nanoparticles. The stimuli-responsive cargo release kinetic profile was obtained and its application was confirmed in a monolayer THP-1 cell culture and in a microchip device mimicking capillary vessels.

Chapters five and six focus on a new therapeutic strategy, empowering the immune system action on tumors to reach tumor cell death. In the first of these experimental chapters, JQ-1 and transforming growth factor-beta (TGF- β) siRNA-loaded nanoparticles were used as efficient tumor immunotherapy. This nanodevice is based on MSNs loaded with JQ-1 drug, functionalized with polyethyleneimine (PEI) and a siRNA targeting TGF- β was binding through electrostatic interaction. The endosomal escape and efficient cytosolic delivery of siRNA by PEI was accomplished by using these nanoparticles, along with the programmed death-ligand 1 (PD-L1) downregulation and TGF- β silencing. Lastly, its application was confirmed by triggering a specific immunogenic removal of tumor cells in melanoma A375 cells pre-treated with nanoparticles.

In chapter six, the development of a new communication-based immunotherapeutic approach is reported. In this case, we employ Janus gold-MSN functionalized with a peptide called pHLIP onto silica face and anti-PD-1 antibody bound to gold face (J-pHLIP-PD1). Tumor cell membrane is decorated by this nanodevice through pHLIP self-insertion, leaving exposed on the surface PD-1 antibody. This antibody catches circulating T lymphocytes, which express PD-1, and facilitates cytotoxic synapse and communication

with cancer cells, provoking immune system-induced-tumor leveling. Moreover, J-pHLIP-PD1 treatment-associated reduction of metastatic burden was also proven in a B16-F10-Luc metastatic model.

Finally, in the seventh and eighth chapter, the general discussion and conclusions derived from the presented experimental studies of this Ph.D. thesis are exposed. In conclusion, the preparation of mesoporous silica nanoparticles and their combination with metal particles and/or organic groups such as molecular gates, enzymatic effectors, environment modifiers, communication mediators, and drugs are presented in this thesis as a potential strategy to overcome tumor treatments limitations. We hope that the results obtained will open up new research opportunities and inspire the development of new advanced strategies with smart materials applied not only in the field of tumor therapy, but also in other biomedical areas to solve patient's needs.

Publications

Results of this PhD thesis and other contributions have resulted in the following scientific publications.

- **Lucena-Sánchez, E.**, Hicke, F.J., Ortuño-Bernal, A., Escudero, A., Jiménez-Alduan, N., Díez, P. García-Fernández, A. and Martínez-Máñez, R. Nanoparticles to re-establish communication between cancer and immune cells as a new immunotherapeutic strategy. *Project in progress* (2024)
- **Lucena-Sánchez, E.**, Hicke, F. J., Sandra Clara-Trujillo, García-Fernández, A. and Martínez-Máñez, R. Nanoparticle-mediated tumor microenvironment remodeling favors the communication with the immune cells for tumor killing. *Advanced Therapeutics*, 2400004, 1-11 (2024)
- Díez, P., **Lucena-Sánchez, E.**, Escudero, A., Llopis-Lorente, A., Villalonga, R. and Martínez-Máñez, R. Ultrafast Directional Janus Pt–Mesoporous Silica Nanomotors for Smart Drug Delivery. *ACS Nano*, 15, 3, 4467–4480 (2021).
- Llopis-Lorente, A., García-Fernández, A., **Lucena-Sánchez, E.**, Díez, P., Sancenón, F., Villalonga, R. and Wilson, D.A. Stimulus-responsive nanomotors based on gated enzyme-powered Janus Au–mesoporous silica nanoparticles for enhanced cargo delivery. *Chem. Commun.*, 55, 13164 (2019).
- Escriche-Navarro, B., Escudero, A., **Lucena-Sánchez, E.**, Sancenón, F., García-Fernández, A. and Martínez-Máñez, R. Mesoporous Silica Materials as an Emerging Tool for Cancer Immunotherapy. *Adv. Sci.*, 9, 2200756 (2022).
- Mayol, B., Dato, V., Rodríguez, M., **Lucena-Sánchez, E.**, Villalonga, A., Díez, P., Jimenez-Falcao, S., Sancenón, F., Sánchez, A., Vilela, D., Martínez-Ruiz, P., Martínez-Máñez, R. and Villalonga, R. An enzyme-controlled mesoporous nanomachine for triple-responsive delivery. *J. Mater. Chem. B*, 10, 6983-6990 (2022).

- Mayol, B., Díez, P., Sánchez, A., de la Torre, C., Villalonga, A., **Lucena-Sánchez, E.**, Sancenón, F. Martínez-Ruiz, P., Vilela, D., Martínez-Mañez, R. and Villalonga, R. A glutathione disulfide-sensitive Janus nanomachine controlled by an enzymatic AND logic gate for smart delivery. *Nanoscale*, 13, 18616-18625 (2021).

Abbreviations and Acronyms

A

Abs. Absorbance

ABTS. 2,2'-azino-bis-(3-ethylbenzthiazoline-6-sulphonic acid

APC. Antigen-presenting cell / Allophycocyanin

ApSF. Antheraea pernyi silk fibroin

APTES. (3-Aminopropyl)triethoxysilane

AuNPs. Gold nanoparticles

B

BCA. Bicinchoninic acid

BET. Brunauer, Emmett and Teller

BET domain. Bromo- and Extra-Terminal domain

BJH. Barret, Joyner and Halenda

BiTes. Bispecific T-cell engagers

BSA. Bovine serum albumin

C

CAR. Chimeric antigen receptors

C-dots. Cornell dots

CpG-ODN. CpG oligodeoxynucleotides

CTAB. Cetyltrimethyl-ammonium

CTL. Cytotoxic T lymphocyte

CTLA-4. Cytotoxic T lymphocyte antigen 4

Cy-7. Cyanine 7

D

D. Diffusion coefficient

DAMP. Damage-associated molecular patterns

DC. Dendritic cell

DIM. ApSF-coated MSNs loading with photosensitizers and doxorubicin

DLS. Dynamic light scattering

DMEM. Dulbecco's Modified Eagle's Medium

DMS. Dox-loaded MSNs

DNA. Deoxyribonucleic acid

Doxo. Doxorubicin

E

EDC. N-(3-dimethylaminopropyl)-N-ethylcarbodiimide hydrochloride

EDX. Dispersive X-ray spectroscopy

ELISA. Enzyme-linked immunosorbent assay

EPR. Enhanced permeability and retention effect

F

FBS. Fetal Bovine Serum

Fcc. Face-centered cubic

FDA. U.S. Food and drug administration

F_{drag}. Drag force

FFT. Fast Fourier transform

F_{prop}. Propulsion force

G

GM-CSF. Granulocyte-macrophage colony stimulating factor

GSH. Glutathione

H

HER2. Receptor tyrosine-protein kinase erbB-2

H&E. Hematoxylin and eosin

HPLC. High-performance liquid chromatography

HR-TEM. High resolution transmission electron microscopy

I

ICD. Immunological cell death

IDO. Indoleamine 2,3-dioxygenase

IFN- γ . Interferon gamma

IL-2. Interleukin 2

IUPAC. International Union of Pure and Applied Chemistry

IVIS. In vivo imaging system

I.V. Intravenously

L

LC. Liquid chromatography

M

MCS. Multicellular spheroids

MHC. Major histocompatibility complex

MPTS. (3-mercaptopropyl)trimethoxysilane

MSD. Mean squared displacement / Mass spectrometry detector

MSNs. Mesoporous silica nanoparticles

MSR. Mesoporous silica rods

N

NHS. N-hydroxysuccinimide

NIR. Near-infrared

NK cells. Natural killer cells

NPs. Nanoparticles

NTA. Nanoparticles-tracking analysis

O

OEG. Oligo(ethylene glycol)

P

PBS. Phosphate Buffered Saline

PCL-AuNC/Fe(OH)3-PAA. Poly(3-capro-lactone)-gold nanocage/ferric hydroxide-poly(acrylic acid)

PDI. Polydispersity index

PD-1. Programme cell death protein 1

PD-L1/2. Programmed cell death ligand 1/2

PEG. Poly(ethylene glycol)

PEI. Polyethyleneimine

PE. Phycoerythrin

PFA. Paraformaldehyde

PLGA. Poly(lactic-co-glycolic acid)

PRR. Pattern recognition receptors

PtNds. Platinum nanodendrites

PVP. Polyvinylpyrrolidone

PXRD. Powder X-ray diffraction

R

RBITC. Rhodamine B isothiocyanate

RES. Reticuloendothelial system

RNA_m. Messenger ribonucleic acid

RNA_i. Interference ribonucleic acid

ROS. Reactive oxygen species

S

SDS-Page. Sodium dodecyl-sulfate polyacrylamide gel electrophoresis

SEM. Scanning electron microscopy

siRNA. Small interfering RNA

STEM. Scanning transmission electron microscopy

T

TCR. T cell receptor

TEA. Triethylamine

TEM. Transmission electron microscopy

TEOS. Tetraethylorthosilicate

TGF- β . Transforming growth factor B

TGA. Thermogravimetric analysis

Th. T helper

TLR. Toll-like receptor

TME. Tumor microenvironment/extracellular matrix

TNF α . Tumor necrosis factor alpha

Treg cells. Regulatory T cells

U

UV. Ultraviolet

V

VEGF. Vascular endothelial growth factor

W

WGA. Wheat Germ Agglutinin

WST-1. Water-soluble tetrazolium salt

General index

GENERAL INTRODUCTION.....	3
1. NANOTECHNOLOGY AND NANOMEDICINE	3
2. MESOPOROUS SILICA MATERIALS.....	6
2.1. <i>Synthesis of mesoporous silica materials</i>	7
2.2. <i>Functionalisation of mesoporous silica materials</i>	8
2.3. <i>Characterization</i>	9
2.4. <i>Stimuli-responsive gated materials</i>	12
3. JANUS NANOPARTICLES	14
4. MESOPOROUS HYBRID MATERIALS FOR BIOMEDICAL APPLICATIONS	17
4.1. <i>Cell uptake, biocompatibility and biodistribution of hybrid nanoparticles</i>	17
4.1.1. MSNs.....	18
4.1.2. Gold nanoparticles.....	21
4.1.3. Platinum nanoparticles	23
4.2. <i>Clinical relevance of hybrid mesoporous silica nanoparticles</i>	24
5. NANOMEDICINE FOR CANCER THERAPY.....	27
6. NANOMOTORS	30
7. NANOTECHNOLOGY FOR IMPROVING CANCER IMMUNOTHERAPY	35

7.1.	<i>Immune evasion and main strategies in cancer immunotherapy</i>	35
7.2.	<i>Nanoparticles-based approaches</i>	41
8.	REFERENCES	45
OBJECTIVES		63
CHAPTER I STIMULUS-RESPONSIVE NANOMOTORS BASED ON GATED ENZYME- POWERED JANUS AU-MESOPOROUS SILICA NANOPARTICLES FOR ENHANCED CARGO DELIVERY		67
1.	ABSTRACT	71
2.	INTRODUCTION.....	71
3.	RESULTS AND DISCUSSION.....	73
4.	CONCLUSIONS	79
5.	MATERIALS AND METHODS	80
5.1.	<i>Chemicals</i>	80
5.2.	<i>General methods</i>	80
5.3.	<i>Synthesis of mesoporous silica nanoparticles (MSNs)</i>	81
5.4.	<i>Synthesis of gold nanoparticles (AuNPs)</i>	81
5.5.	<i>Synthesis of Janus Au-MSNs (S0)</i>	82
5.6.	<i>Synthesis of gated nanoparticles S1</i>	82
5.7.	<i>Preparation of enzyme-functionalized gated nanoparticles (S1_{cat})</i>	83

5.8.	<i>Preparation of S1_{dox-cat}</i>	83
5.9.	<i>Catalase activity</i>	84
5.10.	<i>Motion analysis</i>	85
5.11.	<i>Release experiments</i>	86
5.12.	<i>Experiments with Hela cells</i>	86
5.12.1.	Cell culture conditions.....	86
5.12.2.	Confocal microscopy studies of doxorubicin controlled release.....	87
6.	REFERENCES.....	87
7.	SUPPORTING INFORMATION.....	91
7.1.	<i>Materials characterization</i>	91
7.2.	<i>Motion analysis</i>	94
7.3.	<i>Release experiments</i>	95
CHAPTER II ULTRA-FAST DIRECTIONAL JANUS PT-MESOPOROUS SILICA NANOMOTORS FOR SMART DRUG DELIVERY		97
1.	ABSTRACT.....	101
2.	INTRODUCTION.....	102
3.	RESULTS AND DISCUSSION.....	105
3.1.	<i>Nanomotors synthesis and characterization</i>	105

3.2.	<i>Motion analysis</i>	109
3.3.	<i>Control Release Studies</i>	113
3.4.	<i>Self-propel and drug release capabilities in cells</i>	115
4.	CONCLUSIONS	121
5.	MATERIALS AND METHODS	122
5.1.	<i>Chemicals</i>	122
5.2.	<i>General methods</i>	123
5.3.	<i>Synthesis of mesoporous silica nanoparticles (MSNs)</i>	123
5.4.	<i>Synthesis of platinum nanodendrites (PtNds)</i>	124
5.5.	<i>Synthesis of Janus Pt-MSN nanoparticles (S₀)</i>	124
5.6.	<i>Synthesis of Janus Pt-MSN (Ru)-PEG (S₁)</i>	124
5.7.	<i>Synthesis of Janus Pt-MSN (Doxorubicin)-PEG (S₂)</i>	125
5.8.	<i>Peroxidase-like activity assay</i>	125
5.9.	<i>Motion analysis by MSD calculation</i>	126
5.10.	<i>Control release studies</i>	127
5.11.	<i>Cell culture conditions</i>	128
5.12.	<i>Viability Assay</i>	128
5.13.	<i>Cell uptake of nanomotors by confocal microscopy</i>	129

5.14.	<i>Cell uptake of nanomotors by TEM</i>	129
5.15.	<i>Self-propel and drug release capabilities of S_2 in microchip device</i>	129
6.	REFERENCES	130
7.	SUPPORTING INFORMATION	142
7.1.	<i>Nanomaterial characterization</i>	144
7.1.1.	Powder X-ray diffraction analysis.....	145
7.1.2.	N_2 adsorption-desorption isotherms	145
7.1.3.	Thermogravimetric assay.....	147
7.1.4.	DLS analysis.....	148
7.2.	<i>Motion analysis</i>	148
7.2.1.	Peroxidase-like activity assay.....	148
7.3.	<i>Control release studies</i>	151
7.4.	<i>Cell assays</i>	151
 CHAPTER III NANOPARTICLE-MEDIATED TUMOR MICROENVIRONMENT REMODELING FAVORS THE COMMUNICATION WITH THE IMMUNE CELLS FOR TUMOR KILLING		
1.	ABSTRACT	157
2.	INTRODUCTION.....	157
3.	RESULTS AND DISCUSSION.....	162
3.1.	<i>Design, synthesis, and characterization of nanodevices</i>	162

3.2.	<i>MSN(JQ1)-PEI-siRNA nanoparticles are efficiently internalized with the subsequent siRNA delivery.....</i>	165
3.3.	<i>MSNs as a versatile nanosystem for the codelivery of JQ-1 and TGF- β siRNA</i> <i>.....</i>	167
3.4.	<i>The codelivery of JQ-1 and TGF-β restores cancer cell death.....</i>	170
4.	CONCLUSIONS	172
5.	MATERIALS AND METHODS	173
5.1.	<i>General methods.....</i>	173
5.2.	<i>Synthesis of MSNs MCM-41 type</i>	173
5.3.	<i>Preparation of MSN(JQ1)-PEI and MSN-PEI nanoparticles</i>	174
5.4.	<i>Quantification of JQ1 delivered.....</i>	174
5.5.	<i>Assembly optimization of TGF-β siRNA to PEI-coated MSNs.....</i>	175
5.6.	<i>Synthesis of MSN(JQ1)-PEI-siRNA, MSN-PEI-siRNA, and MSN(JQ1)-PEI-BlockiT ..</i> <i>.....</i>	175
5.7.	<i>Cell culture conditions</i>	175
5.8.	<i>Toxicity studies</i>	176
5.9.	<i>Endosomal escape.....</i>	176
5.10.	<i>Evaluation of PD-L1 expression by Western Blot.....</i>	177
5.11.	<i>Flow cytometric determination of PD-L1 expression.....</i>	177

5.12.	<i>Silencing assay</i>	178
5.13.	<i>Evaluation of T-cell-mediated killing of melanoma cells</i>	178
5.14.	<i>Statistical analysis</i>	179
6.	REFERENCES	179
7.	SUPPORTING INFORMATION	188
CHAPTER IV NANOPARTICLES TO RE-ESTABLISH COMMUNICATION BETWEEN CANCER AND IMMUNE CELLS AS A NEW IMMUNOTHERAPEUTIC STRATEGY		195
1.	ABSTRACT	199
2.	INTRODUCTION.....	199
3.	RESULTS AND DISCUSSION.....	202
3.1.	<i>Design, synthesis, and characterization of nanoparticles</i>	202
3.2.	<i>J-pHLIP-PD1 nanoparticles attach to cancer cell membrane and capture of T-lymphocytes</i>	206
3.3.	<i>Cellular communication and therapeutic effect of J-pHLIP-PD1</i>	210
3.4.	<i>J-pHLP-PD1 reduces metastatic clusters in a B16-F10-Luc mouse metastatic model</i>	211
4.	CONCLUSIONS	215
5.	MATERIALS AND METHODS	216
5.1.	<i>General Techniques</i>	216

5.2.	<i>Synthesis of mesoporous silica nanoparticles</i>	217
5.3.	<i>Synthesis of gold nanoparticles</i>	217
5.4.	<i>Synthesis of Janus MSN-Au nanoparticles</i>	218
5.5.	<i>Synthesis of RBITC-APTES dye derivative</i>	218
5.6.	<i>Synthesis of J*-pHLIP and J-pHLIP</i>	219
5.7.	<i>Preparation of J-PD1, J*-pHLIP-PD1 and J-pHLIP-PD1 nanoparticles</i>	219
5.8.	<i>Cell culture conditions</i>	220
5.9.	<i>Evaluation of PD-1 expression by Western Blot</i>	220
5.10.	<i>Flow cytometric determination of PD-1 expression</i>	221
5.11.	<i>Evaluation of nanoparticle attachment to cell membrane</i>	221
5.12.	<i>Lymphocytes migration and retention assay</i>	222
5.13.	<i>Evaluation of therapeutic effect in cocultures</i>	222
5.14.	<i>B16-F10-Luc Metastatic Model</i>	223
5.15.	<i>Histological analysis of lungs for metastasis evaluation</i>	223
5.16.	<i>Isolation and immunophenotyping of plasma cells from ex vivo lungs of mice</i>	224
5.17.	<i>Statistical analysis</i>	224
6.	REFERENCES	225

7. SUPPORTING INFORMATION 233

DISCUSSION..... 239

CONCLUSIONS 247

General introduction

1. Nanotechnology and nanomedicine

Nanotechnology is defined as the understanding and control of matter on the order of nanometers, at dimensions between 1 and 100 nm, to create materials with fundamentally new properties and functions^{1,2}. It is involved in the design, synthesis, characterization and applications of materials and devices whose smallest functional organization is on the nanometer scale. A nanometer is one billionth of a meter and three orders of magnitude smaller than a micron, for example, a DNA molecule is about 2.5 nm long while a sodium atom is about 0.2 nm (Figure 1)^{3,4}. Besides, nanotechnology is not a single emerging scientific discipline, but rather it is a multidisciplinary area, a meeting of traditional science such as chemistry, physics, materials science, and biology³.

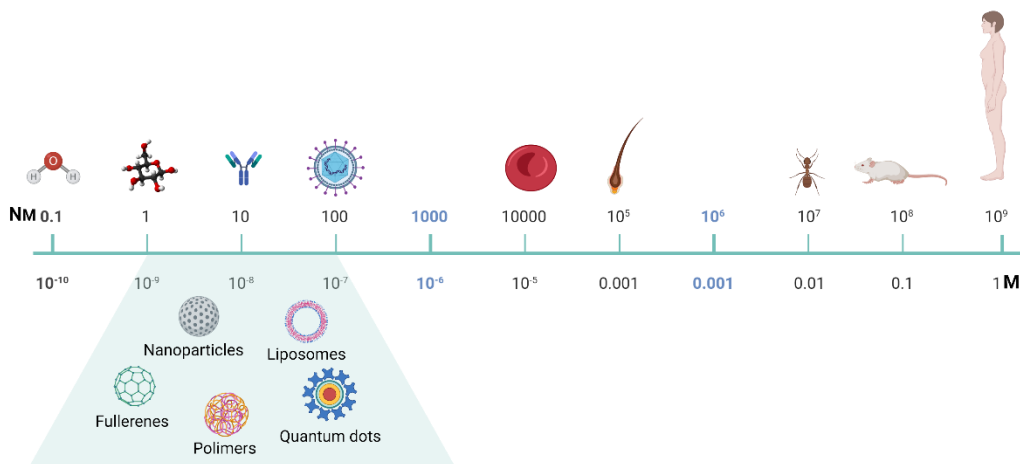


Figure 1. Scheme of nanomaterials scale compared to biomolecules, cells, and other items. Adapted from Chakraborty et al., 2016⁴

In 1959, Richard Feynman presented a lecture entitled “There’s plenty of room at the bottom”, outlining the principle of manipulating matter at the atomic level^{1,5}. He pictured new ways of thinking and is considered the father of nanotechnology¹. It was not until 15 years later when Norio Taniguchi used for the first time the term “nanotechnology” to describe semiconductor processes that occurred on the order of a nanometer¹. However, the capability to control the materials and devices’ molecular

synthesis and assembly to obtain tailor-made materials, with specific and controlled bulk chemical and physical properties is very recent^{3,6}. There has been an explosive growth of nanoscience and technology in the last decade, with the development of nanoscale materials that have unique optical, electronic, and magnetic properties depending on their size and shape^{6,7}. Some examples of these nanostructures are lipid micelles, polymeric, protein constructs, carbon nanotubes, and graphene as well as inorganic materials such as mesoporous silica nanoparticles, superparamagnetic iron oxide nanoparticles, quantum dots, gold nanoparticles, etc.⁷

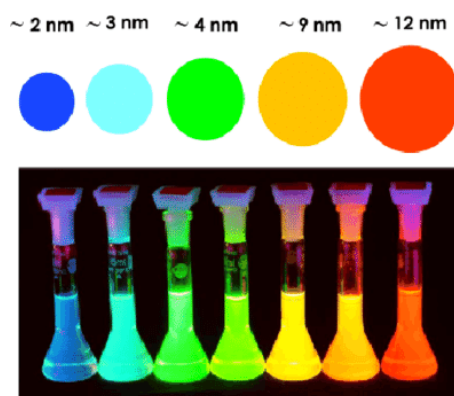


Figure 2. Fluorescence emission change of (CdSe)ZnS quantum dots depending on the size. Adapted from Pelaz et al., 2017⁸

Molecular self-assembling into macroscopic higher-ordered structures displays desirable chemical and physical properties not presented in the constituent molecules themselves³. Small changes in size and shape significantly affect the properties of the nanoparticles, for example, the change in size to the nanoscale of quantum dots can control their optical properties, the photoemission, and as a consequence the colour of the material (Figure 2)⁸. These size-dependent properties have been revealed in the last decades through powerful characterization tools such as electron microscopy, crystallography, spectroscopy, etc⁷. Their relevance is such that M. G. Bawendi, L. E. Brus and A. Yekimov have been awarded with the Nobel Prize in Chemistry 2023 for the

discovery and synthesis of quantum dots, which was an important step in the development of nanoscience⁹⁻¹¹.

Regarding nanotechnology, it has been applied to different fields, such as energy¹², drug delivery¹³, cosmetics¹⁴, biology¹⁵, biotechnology¹⁶, tissue engineering¹⁷, bioinformatics¹⁸ or agriculture and food^{19,20}. Nanotechnology has also been applied to medicine (nanomedicine) aiming as the application of nanotechnology and nanoscience to the prevention and treatment of human diseases²¹. In this field, nanoparticles used in disease treatments (nanotherapeutics) often overcome obstacles that limit conventional drugs, usually involving low toxicity, improved bioavailability and enhanced pharmacokinetics and therapeutic effect²¹.

Historical progress in nanomedicine can be divided into three stages. The first stage involved the discovery of the nanostructure such as liposomes. The second stage involved clinical validation and commercialization of some nanotherapeutics (for instance the first liposomal drug was approved in 1995 by the FDA). Finally, the third stage has witnessed rapid progress in the expansion and refinement of nanomedicine applications (Figure 3). However, despite exhibiting better clinical outcomes than conventional drugs, there are still many challenges to overcome, such as nonspecific toxicity or low efficacy. Hence, nanomedicine is in a constant progress and new advanced and smart nanodevices appear every year²¹.

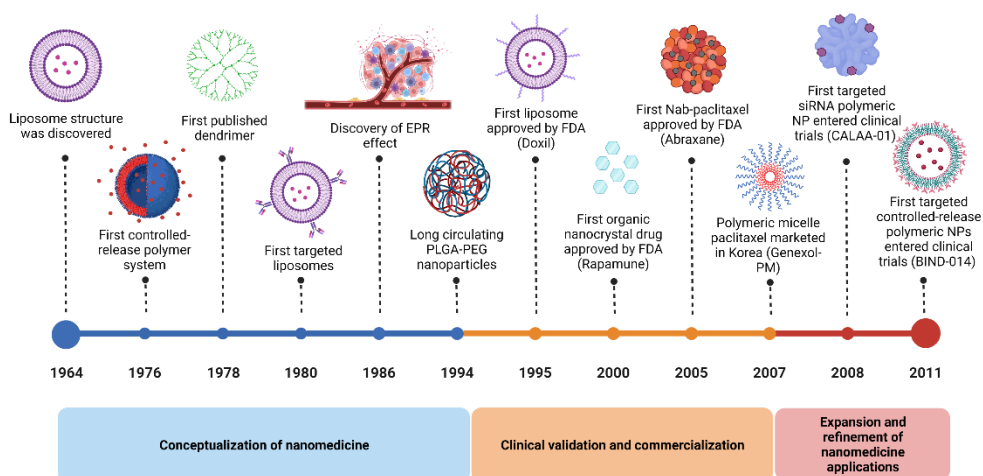


Figure 3. Milestones in nanomedicine. Adapted from Zhang et al., 2020²²

2. Mesoporous silica materials

During recent decades, the interest in porous materials has grown due to their physicochemical properties and their versatility. They can be classified according to the IUPAC based on their pore size into microporous, mesoporous, and macroporous materials which have pores sizes less than 2 nm, between 2-50 nm and greater than 20 nm, respectively²³. Among various mesoporous materials, mesoporous silica materials have attracted special attention after the discovery of a new family of molecular sieve called M41S by Kuroda et al. and Mobil Oil Scientists in 1990^{23–26}. The family M41S includes three main mesophase types: MCM-41 with hexagonal pores, MCM-48 with cubic pores and MCM-50 with lamellar structure²⁴. These materials are characterized by large surface areas (500-100 m²/g), ordered pore systems (2-10 nm) and high pores volumes (1 cm³/g)²⁷.

The unique properties of mesoporous silica nanoparticles (MSNs) such as controllable particle size, porosity, morphology, and high chemical stability make nanoparticles highly attractive for applications as carriers, diagnostic, catalysis, separation, and sensing^{24,25}. The first use of mesoporous silica as drug carrier was reported

in 2001²⁸ and since then, the use of mesoporous silica as a delivery system in biomedical applications has been widely studied²⁹.

2.1. Synthesis of mesoporous silica materials

Silica nanoparticles are conventionally produced through the hydrolytic sol-gel process using surfactants as structure-directing agents and involving the hydrolysis and condensation of silicon alkoxide precursors under acidic or basic catalysis^{23,25,29}. When the surfactant concentration is above the critical micelle concentration, it self-aggregates into micelles and the precursors condense and form an oxide network through siloxane bonds (Si-O-Si) around surfactant molecules²⁹. That leads to a colloidal solution composed of silica monomers that gradually evolves towards the formation of a gel^{25,29}. The synthetic process is based on the Stöber method described but performed in the presence of cationic surfactants³⁰. The type of surfactant together with concentration, pH and temperature have a strong influence on the self-assembling process and consequently, on the final mesostructure of the material²⁵.

In a typical synthesis of the MCM-41 type mesoporous silica nanoparticles, the silica source, tetraethylorthosilicate (TEOS), is added into a heated basic aqueous solution of the templating surfactant, cetyltrimethyl-ammonium bromide (CTAB). Once nanoparticles are formed, the surfactant template is removed through solvent extraction or calcination and as a result, spherical nanoparticles with a diameter of ca. 100 nm and 2D-hexagonally arranged pores with a size of ca. 2.8 nm (according to packed micelle structures of the surfactant) are obtained (Figure 4)^{27,31}.

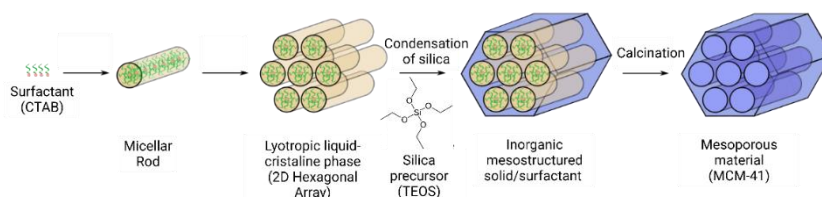


Figure 4. Schematic representation of the synthetic route of mesoporous silica MCM-41 type. Adapted from Carvalho et al., 2020³¹

2.2. Functionalisation of mesoporous silica materials

The possibility of introducing various organic functional groups, either through covalent bonding or electrostatic interactions, provides high level of versatility to the mesoporous silica scaffolds. The functionalisation is a suitable method to modify the properties of the surface of the mesoporous support such as reactivity, hydrophobicity, hydrophilicity, etc. The **covalent attachment** involves introducing organic structures in the silica framework using co-condensation or post-synthetic grafting methods²⁷.

- Co-condensation method. During the formation of particles, the hydrolysis of functional silanes is feasible, allowing the incorporation of molecules into the silica frameworks. Both the silica precursor and the organosilane are introduced simultaneously in the synthesis procedure and undergo condensation. In this case, surfactant removal is only suitable by extraction. This method enables the production of a silica material with a huge amount of uniformly distributed organic groups; however, they may impact on the interactions with the surfactant, leading to alterations in structure and morphology.
- Post-synthetic grafting. The functional groups are introduced to the exposed silica surface after the formation of the mesoporous silica. The surface of silica materials has a high concentration of silanol groups (Si-OH) that can anchor organosilanes.

Moreover, functional moieties can also be introduced through **electrostatic interactions**, for example, cationic polymers (such as polyethyleneimine) can be electrostatically adsorbed onto the negative particle's surface for instance to provide nucleic acid binding properties²⁷.

Another crucial property that makes mesoporous silica materials promising for drug delivery applications is the possibility to encapsulate different cargo molecules within their pores which may protect many therapeutic agents from degradation. The particles are usually loaded by soaking them in a drug solution, although there are other

methods such as impregnation^{27,32} The combination of the payloads with the functional modifications might allow for control cargo release at the targeted tissues, with no premature delivery during their circulation²⁷.

2.3. Characterization

Given the nature of mesoporous silica nanoparticles applications, it is crucial to characterize these nanoparticles using different physical, chemical, and biological techniques³³.

Particle shape and size is the most basic information collected and determines the suitability of nanoparticles for a specific application. Dynamic light scattering (DLS) and electron microscopy are used to obtain information about nanoparticles morphology. **DLS** is the most common approach to analyze hydrodynamic particle size and distribution. DLS measures light interference based on the Brownian motion of nanoparticles in suspension. **Electron microscopy** can be employed to reveal the details of the mesoporous structure and nanoparticles shape and surface (Figure 5.A)^{33,34}. Transmission Electron Microscopy (TEM) utilizes energetic electrons to obtain the finest morphological, compositional, and crystallographic information from samples^{35,36}. Among electron microscopy techniques, there is also scanning transmission electron microscopy (SEM) (Figure 5.B)³³. Electron microscopies can be combined with energy dispersive X-ray spectroscopy providing information on mesoporous silica material elemental composition^{31,32}. However, biomolecule-coated particles might result in poor quality electron microscopy images³³.

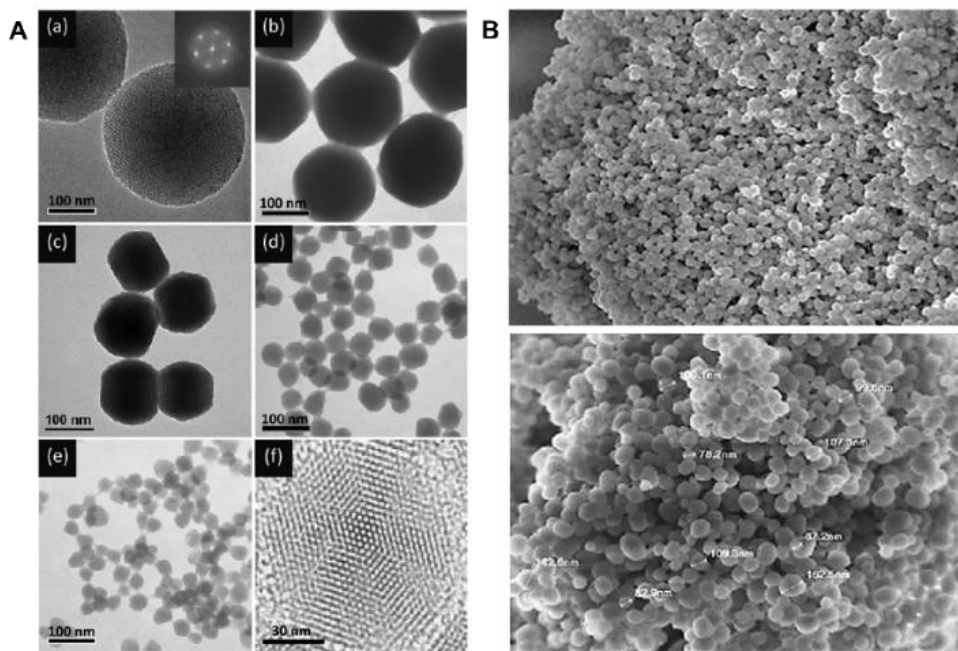


Figure 5. A. TEM images of mesoporous silica with different average sizes: a) 280 nm; inset: FFT analysis of the TEM image; b) 170, c) 110, d) 50, e) 30 nm. f) High-resolution TEM image of a single particle in (c). Reprinted with permission from Lu, F. et al., 2009³⁴. B. SEM micrographs of the produced MCM-41 particles. Adapted from Christoforidou, T. et al., 2021³⁷.

Surface data can be obtained using topography techniques, such as gas adsorption-desorption isotherms. These curves give information of the amount of N_2 adsorbed onto the porous material as function of the relative pressure. This technique, based on the **Brunauer-Emmett-Teller theory** and **Barrett-Joyner-Halenda analysis**, is employed for surface area and pore size estimation, respectively. Furthermore, surface charge analysis is determined by **Zeta potential** measurement. Nanoparticles have a charge on the surface that attracts a thin layer of counter ions to the nanoparticle surface (Stem layer). This double layer travels with the nanoparticle as it diffuses throughout the solution and the velocity is proportional to the electrical potential of the particle at the shear plane. This electrical potential is known as the zeta potential^{33,36}. Its values typically range from +100 to -100 mV and are predictive of the colloidal stability of the solution³³.

Besides, we can obtain information about the structure of crystalline materials by using **X-ray diffraction**. When an incident beam of monochromatic X-rays interacts with a target material, the scattering of those X-rays from atoms occurs. In materials with regular structures, the scattered X-rays undergo constructive and destructive interference. X-rays are characteristics of a certain ordered material, and the diffraction pattern depends on the atomic arrangement and the type of atoms^{32,35,38}. In the case of MCM-41 based mesoporous silica, the typical pattern is characterized by four peaks appearing at low angles indexed as (100), (110), (200), and (210) Bragg peaks (Figure 6).

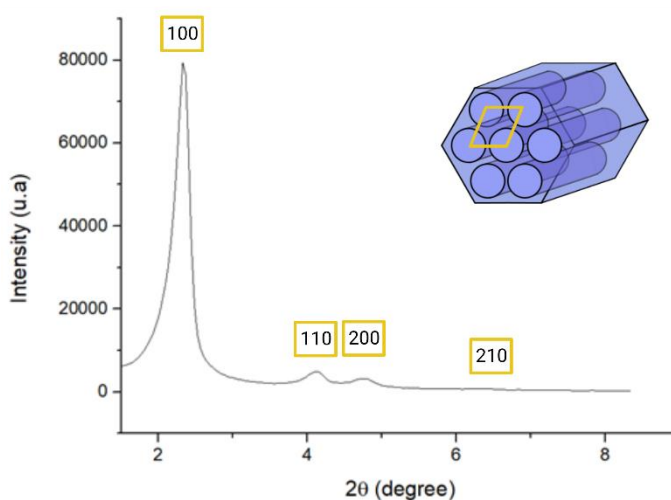


Figure 6. Scheme of unit cell and characteristic PXRD pattern of MCM-41 material with its typical Bragg peaks, indexed as (100), (110), (200), and (210).

Chemical knowledge about nanoparticles can be also acquired through characterization, using methods like **UV-visible spectroscopy**. This is a spectroscopy in which light of the UV-visible region is absorbed, and it is a simple and reliable method to monitor load and delivery from mesoporous silica of molecules displaying absorption bands in the UV-visible range. For instance, this can be used for the quantification of the efficiency of cargo encapsulation and to determine cargo release kinetics³⁹.

The organic content in the prepared materials can be determined by thermogravimetric measurements (TGA) or high-performance liquid chromatography

(HPLC). **Thermogravimetric analysis** (TGA) allows the monitoring of the mass as a function of temperature³⁵. It provides information concerning the mass and composition. In TGA, the material is heated and the components with different degradation temperatures decompose and/or vaporise, and a change of mass is recorded. The type and quantity of organic matter can be determined³⁸. **High-performance liquid chromatography** stands as the most used chromatographic technique, serving for the separation and quantification of chemical substances. In essence, it involves the injection of the liquid sample into a flowing mobile phase that passes through a separative column comprising a stationary phase. The molecules present in the sample are retained by the column according to their nature. The number and strength of the interactions between the molecules and the column filling dictate the timing of their elution. Further, a detector system is employed to identify the presence of a compound, yielding a chromatogram, which ideally shows peaks for each compound⁴⁰.

2.4. Stimuli-responsive gated materials

Gated materials are predesigned to finely tune the movement of chemical or biochemical species from voids of porous supports to a solution and vice versa, in response to a selected stimulus⁴¹. Such gated materials are composed mainly of two subunits: (1) a porous inorganic scaffold to load a cargo (e.g. dyes, fluorophores, small biomolecules, drugs, etc.) and (2) certain molecular entities grafted onto the external surface, which work as molecular gates (also known as gatekeeper or nanovalves) allowing on-command delivery of the mass from pores⁴²⁻⁴⁴. The role of gatekeepers is to confine the cargo in the inner of the porous support and to allow its release in the presence of a specific stimulus which makes the gate change its size/shape/conformation or be simply displaced. Moreover, gated nanoparticles can be designed to target selected cells or tissues by adding biological ligands onto their surface⁴⁵.

In regard to the inorganic support, one of the most commonly used material for obtaining gated nanodevices is the mesoporous silica material MCM-41 according to their unique characteristics as high loading capacity, biocompatibility, chemical inertness and high surface area which can be easily functionalized using the well-known alkoxy silane chemistry^{41,43-46}. Different nature cargos (e.g. dyes, fluorophores, small biomolecules, and drugs) have been loaded into the inorganic ordered pore network present in MCM-41 scaffold⁴⁶ and its external silanol-containing selectively modified by stimuli responsive groups (Figure 7)⁴²⁻⁴⁴. In terms of *in vitro* and *in vivo* applications two types of stimuli can be identified: (i) endogenous (including pH, redox, biomolecules, enzymes, etc.) and (ii) exogenous or external stimuli (including temperature, light, magnetic fields, ultrasound etc.)⁴⁶.

In addition, these materials can act as controlled drug delivery systems, which can lead to numerous applications in the field of human health⁴⁴. A drug-delivery system can be described as a formulation that permits the tailoring of release profiles with spatial, temporal and dosage control^{43,44}. This strategy achieves a significant reduction of side effects caused by drug's impact on "off-target" areas as well as safeguarding the drug against premature degradation or solubilization. Another crucial element is the capacity of the drug to be released upon applying a stimulus to the carrier, enabling the unloading of its cargo at the target site⁴⁶. The silica mesoporous material MCM-41 was proposed as a drug delivery system in 2001 and since then a huge variety of complex and advanced drug delivery systems based on this support has been developed⁴⁷.

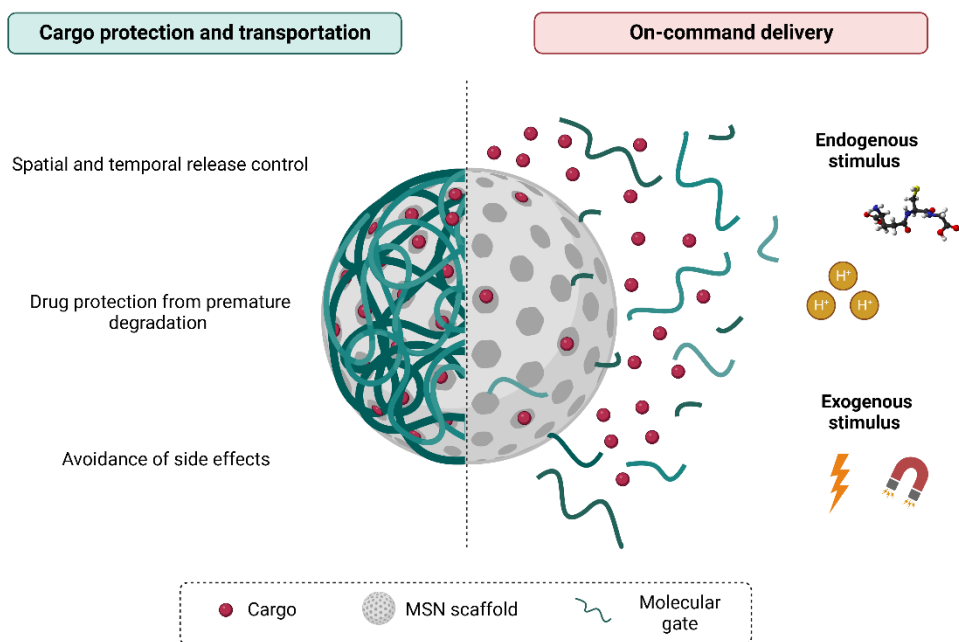


Figure 7. Scheme of the operation of a molecular gate and the principal components present in a drug delivery system.

3. Janus nanoparticles

Nanotechnology has evolved extremely rapidly and expanded into a broad variety of areas in the medical, industrial, chemical, and physical fields in recent years. One of the major goals in materials science is the preparation of novel biologically inspired nanomachines and smart drug delivery systems. This requires the artificial design of nanoparticle structures and endows them with new chemical functionalities⁴⁸.

Hybrid nanoparticles can be defined as well-organized nanomaterials consisting of two or more types of individual nanocomponents. The nanocompounds integrating hybrid nanoparticles can be bound via organic/inorganic molecular bridges or directly attached to one another⁴⁸. Among these nanomaterials, the preparation of anisotropic colloidal particles which exhibit two surfaces of different chemical compositions have recently aroused interest in scientific community. These so-called “Janus nanoparticles”, referring

to the dual-faced Roman god, Janus, have two faces which can be independently modified with selected ligands^{49,50}. The majority of nanometre-sized “Janus particles” refer to bifunctional heterodimers that consist of two different materials segregated in the particle cores, obtaining building blocks and controlled assemblies of structural units into functional architectures⁵⁰. In addition to the properties of each homogeneous component present in Janus, they include also new physicochemical properties in the same particle, leading to the development of novel functionalities in different areas⁵¹.

A typical synthetic procedure of Janus nanoparticles involves partial masking of the particle’s surface prior to selective engineering and functionalization of the exposed area⁵⁰. This means that asymmetric functionalization of the nanoparticles is achieved by exposing only one hemisphere (or a portion) of their surface to an environment, where reaction is carried out, while the remaining part of the surface is protected⁵². The surface functionalization includes different techniques, such as coating by vapor deposition of metal thin films/particles, electrostatic deposition, layer-by-layer self-assembly, the Pickering emulsion method, photopolymerization in microfluidic devices, cross-linking of block copolymers, etc⁵⁰. Among them, the Pickering emulsion method is one of the most feasible procedures for preparing Janus particles. This method consists of the immobilization of homogeneous particles on an interface between two liquid immiscible phases. It generally employs an oily phase (wax) and an aqueous phase (water/ethanol) mixture stabilized by particles at high temperature. After cooling down this emulsion below its melting temperature, the wax is solidified, and the particles are partially embedded at the interface of the Pickering emulsion. At this point, one part of the particle is unmasked and exposed to the liquid phase whereas the other is fixed in the wax, thus allowing the chemical modification of the desired area^{52,53}. This method was adapted by Villalonga, Martínez-Máñez and co-workers to develop the synthesis procedure used in this thesis for the preparation of Janus Au-MSN and Pt-MSN⁴⁹. In particular, as shown in Figure 8, the synthesis of Janus Au-MSN and Pt-MSN is based on the use of MSNs which are partially trapped on wax and exposed for further partial functionalization. The

exposed face is decorated with reactive thiol groups by reaction with a thiolated silane derivative (mercaptopropyl trimethoxysilane), following by the chemisorption of gold or platinum nanoparticles upon reaction with the thiol moieties. Finally, the wax is dissolved in organic solvents like hexane or chloroform and the particles recovered.

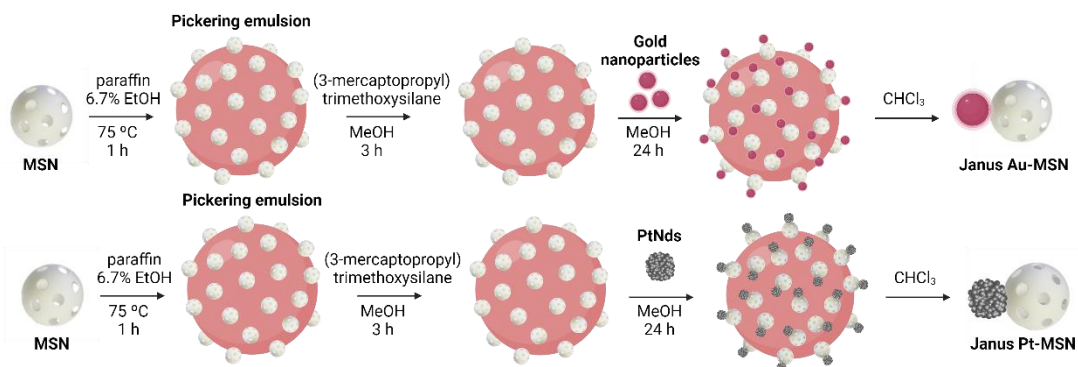


Figure 8. Schematic representation of the preparation of the Janus MSN-Au and MSN-Pt nanoparticle based on the pickering emulsion method.

These Janus particles have unique properties⁴⁶ and have been used for the development of self-propelling micro/nanomotors, catalysts, biological sensors, drug delivery platforms, etc^{51,53}. For instance, the development of self-propelled artificial motors, opens new potential applications in the complex biological environment. The self-propulsion capability of these motors helps to improve drug transport and overcome biological barriers compared to non-propelled nanoparticles⁴⁵. An example was reported by Xuan, M. and co-workers in which a Janus nanomotor based on mesoporous silica nanoparticles with chromium/platinum metallic caps was loaded with doxorubicin and propelled by decomposing hydrogen peroxide to generate oxygen as a driving force. The nanoparticles internalization inside tumor cells is higher when they are setting in motion⁵⁴. Further, Janus nanoparticles have been also explored as drug delivery nanocarriers taking advantage of their two different faces for combining several drugs, as it happens in the work developed by Zhang, L. et al. Herein, a unique amphiphilic PCL-AuNC/Fe(OH)₃-PAA Janus nanoparticle was developed to simultaneously preserve and co-deliver the hydrophilic drug doxorubicin and the hydrophobic molecule docetaxel, along with a significant improvement in cancer therapy effectivity⁵⁵.

4. Mesoporous hybrid materials for biomedical applications

The current advance of nanotechnology has led to the development of a large number of nanomaterials for biomedical applications, such as drug delivery, diagnosis and imaging. Silica-based mesoporous materials are progressively gaining value in biomedical applications due to two distinctive features: a well-established behaviour in drug delivery and their versatility for the preparation of advanced hybrid materials. In the last decade, the integration of mesoporous silica with other nanomaterials has facilitated the combination of multiple components into single entities at the nanoscale, allowing additional functionalities to be integrated into nanosystems with drug-loading capabilities⁵⁶. Moreover, the design of smart functional nanosystems for biomedical applications requires a thorough understanding of the mechanisms by which nanoparticles interact with biological systems⁵⁷. Cell uptake and biodistribution are key aspects to be taken into account when designing suitable nanomedical devices³⁴. In addition, biocompatibility, degradability and disposal are factors that must also be considered for the translation of MSNs into medical areas⁵⁶. In order to reach clinical approval, the synthesis of nanoparticles that possess optimal *in vivo* characteristics is required. These characteristics are crucial not only for achieving therapeutic efficacy but also for addressing concerns related to biosafety.

4.1. Cell uptake, biocompatibility and biodistribution of hybrid nanoparticles

Since hybrid nanoparticles have only recently been developed and their research and clinical translation are still in their infancy, there are not common protocols or a consensus regarding the way a nanoparticle should be studied in terms of biodistribution, excretion and potential toxicity, and thus no relevant and accurate studies on their behaviour in complex organisms. Thereby, this section addresses separately the different materials employed in the doctoral thesis.

4.1.1. MSNs

Since the cell membrane is the biggest barrier for intracellular drug delivery, it is essential to investigate the cellular internalization and trafficking of MSNs. Generally, the uptake pathways are divided in two groups: phagocytosis and pinocytosis (micropinocytosis and endocytosis). In particular, phagocytosis occurs in specialized cells such as monocytes, neutrophils, macrophages, etc., for particles with minimum size of 1 μm . Small nanoparticles with sizes under 200-300 nm (as usually MSNs have) are taken up via endocytic pathways⁵⁸. Endocytosis is mediated by at least four basic mechanisms: clathrin-mediated endocytosis, caveolae-mediated endocytosis and clathrin-caveolae and dynamin-independent endocytosis⁵⁷. Particle size determines the mechanism and rate of cell uptake, as well as their ability to permeate through tissues³⁴. In addition, the endocytic process occurs through specific or non-specific cellular uptake, usually depending on the surface properties of the nanoparticles. Recent observations in biological systems suggest that other physical parameters of nanoparticles, such as shape and surface charge, can also affect their uptake by cells and induce cellular responses⁵⁷. After being internalized, MSNs are transported to large vesicular endosomes and then fused with lysosomes. Several strategies, such as PEI coating, are able to achieve lysosomes disruption and escape from them^{59,60}. Briefly, endocytosis is a very complex process and the prediction of which endocytic pathway will be followed by nanoparticles is a really arduous task, there is no “rule of thumb”⁶¹.

Furthermore, biodistribution refers to the process of monitoring the localization of compounds of interest within the organs and tissues of experimental animals, enabling the assessment of their accumulation in different regions of the body. Systemic nanoparticle distribution is revealed in the bloodstream along with the generation of protein corona (proteins from plasma adsorbed on the nanoparticles' surface). The reticuloendothelial system (RES) cells opsonize the nanoparticles and accumulate in these organs (liver, spleen, and lung) as a result (Figure 9)⁶²⁻⁶⁴. Besides, MSNs nanoparticles tend

to accumulate preferentially in tumors by the passive mechanism EPR effect⁶⁵. In addition, there is an effect of size and shape in the nanoparticles' biodistribution; smaller nanoparticles have longer blood circulation lifetimes whereas liver and spleen accumulation increases with the size. According to the shape of the nanoparticles, MSNs with a short rod-shape accumulate in the liver and long rod-shaped nanoparticles accumulate in the spleen. Another property that affects the biodistribution of nanoparticles is the chemical properties of the surface, such as the charge of the nanoparticles. Experimental investigations have demonstrated that positively charged nanoparticles are excreted from the liver into the gastrointestinal tract and subsequently eliminated from the animal through feces. Conversely, negatively charged MSNs tend to be sequestered within the liver^{64,65}. Along with this, the modification of nanoparticles surface has a direct impact on distribution, for example a PEG coating on the nanoparticles evades phagocytosis and collection by RES, thus prolonging their blood circulation lifetime⁵⁶.

Regarding biocompatibility, silica has been catalogued as "Generally Recognized as Safe" by the FDA and bulk silica is widely present in food additives and cosmetic products, which indicates low toxicity in the body. Despite these facts, one of the key challenges for clinical translation is the possibility of prolonged retention within the body. Recent preclinical research using MSNs provides supporting evidence related to nanoparticle degradation and excretion. The MSNs framework is prone to be hydrolysed when exposed to aqueous media and its physical properties (surface area, pore size, shape, aggregation, etc.) determine the rate of degradation. It is generally slow, as much as 32% of biodegradation after 15 days for MSNs with a significant Si-O-Si bond condensation. In addition, calcination, and the absence of mesopores in silica nanoparticles reduce the degradation rate, as opposed to the acceleration caused by large pore size and surface functionalisation, especially with polymers^{64,66}.

On the other hand, the possibility of glomerular clearance relies on the size of nanoparticles, MSNs are too large to experience rapid renal clearance (> 6 nm) but not to be caught by the reticuloendothelial system with the consequent renal and hepatobiliary excretion (Figure 9). First, MSNs undergo degradation into smaller fragments that enter again into the bloodstream before elimination. Then, these fragments are filtered and eliminated through the urine in the case of renal excretion. For hepatobiliary clearance, the fragments are transported to the liver, processed in the biliary conduct, and eliminated through feces⁶⁷. Accordingly, the excretion of MSNs through the urine and feces has been reported by various groups, with up to 94% of excretion in 4 days after injection^{64,65}.

Recently MSNs-associated toxicity has been investigated, identifying hepatotoxicity and spleen alteration as the main subchronic toxic effects. However, given the insufficient and variability between available data, it is challenging to draw firm conclusions in this area^{65,68,69}. Another main concern is hemolytic activity given that it has been related to the presence of silanol groups in the surface interacting with blood cell membrane phospholipids. Several works have addressed this issue and demonstrated that it can be avoided by modifying these groups^{65,70}. Overall, the safety has to be evaluated in each case considering the specific physicochemical characteristics of each nanoparticle that determine their biological activity as well as factors such as route of administration, dose, duration, frequency, etc.

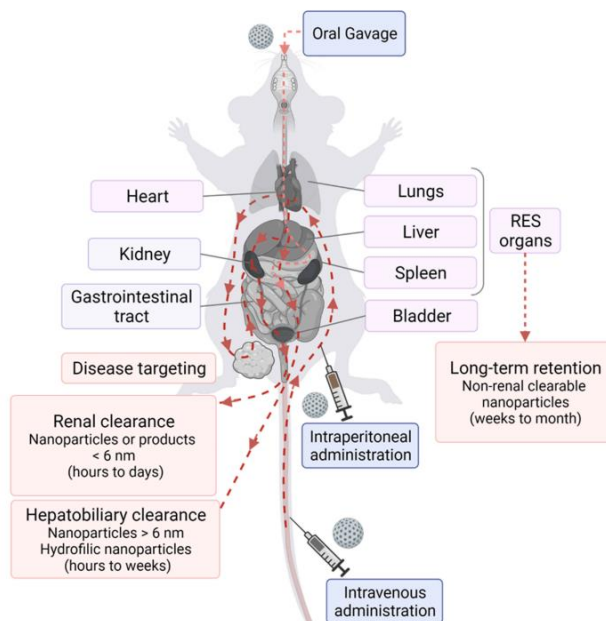


Figure 9. Scheme of the main pathways from MSNs clearance. Reproduced with permission from Lerida-Viso et al., 2023⁶⁴

4.1.2. Gold nanoparticles

In the case of gold nanoparticles, the main cell uptake mechanisms are clathrin- and caveolin-mediated endocytosis⁷¹. Moreover, gold nanoparticles exhibit toxicity mediated by oxidative damage to cell and tissues. The most affected organs are the liver, spleen and kidney. However, the extend of toxicity depends on various factors including size, shape, surface modification and administration route. Research on the toxicity of gold nanoparticles has yielded contradictory findings, particularly regarding the size and surface characteristics. Most of the studies suggest that small-sized particles show cytotoxicity and DNA damage due to their high surface area-to-mass ratio^{72–75}. Conversely, large particles seem to be non-toxic even at higher concentrations^{72,73}. The shape of nanoparticles also affects cells uptake and toxicity, with rod-shaped particles exhibiting greater toxicity and less efficient internalization compared to spheres due to the presence of CTAB used in their synthesis^{72,75}. Regarding surface, the charge plays a

role, as cationic nanoparticles may disrupt cell membranes, while anionic counterparts may be non-toxic⁷⁵. Surface modification, such as PEGylation, can mitigate toxicity by preventing nonspecific binding and enhancing circulation time^{72,75,76}. Moreover, toxicity varies with administration route, with intravenous injection generally considered the safest. Intraperitoneal administration shows a slightly higher toxicity than intravenous injection but less than oral administration^{72,75}.

For example, higher toxicity was found when oral and intraperitoneal administration was performed in comparison with intravenous injection⁷⁷. According to the size, numerous studies have suggested that as it is reduced, the cytotoxic effect is increased. Pan et al. reported that 1.4 nm gold nanoparticles yielded necrosis in L929 fibroblasts or cervix carcinoma epithelial cells (Hela), whereas larger ones of approximately 15 nm were shown to be noncytotoxic⁷⁸. A hypothesis that could explain the small-sized gold nanoparticles associated toxicity is the presence of a high surface area relative to their volume⁷⁵. This leads to broadened absorption capacity, thus increasing the possibility of interacting with biomolecules. Nonetheless, other studies reported a higher cytotoxic effect for larger gold nanoparticles⁷⁹, which therefore makes it difficult to establish a systematic relation between nanoparticle size and toxicity from the literature reported. In the same way, gold nanoparticles shape and surface charge can also modulate their toxicity. Rods gold particles seemed to be the most toxic to human cells, while spheres were the safest^{75,80}. Regarding surface charge, cationic gold nanoparticles were moderately toxic unlike anionic ones which were nontoxic⁸¹. The most important impact of gold nanoparticles is their ability to cause DNA damage, either directly by binding protein or DNA or indirectly through the generation of ROS⁸².

Although persistent accumulation of gold nanoparticles in liver and spleen has been described, size plays a crucial role in nanoparticle biodistribution^{72,76}. Larger particles predominantly accumulated in the liver and spleen, with minimal distribution in other organs^{74,76}. However, smaller nanoparticles displaying wider in vivo distribution across

organs such as the thymus, kidney, heart, lung and brain, in addition to the liver and spleen^{76,83}. This accumulation suggest inefficient removal mechanisms since renal clearance is desirable for preventing nanoparticle accumulation in healthy organs, but the size and charge of nanoparticles influence renal clearance efficiency^{72,76}. For instance, smaller nanoparticles (<6 nm) are excreted faster via renal excretion and found in urine, while larger ones are accumulated in the liver and cleared through the hepatobiliary system⁷⁴⁻⁷⁶. Excretion of gold nanoparticles occurred within 30 days for most particles, although traces remained in the liver and spleen for up to 90 days, especially for larger particles^{74, 83, 82, 84, 85}.

4.1.3. *Platinum nanoparticles*

There are few studies about platinum nanoparticles biocompatibility, biodistribution and excretion. Platinum nanoparticles were correlated with oxidative stress, DNA damage and cell cycle arrest⁸⁶. Further observations support the release of Pt ions as a mechanism of cytotoxicity and cellular damage^{87,88}. As for other nanoparticles, the distribution profile and stability of Pt nanoparticles within the body are determined by their physicochemical characteristics. Various surface modifications and particle sizes can influence the interaction of nanoparticles with different organs and tissues, consequently impacting their biocompatibility. For instance, several studies examined the toxic effects of polymer-coated platinum nanoparticles *in vivo*. Small nanoparticles (1 nm) induce nephrotoxicity while those of larger sizes show a safer biocompatibility profile. Intriguingly, the administration of platinum nanoparticles was found to decrease inflammatory cytokine production *in vitro*^{86,87}.

About the biodistribution of platinum nanoparticles in tumor-bearing mice, one study from Sun, C. and co-workers showed an accumulation in the liver and spleen after 24 h exposure. Otherwise, tumors accumulate approximately 3% of the injected platinum. Moreover, after the course of weeks, nanoparticles accumulated in other organs or

tissues were also transported to the liver where they are unable to be metabolically processed for excretion or removed at the studied time. The increase in total Pt in the spleen, a portion of the lymphatic system, suggests that some particles are scavenged through the lymph system and trafficked to the spleen⁸⁸. Despite the nanoparticles were well tolerated, further preclinical work is still necessary to address biosafety issues when designing nanomaterials containing platinum for medical applications.

4.2. Clinical relevance of hybrid mesoporous silica nanoparticles

Nanoparticle-based therapies have found their way into various clinical applications, with more than 30 nanoformulations approved and over 100 in clinical trials (Figure 10)⁸⁹. Furthermore, the rapid development of two COVID-19 mRNA vaccines based on lipid nanoparticles has showcased the clinical potential of nanoparticle-based therapeutics and initiated a new wave of preclinical and clinical research endeavors to develop nanoparticle-based systems^{89,90}. Other examples of approved nanoparticle-based formulations in the clinic include anti-cancer medications (Doxil, Abraxane, Myocet and MEPACT), contrast agents, anaesthetics, antifungal drugs, RNAi drugs and vaccines⁸⁹.

In particular, silica nanoparticles are being explored as multifunctional delivery carriers in a variety of biomedical applications, including diagnosis, sensing and drug delivery. As a material, colloidal silica has been employed as a glidant in tablet manufacturing for numerous decades and the widely used food additive E551 consists of silica nanoparticles with a size of 100 nm. The safety profile of silica nanoparticles in humans is evident from 11 clinical trials and 2 clinical studies. Silica nanoparticles administered orally have demonstrated good tolerability with no notable adverse effects, enhancing the pharmacokinetic profile of hydrophobic drugs. In one of the first human studies, a silica-lipid hybrid formulation was used to orally deliver ibuprofen to 16 healthy adults, demonstrating an increase in bioavailability by 1.95 times^{89,91}. In a separate clinical trial involving 12 healthy adults, the oral administration of mesoporous silica

nanoparticles resulted in a 54% improvement in the bioavailability of fenofibrate when compared to the commercially available formulation^{89,91}. In addition to drug delivery, silica nanoparticles have been applied for plasmonic resonance therapy to treat cardiovascular diseases, to detect difficult-to-treat tumors and to thermally ablate tumors⁸⁹. In contrast to organic nanoparticles, silica particles offer the advantage of facile modification with iron oxide and gold, enabling their utilization for localized plasmonic and thermal ablation therapy. Encouraging findings from a completed phase I clinical trial demonstrated that plasmonic resonance therapy employing ferromagnetic core-shell silica-gold nanoparticles resulted in a significant reduction of coronary atherosclerosis (NANO-FIM; NCT01270139)^{64,89,92,93}. Moreover, the silica-containing “Cornell dots” (C-dots) was approved by the FDA in 2012 for their use in clinical trials (NCT01266096, NCT02106598 and NCT03465618). They are ultrasmall inorganic silica nanoparticles (6-10 nm) developed as a fluorescent tool for sentinel lymph node detection prior to cancer surgery. Their small size allows them to be rapidly cleared by the kidneys, without any adverse effects documented^{94,95}.

Besides, different clinical trials based on PEGylated gold-silica nanoshells are conducted by the company AuroLase (Nanospectra Bioscience) for the treatments of different types of cancer (NCT00848042, NCT02680535, NCT04240639, and NCT04656678). Although the estimated finished date for this clinical trial is November 2023, preliminary findings demonstrate that it is a technically feasible and safe procedure for the removal of tumors⁹⁶.

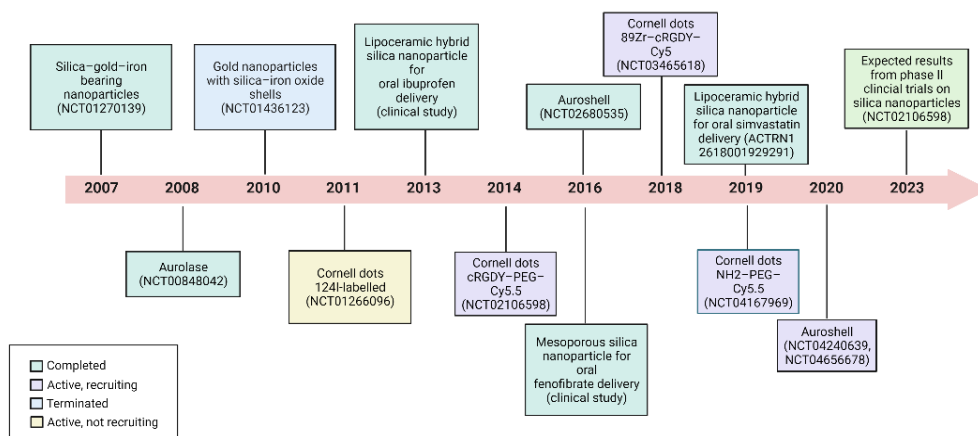


Figure 10. Clinical trials of silica nanoparticles. Adapted from Janjua et al, 2021⁸⁹

Despite the demonstrated safety and efficacy from clinical trials, the rate of clinical translation of silica nanoparticles remains sluggish. For instance, the development of gold shell-silica nanoparticles began in the 1990s, yet it took approximately two decades for this technology to progress to clinical trials. Organic nanoparticles like liposomes and lipid nanoparticles have been successfully translated into clinical applications. However, compared with organic nanoparticles, silica nanoparticles possess numerous advantages that warrant further clinical investigations. By modulating their structural and physicochemical properties, such as size, charge, surface, functionality, and shape, silica nanoparticles can facilitate drug delivery across biological barriers. Additionally, they can easily be hybridized with other inorganic particles, such as gold and platinum nanoparticles⁸⁹. Nonetheless, several key hurdles must be addressed for successful clinical translation. These challenges include establishing safety in the context of chronic exposure, determining long-term toxicological profiles for various routes of administration, exploring reliable scale-up methods, and synthesizing reproducible silica nanoparticles with minimal batch-to-batch variation⁸⁹. Even given that some challenges have still been overcome, the increasing knowledge about MSNs in the body joint to the incipient improvements in silica mesoporous nanoformulations suggested the suitability of hybrid mesoporous silica nanoparticles to reach clinical translation.

5. Nanomedicine for cancer therapy

Cancer is one of the major causes of death worldwide and surgery, radiotherapy and chemotherapy are the three major therapeutic approaches for its treatment. Surgery and radiotherapy are useful in achieving local control of the primary tumor. Moreover, to prevent the development of metastasis or improve tumor reduction, these local treatments are usually combined with chemotherapy⁹⁷. In fact, chemotherapy remains the treatment modality of choice for most advanced cancers, alone or in combination⁹⁸. Despite advances in the development of new chemotherapeutic drugs, they often fall short of the goal of controlling tumor progression due to their limitations⁹⁹. Chemotherapeutics often exhibit a lack of aqueous solubility, lack of selectivity and resistance. The hydrophobic nature of compounds leads to low bioavailability. Moreover, the lack of selectivity of anticancer drug toward cancerous cells causes significant damage to rapidly proliferating normal cells. Also, cancer cells can develop multidrug resistance which is mainly due to increased efflux pumps in the cell membrane responsible for the transport of various anticancer drugs out of cells¹⁰⁰. The development of tumor cell resistance to chemotherapy and radiation therapy as well as the toxicity of these modalities limit the success of treatment and necessitate the search for better treatment options. Also, the genetic heterogeneity of cancer and the multifactorial nature of drug resistance limit the efficacy of the treatments⁹⁹.

Nanotherapeutics is rapidly progressing aiming to solve the limitations of conventional tumor therapies. Nanoparticle drug delivery systems allow to incorporate of both hydrophilic and hydrophobic substances, provide longer shelf life and improve biodistribution to overcome poor solubility. To reduce the toxicity and improve the selectivity of chemotherapeutic drugs, numerous drug delivery systems have been developed in recent years. The accumulation of nanoparticles in tumours often takes advantage of active or passive targeting. Active targeting involves the conjugation of targeting molecules on the surface of the nanoparticles (like antibodies, peptides, nucleic

acids, etc.) able to bind receptors overexpressed on the tumor cell surface, whereas passive targeting is based on the EPR effect¹⁰⁰.

In fact, several studies suggest that nanoparticles can enhance drug accumulation at the tumour site due to the EPR effect, which ultimately reduces side effects and enhances the anti-tumour efficacy. The EPR effect has been accepted as one of the universal pathophysiological characteristics of solid tumors and acts as a fundamental principle for designing and developing tumor-targeting delivery anticancer drugs. It is based on massive irregular neovascularization in tumors with structural and functional abnormalities in tumor blood vessels. To meet urgent demands for nutrient and oxygen supplies, the tumor vasculature is very dense and tortuous, with deficient basement membranes and fenestrated structures of endothelial tubes in some immature vessels. These structures render them highly permeable to nutrients, to be extravasated from tumor blood vessels into the interstitial space of tumor tissue. Also, this EPR effect is sustained by an elevated expression of inflammatory factors and a lack of efficient drainage of lymphatic systems in solid tumor tissue which results in the retention of extravasated nanoparticles in tumor tissues and provides the opportunity for passive targeting delivery of nanoparticles as anticancer drugs (Figure 11)¹⁰¹.

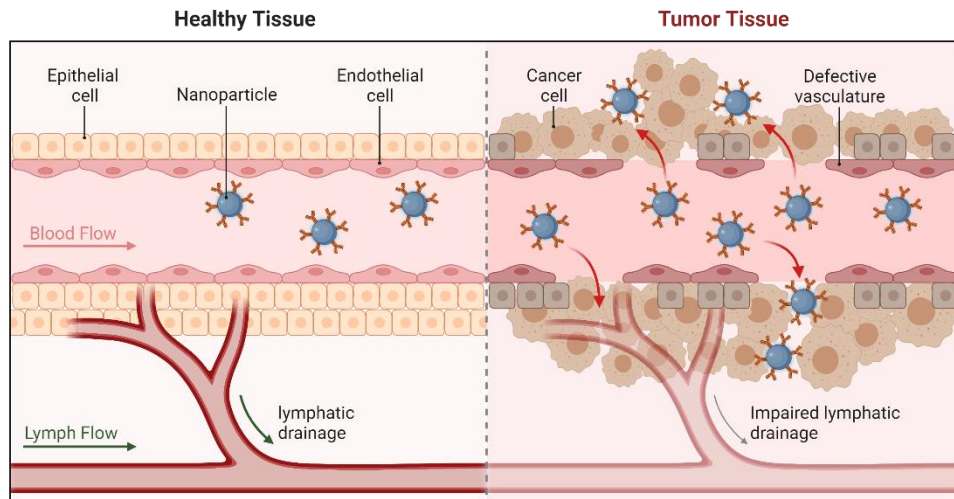


Figure 11. EPR effect and passive targeting. Nanocarriers can extravasate into the tumours through the gaps between endothelial cells and accumulate due to impaired lymphatic drainage.

Nevertheless, increased permeability is not uniform throughout the tumor and areas of increased permeability alternate with areas of conserved barrier function. While the EPR effect facilitates extravasation and retention of nanoparticles, it is counteracted by a decrease or loss of the transvascular pressure gradient¹⁰². Together with the growing population of tumor cells within a confined space that generate solid stress, the uptake and penetration of antitumor drugs are negatively impacted. Consequently, antitumor drugs that extravasate from tumor vessels tend to preferentially act on the first cell layers encountered, while the deeper layers of tumor cells that are more distant from blood vessels remain untreated. This restricted and non-homogeneous distribution of antitumor drugs has been identified as a significant and unrecognized cause of clinical drug resistance. This insight has fostered efforts to enhance the uptake and penetration of antitumor treatments based on nanomedicines¹⁰³.

6. Nanomotors

Based on the above, nanoparticles need to overcome the pressure gradient specific to the tumor site to penetrate deep into the tumor. At the same time, vascular abnormalities in the tumor tissue site are also important factors that hinder the deep penetration of nanotherapeutics into tumor¹⁰⁴. One possibility to achieve deeper tumor penetration and improved therapeutics efficacy is the use of nanomotors. A nanomotor is a tiny smart device that shows in situ energy conversion resulting in movement¹⁰⁵. Due to their exceptional ability to convert external energy (such as chemical, biochemical, or electromagnetic energy) into its own kinetic energy, nanomotors possess the ability of movement that is absent in traditional passive nanoparticles. This capability offers potential solutions to overcome the challenges encountered in the treatment of various diseases, including cancer. The nanomotors can be divided into three types, including biological, physical, and chemical according to the different driving ways (Figure 12)^{104,106}.

- Biological nanomotors. This category refers to a class of nanomotors that leverage the motion capabilities of biologically active substances to propel the microdevices.
- Physical nanomotors. It is generally referred to those who use external field stimuli such as electric, light, ultrasound, and magnetic fields as power sources. The on-off movement could be adjusted by the external physical stimulation.
- Chemical nanomotors. These nanomotors acquire self-driving capabilities through chemical reactions without the need of specific storage. It enables them to achieve self-propelled movement devoid of additional devices¹⁰⁴.

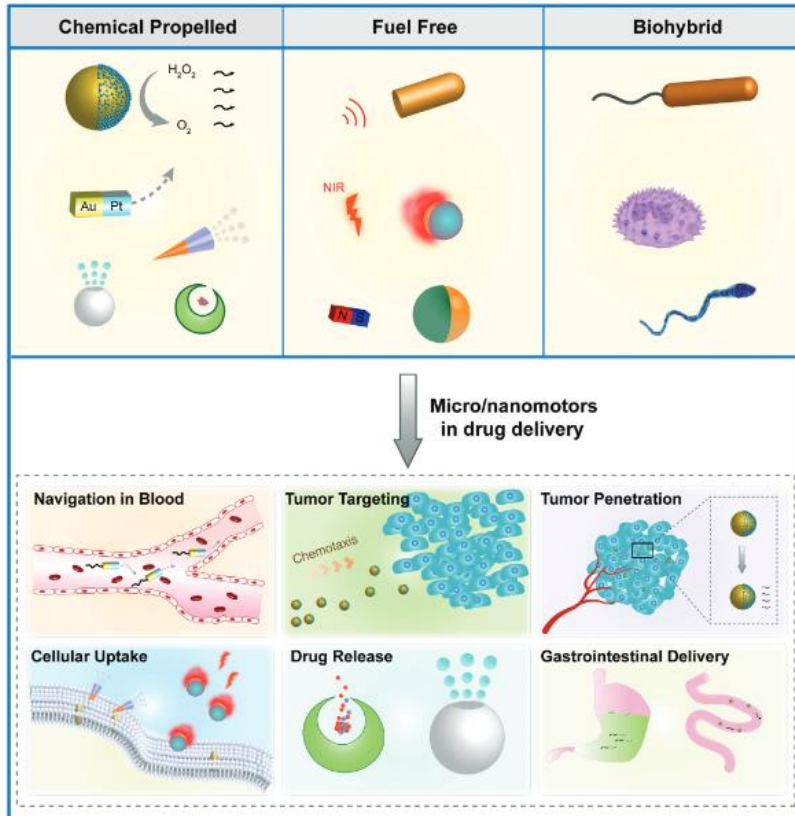


Figure 12. A schematic presentation of micro/nanomotors for drug delivery. Reproduced with permission from Lin et al., 2021¹⁰⁶

The mobility of micro/nanomotors can be quantified through parameters such as speed or diffusivity. Speed calculations are typically conducted for nanomaterials exhibiting specific motion patterns (e.g., ballistic directional motion), whereas diffusivity analysis is more appropriate for nano-sized motors with enhanced diffusion. Tracking the particles is essential to determine these parameters, and it can be achieved through techniques such as optical microscopy or light scattering. On the one hand, optical tracking is usually carried out for nanoparticles larger than 200 nm due to the resolution limits. On the other hand, dynamic light scattering (DLS) is used for nano-scaled particles. Besides, in recent years, nanoparticles-tracking analysis (NTA) has emerged as a valuable tool for the dynamic analysis of these motors. NTA offers some advantages on particle

tracking, which addresses limitations associated with DLS, such as the ability to identify aggregates and provide more detailed information on particle's behavior¹⁰⁷. For motors in nanoscales, the most appropriate way to quantify the moving dynamics is the calculation of the mean squared displacement (MSD). MSD refers to the position change of a particle over time. Typically, two situations can be observed. In the first scenario, over shorter time intervals, the motor particle exhibits continuous movement in a specific direction. In this case, the mean squared displacement (MSD) is proportional to Δt , which can be calculated using the following equation.

$$MSD = 4D_t \cdot \Delta t + v^2 \cdot \Delta t^2 (\Delta t \gg \tau)$$

Where v is the speed, D and τ are the translational diffusion coefficient and rotational diffusion time respectively. This equation usually displays a parabolic curve from the motor with a propulsive or ballistic moving trajectory^{107,108}.

On the contrary, over longer time intervals, the motor particle exhibits characteristics of Brownian motion or effective diffusion. In this case, the mean squared displacement (MSD) can be obtained using this second equation.

$$MSD = 4D_r \cdot \Delta t (\Delta t \gg \tau)$$

Where D represents the effective diffusion coefficient. This is normally defined as the linear regime^{107,108}.

Micro/nanomotors can achieve self-propulsion by converting surrounding energies into mechanical motion, which breaks the shackles of irregular Brownian motion and low Reynolds number on the movement at micro and nanoscales. The propulsive force empowers micro/nanomotors to autonomously cross biological barriers, including dense extracellular matrix^{109, 110} and the blood-tumor barrier¹¹¹, instead of merely passively circulating within the bloodstream.

Therefore, micro/nanomotors hold significant promise for achieving deep penetration into tumors. The special movement also influences their cellular entry characteristics. Studies have indicated that self-propelled micro/nanomotors tend to exhibit enhanced cellular internalization, and can bypass entrapment, or degradation within lysosomes¹⁰⁶. Some applications of nanomotors aiming for deep tumor penetration have been reported. For instance, Hortelao et al. demonstrated the improved penetration of urease-powered nanomotors into the 3D bladder cancer spheroid. The active nanomotors in the presence of urea displayed a threefold higher internalization efficiency than the passively diffusing controls^{106,112}. Rosli et al. explored arsenene nanoparticles modified with platinum to form Janus As-Pt nanomotors. Fast circular propulsion of nanomotors was demonstrated at a significantly low concentration of H₂O₂ and a high cellular uptake and promising doxorubicin delivery capabilities were investigated in A549 cells^{105,113}.

Besides, physical nanomotors that used external fields have been also widely developed. For example, Figure 13 shows a near-infrared (NIR)-driven nanomotor with a mesoporous silica nanoparticle as the core and end-capped with Antheraea pernyi silk fibroin (ApSF) constructed by Zhang et al. Upon NIR irradiation, the resulting ApSF-coated nanoparticles loading with photosensitizers and chemotherapeutic drugs efficiently penetrated into the internal tumor tissue and achieved effective phototherapy¹¹⁴.

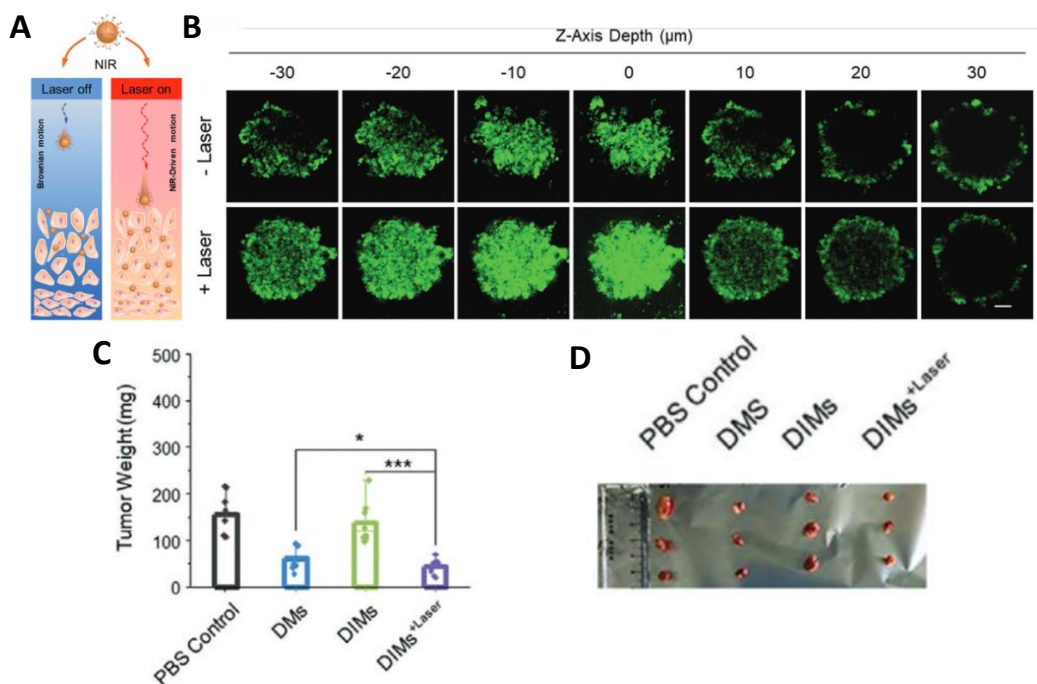


Figure 13. A. Schematic illustration and B. penetration profile of DIMs in MCSs (Multicellular spheroids) with or without laser irradiation ($1.5 \text{ W cm}^{-2} \cdot 60 \text{ s}$). Scales bar represents $100 \mu\text{m}$. C. Tumor growth curve of distant tumors from different mouse groups receiving various treatment strategies at day 14. D. Representative photographic images of distant tumors. DMS: Dox-loaded MSN; DIM: ApSF-coated MSNs loading with photosensitizers and doxorubicin. Adapted with permission from Zhang et al., 2022¹¹⁴

Biohybrid micro/nanomotors also exhibit great application value for deep tumor delivery. Felfoul and co-workers proposed a strategy for drug delivery to tumor hypoxic regions by using nanoliposomes covalently bound to MC-1 cells (*Magnetococcus marinus* strain). These MC-1 cells have magneto-aerotaxis since they contain a chain of magnetic iron-oxide nanocrystals inside and can swim along the local magnetic field. By using this characteristic, the MC-1 cells covalently bounded to drug-containing nanoliposomes were guided by a magnetic field to penetrate from peritumoral regions to the hypoxic zone^{106,115}.

7. Nanotechnology for improving cancer immunotherapy

7.1. Immune evasion and main strategies in cancer immunotherapy

Immune surveillance, also known as immunoediting, is the concept that envisages prevention of the development of tumors by the early destruction of abnormal cells by the immune system of the host¹¹⁶. This process consists of three phases: (1) Eradication of nascent malignant cells by the immune system. Immune cells recognize and destroy developing tumors, thus protecting the host against cancer (elimination); (2) Failure of elimination phase, resulting in tumor dormancy as well as in the establishment of an immunological pressure that sculpts genetically unstable cancer cells. Cancer cells can locally proliferate but neoplastic masses do not expand or metastasize because of immune control (equilibrium); (3) Selection of cancer cell variants that are not recognized or eliminated by the immune system, which develop into clinically apparent tumors, become able to infiltrate adjacent tissues and ultimately generate distant metastases (escape)¹¹⁷⁻¹¹⁹.

Briefly, the cancer immunity cycle (Figure 14) can be summarized in the following main steps: first, dying cancer cells release immunostimulatory signals, referred to damage-associated molecular patterns (DAMPs) to the tumoral microenvironment, which could be induced by some conventional chemotherapies or radiation therapies^{117,119}. These DAMPs bind to pattern recognition receptors (PRRs) on the surface of antigen-presenting cells (APCs) (such as TLR4), which expose them into their major histocompatibility complexes (MHC-I and MHC-II)^{117,119}. Then these molecules are presented in lymphoid organs to T-cells and recognized through their TCR receptors, which results in T-cell priming (CD4+ which includes Tregs and Thelpers, or CD8+ cytotoxic cells) and activation to respond to the shown neoantigens. The activated T-cells migrate and infiltrate the tumor bed, recognize cancer cells as foreign bodies, and bind to them through the interaction of the T-cell receptor (TCR) with its cognate antigen attached to MHC-I. Finally, cytotoxic T-cells can mediate direct cytotoxic effects and eradicate

malignant cells by a process named immunological cell death (ICD), while Th1 CD4+ T lymphocytes produce a large panel of immunostimulatory cytokines^{117,119}. This contributes to the release of more neoantigens to, thus, amplify the cycle¹²⁰. However, cancers are like a complex organ in which malignant cells builds an environment in such a way that the non-malignant cells like immune system cells support tumor growth instead of tumor suppression¹¹⁶. Consequently, cancer development may be associated with evasion of tumor cells from the surveillance of the immune system¹²¹.

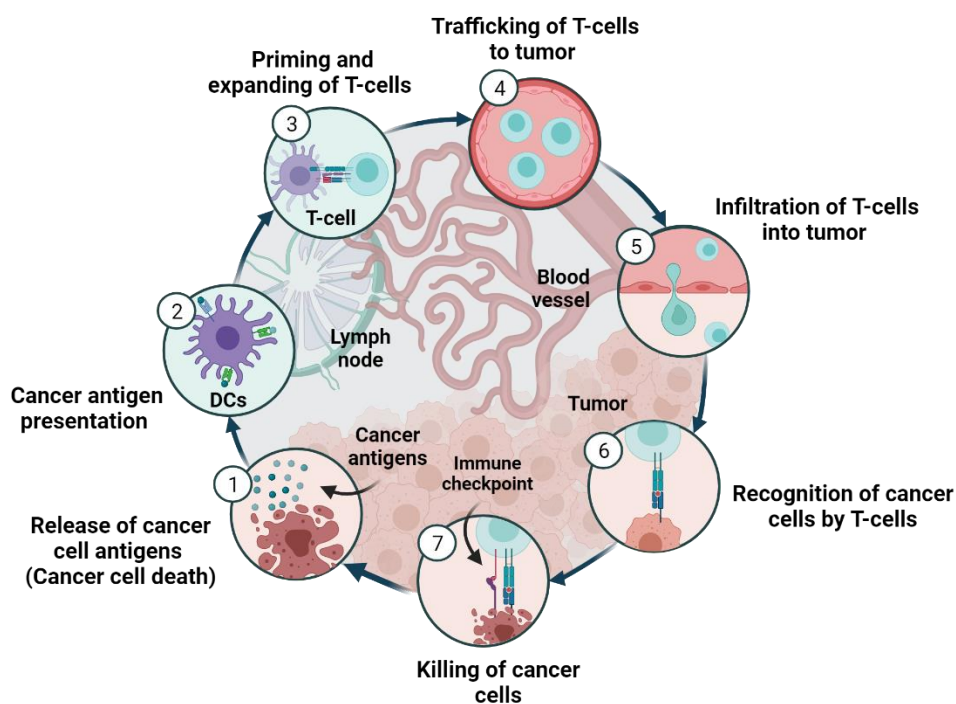


Figure 14. The cancer immunity cycle. Adapted with permission from Escriche-Navarro et al., 2022¹²⁰

Within this context, cancer immunotherapy has significantly developed as an alternative modality of cancer treatment to restore reactivity of the host's immune system to combat cancer during the last decades¹²¹. The history of cancer immunotherapy dates to the historical observation of antitumor effects from the bacterial concoction

known as Coley's toxins, and recognition that antibodies might be "magic bullets" for cancer therapy¹²². Cancer immunotherapy is now recognized as the "fourth pillar" of cancer treatment, after surgery, chemotherapy, and radiotherapy¹²³. In contrast to the other therapeutic concepts, immunotherapy primarily aims to prevent the metastatic spread of the disease and to generate immunological memory, thereby improving the quality of life of the affected individuals. Approaches that are applied in immunotherapy are based on complementation or stimulation of the immune system^{98,121}.

According to the aforementioned, tumor cells display multiple immunosuppressive mechanisms to evade immune recognition. One of the fundamental tumor evasion mechanisms to avoid T cell recognition is impaired antigen presentation. In this regard, cancer cells that no longer express the tumor antigen may escape destruction by cytotoxic T-lymphocytes-(CTLs) and grow progressively. In addition to the generation of antigen loss variants, down-modulation of antigen processing machinery affecting the MHC-I pathway is considered one of the most common immunosuppressive strategies exploited by tumor cells^{118,119}. Thus, the expression of tumor antigens is downregulated, which can lead to enhanced tumor incidence and metastasis because cytotoxic T lymphocytes can no longer recognize target antigens on the tumor cells^{120,124}.^{120,124} Several cancer therapies are directed to reinforce tumor antigen presentation by the delivery of peptidic or DNA vaccines (BCG, Sipuleucel-T and IMLYGIC have been approved by the FDA) and TLR agonists¹²⁰. Recently, in April 2023, a new RNAm vaccine against melanoma has been developed by Moderna company to prevent the recurrence of eradicated tumors¹²².

Moreover, malignant lesions favor the release from the bone marrow of a heterogeneous panel of relatively immature cells that exert immunosuppressive functions both intratumorally and systemically¹¹⁹. The effectiveness of T-cell priming, and activation depends on TCR, co-stimulatory molecules, and cytokine stimulation. It can be disrupted in a contact dependent manner through alterations in the expression of costimulatory molecules required for the presentation of foreign antigens or their attachment to

inhibitory molecules (such as cytotoxic T-lymphocyte-associated protein 4 (CTLA-4)) in the surface of T-cells. Different strategies based on the modulation of these factors have been developed. One approach is to use immune checkpoint inhibitors, for instance the antibodies addressed to cytotoxic T-lymphocyte antigen-4 (CTLA-4) like Ipilimumab. In contrast, another strategy is based on the activation of co-stimulatory receptors like CD27, CD137, and OX40 (TNF- α receptors) with agonist antibodies, such as Urelumab or polynucleotide-based aptamers. Additionally, the administration of immunostimulatory cytokines like recombinant interleukin-2 (IL-2) has also demonstrated anticancer activity via T-cell activation and expansion in preclinical and clinical studies¹²⁰.

Activated effector T-cells circulate through the bloodstream from lymph nodes to tumors where they infiltrate. Several factors are important in this step, including the appropriate match between the tumor-secreted chemokines and receptors expressed in T-cells, the presence of an aberrant vasculature, and interactions with adhesion molecules on endothelial cells. Among immunotherapies developed, bevacizumab is an antibody that blocks the vascular endothelial growth factor (VEGF) secreted by tumors to enhance the infiltration of lymphocytes by promoting “vascular normalization” and endothelial cells activation¹²⁰.

After having infiltrated the tumor, T-cells specifically recognize and bind to cancer cells through the interaction between the TCR receptor and the tumor antigen bound to MHC-I. In cancer patients, T-cells may recognize tumor antigens as self and, therefore, create T regulatory cell responses rather than effector responses. Further, cognate interactions between tumor and immune cells may result in impairment of TCR signaling in tumor infiltrating lymphocytes, thus inhibiting CTL lytic functions and inactivates the effector phase of antitumor responses¹¹⁸. The challenge of cancer immunotherapy in this step lies in reinitiating a self-sustaining cancer immunity cycle to enable T-cells to recognize tumors. Two main approaches for T-cell redirection involve their genetic modification with chimeric antigen receptors (CAR), like Axicabtagene ciloleucel and

Tisagenlecleucel, or the use of recombinant proteins designated bispecific T-cell engagers (BiTes), such as Catumaxomab and Blinatumomab¹²⁰.

In addition, malignant lesions attempting to escape immunosurveillance harness multiple control mechanisms normally used by the immune system to control overstated responses¹¹⁷. As revealed by immune cells failing to kill cancer cells due to the expression of inhibitory or checkpoint molecules such as programmed cell death (PD-L1). These molecules have been shown to cause deletion or anergy on tumor reactive cells^{120,125}. Under normal physiological conditions, immune checkpoints play an important role in the prevention of autoimmunity and tissue damage for the immune reaction. However, the expression of immune checkpoint molecules can be dysregulated in tumors, resulting in an innate and adaptive immune resistance of tumors¹²⁶. When T-cells are activated, they express PD-1, which binds to its ligands and negatively regulates effector T-cell activity. To evade recognition and elimination by T-cells, tumor cells express this ligand (PD-L1) by generating an immunosuppressive effect. FDA approved therapies using monoclonal antibodies to prevent those interactions and, therefore, stimulate antitumor immunity. In addition, many trials involving checkpoint inhibitors in combination with other agents are ongoing (>700)^{120,124}.

Besides, tumors can evade immune surveillance by crippling cytotoxic T lymphocyte (CTL) functionality via deprivation of essential metabolic substrates such as tryptophan and arginine in the tumor extracellular matrix (TME).. Increasing these factors may reactivate cells for antitumor immunity with approaches targeting the enzymes indoleamine 2,3-dioxygenase (IDO) and arginase, which reduce their activity^{117,119}. In clinics, IDO and arginase inhibitors are being tested in clinical trials with patients, for example, CB-1158. In the same way, suppressive cytokines are crucial for controlling the development of excessive immune responses and for maintaining immune homeostasis. However, tumors have adapted and secrete these cytokines such as transforming growth factor beta (TGF- β) to promote immunological tolerance. In the premalignant cells phase,

TGF- β directly suppress the cytolytic activity of NK and CTL. However, in a late cancer development stage, high TGF- β levels stimulate tumor progression via effects on the stroma. Its inhibition has been widely studied as antitumor therapy in many clinical trials, using different strategies, such as antisense oligonucleotides, TGF- β -neutralizing antibodies, and TGF- β receptor kinase inhibitors^{120,125}.

Many of the immune treatments commented above have reached preclinical studies, but translation into patients remains challenging and raises concerns, including the development of autoimmune toxicities, the targeting of homeostatic functions like angiogenesis and the risk of developing new malignancies^{120,127}. Similarly, response rates to immunotherapy are still modest because of the complexity of immune-tumor interactions and the existence of redundant mechanisms of tumor-mediated immune suppression. In general, cytokines, checkpoint inhibitors and agonistic antibodies produce substantial autoimmunity and adverse effects, which limit the allowed dose. Hence, the single use of cancer immunotherapy has suffered from restricted efficacy, limited to 20-30% of the treated population. Moreover, given their short half-life, effective treatments require high-dose injections that cause vascular leakage and cytokine release syndrome. The limited efficacy of cancer immunotherapy underlies the need to design new concepts in immunotherapy such as targeted, controlled and/or combination release of therapeutics to minimize off-target effects in which nanotechnology might play a role^{102,120,126}.

Moreover, most tumors are categorized as “immunologically cold”-type, characterized by low immunogenicity and immunosuppressive tumor microenvironment. This microenvironment implies the lack of sufficient pre-existing tumor-infiltrating lymphocytes that recognize tumor cells through T-cell receptors and difficulties in generating long-term antitumor immunity. In this way, a promising targeting of this kind of tumors could involve the formation of the immunological cytolytic synapse between target cancer cells and T cells and lead to target cell lysis¹²⁷. The application of nanodevices

as engagers open a new avenue for enhancing the efficacy and reducing possible side effects of immunotherapies^{124,126}.

7.2. Nanoparticles-based approaches

Notwithstanding the recent achievements in clinical trials, promising approaches in immunotherapy still encounter significant hurdles for effective clinical translation. These challenges include the integration of multiple strategies, combination with conventional therapies, monitor immune responses, and optimizing therapeutic delivery. In this context, nanotechnology emerges as a crucial tool in designing nanoparticles, nanovaccines, and therapeutic agents to address the challenges faced in cancer immunotherapy¹²⁶.

In general, nanoparticles act by protecting immunotherapeutic agents through blood circulation to the target site, thus improving both efficacy and safety. Nanomaterials are also considered good candidates for immunotherapy given their intrinsic ability to target lymph nodes, immune cells as well as tumors. Besides, specific targeting ligands can be used to enhance the delivery of immunotherapeutic agents. In this way, nanoparticles can help to achieve a more controllable immune response through selective cargo delivery and can limit immune response overreaction or systemic toxic effects from some treatments. In addition, nanoparticles can also enhance the immunostimulatory effect by helping to achieve a suitable immune response. Indeed, a potential advantage of nanomaterials to be exploited in immunotherapy is their intrinsic immunogenicity. For example, cationic and small-sized nanoparticles are easily internalized by some APC types like macrophages and DC, which make them suitable for cancer vaccine development. Compared to traditional adjuvants, nanomaterials can induce both tumoral and cell-mediated immune responses. Bearing in mind the increasing demand for combinatorial therapies to improve the effectiveness of cancer

immunotherapy, another key advantage of using nanomaterials is the possibility of combining different therapeutic strategies in the same nanocarrier¹²⁰.

Several nanomaterials have been developed in order to achieve an accurate antigen presentation. For example, Xu et al. synthesized biocompatible aminated MSNs carriers to load CpG ODN (the commonest adjuvant which targets toll-like receptors 9) to prevent degradation from serum nucleases and to achieve greater immune stimulation^{120,128}. Another approach to improve cancer immunotherapy in this step is based on the development of injectable or implantable 3D materials for the spatio-temporal modulation of immune cell populations, including DC and cytotoxic T-cells. Kim et al. developed mesoporous silica rods (MSR) co-loaded with GM-CSF (a chemoattractant to immune DC), CpG-ODN, and ovalbumin (antigen model) to examine their potential as cancer vaccines. These authors demonstrated the ability of MSR to spontaneously form 3D platforms *in vivo* with a significant increase in host immune cell recruitment and the activation of DC in lymph nodes leading to the inhibition of tumor growth *in vivo*^{120,129}.

Moreover, infiltration of immune cells in tumors can be promoted using chemokines, a type of cytokine that attracts and modulates specific subsets of effector leukocytes to develop antitumor immunity. Following this approach, Lee et al. developed upconversion fluorescent nanoparticles loaded with chemokine ligand 21 (CCL21) to induce the migration of immune cells to tumor cells. They demonstrated that these nanoparticles were able to cross an endothelial cell monolayer and specifically targeted an ovarian carcinoma cell line. They also found that nanodevices increase the lymphocyte and DC. These results indicate that employing nanomaterials to specifically deliver chemokines to tumors is a promising approach for immunotherapy due to their ability to host large molecules given the huge potential to induce immune cell trafficking across biological barriers and the TME^{120,130,131}.

Another nanoparticle-based immunotherapy arousing interest in recent years is cell engineering which acts as engager to improve T-cells recognition and binding to tumor¹²⁶. Here, a variety of methods have been developed, for example, liposomes and lipid-coated PLGA nanoparticles conjugated to T-cells and hematopoietic stem cells were used for targeting antigen-expressing tumors^{126,132}. Also, Kim and colleagues developed a multivalent bi-specific nanobioconjugate engager utilizing polystyrene nanoparticles conjugated with anti-HER2 antibody and calreticulin. This nanodevice effectively engaged with professional antigen-presenting cells (APCs), leading to the activation of both innate and subsequent adaptive immune responses, thereby enhancing host T-cell immunity. This promoted receptor-targeted macrophage phagocytosis of cancer cells, facilitated downstream immune activation by professional APCs, elicited antitumor immune responses *in vivo*, and induced systemic and long-lasting antitumor immunity^{126,133}.

The final step in the cancer immunity cycle aims to kill cancer cells. In this way, nanoparticles are potential tools to undergo different types of therapies to enhance antitumor therapy and, thus, maximize cancer cell death. Several approaches using nanoparticles have been described by combining several therapeutic agents such as conventional chemotherapeutics, vaccines, and/or the inhibition of immune checkpoints. Immunotherapy based on checkpoint blockade has been one of the most successful approaches to cancer treatment¹²⁰. Accordingly, two key immune checkpoint molecules involved in regulating T-cell activity are cytotoxic T-lymphocyte-associated antigen 4 (CTLA-4), expressed on activated T-cells, and programmed cell death protein 1 (PD-1), which can bind to its ligands PD-L1 and PD-L2. These molecules have been extensively utilized to modulate antitumor immune responses. However, current antibody-based immune checkpoint therapies may still result in side effects due to the non-specific accumulation of antibodies in normal organs¹²⁶. Recent studies have shown a diverse set of nanoparticles that could improve anticancer immunity with immune checkpoint blockade treatment. Based on their inherent properties, engineered nanoparticles have been employed to enhance the delivery efficiency of immune checkpoint modulators,

aiming for effective cancer immunotherapy¹²⁶. In a study by Yang et al., the authors reported the use of complexes of folic acid-modified polyethyleneimine derivatives loaded with PD-L1 siRNA. This approach efficiently inhibited tumor cells by targeting PD-L1, thereby sensitizing them to T-cell killing *in vitro*^{126,134}. Also, Wang et al. developed anti-PD-L1 antibody conjugated platelets which could enhance the delivery and efficacy of anti-PD-L1, resulting in a reduction of risk in cancer regrowth and metastatic spread. This system successfully induced T-cell mediated immune responses *in vivo* by improving infiltration of both CD8+ and CD4+ T cells (Figure 15)^{126,135}.

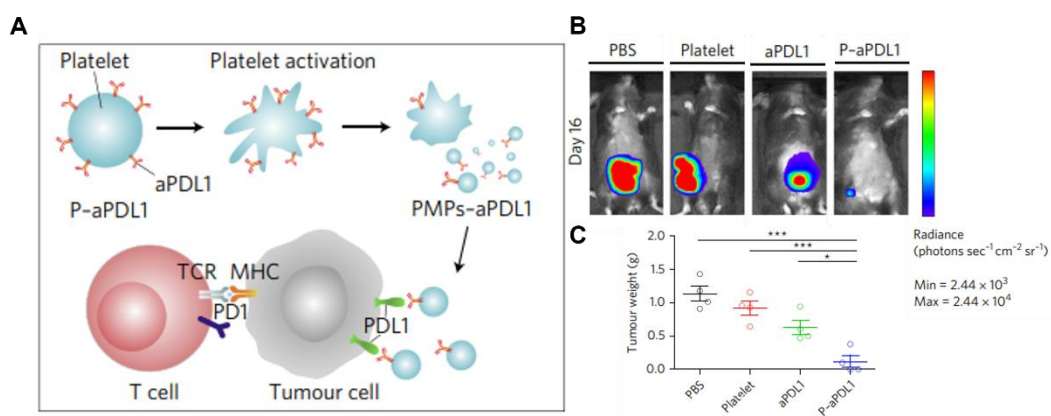


Figure 15. A. Schematic illustration of the delivery of aPD-L1 to the tumor site by platelets, where TCR is T cell receptor and MHC is major histocompatibility complex. B. In vivo bioluminescence imaging of B16F10 tumours after removal of the primary tumour. C. Tumor weight of different groups. Adapted with permission from Wang et al., 2017¹³⁵

An alternative approach for immune modulation involves the targeted delivery of immune modulation compounds (present in the TME) specifically to CD8+ T cells^{126,136,137}. Goldberg et al. developed anti-PD1 fragments-conjugated poly(ethylene glycol)-poly(lactic-co-glycolic acid) (PEG-PLGA) nanoparticles. These nanoparticles were loaded with transforming growth factor β (TGF- β) inhibitors. Through this approach, the nanodevice effectively targeted PD1+ T cells in both blood and tumors, delivering the TGF- β inhibitors. The presence of the delivered inhibitors increased the number of tumor-

infiltrating CD8+ T cells, leading to the inhibition of tumor growth and prolonged survival in tumor-bearing mice^{126,138}.

Given all this encouraging research, mesoporous silica materials are potential candidates for application in cancer treatment and diagnosis. However, despite numerous promising studies in cellular and animal models, translation to the clinic remains a considerable challenge. In order to go beyond the preclinical phases, it is necessary to discover new advanced systems to overcome typical limitations such as the limited tumour penetrability of chemotherapy or the restricted efficacy of cancer immunotherapy. Based on this, this PhD thesis aims to advance the use of mesoporous silica and is divided into two main sections focused on the improvement of tumour therapies through the development of advanced nanosystems.

8. References

1. Hulla, J. E., Sahu, S. C. & Hayes, A. W. Nanotechnology: History and future. *Hum Exp Toxicol* **34**, 1318–21 (2015).
2. Sanchez, F. & Sobolev, K. Nanotechnology in concrete - A review. *Constr Build Mater* **24**, 2060–2071 (2010).
3. Silva, G. A. Introduction to nanotechnology and its applications to medicine. *Surg Neurol* **61**, 216–20 (2004).
4. Chakraborty, K., Roy, T. & Mondal, S. Development of DNA Nanotechnology and Uses in Molecular Medicine and Biology. *Insights in Biomed* **1**, 1–10 (2016).
5. Emerich, D. F. & Thanos, C. G. Nanotechnology and medicine. *Expert Opin Biol Ther* **3**, 655–663 (2003).

6. Rao, C. N. R. & Cheetham, A. K. Science and technology of nanomaterials: Current status and future prospects. *J Mater Chem* **11**, 2887–2894 (2001).
7. Pelaz, B. *et al.* Diverse Applications of Nanomedicine. *ACS Nano* **11**, 2313–2381 (2017).
8. Sapsford, K., Pons, T., Medintz, I. & Mattoussi, H. Biosensing with Luminescent Semiconductor Quantum Dots. *Sensors* **6**, 925–953 (2006).
9. Murray, C. B., Norris, D. J. & Bawendi, M. G. Synthesis and Characterization of Nearly Monodisperse Cde (E = S, Se, Te) Semiconductor Nanocrystallites. *J Am Chem Soc* **115**, 8706–8715 (1993).
10. Yekimov, A. I. & Onushchenko, A. A. Quantum Size Effect in Three-Dimensional Microscopic Semiconductor Crystals. *JETP Lett+* **34**, 345–349 (1981).
11. Brus, L. E. A Simple-Model for the Ionization-Potential, Electron-Affinity, and Aqueous Redox Potentials of Small Semiconductor Crystallites. *J Chem Phys* **79**, 5566–5571 (1983).
12. Raimondi, F., Scherer, G. G., Kötz, R. & Wokaun, A. Nanoparticles in Energy Technology: Examples from Electrochemistry and Catalysis. *Angewandte Chemie International Edition* **44**, 2190–2209 (2005).
13. Couvreur, P. Nanoparticles in drug delivery: Past, present and future. *Adv Drug Deliv Rev* **65**, 21–23 (2013).
14. Chiari-Andréo, B. G. *et al.* Nanoparticles for cosmetic use and its application. in *Nanoparticles in Pharmacotherapy* vol. 2019 113–146 (Elsevier, 2019).

15. De, M., Ghosh, P. S. & Rotello, V. M. Applications of nanoparticles in biology. *Advanced Materials* **20**, 4225–4241 (2008).
16. Berry, C. C. Applications of inorganic nanoparticles for biotechnology. in *Frontiers of Nanoscience* vol. 4 159–180 (Elsevier, 2012).
17. Hasan, A. *et al.* Nanoparticles in tissue engineering: Applications, challenges and prospects. *Int J Nanomedicine* **13**, 5637–5655 (2018).
18. Gavanji, S., Mohabbatkar, H., Baghshahi, H. & Zarrabi, A. Bioinformatics Prediction of Interaction Silver Nanoparticles on the Disulfide Bonds of HIV-1 Gp120 Protein. *International Journal of Scientific Research in Knowledge* **2**, 67–74 (2014).
19. Ranjan, S., Dasgupta, N. & Lichtfouse, E. *Nanoscience in Food and Agriculture 1*. vol. 20 (Springer International Publishing, Cham, 2016).
20. Fulekar, M. H. *Nanotechnology: Importance and Applications*. (IK International Pvt Ltd., 2010).
21. Zhang, C. *et al.* Progress, challenges, and future of nanomedicine. *Nano Today* **35**, 1–13 (2020).
22. Zhang, C. *et al.* Progress, challenges, and future of nanomedicine. *Nano Today* **35**, 1–13 (2020).
23. Jafari, S. *et al.* Mesoporous silica nanoparticles for therapeutic/diagnostic applications. *Biomedicine and Pharmacotherapy* **109**, 1100–1111 (2019).
24. Mehmood, A., Ghafar, H., Yaqoob, S., Gohar, U. F. & Ahmad, B. Mesoporous Silica Nanoparticles: A Review. *J Dev Drugs* **06**, 1–14 (2017).

25. Manzano, M. & Vallet-Regí, M. Mesoporous Silica Nanoparticles for Drug Delivery. *Adv Funct Mater* **30**, 1–13 (2020).
26. Beck, J. S. *et al.* A New Family of Mesoporous Molecular Sieves Prepared with Liquid Crystal Templates. *J. Am. Chem. Soc.* **114**, 10834–10843 (1992).
27. Li, Z., Barnes, J. C., Bosoy, A., Stoddart, J. F. & Zink, J. I. Mesoporous silica nanoparticles in biomedical applications. *Chem Soc Rev* **41**, 2590–2605 (2012).
28. Vallet-Regí, M., Rámila, A., Del Real, R. P. & Pérez-Pariente, J. A new property of MCM-41: Drug delivery system. *Chemistry of Materials* **13**, 308–311 (2001).
29. Tang, F., Li, L. & Chen, D. Mesoporous silica nanoparticles: Synthesis, biocompatibility and drug delivery. *Advanced Materials* **24**, 1504–1534 (2012).
30. Ghimire, P. P. & Jaroniec, M. Renaissance of Stöber method for synthesis of colloidal particles: New developments and opportunities. *J Colloid Interface Sci* **584**, 838–865 (2021).
31. Carvalho, G. C. *et al.* Highlights in Mesoporous Silica Nanoparticles as a Multifunctional Controlled Drug Delivery Nanoplatform for Infectious Diseases Treatment. *Pharm Res* **37**, 1–30 (2020).
32. Seljak, K. B., Kocbek, P. & Gašperlin, M. Mesoporous silica nanoparticles as delivery carriers: An overview of drug loading techniques. *J Drug Deliv Sci Technol* **59**, 1–9 (2020).
33. Kumar, A. & Dixit, C. K. Methods for characterization of nanoparticles. in *Advances in Nanomedicine for the Delivery of Therapeutic Nucleic Acids* 44–58 (Elsevier Inc., 2017).

34. Lu, F., Wu, S. H., Hung, Y. & Mou, C. Y. Size effect on cell uptake in well-suspended, uniform mesoporous silica nanoparticles. *Small* **5**, 1408–1413 (2009).
35. Chirayil, C. J., Abraham, J., Mishra, R. K., George, S. C. & Thomas, S. Instrumental Techniques for the Characterization of Nanoparticles. in *Thermal and Rheological Measurement Techniques for Nanomaterials Characterization*. vol. 3 1–36 (Elsevier, 2017).
36. Titus, D., James Jebaseelan Samuel, E. & Roopan, S. M. Nanoparticle characterization techniques. in *Green Synthesis, Characterization and Applications of Nanoparticles* 303–319 (Elsevier, 2019).
37. Christoforidou, T. *et al.* Oral drug delivery systems based on ordered mesoporous silica nanoparticles for modulating the release of aprepitant. *Int J Mol Sci* **22**, 1–18 (2021).
38. Mourdikoudis, S., Pallares, R. M. & Thanh, N. T. K. Characterization techniques for nanoparticles: Comparison and complementarity upon studying nanoparticle properties. *Nanoscale* **10**, 12871–12934 (2018).
39. Li, Z., Zhang, Y. & Feng, N. Mesoporous silica nanoparticles: synthesis, classification, drug loading, pharmacokinetics, biocompatibility, and application in drug delivery. *Expert Opin Drug Deliv* **16**, 219–237 (2019).
40. Fornaguera, C. & Solans, C. Analytical Methods to Characterize and Purify Polymeric Nanoparticles. *Int J Polym Sci* **2018**, 1–10 (2018).
41. Aznar, E. *et al.* Gated Materials for On-Command Release of Guest Molecules. *Chem Rev* **116**, 561–718 (2016).

42. Dave, P. N. & Chopda, L. v. A review on application of multifunctional mesoporous nanoparticles in controlled release of drug delivery. *Materials Science Forum* **781**, 17–24 (2014).
43. Baeza, A., Manzano, M., Colilla, M. & Vallet-Regí, M. Recent advances in mesoporous silica nanoparticles for antitumor therapy: Our contribution. *Biomater Sci* **4**, 803–813 (2016).
44. Vallet-Regí, M., Balas, F. & Arcos, D. Mesoporous materials for drug delivery. *Angewandte Chemie - International Edition* **46**, 7548–7558 (2007).
45. García-Fernández, A., Aznar, E., Martínez-Máñez, R. & Sancenón, F. New Advances in In Vivo Applications of Gated Mesoporous Silica as Drug Delivery Nanocarriers. *Small* **16**, 1–62 (2020).
46. Abdo, G. G., Zagho, M. M. & Khalil, A. Recent advances in stimuli-responsive drug release and targeting concepts using mesoporous silica nanoparticles. *Emergent Mater* **3**, 407–425 (2020).
47. Živojević, K. *et al.* Advanced mesoporous silica nanocarriers in cancer theranostics and gene editing applications. *Journal of Controlled Release* **337**, 193–211 (2021).
48. López-Lorente, A. I., Simonet, B. M. & Valcárcel, M. Analytical potential of hybrid nanoparticles. *Anal Bioanal Chem* **399**, 43–54 (2011).
49. Villalonga, R. *et al.* Enzyme-controlled sensing-actuating nanomachine based on janus au-mesoporous silica nanoparticles. *Chemistry - A European Journal* **19**, 7889–7894 (2013).
50. Song, Y. & Chen, S. Janus nanoparticles: Preparation, characterization, and applications. *Chem Asian J* **9**, 418–430 (2014).

51. Zhang, X., Fu, Q., Duan, H., Song, J. & Yang, H. Janus Nanoparticles: From Fabrication to (Bio)Applications. *ACS Nano* **15**, 6147–6191 (2021).
52. Lattuada, M. & Hatton, T. A. Synthesis, properties and applications of Janus nanoparticles. *Nano Today* **6**, 286–308 (2011).
53. Agrawal, G. & Agrawal, R. Janus Nanoparticles: Recent Advances in Their Interfacial and Biomedical Applications. *ACS Appl Nano Mater* **2**, 1738–1757 (2019).
54. Xuan, M., Shao, J., Lin, X., Dai, L. & He, Q. Self-propelled janus mesoporous silica nanomotors with sub-100 nm diameters for drug encapsulation and delivery. *ChemPhysChem* **15**, 2255–2260 (2014).
55. Zhang, L. *et al.* Dual drug delivery and sequential release by amphiphilic Janus nanoparticles for liver cancer theranostics. *Biomaterials* **181**, 113–125 (2018).
56. Castillo, R. R. & Vallet-Regí, M. Functional mesoporous silica nanocomposites: Biomedical applications and biosafety. *Int J Mol Sci* **20**, 1–30 (2019).
57. Huang, X., Teng, X., Chen, D., Tang, F. & He, J. The effect of the shape of mesoporous silica nanoparticles on cellular uptake and cell function. *Biomaterials* **31**, 438–448 (2010).
58. Zhou, Y. *et al.* Mesoporous silica nanoparticles for drug and gene delivery. *Acta Pharm Sin B* **8**, 165–177 (2018).
59. Ahmad, A., Khan, J. M. & Haque, S. Strategies in the design of endosomolytic agents for facilitating endosomal escape in nanoparticles. *Biochimie* **160**, 61–75 (2019).

60. Varkouhi, A. K., Scholte, M., Storm, G. & Haisma, H. J. Endosomal escape pathways for delivery of biologicals. *Journal of Controlled Release* **151**, 220–228 (2011).
61. Vivero-Escoto, J. L., Slowing, I. I., Lin, V. S. Y. & Trewyn, B. G. Mesoporous silica nanoparticles for intracellular controlled drug delivery. *Small* **6**, 1952–1967 (2010).
62. Dobrovolskaia, M. A., Aggarwal, P., Hall, J. B. & McNeil, S. E. Preclinical Studies To Understand Nanoparticle Interaction with the Immune System and Its Potential Effects on Nanoparticle Biodistribution. *Mol Pharm* **5**, 487–495 (2008).
63. Lazarovits, J., Chen, Y. Y., Sykes, E. A. & Chan, W. C. W. Nanoparticle–blood interactions: the implications on solid tumour targeting. *Chemical Communications* **51**, 2756–2767 (2015).
64. Léri-da-Viso, A., Estepa-Fernández, A., García-Fernández, A., Martí-Centelles, V. & Martínez-Máñez, R. Biosafety of mesoporous silica nanoparticles; towards clinical translation. *Adv Drug Deliv Rev* **201**, 1–34 (2023).
65. Bharti, C., Gulati, N., Nagaich, U. & Pal, A. Mesoporous silica nanoparticles in target drug delivery system: A review. *Int J Pharm Investig* **5**, 124–133 (2015).
66. Hao, N. *et al.* *In Vitro* Degradation Behavior of Silica Nanoparticles Under Physiological Conditions. *J Nanosci Nanotechnol* **12**, 6346–6354 (2012).
67. Longmire, M., Choyke, P. L. & Kobayashi, H. Clearance properties of nano-sized particles and molecules as imaging agents: considerations and caveats. *Nanomedicine* **3**, 703–717 (2008).
68. Huang, X. *et al.* The shape effect of mesoporous silica nanoparticles on biodistribution, clearance, and biocompatibility in vivo. *ACS Nano* **5**, 5390–5399 (2011).

-
69. Lu, J., Liong, M., Li, Z., Zink, J. I. & Tamanoi, F. Biocompatibility, biodistribution, and drug-delivery efficiency of mesoporous silica nanoparticles for cancer therapy in animals. *Small* **6**, 1794–1805 (2010).
 70. Slowing, I. I., Wu, C. W., Vivero-Escoto, J. L. & Lin, V. S. Y. Mesoporous silica nanoparticles for reducing hemolytic activity towards mammalian red blood cells. *Small* **5**, 57–62 (2009).
 71. Okoampah, E., Mao, Y., Yang, S., Sun, S. & Zhou, C. Gold nanoparticles–biomembrane interactions: From fundamental to simulation. *Colloids Surf B Biointerfaces* **196**, 1–13 (2020).
 72. Kozics, K. *et al.* Pharmacokinetics, Biodistribution, and Biosafety of PEGylated Gold Nanoparticles In Vivo. *PEGylated Gold Nanoparticles In Vivo. Nanomaterials* **11**, 1702 (2021).
 73. Sani, A., Cao, C. & Cui, D. Toxicity of gold nanoparticles (AuNPs): A review. *Biochem Biophys Rep* **26**, (2021).
 74. Li, X. *et al.* The systematic evaluation of size-dependent toxicity and multi-time biodistribution of gold nanoparticles. *Colloids Surf B Biointerfaces* **167**, 260–266 (2018).
 75. Adewale, O. B., Davids, H., Cairncross, L. & Roux, S. Toxicological Behavior of Gold Nanoparticles on Various Models: Influence of Physicochemical Properties and Other Factors. *Int J Toxicol* **38**, 357–384 (2019).
 76. Haute, D. Van & Berlin, J. M. Challenges in realizing selectivity for nanoparticle biodistribution and clearance: Lessons from gold nanoparticles. *Ther Deliv* **8**, 763–774 (2017).

77. Zhang, X. D. *et al.* Toxicologic effects of gold nanoparticles in vivo by different administration routes. *Int J Nanomedicine* **5**, 771–781 (2010).
78. Pan, Y. *et al.* Size-dependent cytotoxicity of gold nanoparticles. *Small* **3**, 1941–1949 (2007).
79. Zhang, X. D. *et al.* Size-dependent in vivo toxicity of PEG-coated gold nanoparticles. *Int J Nanomedicine* **6**, 2071–2081 (2011).
80. Wang, S. *et al.* Challenge in understanding size and shape dependent toxicity of gold nanomaterials in human skin keratinocytes. *Chem Phys Lett* **463**, 145–149 (2008).
81. Goodman, C. M., McCusker, C. D., Yilmaz, T. & Rotello, V. M. Toxicity of gold nanoparticles functionalized with cationic and anionic side chains. *Bioconjug Chem* **15**, 897–900 (2004).
82. Kus-lińkiewicz, M., Fickers, P. & Ben Tahar, I. Biocompatibility and cytotoxicity of gold nanoparticles: Recent advances in methodologies and regulations. *Int J Mol Sci* **22**, 1–21 (2021).
83. Sonavane, G., Tomoda, K. & Makino, K. Biodistribution of colloidal gold nanoparticles after intravenous administration: Effect of particle size. *Colloids Surf B Biointerfaces* **66**, 274–280 (2008).
84. Xu, J. *et al.* Dose Dependencies and Biocompatibility of Renal Clearable Gold Nanoparticles: From Mice to Non-human Primates. *Angewandte Chemie - International Edition* **57**, 266–271 (2018).

85. Zhang, G. *et al.* Influence of anchoring ligands and particle size on the colloidal stability and in vivo biodistribution of polyethylene glycol-coated gold nanoparticles in tumor-xenografted mice. *Biomaterials* **30**, 1928–1936 (2009).
86. Xiang, A. D. *et al.* In Vivo and in Vitro Biocompatibility Studies of Pt Based Nanoparticles: a New Agent for Chemoradiation Therapy. *J Clust Sci* **34**, 2653–2663 (2023).
87. Pedone, D., Moglianetti, M., De Luca, E., Bardi, G. & Pompa, P. P. Platinum nanoparticles in nanobiomedicine. *Chem Soc Rev* **46**, 4951–4975 (2017).
88. Brown, A. L., Kai, M. P., DuRoss, A. N., Sahay, G. & Sun, C. Biodistribution and toxicity of micellar platinum nanoparticles in mice via intravenous administration. *Nanomaterials* **8**, 1–14 (2018).
89. Janjua, T. I., Cao, Y., Yu, C. & Papat, A. Clinical translation of silica nanoparticles. *Nat Rev Mater* **6**, 1072–1074 (2021).
90. Anselmo, A. C. & Mitragotri, S. Nanoparticles in the clinic: An update post COVID-19 vaccines. *Bioeng Transl Med* **6**, 1–20 (2021).
91. Tan, A., Eskandar, N. G., Rao, S. & Prestidge, C. A. First in man bioavailability and tolerability studies of a silica-lipid hybrid (Lipoceramic) formulation: A Phase I study with ibuprofen. *Drug Deliv Transl Res* **4**, 212–221 (2014).
92. Kharlamov, A. N. *et al.* Silica-gold nanoparticles for atheroprotective management of plaques: Results of the NANOM-FIM trial. *Nanoscale* **7**, 8003–8015 (2015).
93. Kharlamov, A. N. *et al.* Plasmonic photothermal therapy of atherosclerosis with nanoparticles: Long-term outcomes and safety in NANOM-FIM trial. *Future Cardiol* **13**, 345–363 (2017).

94. Phillips, E. *et al.* Clinical translation of an ultrasmall inorganic optical-PET imaging nanoparticle probe. *Sci Transl Med* **6**, 1–23 (2014).
95. Zanoni, D. K. *et al.* Use of Ultrasmall Core-Shell Fluorescent Silica Nanoparticles for Image-Guided Sentinel Lymph Node Biopsy in Head and Neck Melanoma. *JAMA Netw Open* **4**, 1–14 (2021).
96. Rastinehad, A. R. *et al.* Gold nanoshell-localized photothermal ablation of prostate tumors in a clinical pilot device study. *Proceedings of the National Academy of Sciences* **116**, 18590–18596 (2019).
97. Qiao, J., Liu, Z. & Fu, Y. X. Adapting conventional cancer treatment for immunotherapy. *J Mol Med* **94**, 489–495 (2016).
98. Lake, R. A. & Robinson, B. W. S. Immunotherapy and chemotherapy — a practical partnership. *Nature Reviews* **5**, 397–405 (2005).
99. Ramakrishnan, R., Antonia, S. & Gabrilovich, D. I. Combined modality immunotherapy and chemotherapy: A new perspective. *Cancer Immunology, Immunotherapy* **57**, 1523–1529 (2008).
100. Moorthi, C., Manavalan, R. & Kathiresan, K. Nanotherapeutics to Overcome Conventional Cancer Chemotherapy Limitations. *J Pharm Pharmaceut Sci* **14**, 67–77 (2011).
101. Wu, J. The enhanced permeability and retention (Epr) effect: The significance of the concept and methods to enhance its application. *J Pers Med* **11**, 1–8 (2021).
102. Marcucci, F. & Corti, A. How to improve exposure of tumor cells to drugs - Promoter drugs increase tumor uptake and penetration of effector drugs. *Adv Drug Deliv Rev* **64**, 53–68 (2012).

103. Marcucci, F. & Corti, A. Improving drug penetration to curb tumor drug resistance. *Drug Discov Today* **17**, 1139–1146 (2012).
104. Li, T., Wan, M. & Mao, C. Research Progress of Micro/Nanomotors for Cancer Treatment. *Chempluschem* **85**, 2586–2598 (2020).
105. Rastmanesh, A. *et al.* Bioinspired micro/nanomotors towards a self-propelled noninvasive diagnosis and treatment of cancer. *Mol Syst Des Eng* **6**, 566–593 (2021).
106. Lin, R., Yu, W., Chen, X. & Gao, H. Self-Propelled Micro/Nanomotors for Tumor Targeting Delivery and Therapy. *Adv Healthc Mater* **10**, 1–19 (2021).
107. Li, H. *et al.* Medical micro- and nanomotors in the body. *Acta Pharm Sin B* **13**, 517–541 (2023).
108. Wang, W. & Mallouk, T. E. A Practical Guide to Analyzing and Reporting the Movement of Nanoscale Swimmers. *ACS Nano* **15**, 15446–15460 (2021).
109. Chen, Z. *et al.* Enzyme-powered Janus nanomotors launched from intratumoral depots to address drug delivery barriers. *Chemical Engineering Journal* **375**, 1–12 (2019).
110. Joseph, A. *et al.* Chemotactic synthetic vesicles: Design and applications in blood-brain barrier crossing. *Sci Adv* **3**, 1–12 (2017).
111. Zhang, Z. *et al.* Icebreaker-inspired Janus nanomotors to combat barriers in the delivery of chemotherapeutic agents. *Nanoscale* **13**, 6545–6557 (2021).

112. Hortelao, A. C., Carrascosa, R., Murillo-Cremaes, N., Patino, T. & Sánchez, S. Targeting 3D Bladder Cancer Spheroids with Urease-Powered Nanomotors. *ACS Nano* **13**, 429–439 (2019).
113. Rosli, N. F. *et al.* Arsenene nanomotors as anticancer drug carrier. *Appl Mater Today* **21**, 1–8 (2020).
114. Zhang, X. *et al.* Near-Infrared-Enabled Nanomotor-Mediated Targeted Chemotherapy and Mitochondrial Phototherapy to Boost Systemic Antitumor Immunity. *Adv Healthc Mater* **11**, 1–17 (2022).
115. Felfoul, O. *et al.* Magneto-aerotactic bacteria deliver drug-containing nanoliposomes to tumour hypoxic regions. *Nat Nanotechnol* **11**, 941–947 (2016).
116. Kalyane, D. *et al.* Employment of enhanced permeability and retention effect (EPR): Nanoparticle-based precision tools for targeting of therapeutic and diagnostic agent in cancer. *Materials Science and Engineering C* **98**, 1252–1276 (2019).
117. Kroemer, G., Chan, T. A., Eggermont, A. M. M. & Galluzzi, L. Immunosurveillance in clinical cancer management. *CA Cancer J Clin* **74**, 187–202 (2024).
118. Rabinovich, G. A., Gabrilovich, D. & Sotomayor, E. M. Immunosuppressive strategies that are mediated by tumor cells. *Annu Rev Immunol* **25**, 267–296 (2007).
119. Galluzzi, L., Buqué, A., Kepp, O., Zitvogel, L. & Kroemer, G. Immunological Effects of Conventional Chemotherapy and Targeted Anticancer Agents. *Cancer Cell* **28**, 690–714 (2015).

120. Escriche-Navarro, B. *et al.* Mesoporous Silica Materials as an Emerging Tool for Cancer Immunotherapy. *Advanced Science* **9**, 1–24 (2022).
121. Schuster, M., Nechansky, A., Loibner, H. & Kircheis, R. Cancer immunotherapy. *Biotechnol J* **1**, 138–147 (2006).
122. Dillman, R. O. Cancer immunotherapy. *Cancer Biother Radiopharm* **26**, 1–64 (2011).
123. Au, K. M., Park, S. I. & Wang, A. Z. Trispecific natural killer cell nanoengagers for targeted chemoimmunotherapy. *Sci Adv* **6**, 1–15 (2020).
124. Le, Q. V., Choi, J. & Oh, Y. K. Nano delivery systems and cancer immunotherapy. *J Pharm Investig* **48**, 527–539 (2018).
125. Vinay, D. S. *et al.* Immune evasion in cancer: Mechanistic basis and therapeutic strategies. *Semin Cancer Biol* **35**, S185–S198 (2015).
126. Yoon, H. Y. *et al.* Engineering nanoparticle strategies for effective cancer immunotherapy. *Biomaterials* **178**, 597–607 (2018).
127. Shen, M. *et al.* Systemic Delivery of mPEG-Masked Trispecific T-Cell Nanoengagers in Synergy with STING Agonists Overcomes Immunotherapy Resistance in TNBC and Generates a Vaccination Effect. *Advanced Science* **9**, 1–15 (2022).
128. Xu, Y., Claiden, P., Zhu, Y., Morita, H. & Hanagata, N. Effect of amino groups of mesoporous silica nanoparticles on CpG oligodeoxynucleotide delivery. *Sci Technol Adv Mater* **16**, 1–11 (2015).

129. Kim, J. *et al.* Injectable, spontaneously assembling, inorganic scaffolds modulate immune cells in vivo and increase vaccine efficacy. *Nat Biotechnol* **33**, 64–72 (2015).
130. Wimalachandra, D. C. *et al.* Microfluidic-Based Immunomodulation of Immune Cells Using Upconversion Nanoparticles in Simulated Blood Vessel-Tumor System. *ACS Appl Mater Interfaces* **11**, 37513–37523 (2019).
131. Lee, K. Y., Seow, E., Zhang, Y. & Lim, Y. C. Targeting CCL21-folic acid-upconversion nanoparticles conjugates to folate receptor- α expressing tumor cells in an endothelial-tumor cell bilayer model. *Biomaterials* **34**, 4860–4871 (2013).
132. Stephan, M. T., Moon, J. J., Um, S. H., Bersthteyn, A. & Irvine, D. J. Therapeutic cell engineering with surface-conjugated synthetic nanoparticles. *Nat Med* **16**, 1035–1041 (2010).
133. Yuan, H. *et al.* Multivalent bi-specific nanobioconjugate engager for targeted cancer immunotherapy. *Nat Nanotechnol* **12**, 763–769 (2017).
134. Teo, P. Y. *et al.* Ovarian Cancer Immunotherapy Using PD-L1 siRNA Targeted Delivery from Folic Acid-Functionalized Polyethylenimine: Strategies to Enhance T Cell Killing. *Adv Healthc Mater* **4**, 1180–1189 (2015).
135. Wang, C. *et al.* In situ activation of platelets with checkpoint inhibitors for post-surgical cancer immunotherapy. *Nat Biomed Eng* **1**, 1–10 (2017).
136. Stephan, M. T., Stephan, S. B., Bak, P., Chen, J. & Irvine, D. J. Synapse-directed delivery of immunomodulators using T-cell-conjugated nanoparticles. *Biomaterials* **33**, 5776–5787 (2012).

137. McHugh, M. D. *et al.* Paracrine co-delivery of TGF- β and IL-2 using CD4-targeted nanoparticles for induction and maintenance of regulatory T cells. *Biomaterials* **59**, 172–181 (2015).
138. Schmid, D. *et al.* T cell-targeting nanoparticles focus delivery of immunotherapy to improve antitumor immunity. *Nat Commun* **8**, 1–12 (2017).

Objectives

Given the challenges of current tumour therapies and the growing interest in advanced smart nanodevices with biomedical applications, the main objective of this PhD thesis is the design, synthesis, characterisation, and evaluation of new hybrid mesoporous silica-based nanoparticles functionalised with different biomolecules in order to overcome the current limitations of cancer treatment. This PhD thesis therefore aims to generate novel therapies, which could improve treatment effectiveness and safety, while decreasing common side effects.

This global aim frames the following specific objectives:

- To develop and evaluate an enzymatic self-propelled system based on stimuli-responsive Janus Au-mesoporous silica nanoparticles for anti-tumor treatment.
- To synthesize and evaluate the efficacy of a moving Janus Pt-mesoporous silica-based nanodevice for enhanced drug delivery.
- To design and study a delivery system based on mesoporous silica nanoparticles for the co-delivery of a double-stranded small interfering RNA and an entrapped cargo, for cancer immunotherapy.
- To explore the beneficial effects of restored cytotoxic synapse and communication between tumor and immune system through a double-functionalized Janus Au-mesoporous silica nanoengager.

**Chapter I | Stimulus-Responsive Nanomotors Based on
Gated Enzyme-Powered Janus Au-Mesoporous Silica
Nanoparticles for Enhanced Cargo Delivery**

Stimulus-Responsive Nanomotors Based on Gated Enzyme-Powered Janus Au-Mesoporous Silica Nanoparticles for Enhanced Cargo Delivery

Antoni Llopis Lorente,^{a,b,c} Alba García-Fernández,^{a,b,c} Elena Lucena,^{a,b} Paula Díez,^{a,b} Félix Sancenón,^{a,b,c} Reynaldo Villalonga,^d Daniela A. Wilson^{*e} and Ramón Martínez-Máñez^{*abc}

^aInstituto Interuniversitario de Investigación de Reconocimiento Molecular y Desarrollo Tecnológico (IDM), Universitat Politècnica de València, Universitat de Valencia, Spain.

^bUnidad Mixta UPV-CIPF de Investigación en Mecanismos de Enfermedades y Nanomedicina, Valencia, Universitat Politècnica de València, Centro de Investigación Príncipe Felipe, València, Spain.

^cCIBER de Bioingeniería, Biomateriales y Nanomedicina (CIBER-BBN) (Spain).

^dDepartment of Analytical Chemistry, Faculty of Chemistry, Complutense University of Madrid, 28040, Madrid, Spain.

^eDepartment of Systems Chemistry, Institute for Molecules and Materials, Radboud University. Heyendaalseweg 135, 6525 AJ, Nijmegen (The Netherlands).

*Corresponding authors. Email: d.wilson@science.ru.nl; rmaez@qim.upv.es

Published online: October 8, 2019

(Reprinted with permission from Chemical Communications, 2019, Oct 8. © The Royal Society of Chemistry 2019)

1. Abstract

Here we report functional stimulus-responsive nanomotors based on Janus Au-mesoporous silica nanoparticles capable of self-propelling via the biocatalytic conversion of chemical fuel, read information from the environment (the presence of glutathion) and accordingly deliver a cargo.

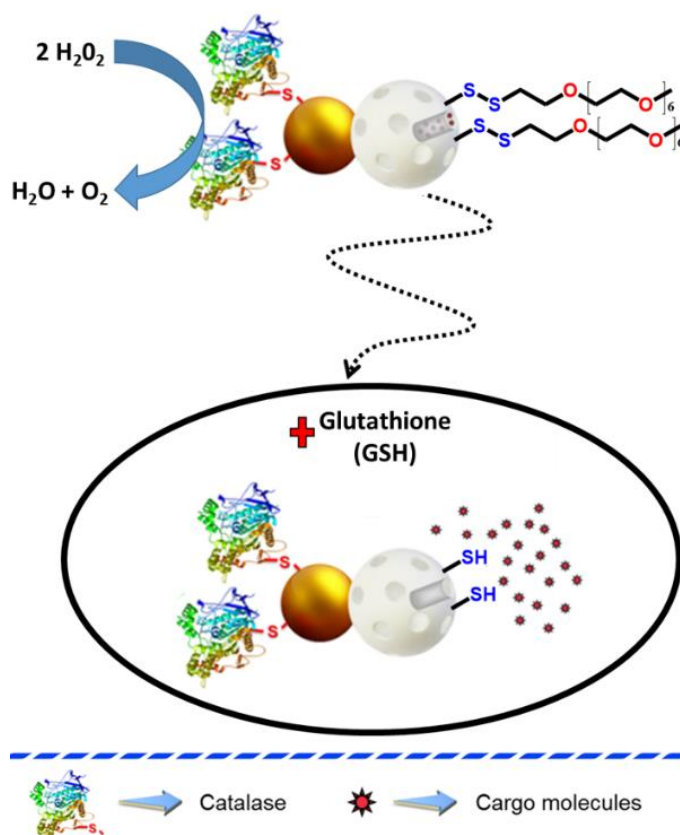
2. Introduction

The design of smart nanodevices (also called nanorobots or nanobots) is one of the most exciting topics within the nanotechnology field¹. Futuristic nanobots are envisioned to work autonomously in physiological environments and perform advanced tasks such as sensing, drug delivery and tissue repair. Ideal nanobots for drug delivery should be able to transport the therapeutic drug, have autonomous motion, sense the environment and deliver the drug at the specific targeted site, thus avoiding the premature release of the drug and minimizing side-effects.

Recently, micro- and nanomotors have emerged as a novel revolutionary technology with potential applications in different areas². Catalytic micro- and nanomotors are small devices that exhibit self-propulsion by converting a chemical fuel into autonomous motion³. Typically, platinum has been used as the catalytic component that transforms hydrogen peroxide (H_2O_2) into water and oxygen⁴. Notwithstanding, a more versatile and biocompatible approach is the use of enzyme catalysis⁵. Some proof-of-concept studies toward the application of catalytic nanomotors in cargo delivery have recently been conducted⁶. However, there are many challenges to address in this area such as improving loading capacity, introducing stimuli-responsive controlled release capabilities or developing versatile fabrication processes.

From another viewpoint, in the last decade, developing stimuli-responsive nanocarriers capable of releasing therapeutic drugs on-command have attracted significant attention, due to their potential benefits compared to classical systems in which cargo is released by simple diffusion⁷. Among them, mesoporous silica nanoparticles (MSNs) have appealing properties such as high loading capacity, biocompatibility, and the possibility to functionalize them with gatekeepers that block the pore outlets and prevent cargo release until a certain stimulus is applied⁸. A variety of gatekeepers that respond to (bio)chemical and physical stimuli have been developed⁹. However, as far as we know, gated MSNs showing autonomous motion have not yet been reported. The motor function in nanocarriers could be used for enhancing drug delivery and penetration in certain tissues, organs, or cells.

Here we present the design, preparation, and characterization of functional nanomotors (nanobots) based on Janus Au-MSNs that exhibit both self-propulsion (powered by enzyme-catalysis) and stimuli-responsive cargo delivery (controlled by gatekeepers) (Scheme 1). As a proof of concept, the silica face of the Janus particles is loaded with a model cargo ($[\text{Ru}(\text{bpy})_3]\text{Cl}_2$ (bpy=2,2'-bipyridine)) and capped with disulfide-linked oligo(ethylene glycol) (SS-OEG) chains; whereas the gold face is used for grafting the catalase enzyme. In the presence of the enzyme substrate (hydrogen peroxide (H_2O_2)), nanobots show self-propulsion due to the enzyme catalysed reaction (formation of oxygen and water from H_2O_2). The role of SS-OEG chains is to act as redox-responsive gatekeepers that prevent cargo release but “opens” in the presence of glutathione (GSH). Importantly, GSH is a reducing tripeptide found in intracellular compartments at much higher concentration (ca. 10000 μM) than in plasma (2 μM)¹⁰.



Scheme 1. Schematic representation of the performance of nanobots (S1_{cat}) with self-propulsion and glutathione-responsive cargo delivery capabilities.

3. Results and discussion

Our Janus particles were prepared via a Pickering emulsion route (see SI for details), which allows to obtain considerable higher amounts compared to typical electrochemical or physical vapour deposition techniques for the preparation of other Janus nanoparticles and avoids the use of expensive equipment. Briefly, MSNs were partially masked by confinement at the interface of an emulsion between paraffin wax and water and were partially functionalized with thiol groups by addition of (3-mercaptopropyl)trimethoxysilane on the exposed surface. Au nanoparticles were then attached by the formation Au-S bonds on the silica surface. Removal of paraffin by

washing with CHCl_3 , yielded the starting Janus Au-MSNs (**S0**)¹¹. **S0** was treated with 3-mercaptopropionic acid to functionalize the Au surface with carboxylic groups and the mesoporous scaffold was loaded with $[\text{Ru}(\text{bpy})_3]\text{Cl}_2$. Afterward, the external silica surface was functionalized with thiol groups that were reacted with 2,2-dipyridyl disulfide. Substitution of dipyridyl groups by reaction with O-(2-mercaptoethyl)-O-methyl-hexa(ethylene glycol) resulted in the capping of the mesoporous scaffold with disulfide-linked chains (SS-OEG). The resulting solid (**S1**) was then functionalized with catalase via reaction of carboxylic groups on the gold surface with lysine residues of the enzyme, yielding the final nanodevice **S1**_{cat}.

The nanomaterials were characterized by standard techniques (see SI for details). Transmission electron microscopy (TEM) allowed the imaging of Janus nanoparticles (**S0**) with Au (ca. 20 nm) and mesoporous silica (ca. 80 nm) on opposite faces of the hybrid anisotropic nanostructure (Figure 1 and SI-3). Scanning transmission electron microscopy coupled with energy dispersive x-ray spectroscopy (STEM-EDX) showed the mapping of different atoms on the final **S1**_{cat} (Figure 1B-F): Au and Si (attributed to the Janus scaffold), N (attributed to the cargo and the enzyme) and Fe atoms (corresponding to the heme group in the catalase enzyme). Moreover, the formation of the porous network was confirmed by N_2 adsorption-desorption isotherms (Figure SI-4). From elemental analysis, $[\text{Ru}(\text{bpy})_3]\text{Cl}_2$ and SS-OEG content on **S1** were determined as 107 mg and 52 mg per g of nanoparticles respectively. From dynamic light scattering (DLS) measurements, the hydrodynamic diameter and zeta potential of the final nanobots **S1**_{cat} were determined to be 114 ± 8 nm and -33.5 ± 4.1 mV respectively, with a single population distribution which indicated the good dispersion of the particles (Figure SI-5).

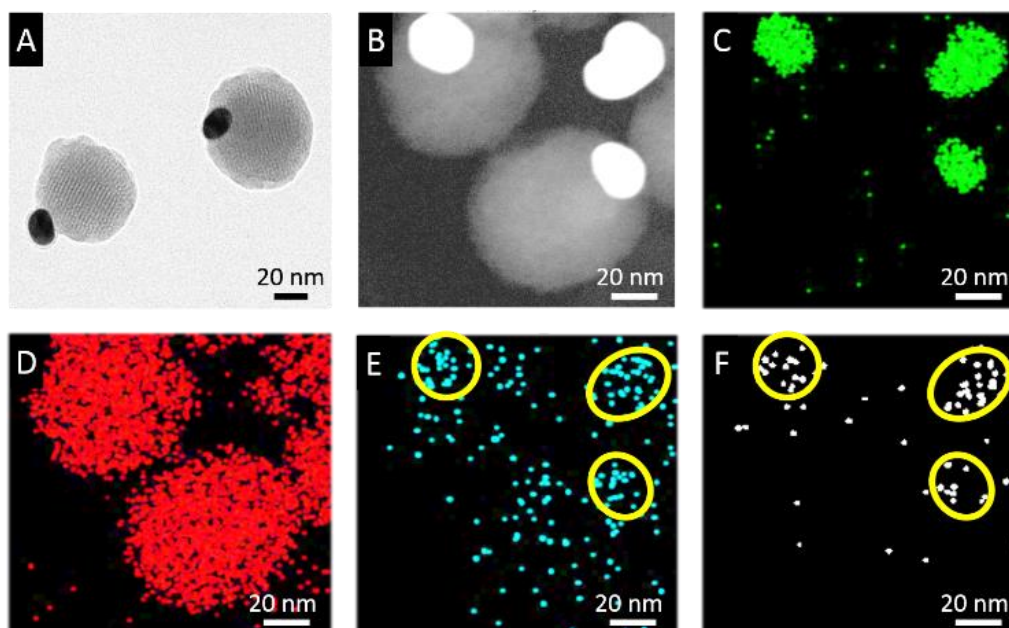


Figure 1. A) Representative TEM image of the Janus Au-MSNs (**S0**). B) STEM image and STEM-EDX elemental mapping of Au atoms (C), Si atoms (D), N atoms (E, attributed to the cargo and the enzyme), and Fe atoms (F, attributed to the heme group in the catalase enzyme) in the final nanobots (**S1_{cat}**). Yellow circles show the enrichment of the gold side with enzyme-associated atoms.

The catalytic activity of the nanobots **S1_{cat}** was evaluated by means of a catalase specific spectrophotometric assay (see SI for details). As showed in Figure 2A, in the presence of **S1_{cat}** a linear variation in H₂O₂ absorbance/consumption occurred. The activity of immobilized catalase enzyme on **S1_{cat}** was calculated as 152 U per g of nanoparticles, by applying Supplementary Equation SI-1. As a control experiment, we confirmed that the Janus scaffold (**S1**) did not induce H₂O₂ decomposition.

Nanoparticle tracking analysis (NTA)¹² was employed in order to investigate the motion capability of the nanobots. For these experiments, **S1_{cat}** was diluted in PBS buffer (1X, pH 7.5) and measured with the NanoSight NS300 instrument in the absence and in the presence of various amounts of H₂O₂ to obtain the tracking trajectories of nanobots (Figure 2B). From the x,y coordinates of multiple particles (N=20), the mean square displacement (MSD) was calculated (Figure 2C) by applying Supplementary Equation SI-2.

In the absence of fuel, MSD increased linearly with time, as expected for typical Brownian motion. Also, a linear increase in MSD vs. Δt was observed in the presence of fuel, but with higher MSD values, indicating an enhanced diffusion. From the linear fitting of MSD vs. Δt , the diffusion coefficient (D) was calculated by applying the well-known equation $MSD=4\cdot D\cdot\Delta t^{13}$. As depicted in Figure 2D, diffusion coefficient increased from $3.17\ \mu\text{m}^2/\text{s}$ in the absence of fuel, to $4.12\ \mu\text{m}^2/\text{s}$ and $5.24\ \mu\text{m}^2/\text{s}$ in the presence of 0.15% v/v (50 mM) and 0.30% v/v (100 mM) of fuel, respectively. Additionally, in the presence of fuel, a reduction of the apparent hydrodynamic size was observed by DLS, thus confirming the enhanced diffusion observed by NTA (Figure SI-6).

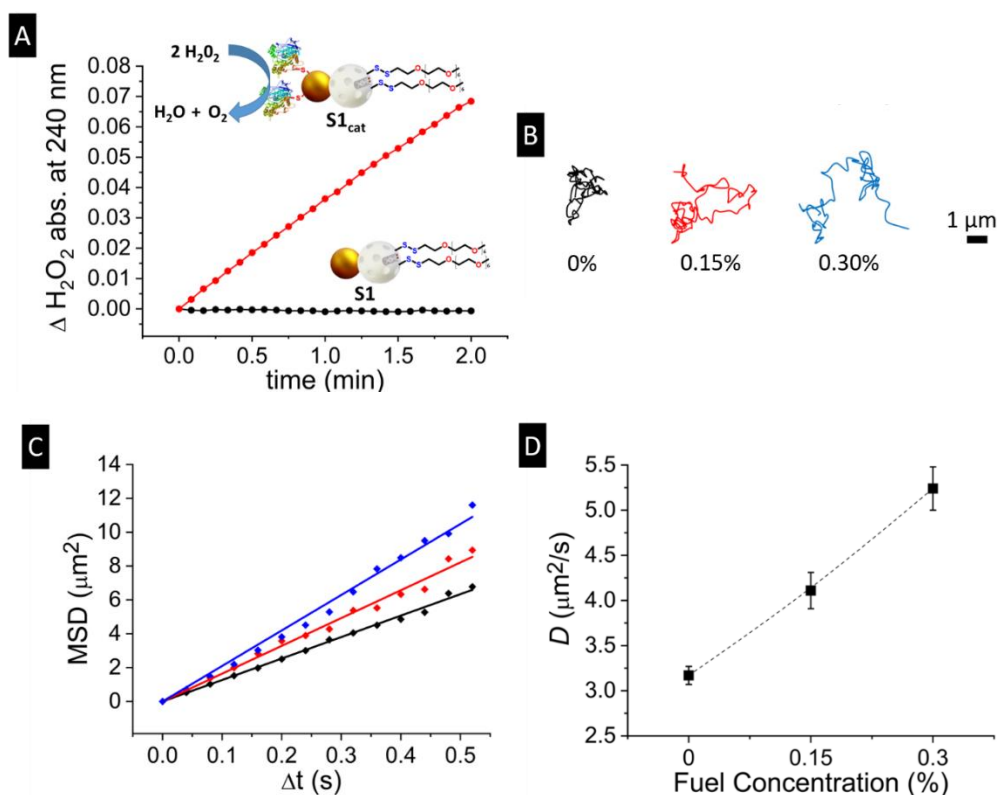


Figure 2. A) Catalytic activity of the nanoparticles. Monitoring of variation in H_2O_2 absorbance [Abs.(t=0)-Abs.(t=x)] at 240 nm as a function of time (H_2O_2 conversion) in the presence of **S1** and **S1_{cat}**. B) Typical tracking paths of nanobots **S1_{cat}** at different fuel concentrations (t=5s). C) MSD plots of nanobots **S1_{cat}** at 0% (black), 0.15% (red), and 0.30% (blue) fuel concentration. D) Diffusion coefficient of nanobots **S1_{cat}** at different fuel concentration (N=20).

Payload release experiments from nanobots **S1_{cat}** were carried out in aqueous media in the absence and in the presence of typical intracellular GSH concentration (10 mM)¹⁰. At scheduled times, aliquots were taken, centrifuged to remove nanoparticles, and the amount of cargo released in the supernatant was determined by measuring [Ru(bpy)₃]Cl₂ absorbance at 453 nm. As depicted in Figure 3 (continuous lines), release was negligible in the absence of GSH (a), thus confirming the correct capping of the pores by the SS-OEG gatekeepers. In contrast, a significant release occurred in the presence of GSH (14 µg of cargo per mg of **S1_{cat}**), which was ascribed to the cleavage of disulfide bonds, resulting in uncapping of the pores and cargo delivery (b).

Nanomotors for biomedical applications should propel in the presence of fuel with minimal premature cargo leakage, and deliver the payload once target cells or tissues are reached. Bearing this in mind, the effect of nanobots propulsion (in the presence of fuel) on cargo release was evaluated (Figure 3, dashed lines). Experiments were carried out as explained above but with the presence of H₂O₂ (0.3% v/v) in the media. In the absence of GSH and presence of fuel (c), the amount of cargo release was very low (2 µg of cargo per mg of **S1_{cat}**), thus indicating the correct blockage of the pores by the SS-OEG units even when fuel was present. Remarkably, a fast and massive cargo release (27.5 µg of cargo per mg of **S1_{cat}**) was observed in the presence of both fuel and GSH (ON behaviour). Thus, a significant enhancement of cargo delivery was found in the presence of GSH when fuel was present (curve d). This increased cargo release was attributed to the uncapping of the pores by GSH and the enhanced diffusion of nanobots produced by self-propulsion in the presence of fuel, which could generate a flow through the non-capped nanocarrier surface¹⁴. Additionally, we conducted release studies with **S1** (without catalase enzyme, Figure SI-7 and SI-8). In this case the presence of H₂O₂ did not have any effect in the release of **S1**, which points out the key role played by the catalase enzyme. We also checked that the cargo ([Ru(bpy)₃]Cl₂) absorbance was not affected by the presence of H₂O₂ (Figure SI-9).

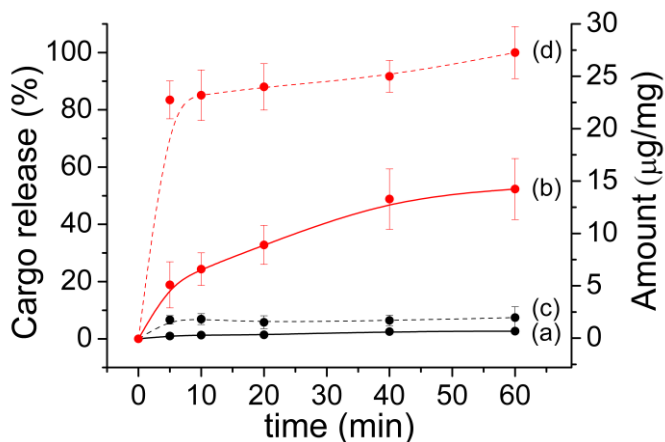


Figure 3. Cargo release from nanobots **S1_{cat}** in phosphate buffer (pH 7.5) under different conditions: (a) control (no fuel and no GSH), (b) presence of GSH (10 mM), (c) presence of fuel (H₂O₂ 0.3%), and (d) presence of GSH (10 mM) and fuel (H₂O₂ 0.3%). Y-axes represent relative release (%) and released amount per mg of **S1_{cat}**. Error bars represent SD from three independent experiments.

Encouraged by the above mentioned results (i.e., self-propulsion and controlled release capabilities), we prepared nanobots **S1_{dox-cat}** (similar to **S1_{cat}** but loaded with the drug doxorubicin (dox)) and used confocal fluorescence microscopy to directly visualize dox delivery in Hela cells. For these experiments, cells were treated with 50 µg·ml⁻¹ of **S1_{dox-cat}** and incubated in the absence and in the presence of H₂O₂. At scheduled times (1 and 6 h), cells were washed to remove non-internalized particles, stained with nucleic marker Hoechst 3342, and then confocal images were acquired. As showed in Figure 4, a clear intracellular dox-associated fluorescence was observed indicating nanobot internalization and the cleavage of SS-OEG chains by intracellular GSH in both cases (absence or presence of fuel). Notwithstanding, a larger intracellular dox release was observed for nanobots incubated with H₂O₂ after 1 and 6 hours. This is ascribed to the enhanced diffusion of the nanobots in the presence of fuel, resulting in an enhanced cell internalization and a larger intracellular cargo release. As a control experiment, we confirmed that this effect was not observed for nanoparticles without catalase (Figure SI-10).

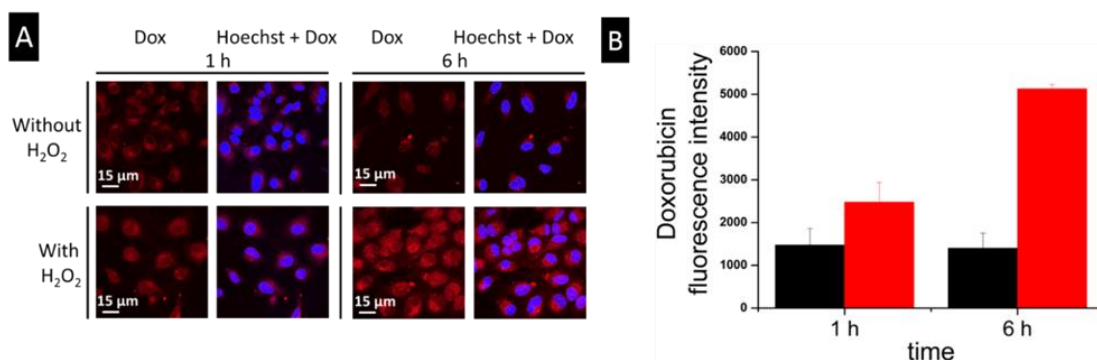


Figure 4. A) Confocal microscopy images of HeLa cells incubated with S1_{dox} for 1 and 6 hours in the absence and in the presence of H₂O₂. B) Quantification of dox-fluorescence in cells incubated with S1_{dox} in the absence (black) and in the presence of H₂O₂ (red), using the ImageJ software. Error bars represent SD from three independent experiments.

4. Conclusions

In summary, we have presented here the design of novel functional nanomotors (nanobots) based on gated enzyme-powered Janus Au-MSNs with self-propulsion and controlled drug release capabilities. Janus Au-MSNs are prepared via a Pickering emulsion technique, functionalized with disulfide-linked gatekeepers on the mesoporous face and with catalase enzyme on the gold face. These functional nanobots exhibit autonomous motion via catalytic decomposition of fuel (H₂O₂). Additionally, nanobots remain capped and only deliver their payload upon recognition of the reducing agent GSH, due to the cleavage of the gatekeepers. Moreover, in the presence of fuel a remarkable more efficient delivery of the drug (dox) in cancer cells was observed. Thus, the nanodevice displays desired features for nanobots for biomedical applications: (i) autonomous motion and (ii) the ability to sense the environment and deliver the drug only in the presence of a stimulus (GSH). Given the easy preparation of the Janus Au-MSNs and the number of stimuli-responsive gatekeepers available that can be tested in combination with different enzymes, we believe that this is a promising and versatile strategy for the

development of functional nanobots, having autonomous motion and only releasing the cargo inside cells, for advanced controlled delivery applications.

5. Materials and methods

5.1. Chemicals

Tetraethyl orthosilicate (TEOS), n-cetyltrimethylammonium bromide (CTABr), sodium hydroxide (NaOH), paraffin wax, (3-mercaptopropyl)trimethoxysilane, hydrogen tetrachloroaurate(III) ($\text{HAuCl}_4 \cdot 3\text{H}_2\text{O}$), sodium citrate tribasic dihydrate, 3-mercaptopropionic acid, tris(2,2'-bipyridyl)dichlororuthenium(II) hexahydrate ($[\text{Ru}(\text{bpy})_3]\text{Cl}_2 \cdot 6\text{H}_2\text{O}$), 2,2'-dipyridyl disulfide, O-(2-Mercaptoethyl)-O'-methylhexa(ethylene glycol) (OEGSH), N-(3-dimethylaminopropyl)-Nl-ethylcarbodiimide hydrochloride (EDC), N-hydroxysuccinimide (NHS), catalase from bovine liver, hydrogen peroxide (30%), L-glutathione reduced (GSH), and sodium hydrogen phosphate monohydrate were provided by Sigma-Aldrich. Disodium hydrogen phosphate heptahydrate, methanol, absolute ethanol, chloroform and acetonitrile were provided by Scharlau. For cell culture, Dulbecco's Phosphate Buffered Saline (PBS), Dulbecco's Modified Eagle's Medium (DMEM) - high glucose, and Fetal Bovine Serum (FBS) and Hoechst 33342 were purchased from Sigma-Aldrich. Hela human cervix adenocarcinoma cells were purchased from the German Resource Centre for Biological Materials (DSMZ).

5.2. General methods

UV-visible measurements were recorded with a JASCO V-650 Spectrophotometer. Powder X-ray diffraction (PXRD) measurements were carried using a Seifert 3000TT diffractometer using $\text{CuK}\alpha$ radiation. N_2 adsorption-desorption isotherms were recorded using a Micromeritics TriStar II Plus automated analyzer. Transmission electron microscopy (TEM) images were acquired using a JEOL TEM-1010 Electron microscope. Scanning transmission electron microscopy coupled with energy dispersive x-ray

spectroscopy (STEM-EDX) was carried out using a JEM 2100F instrument. Elemental analysis was performed using a LECO CHNS-932 Elemental Analyzer. Dynamic light scattering (DLS) experiments were performed using a ZetaSizer Nano ZS (Malvern). Nanoparticle tracking experiments were performed using a Nanosight NS300 (Malvern). Confocal microscopy imaging was performed with a Leica TCS SP8 AOBS inverted laser scanning confocal microscope.

5.3. Synthesis of mesoporous silica nanoparticles (MSNs)

First, the surfactant CTABr (1.00 g, 2.74 mmol) was dissolved in 480 ml of deionized water at 30 °C. Then, the media was basified by addition of 3.5 mL of a NaOH solution (2 M). Next, the temperature was increased to 80 °C and 5 ml of TEOS (22.4 mmol) were added to the stirring solution. The mixture was further stirred for 2 hours at 80 °C. Afterward, the mixture was cooled down at room temperature and the white precipitate was isolated by centrifugation. The resulting solid was washed several times with deionized water and dried in an oven at 70 °C overnight. Finally, the surfactant was removed by calcination at 550 °C in an oxidant atmosphere for 5 hours, which yielded the starting MSNs.

5.4. Synthesis of gold nanoparticles (AuNPs)

100 ml of $\text{HAuCl}_4 \cdot 3\text{H}_2\text{O}$ aqueous solution (0.0116%) were brought to reflux under magnetic stirring. Then, 1.57 ml of freshly prepared 1% sodium citrate aqueous solution were added to induce the reduction of Au(III) and the formation of 20 nm gold nanoparticles. The initial faint yellow colour turned to blue-black and finally to red wine in a few minutes. The colloidal suspension was let to cool at room temperature. This process was repeated four times, yielding the as-synthesized AuNPs.

5.5. Synthesis of Janus Au-MSNs (S0)

180 mg of MSNs were dispersed in 9 ml of aqueous solution (6.7% ethanol). Then, 1 μ M (final concentration) of CTABr were added. The mixture was stirred and heated in a water bath at 75 °C, followed by addition of 1 g of paraffin wax. Once the paraffin was melted, the mixture was emulsified by vigorously stirring using an Ultra-Turrax T-25 homogenizer (IKA) for 15 minutes. Afterward, the mixture was further stirred for 1 h at 75 °C using a magnetic stirrer. The resulting Pickering emulsion was then cooled to room temperature, mixed with 9 ml of methanol and treated with 180 μ l of (3-mercaptopropyl)trimethoxysilane for 3 hours. After this time, the solid was collected by centrifugation, washed twice with methanol, and dispersed in 68 ml of methanol. This solution containing the MSNs partially functionalized with thiol moieties was added over 400 ml of the as-synthesized AuNPs. The mixture was stirred overnight. Afterward, the solid was isolated by filtration and exhaustively washed with ethanol and chloroform in order to remove the paraffin. The solid powder was dried at room temperature and ground. This process finally yielded the Janus Au-MSNs (S0).

5.6. Synthesis of gated nanoparticles S1

First, 50 mg of S0 were dispersed in 5 ml of EtOH containing 70 μ l of 3-mercaptopropionic acid and magnetically stirred for 1 h at room temperature, in order to functionalize the gold face with carboxylic groups. The solid was collected by centrifugation, washed with ethanol, and dried at room temperature. Next, in order to load the cargo in the pores, the solid was dispersed in an acetonitrile solution (5 ml) containing 25 mg of [Ru(bpy)₃]Cl₂·6H₂O. The mixture was stirred overnight and the solid was collected by centrifugation and washed with toluene. The resulting solid was redispersed in toluene (1.7 ml) and treated with 97 μ l of (3-mercaptopropyl)trimethoxysilane. After 5.5 h, 110 mg of 2,2'-dipyridyl disulfide (0.5 mmol) were added and the mixture was stirred overnight. Afterward, the solid was

isolated by centrifugation, washed with toluene and dried under vacuum overnight. Finally, this solid was dispersed in 3.3 ml of toluene and reacted with 50 μl of O-(2-Mercaptoethyl)-O'-methyl-hexa(ethylene glycol) (OEGSH), which capped the pores by the formation of disulfide bonds via substitution of dipyridyl moieties. The solid was exhaustively washed with toluene, acetonitrile, and phosphate buffer and dried at room temperature. This process finally yielded the capped nanoparticles **S1**.

5.7. Preparation of enzyme-functionalized gated nanoparticles (**S1_{cat}**)

8 mg of **S1** were dispersed in 4 ml of sodium phosphate buffer (50 mM, pH 7.5). Then, 4 mg of EDC, 4 mg of NHS and 2 mg of commercial catalase were added and the suspension was stirred overnight in an ice bath. The solid was isolated by centrifugation and exhaustively washed with buffer. The solid was divided in several aliquots of 4 mg·ml⁻¹ that were kept refrigerated until use. This process finally yielded the final nanobots **S1_{cat}**.

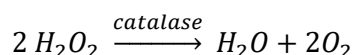
5.8. Preparation of **S1_{dox-cat}**

For the preparation of **S1_{dox-cat}**, the procedure was similar to the one used for **S1_{cat}** but using the drug doxorubicin (dox) as the cargo. Briefly, 50 mg of **S0** were suspended in 5 ml of ethanol and treated with 70 μl of 3-mercaptopropionic acid for 1 hour, in order to functionalize the gold face. The sample was then collected by centrifugation, washed with ethanol and suspended in 5 ml of phosphate buffer containing 25 mg of dox. The mixture was stirred overnight, redispersed in toluene and then 97 μl of (3-mercaptopropyl)trimethoxysilane were added. After 5.5 h, 110 mg of 2,2'-dipyridyl disulfide (0.5 mmol) were added and the mixture was further stirred for 24 h. Finally, the particles were collected by centrifugation, resuspended in 3.3 ml of toluene and capped by addition of 50 μl of O-(2-Mercaptoethyl)-O'-methyl-hexa(ethylene glycol) (OEGSH). The stirring was kept overnight, followed by centrifugation and washing of the solid with acetonitrile and sodium phosphate buffer (50 mM, pH 7.5). The capped solid (**S1_{dox}**) was

dried, and further functionalized with catalase following the same procedure as described above. This process finally yielded the dox-loaded nanobots **S1_{dox-cat}**.

5.9. Catalase activity

Catalase activity was measured by adapting a procedure previously reported¹⁵. Hydrogen peroxide absorbs light at 240 nm. The assay is based on monitoring the transformation of H₂O₂ by catalase which can be followed by the decrease in absorbance at 240 nm due to the following reaction:



In a typical assay, 850 μ l of 50 mM sodium phosphate buffer (pH 7.5) and 100 μ l of H₂O₂ 0.35% were placed in a quartz cuvette. Then, the mixture was completed with either buffer (10 μ l, for blank) or stock of nanoparticles (10 μ l, 0.5 mg·ml⁻¹). The mixture was shaken and the absorbance at 240 nm was monitored during one minute in intervals of 5 seconds. Whereas a flat line was observed for the blank and **S1** nanoparticles, **S1_{cat}** nanobots shown a linear variation (decrease) in H₂O₂ absorbance which confirmed their catalase-activity (see Figure 2A). From the slope of the graph (absorbance vs. time, Figure 2A), the catalase activity was determined by applying Equation 1.

Equation 1:

$$\frac{\text{Enzyme Units}}{\text{g}} = \frac{(\Delta - \Delta_{\text{blank}}) * V_T * F_D}{\epsilon_{H_2O_2} * l * V_{NPS} * C_{NPS}}$$

Where,

Δ is the slope of the graph (min⁻¹)

Δ_{blank} is the slope of for the blank (min⁻¹)

V_T is the total volume in the cuvette

$\epsilon_{H_2O_2}$ is the molar extinction of H₂O₂ at 240 nm (0.0435 μ M⁻¹ · cm⁻¹)

L is the optical path in the cuvette (1 cm)

V_{NPs} is the volume of nanoparticles added (ml)

C_{NPs} is the concentration of the nanoparticle stock solution added ($\text{g}\cdot\text{ml}^{-1}$).

From this formula, the activity of immobilized catalase on **S1_{cat}** was calculated as 152 U per g of nanoparticles. Additionally, the corresponding activity for the commercial enzyme was calculated to be $10138 \text{ U}\cdot\text{mg}^{-1}$, which corresponds to 15 mg of native enzyme per g of nanoparticles.

5.10. Motion analysis

As previously described¹⁶, we used Nanoparticle Tracking Analysis (NTA) for evaluating the motion of the nanoparticles. These experiments were performed on a Nanosight NS300 instrument equipped with an sCMOS camera. This camera is mounted on an optical microscope in order to track the light scattered by the particles that are present in the focus of the beam generated by a single mode laser diode with a 55 mW blue light illumination. Samples were diluted in PBS buffer (1X) at $0.02 \text{ mg}\cdot\text{mL}^{-1}$, passed through PTFE $0.22 \mu\text{m}$ syringe filters, and introduced into the Nanosight chamber at $25 \text{ }^\circ\text{C}$ using a 1 mL syringe. The Brownian motion of the nanoparticles was tracked with 25 frames $\cdot\text{s}^{-1}$. NTA 3.0 software was used to track the particles which gives the x, y coordinates of each particle as a function of time and allows for the calculation of their mean square displacement (MSD) by applying Equation 2.

Equation 2:

$$MSD = \langle (r)^2 \rangle = \frac{1}{N} \sum_{i=0}^N (r_i(t) - r_i(0))^2$$

The apparent diffusion coefficient can be extracted by the linear fitting of MSD vs. Δt by applying the well-known equation $MSD = 2 d \cdot D \cdot t$ (where d = dimensionality (2 in the case of 2-dimensional videos)).

5.11. Release experiments

For release experiments, refrigerated stocks of **S1_{cat}** were diluted with sodium phosphate buffer (10 mM, pH 7.5), washed a couple of times, and divided into fractions of 0.5 mg. Then 1 ml of phosphate buffer (10 mM, pH 7.5) containing the corresponding amount of glutathione and H_2O_2 was added. Release experiments were conducted at room temperature. At scheduled times, aliquots of 150 μ l were taken with a pipette, centrifuged to remove the nanoparticles (12000 rpm, 2 min) and the supernatant absorbance was measured at 453 nm. Three independent experiments were carried out. The amount of released $[Ru(bpy)_3]Cl_2$ dye was determined by applying Beer-Lambert's law (Equation 3).

Equation 3:

$$\text{Absorbance (453 nm)} = \epsilon_{453} \cdot L \cdot C$$

Where ϵ_{453} is the molar extinction of $[Ru(bpy)_3]Cl_2$ at 453 nm ($14600 \text{ M}^{-1} \text{ cm}^{-1}$), L is the optical path of the cuvette (1 cm), and C is the concentration of $[Ru(bpy)_3]Cl_2$.

Release experiments using nanoparticles **S1** (without the catalase) were also carried out. These results are depicted in Figure SI-7 and SI-8.

5.12. Experiments with Hela cells

5.12.1. Cell culture conditions

Hela human cervix adenocarcinoma cells were grown in Dulbecco's Modified Eagle's Medium (DMEM) supplemented with 10% fetal bovine serum (FBS). Cells were incubated at 37°C in an atmosphere of 5% carbon dioxide and 95% air and underwent passage twice a week.

5.12.2. Confocal microscopy studies of doxorubicin controlled release

Internalization and cargo delivery of **S1_{dox-cat}** in HeLa cells was studied by confocal microscopy. For this purpose, HeLa cells were seeded over glass coverslips at 300.000 cells·ml⁻¹ in 6-well culture plates and incubated at 37 °C for 24 h. Then, **S1_{dox-cat}** was added to HeLa cells at 50 µg·ml⁻¹ and incubated at 37 °C for 1 and 6 h in the absence or presence of H₂O₂ (0.2 mg·ml⁻¹). Afterwards, cells were washed several times with PBS to remove non-internalized nanoparticles and stained with DNA marker Hoechst 33342 (2 µg·ml⁻¹). Finally, slides were visualized using a Leica TCS SP2 AOBS confocal microscope. ImageJ software was used for fluorescence quantification. Three independent experiments were carried out, which gave similar results. A control experiment using **S1_{dox}** (without the catalase) was also carried out.

6. References

1. (a) K. Ariga, D. T. Leong, T. Mori. Nanoarchitectonics for Hybrid and Related Materials for Bio-Oriented Applications. *Adv. Funct. Mater.* **28**, 1-23 (2018); (b) J. Li, B. Esteban-Fernández de Ávila, W. Gao, L. Zhang, J. Wang. Micro/Nanorobots for Biomedicine: Delivery, Surgery, Sensing, and Detoxification, *Sci. Robot.* **2**, 1-19 (2017).
2. (a) J. Parmar, D. Vilela, K. Villa, J. Wang, S. Sánchez. Micro- and Nanomotors as Active Environmental Microcleaners and Sensors. *J. Am. Chem. Soc.*, **30**, 9317-9331 (2018); (b) X. Lin, Z. Wu, Y. Wu, M. Xuan, Q. He. Self-Propelled Micro-/Nanomotors Based on Controlled Assembled Architectures. *Adv. Mater.* **28**, 1060-1072 (2016).
3. (a) K. K. Dey, A. Sen. Chemically Propelled Molecules and Machines. *J. Am. Chem. Soc.*, **139**, 7666-7676 (2017); (b) H. Hong, M. Pumera. Fabrication of Micro/Nanoscale Motors. *Chem. Rev.* **115** (16), 8704-8735 (2015).

4. (a) X. Ma, K. Hahn, S. Sánchez. Catalytic Mesoporous Janus Nanomotors for Active Cargo Delivery. *J. Am. Chem. Soc.* **137** (15), 4976-4979 (2015); (b) F. Peng, Y. Men, Y. Tu, Y. Chen, D. A. Wilson. Nanomotor-Based Strategy for Enhanced Penetration across Vasculature Model. *Adv. Funct. Mater.*, **28** (1706117), 1-8 (2018).
5. (a) K. K. Dey, X. Zhao, B. M. Tansi, W. J. Méndez-Ortiz, U. M. Córdova-Figueroa, R. Golestanian, A. Sen. Micromotors Powered by Enzyme Catalysis. *Nano Lett.*, **15** (12), 8311-8315 (2015); (b) X. Ma, A. C. Hortelao, T. Patiño, S. Sánchez. Enzyme Catalysis To Power Micro/Nanomachines. *ACS Nano*, **10** (10), 9111-9122 (2016).
6. F. Peng, Y. Tu, D. A. Wilson. Micro/nanomotors towards in vivo application: cell, tissue and biofluid. *Chem. Soc. Rev.*, **46**, 5289-5310 (2017).
7. (a) S. Mura, J. Nicolas, P. Couvreur. Stimuli-responsive nanocarriers for drug delivery. *Nat. Mater.*, **12** (11), 991-1003 (2013); (b) Q. Hu, H. Li, L. Wang, H. Gu, C. Fan. DNA Nanotechnology-Enabled Drug Delivery Systems. *Chem. Rev.*, **119** (10), 6459-6506 (2019).
8. J. G. Croissant, Y. Fatieiev, A. Almalik, N. Khashab. Mesoporous Silica and Organosilica Nanoparticles: Physical Chemistry, Biosafety, Delivery Strategies, and Biomedical Applications. *Adv. Healthcare Mater.*, **7**, 1-75 (2017).
9. E. Aznar, M. Oroval, L. Pascual, J. R. Murguía, R. Martínez-Máñez, F. Sancenón. Gated Materials for On-Command Release of Guest Molecules. *Chem. Rev.*, **116** (2), 561-718 (2016).
10. (a) D. Montero, C. Tachibana, J. R. Winther, C. Appenzeller-Herzog. Intracellular glutathione pools are heterogeneously concentrated. *Redox Biol.*, **1**, 508-513 (2013);

- (b) H. J. Forman, H. Zhang, A. Rinna. Glutathione: overview of its protective roles, measurement, and biosynthesis. *Mol. Aspects Med.*, **30**, 1-12 (2009).
11. (a) L. Hong, S. Jiang, S. Granick. Simple Method to Produce Janus Colloidal Particles in Large Quantity. *Langmuir*, **22**, 9495-9499 (2006); (b) A. Llopis-Lorente, P. Díez, A. Sánchez, M. D. Marcos, F. Sancenón, P. Martínez-Ruiz, R. Villalonga, R. Martínez-Máñez. Interactive models of communication at the nanoscale using nanoparticles that talk to one another. *Nat. Commun.*, **8**, 1-7 (2017).
12. Y. Tu, F. Peng, X. Sui, Y. Men, P. B. White, J. C. M. van Hest, D. A. Wilson. Self-propelled supramolecular nanomotors with temperature-responsive speed regulation. *Nat. Chem.*, **9**, 480-486 (2017).
13. G. Dunderlade, S. Ebbens, P. Fairclough, J. Howse. Importance of particle tracking and calculating the mean-squared displacement in distinguishing nanopropulsion from other processes. *Langmuir*, **28**, 10997-11006 (2012).
14. A. Hortelao, T. Patiño, A. Perez-Jiménez, A. Blanco, S. Sánchez. Enzyme-Powered Nanobots Enhance Anticancer Drug Delivery. *Adv. Funct. Mater.*, **28**, 1-10 (2018).
15. (a) R. F. Jr., Beers, I. W. Sizer. A spectrophotometric method for measuring the breakdown of hydrogen peroxide by catalase. *J. Biol. Chem.*, **195**, 133-140 (1952) ; (b) K. G. Stern. On the absorption spectrum of catalase. *J. Biol. Chem.*, **121**, 561-572 (1937); (c) Sigma-Aldrich (2018). Enzymatic Assay of Catalase. <http://www.sigmaaldrich.com/technical-documents/protocols/biology/enzymatic-assay-of-catalase.html> (accessed 30 October 2018).

16. (a) D. A. Wilson, R. J. M. Nolte, J. C. M. van Hest. Autonomous movement of platinum-loaded stomatocytes. *Nat. Chem.*, **4**, 268-274 (2012); (b) Y. Tu, F. Peng, X. Sui, Y. Men, P. B. White, J. C. M. van Hest, D. A. Wilson. Self-propelled supramolecular nanomotors with temperature-responsive speed regulation. *Nat. Chem.*, **9**, 480-486 (2017).

Acknowledgments

The authors thank the Spanish Government (Projects MAT2015-64139-C4-1, AGL2015-70235-C2-2-R, CTQ2014-58989-P, CTQ2015-71936-REDT and CTQ2017-87954-P) and the Generalitat Valencia (PROMETEO/2018/024) for support. The Comunidad de Madrid (IND2017/BMD-7642) is also gratefully acknowledged. D. A. W. acknowledges support from the Ministry of Education, Culture and Science (Gravitation program 024.001.035) and NWO Chemische Wetenschappen VIDI grant 723.015.001.

Author contributions

Antoni Llopis-Lorente: Experimental design, nanoparticle development and characterization, data analysis, discussion, and writing. Alba García-Fernández: Experimental design, performing biological experiments, data analysis, discussion, and writing. Elena Lucena-Sánchez: Performing biological experiments and data analysis. Paula Díez: Contributed to nanoparticle characterization analysis. Félix Sancenón: Writing – review & editing. Reynaldo Villalonga: Conceptualization, Writing – review & editing. Daniela A. Wilson: Conceptualization, Project administration, Writing – review & editing, Supervision. Ramón Martínez-Máñez: Conceptualization, Project administration, Writing – review & editing, Supervision. All authors have approved the final version of the manuscript.

Conflicts of interest

There are no conflicts to declare.

7. Supporting information

7.1. Materials characterization

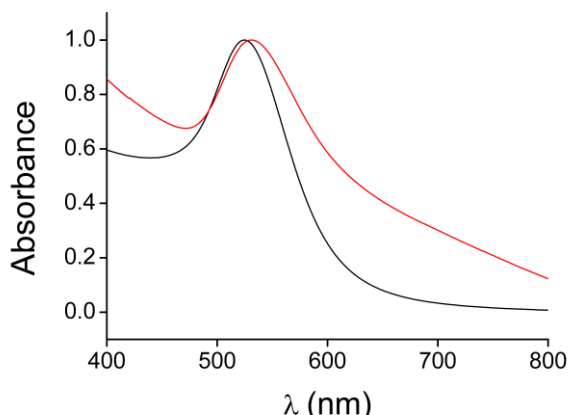


Figure SI-1. Normalized absorbance spectra of the as-synthesized AuNPs (black) and Janus particles **S0** (red).

The UV-visible spectra of the as-synthesised Au nanoparticles showed the characteristic absorption band with a maximum at 525 nm, which was red-shifted to 531 nm for the Janus particles **S0** due to the increase in refractive index around the Au surface induced by silica (Figure SI-1). On the other hand, powder X-ray diffraction (PXRD) at low angles of MSNs showed a main peak around 2.4° which is characteristic of mesoporous nanoparticles with an MCM-41 type structure (Figure SI-2)¹. The preservation of this characteristic peak in the PXRD patterns of **S0** and **S1** indicated that the cargo loading, and functionalization processes had not damaged the mesoporous scaffolding. Furthermore, PXRD patterns at high angles ($35\text{-}80^\circ$) of **S0** and **S1** showed four main peaks that can be indexed as the (100), (200), (220) and (311) Bragg peaks corresponding to the presence of cubic Au crystals².

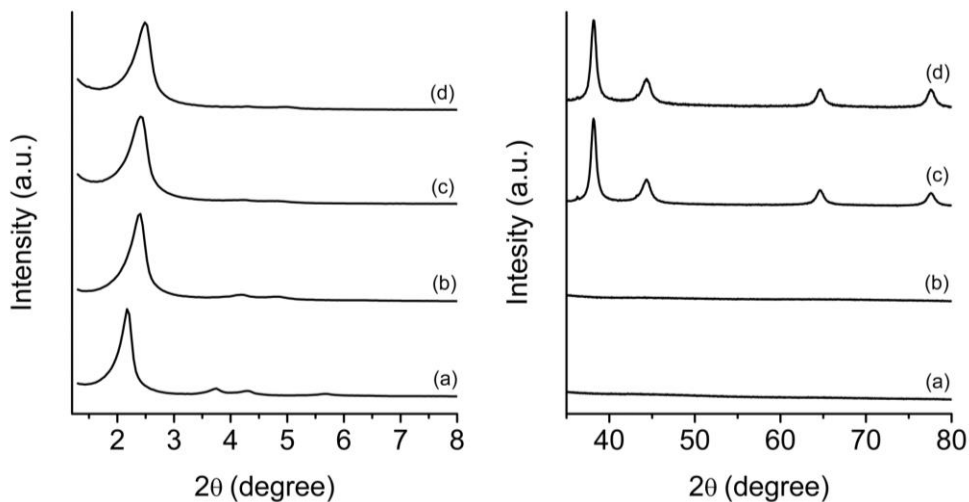


Figure SI-2. PXRD patterns at low angles (left) and at high angles (right) of: (a) as-synthesized MSNs, (b) calcined MSNs, (c) starting Janus Au-MSNs (**S0**) and (d) gated nanoparticles (**S1**).

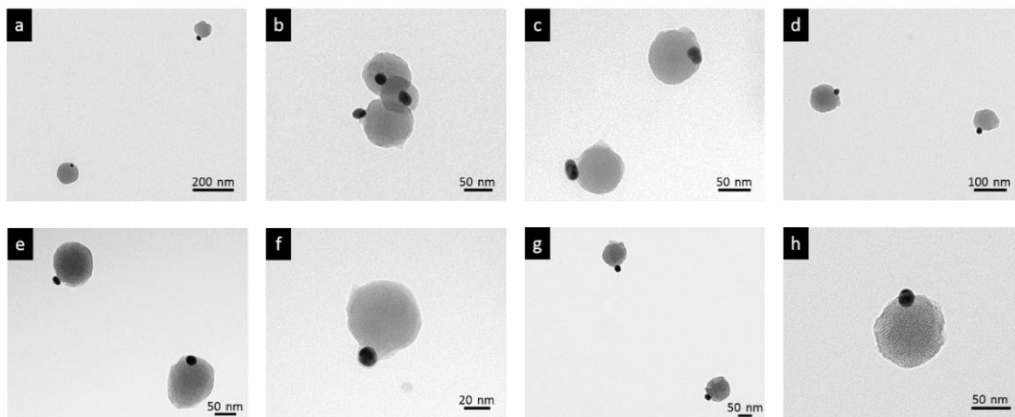


Figure SI-3. Representative TEM images of the Janus nanoparticles.

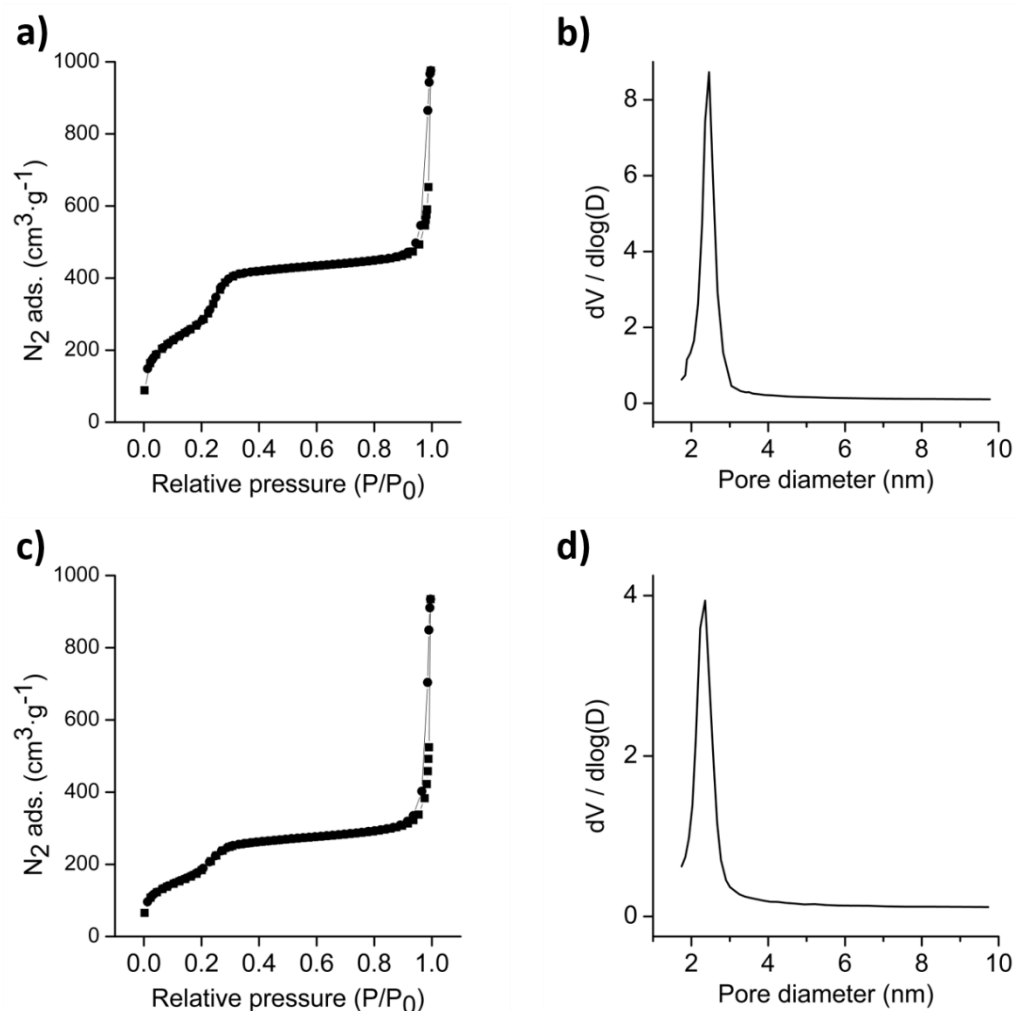


Figure SI-4. a) N₂ adsorption-desorption isotherms for the calcined MSNs and (b) corresponding pore diameter distribution. c) N₂ adsorption-desorption isotherms for the Janus Au-MSNs (S0) and (d) corresponding pore diameter distribution. Pore diameter distributions were determined by applying the BJH model on the adsorption branch of the isotherm for P/P₀ < 0.8, which is associated with the surfactant generated mesopores.

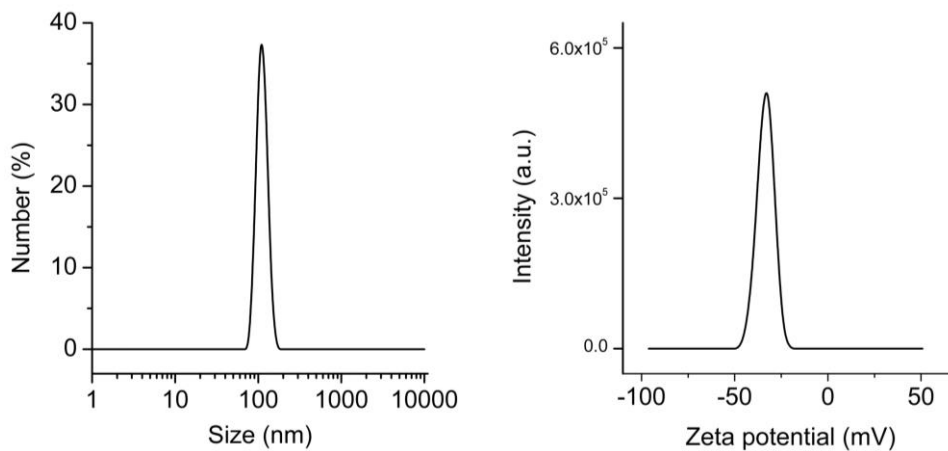


Figure SI-5. Hydrodynamic diameter and zeta potential distributions of the nanodevice ($S1_{cat}$) determined by DLS.

7.2. Motion analysis

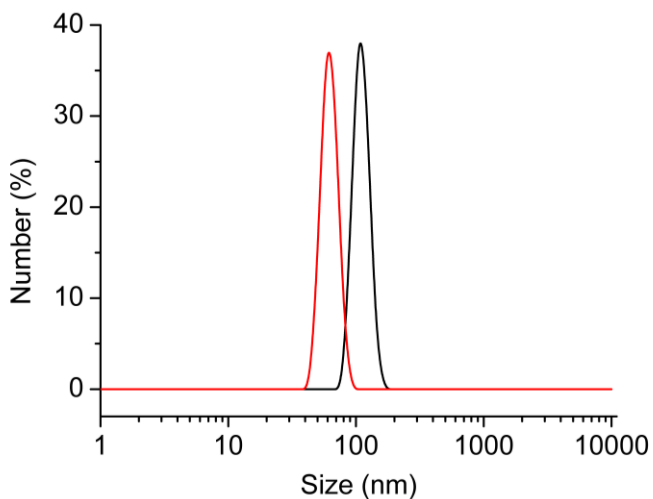


Figure SI-6. Apparent hydrodynamic size distribution of nanobots ($S1_{cat}$) before (black) and after the addition (red) of fuel (0.3% v/v H_2O_2) as measured by DLS.

7.3. Release experiments

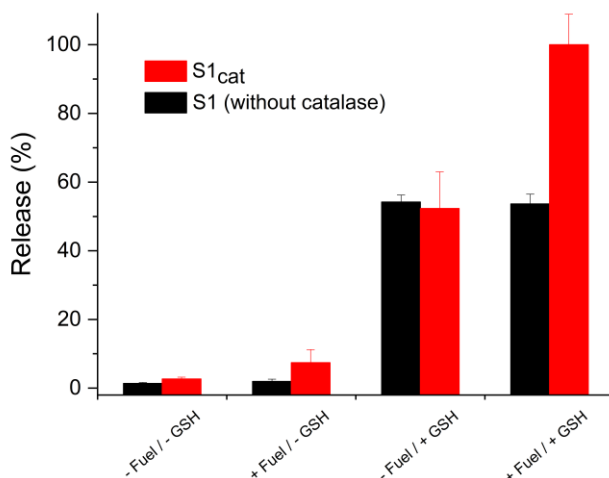


Figure SI-7. Cargo release from nanoparticles **S1** (without the catalase) and nanobots **S1_{cat}** in phosphate buffer (10 mM, pH 7.5) after 60 min under different conditions: (a) control (no fuel and no GSH), (b) presence of H₂O₂ (0.3%), (c) presence of GSH (10 mM), and (d) presence of GSH (10 mM) and H₂O₂ (0.3%).

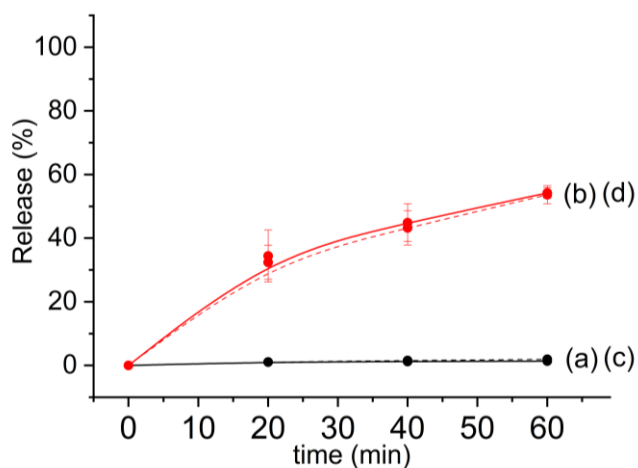


Figure SI-8. Cargo release from nanoparticles **S1** (without the catalase) as a function of time in phosphate buffer (pH 7.5) under different conditions: (a, continuous line) control (no fuel and no GSH), (b, continuous line) presence of GSH (10 mM), (c, dashed line) presence of fuel (H₂O₂ 0.3%), and (d, dashed line) presence of GSH (10 mM) and fuel (H₂O₂ 0.3%).

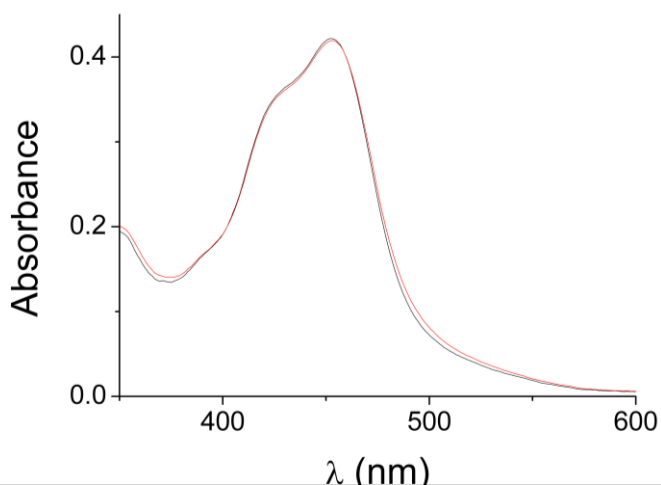


Figure SI-9. Absorbance spectra of the $[\text{Ru}(\text{bpy})_3]\text{Cl}_2$ dye ($30 \mu\text{M}$) in phosphate buffer (10 mM , $\text{pH } 7.5$) in the absence (black curve) and in the presence of H_2O_2 (0.3%) (red curve) after 60 min of incubation.

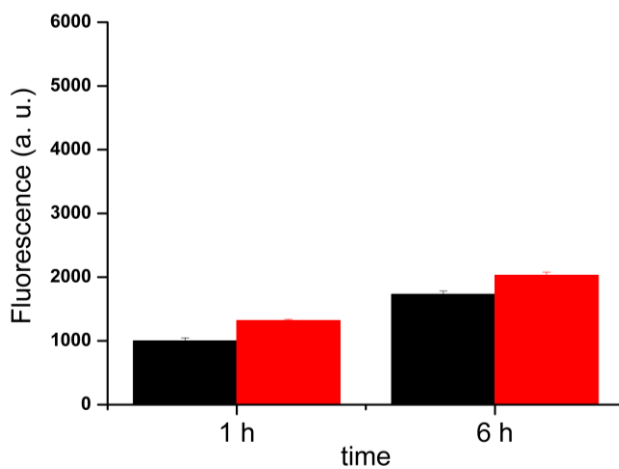


Figure SI-10. Quantification of dox-fluorescence in cells incubated with S1_{dox} (without catalase) in the absence (black) and in the presence of H_2O_2 (red), using the ImageJ software.

References

1. C. T. Kresge, W. J. Roth. The discovery of mesoporous molecular sieves from the twenty year perspective. *Chem. Soc. Rev.*, **42**, 3663-3670. (2013)
2. D.V. Leff, L. Brandt, J.R. Heath. Synthesis and Characterization of Hydrophobic, Organically-Soluble Gold Nanocrystals Functionalized with Primary Amines. *Langmuir*, **12**, 4723-4730. (1996)

**Chapter II | Ultra-Fast Directional Janus Pt-Mesoporous
Silica Nanomotors for Smart Drug Delivery**

Ultra-Fast Directional Janus Pt-Mesoporous Silica Nanomotors for Smart Drug Delivery

Paula Díez,^{abd} Elena Lucena-Sánchez,^{abd} Andrea Escudero,^{abd} Antoni Llopis-Lorente,^{abd} Reynaldo Villalonga,^e Ramón Martínez-Mañez^{*abcd}

^aInstituto Interuniversitario de Investigación de Reconocimiento Molecular y Desarrollo Tecnológico (IDM), Universitat Politècnica de València, Universitat de València, Spain, Camino de Vera s/n, 46022 València, Spain.

^bUnidad Mixta UPV-CIPF de Investigación en Mecanismos de Enfermedades y Nanomedicina, Valencia, Universitat Politècnica de València, Centro de Investigación Príncipe Felipe, 46012 València, Spain.

^cUnidad Mixta de Investigación en Nanomedicina y Sensores. Universitat Politècnica de València, Instituto de Investigación Sanitaria La Fe, 46026 València, Spain.

^dCIBER de Bioingeniería, Biomateriales y Nanomedicina (CIBER-BBN), 28029 Madrid, Spain.

^eNanosensors & Nanomachines Group, Department of Analytical Chemistry, Faculty of Chemistry, Complutense University of Madrid, 28040 Madrid, Spain.

*Corresponding author: rmaez@qim.upv.es

Published online: March 6, 2021

(Reprinted with permission from ACS Nano, 2021, March 6. © American Chemical Society 2021)

1. Abstract

Development of bio-inspired nanomachines with an efficient propulsion and cargo-towing has attracted much attention in last years due to their potential biosensing, diagnostics and therapeutics applications. In this context, self-propelled synthetic nanomotors are promising carriers for intelligent and controlled release of therapeutic payloads. However, the implementation of this technology in real biomedical applications is still facing several challenges. Herein, we report the design, synthesis, and characterization of innovative multifunctional gated platinum-mesoporous silica nanomotors constituted of a propelling element (platinum nanodendrite face), a drug-loaded nanocontainer (mesoporous silica nanoparticle face) and a disulfide-containing oligo(ethylene glycol) chains (S-S-PEG) as a gating system. These Janus-type nanomotors present an ultra-fast self-propelled motion due to the catalytic decomposition of low concentrations of hydrogen peroxide. Likewise, nanomotors exhibit a directional movement which drives the engines towards biological targets, THP-1 cancer cells, as demonstrated using a microchip device that mimics penetration from capillary to post-capillary vessels. This fast and directional displacement facilitates the rapid cellular internalization and the on-demand specific release of a cytotoxic drug into the cytosol, due to the reduction of the disulfide bonds of the capping ensemble by intracellular glutathione levels. In the microchip device and in the absence of fuel, nanomotors are neither able to move directionally nor reach cancer cells and deliver its cargo revealing that the fuel is required to get into inaccessible areas and to enhance nanoparticle internalization and drug release. Our proposed nanosystem shows many of the suitable characteristics for ideal biomedical destined nanomotors, such as rapid autonomous motion, versatility, and stimuli-responsive controlled drug release.

KEYWORDS. Janus nanomotors, directional motion, ultrafast self-propulsion, drug delivery, on-command controlled release.

2. Introduction

Nowadays, one of the most ambitious objectives of nanotechnology is the development of advanced systems that mimic inherent functions of living entities, among which are autonomous movement¹, communication skills², and the ability to recognize and react to environmental signals³. Regarding this topic, synthetic nano/micromotors have attracted much interest in recent decades. Research on these technology-based systems is focused in achieving efficient nanodevices capable of performing multiple “smart” tasks at the same time, as responding to environmental stimuli and self-propelling.

Although there are numerous nano/micro-devices powered by external forces, such as magnetic, acoustic or electric fields, chemically-powered prototypes are the most widely used. These motors autonomous movement is due to the conversion of chemical substances into mechanical energy by different transduction mechanisms, summarized in the generation of bubbles⁴⁻⁷, auto-electrophoresis^{8,9} or auto-diffusiophoresis¹⁰⁻¹². The main geometries that chemically self-propelled engines present are nanowires¹³, microtubes¹⁴, and Janus-type¹⁵, whereas, their composition is usually based on metals with intrinsic catalytic activity, among which platinum (Pt; that decomposes hydrogen peroxide in water and oxygen gas) and zinc (Zn; by Zn auto-oxidation to generate hydrogen bubbles) attract more attention. The propulsion mechanism followed by these active vehicles depends on their geometry but is more strongly influenced by its size, as at the nanometric scale the diffusion-type mechanisms govern the movement and any type of directionality is usually lost in favor of rotational diffusion^{16,17}. This is a drawback as the implementation of this technology in real biotechnological applications, such as drug delivery, environmental bioremediation or biosensing, usually requiring to control the artificial motors speed and direction towards a specific location. Furthermore, the most common and powerful man-made motors developed to date register high speed similar to biological motors, but they are driven by high concentrations of hydrogen

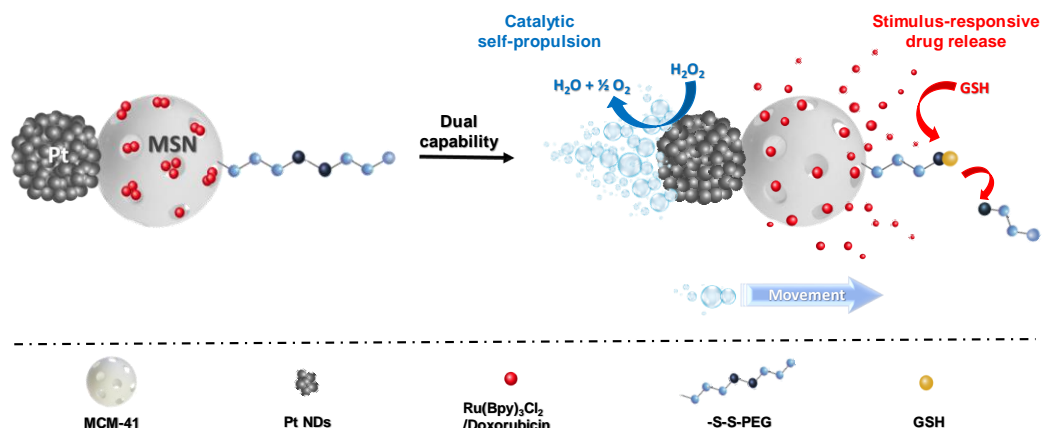
peroxide (H_2O_2), being useful for non-biomedical applications as sensors development, environmental bioremediation or surfaces bacteria elimination¹⁸. Nonetheless, lower levels of hydrogen peroxide can be found in human diseased regions, such as inflamed sites, infections, or cancer and cardiovascular diseases¹⁹ which could be exploited by a nanomotor with low fuel requirements²⁰.

In connection to biomedical applications for artificial devices, selectively release of therapeutic payloads at their destination is highly desired. The advantage that nano/micromotors present compared to other release passive systems is their ability to self-propel and to display tissue penetration. This could be translated into an improvement in drug delivery efficacy to target tissues and cells, reducing side effects²¹⁻²³. A wide variety of nanomaterials have been developed for drug delivery applications, among which we highlight systems based on mesoporous silica nanoparticles (MSNs) due to their high load capacity, biocompatibility, as well as the large external surface that is easily functionalized with supramolecular assemblies to modulate the delivery of payloads^{24,25}. These capping systems provide devices with an intelligent response to specific environmental stimuli, keeping a practically zero cargo delivery until the “opening signal” is recognized in the local environment. MSNs have been widely used as passive and “smart” delivery systems with excellent results, where the cargo is released from the nanopores through a simple diffusion process. However, these gated nanomaterials have practically not been tested for the development of chemical-powered nanomotors with controlled delivery capabilities^{26,27}. To achieve this goal it is necessary to include an element that generates the driving power in the MSN. The few designs published to date, generally integrate thin layers of catalytic metals by physical or chemical deposition on the silica support as “motion system”, creating Janus-type anisotropic spheres, Table SI-1(i)^{11,16,26-33}. This metallic layer considerably reduces the external surface of the silica, which is a great disadvantage to anchor the stimulus-responsive systems that provides the ability to respond towards the environment. Additionally, these designs require high concentrations of toxic fuel to record random Brownian motion through a self-

electrophoresis or self-diffusiophoresis mechanism, making them usually incompatible for implementation on biological samples. More recent examples include highly active enzymes (such as urease and catalase) anchored to the external silica surface as a propellant element that generate the movement based on the enzymatic transformation of chemical substrates³⁹⁻⁴⁴. Although, in these cases the fuel is not an inconvenient, since they are self-propelled at low concentrations of biocompatible propellants, the type of movement is still in some cases Brownian making them difficult to control.

Based on the above, we report herein Janus-type Pt-MSN nanomotors as nanocarriers with multifunctional capabilities, such as catalytic self-propulsion and drug delivery in a specific and glutathione-mediated way for payload release in cells (Scheme 1). In order to provide Janus nanoparticles with improved autonomous motion, compared to typical Janus-type nanoparticles synthesized by electron beam evaporation or sputtering techniques, an innovative nanomaterial was designed based on a toposelective synthesis⁴⁵ founded on a selective surface manipulation (at the Pt/ligand/MSN interface), using a Pickering emulsion where MSNs are partially exposed for the chemisorption of Pt nanodendrites (PtNd) by thiol bonds. In our proposed design, MSN nanoparticles are used as nanocontainer with a redox-sensitive gating mechanism, whereas the PtNd are employed as propelling element to convert chemical energy into a bubble propulsion by the catalytic reduction of H₂O₂.

PtNd were selected as motion system, instead of using Pt layers, due to their major roughness and active catalytic area, which are expected to improve the propulsion capacity. In addition, this anisotropic nanomaterial has the advantage to maintain most of the MSN face available for loading and effective external surface functionalization, when compared to previously Pt-catalytic motors made by sputtering technology. Accordingly, we envisioned that nanomotors would be able to self-propel in presence of



Scheme 1. Schematic illustration of Janus Pt-MSNs nanomotors with a catalytic self-propulsion and a glutathione-mediated drug release.

low concentrations of hydrogen peroxide and would lead to an effective delivery of drugs once a reducing environment is reached in diseased areas. In fact, an ultra-fast self-propelled motion and controlled drug delivery capabilities in THP-1 cancer cells, using a microchip device with physical limits, is demonstrated. The main features and innovation points of our system in comparison to previously reported Janus Pt-MSN nanomotors are summarized in Table SI-2.

3. Results and discussion

3.1. Nanomotors synthesis and characterization

According to the synthetic procedure (SI-Scheme 1), Janus Pt-MSNs were prepared by the conjugation of two different nanoparticles in a single nanodevice⁴⁵⁻⁴⁷. First and briefly, MSNs (calcined MCM-41-type, obtained by an alkaline hydrolysis reaction) were partially imbedded at the interface of the Pickering emulsion, formed by paraffin wax (oily phase) and water-ethanol (aqueous phase). The un-masked MSNs surface was decorated with reactive thiol groups, by reaction with (3-

mercaptopropyl)trimethoxysilane, on which PtNds were subsequently attached. After removing the paraffin with chloroform, Janus Pt-MSNs (S_0) were obtained.

To synthesize the nanomotor, the PtNds in S_0 was protected with 3-mercaptopropionic acid, and the mesoporous nanoparticles were loaded with the dye $Ru(bpy)_3Cl_2$ as model cargo⁴⁸. The silica surface was further modified with (3-mercaptopropyl)trimethoxysilane which was reacted with 2,2-dipyridyl disulfide⁴⁹ and then with O-(2-mercaptoethyl)-O-methyl-hexa(ethylene glycol), allowing the capping of the mesopores with the redox-sensitive molecular gate (S-S-PEG) (S_1). Another similar nanodevice was prepared using the cytotoxic Doxorubicin drug (Doxo) as cargo (S_2) for intracellular delivery studies.

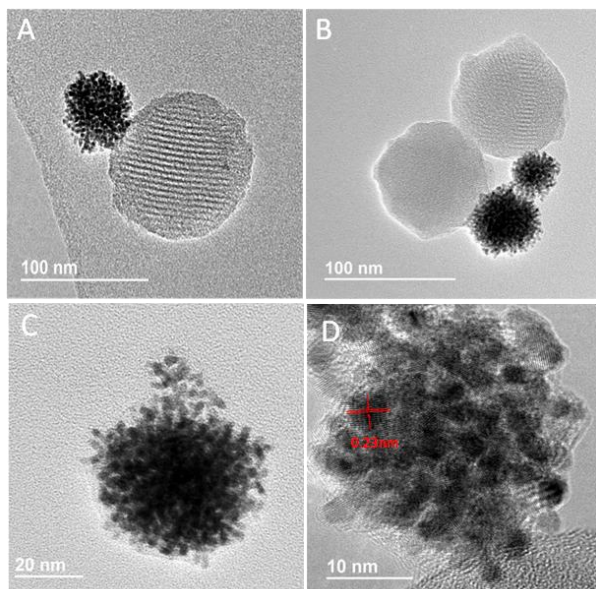


Figure 1. HR-TEM images of Janus Pt-MSNs (S_0) (A-B) and PtNds (C-D), showing the interplanar spacing of 2.3 Å in (111) plane of PtNds crystals.

To confirm the effective synthesis, nanomaterials were characterized using standard methods (see SI for details). The nanostructure morphology (snowman-like Janus) of the starting Pt-MSNs (S_0) and PtNds were confirmed by high resolution transmission electron microscopy (HR-TEM). Figure 1A-B (and SI-Scheme 1) shows the presence of PtNds attached to well-developed MSNs (100 ± 13 nm), confirming the

successful synthesis of the anisotropic nanomaterial. PtNds (Figure 1C-D) are spherical in shape with an average diameter of 20 ± 9 nm. This spherical morphology is caused by the fusion of several Pt seeds of a size of 2.5 ± 0.3 nm. PtNds were synthesized by an autocatalytic surface reduction (SI for details). In the synthesis of PtNds, the formed Pt⁰ sites by chemical reduction of H₂PtCl₆ (Pt⁺⁴) with L-ascorbic acid, serve as catalytic sites for further reduction and atomic addition in the nanocrystal, resulting in a dendritic-controlled growth controlled by absorption of a monolayer of PVP on the Pt surface. This mechanism produces a high increase in surface area and improves the PtNds catalytic capacity towards oxygen reduction^{50,51}. Furthermore, it is important to emphasize the high stability of PtNds that remained as nanodendrites even after PVP removal through heating and washing steps during the Pt-MSNs synthesis. Moreover, no apparent changes in PtNds size or morphology were observed after exposing the material to high concentrations of hydrogen peroxide for a long time (Figure SI-1).

HR-TEM analysis also revealed the presence of crystal faces in the synthesized PtNds with an average inter-planar spacing of 2.3 Å (Figure 1D), which corresponds to the distance between the (111) faces in face-centered cubic (fcc) platinum crystals⁵². The crystalline structure was further demonstrated by powder X-ray diffraction (PXRD) pattern showing four characteristic Pt diffraction peaks at high-angles indexed as (111), (200), (220), and (311) planes, (Figure SI-2). Moreover, the PXRD spectrum shows the characteristic Bragg peak of MCM-41 type structures at 2.63° (indexed as (100) plane) in solids **S₀**, **S₁**, and **S₂**, indicating that mesoporous hexagonal network was not modified throughout the synthesis process, confirming the microstructure morphology observed by HR-TEM.

Additionally, the porous arrangement was corroborated by N_2 adsorption–desorption isotherms of S_0 and S_1 (Figure SI-3). For S_0 , an acute adsorption process is shown at values of 0.1-0.3 P/P_0 due to the condensation of nitrogen within the mesoporous network. However, this absorption step was not observed for the final nanodevice S_1 , which confirms the loading and capping of the pores. Pore size and specific volume and area for S_0 and S_1 were calculated (Table SI-3). The synthesized nanomaterial was also monitored by scanning transmission electron microscopy coupled with energy dispersive X-ray spectroscopy (STEM-EDX). The presence of Si, O and Pt atoms of the Pt-MSNs scaffold are mapped in Figure 2B, C and D images for S_1 , respectively. Moreover, Figures 2E and 2F demonstrated the presence of S atoms (assigned to disulfide-linked chains of the gatekeeper and the functionalization of the Pt surface) and Ru (attributed to the $Ru(bpy)_3Cl_2$ dye loaded in the nanochannels of the silica face).

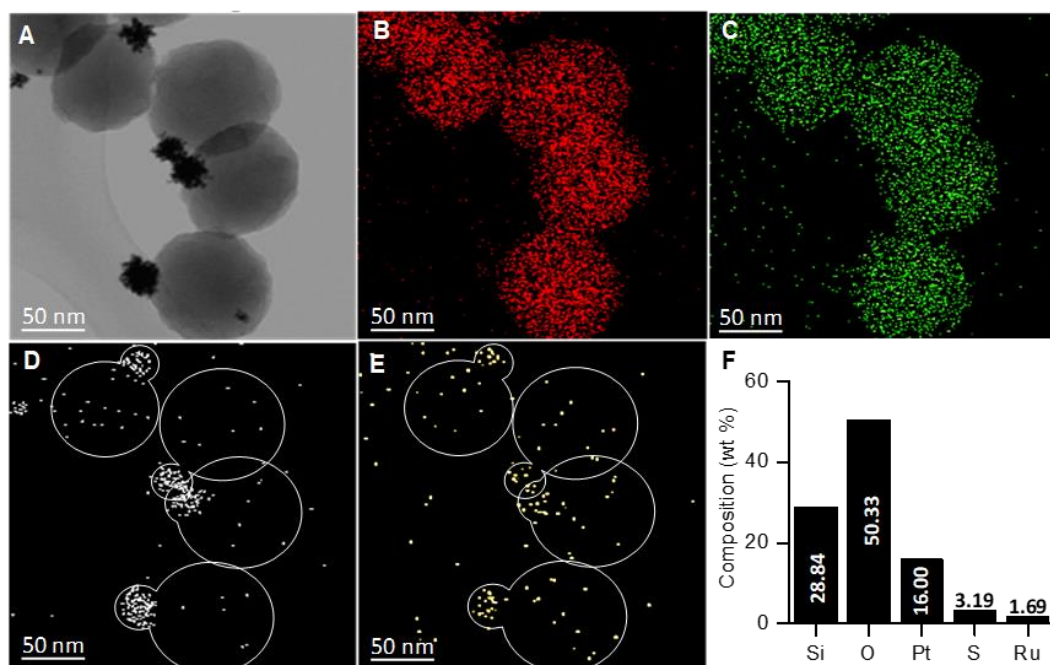


Figure 2. STEM image (A), STEM-EDX elemental mapping of Si atoms (B), O atoms (C), Pt atoms (D), S atoms (E) and wt % composition detected (F) in S_1 Janus Pt-MSNs.

Moreover, the content corresponding to the gatekeeper (S-S-PEG) and the loaded dye, amounted 73.7 mg and 68.5 mg per gram of S_1 , respectively, which were obtained by thermogravimetric (Figure SI-4) and delivery studies. To complete the characterization, nanomotor assembly was evaluated by dynamic light scattering analysis (DLS) (Figure SI-5). Zeta potential showed a decrease in negative surface charge from -52.8 mV for S_0 to -6.3 mV for S_1 , due to the immobilization of the redox-sensitive S-S-PEG gate and the loading with $Ru(bpy)_3Cl_2$ on the MSN face. On the other hand, the average hydrodynamic diameter increased from 145 nm to 335 nm for the initial and final nanodevices, respectively.

3.2. Motion analysis

Prior to characterize the nanomotor motion, the catalytic activity of Pt in S_1 was evaluated using a spectrophotometric assay based on the oxidation of 2,2'-azino-bis-(3-ethylbenzthiazoline-6-sulphonic acid (ABTS) in presence of hydrogen peroxide in the 0-30 mM range. The reaction rate of ABTS oxidation (kinematically recorded by measuring absorbances at 415 nm) catalyzed by Pt in S_1 at different concentrations of H_2O_2 showed a typical Michaelis-Menten behavior (Figure SI-6A). This demonstrated that the nanomotor exhibits a peroxidase-like activity, with an apparent affinity value (K_M) for H_2O_2 which was calculated in 2.3 mM (from a Lineweaver-Burk plot according to equation- S_1), a value that is comparable with native horseradish peroxidase (4.37 mM)⁵³ (Figure SI-6B).

The self-propelled motion of the nanomotor S_1 in PBS was characterized by nanoparticle tracking analysis (NTA) using a Nanosight NS300 instrument. In these experiments, the trajectories of nanomotors were recorded in real time in absence and in presence of different concentrations of the fuel H_2O_2 , from 0% to 0.35%. in buffer PBS solution. From each sample, 5 videos of 30 seconds (30 frames·s⁻¹) length were registered and analyzed. The x-y coordinates of 20 nanoparticles (selected size between 100–200

nm) were extracted by the NTA 3.0 software allowing the estimation of their mean square displacement (MSD) obtained with the equation 1 (See materials and methods section).

Motion studies were performed at short time intervals, $\Delta t < \tau_r$ (rotational diffusion time or time required for the particles to move randomly, theoretically calculated in 0.8s using equation 2 (See materials and methods section), which means that the contribution of the ballistic displacement of fuelled nanomotors is higher than the diffusive motion. At longer times, the ballistic trajectories of the nanomotors would be randomized again⁵⁴.

After representing the calculated MSD values versus different time intervals (Δt), the motion of nanomotors in each fuel concentration was evaluated (Figure 3A). When the movement is Brownian-type, MSD presents a linear correlation with Δt . This diffusive behavior could be observed in the absence of fuel (0% H₂O₂). However, in the presence of H₂O₂ the MSD curves showed a parabolic shape, with an increase in the MSD values as function of hydrogen peroxide concentrations, suggesting a directional movement due to a bubble-propulsion mechanism^{12,55}, which was corroborated by the appearance of visible bubbles at all fuel concentrations tested (Figure SI-7).

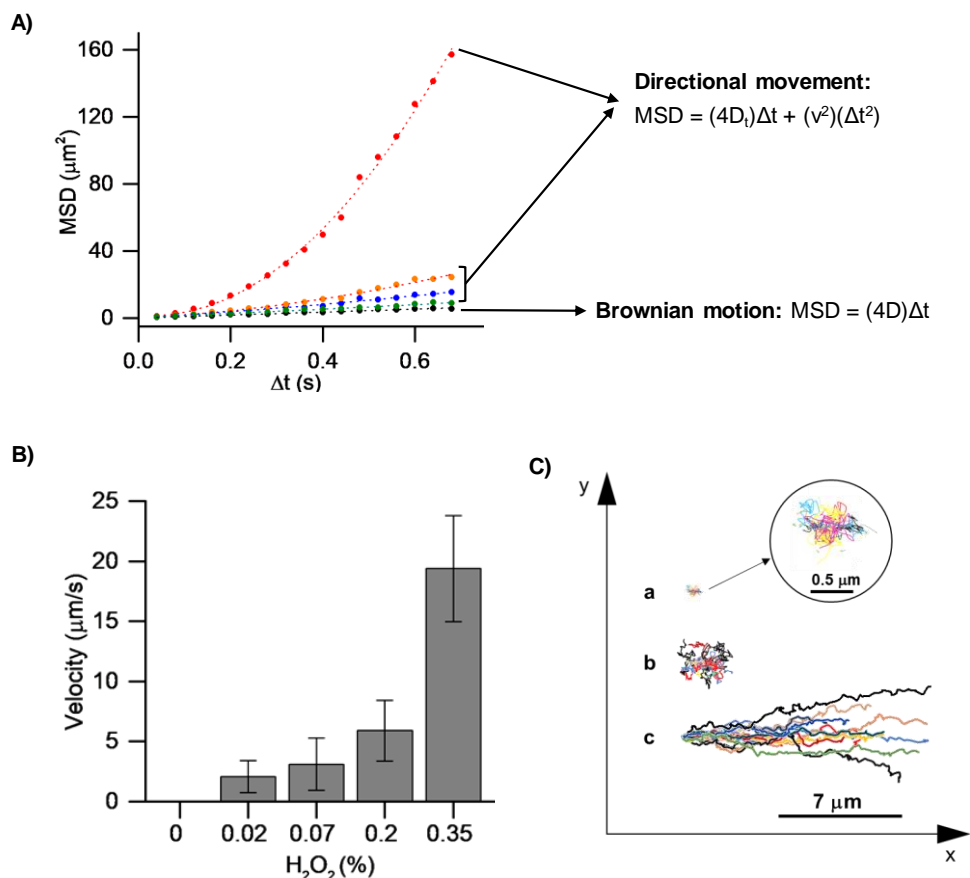


Figure 3. Motion characterization of Janus Pt-MSN S_1 nanomotors. A) Mean squared displacement as a function of time interval for the nanomotors at 0% (black), 0.017% (green), 0.07% (blue), 0.2% (orange) and 0.35% (red) fuel concentration. Curves were fitted using the equations show in the figure. B) Velocity of nanomotors at different fuel concentrations ($N = 20$; error bars represent the standard error of the mean velocities obtained). C) Trajectories for 20 Janus Pt-MSN S_1 nanomotors at: PBS solution (a) and 0.07% (b) and 0.35% (c) of hydrogen peroxide solutions.

As observed in Figure 3B, the propulsion velocity, calculated with the parabolic MSD equation illustrated in Figure 3A, increased from zero to $19.4 \mu\text{m}\cdot\text{s}^{-1}$ at 0 and 0.35% of fuel, respectively. This ultrahigh velocity supposes a relative speed of 149 body length (bl) per second, which, considering the concentration of fuel used, corresponds to a relative velocity of $\sim 426 \text{ bl}\cdot\text{s}^{-1}\cdot\%^{-1}$. To our knowledge, is the maximum speed reported for chemically-powered Janus-type nano/micromotors and also for other nano-designs (Table SI-1)^{11,16,26-38}. Besides, that speed is even higher than that presented by natural mobile microorganism like *Escherichia coli* ($8\text{-}15 \text{ bl}\cdot\text{s}^{-1}$)⁵⁶. We attributed the ultra-fast

velocity shown to a catalytic enhancement due to the rough and large surface area that PtNDs presents, compared with conventional Janus micro/nanomotors made by chemical or physical vapor deposition of platinum.

Based on the velocities registered in Figure 3B, the propulsion force (F_{prop}) applied on the nanomotors was calculated (by equation 3 in materials and methods section), that is equal to the repulsion or drag force (F_{drag}) in our experimental conditions (at low Reynolds numbers)⁵⁷. F_{prop} values raised up to 53fN with the increment of fuel concentration, supporting that the movement is governed by the ballistic force created in the decomposition of H_2O_2 , leading to linear trajectories. Figure 3C, shows the influence of fuel concentrations on nanomotors trajectories, monitoring a huge increase in the linearity of the nanomotor pathways at high fuel concentrations. The directional movement is promoted by the anisotropy of the nanomaterial¹², their high catalytic activity and the location of the bubble growth. In our case it is expected that the center of the bubbles was always along the long axis of the dimer formed by the PtNDs and the MCM. Furthermore, the PtNDs roughness surface participates in the stabilization of the bubbles once they nucleate⁵⁵, which as can be observed with naked eye after only 5 min of fuel addition (Figure SI-7).

Although activated nanomotors are propelled along a straight trajectory, when the images were zoomed (in the y -positions) some Brownian contributions were clearly observed (Figure SI-8). Despite of these reorientation movements, due to nanoparticle collisions with solvent molecules, the directional motion is retained⁵⁹. By last, the self-propelled motion was also evaluated by the translational diffusion coefficient (D_t , calculated with parabolic MSD equation recently mentioned), increasing its value up to $5.4 \mu m^2 \cdot s^{-1}$ with the increment of fuel concentration (Figure SI-9). For non-activated nanomotors, where the motion is controlled by Brownian diffusion, the diffusion value (D , extracted from lineal MSD equation) was $2.06 \mu m^2 \cdot s^{-1}$. These results showed weak

dependence of diffusion coefficients with the concentration of H_2O_2 , in contrast with the velocity behavior.

It would have been interesting to record the positions of the nanomotors at higher time intervals to further characterize their motion like recently have been published by Archer *et al.*^{58,59}, but it was impossible due to technical limitations (NTA provides trajectories of a maximum of 100 frames per particle) as well as the high speed exhibited by our nanosystems, leaving quickly the field of view. Although tracking of motors for longer times has been reported in previous studies using optical microscopes, it should be noted that nanoscale (<200 nm) objects are below the limit of resolution of optical microscopy.

3.3. Control Release Studies

Once directional motion of the nanomotor was confirmed, the ability of S_1 to deliver the cargo under different conditions was evaluated. Release assays were carried out by suspending 0.5 mg of nanomotors in 1 ml of sodium phosphate buffer (PBS) in the presence and absence of GSH at 10 mM (a typical reported intracellular concentration)⁶⁰. GSH is the “key” molecule that triggers the opening of the capping system, releasing the cargo loaded inside the pores of the mesoporous face. Delivery studies were further conducted under static and stirring conditions and in the presence and absence of the fuel (0.1% H_2O_2) to evaluate the effect of the self-propulsion on the release of the $\text{Ru}(\text{bpy})_3\text{Cl}_2$ cargo. Dye release kinetic profiles from S_1 under static condition are illustrated in Figure 4A. In the absence of GSH and H_2O_2 , S_1 remained capped and the delivery of $\text{Ru}(\text{bpy})_3\text{Cl}_2$ was practically negligible (curve a). The same behavior was observed in the presence of H_2O_2 , confirming that the gating system is not affected by the fuel (curve b). Moreover, a slow delivery kinetic from S_1 under static conditions was triggered by the GSH *via* the rupture of disulfide bonds in the S-S-PEG gate (curve c). In contrast, in the presence of the

inputs, H_2O_2 , and glutathione, a faster release was observed due to the synergic effect of the self-propulsion and the uncapping of the nanoparticles by GSH (curve d).

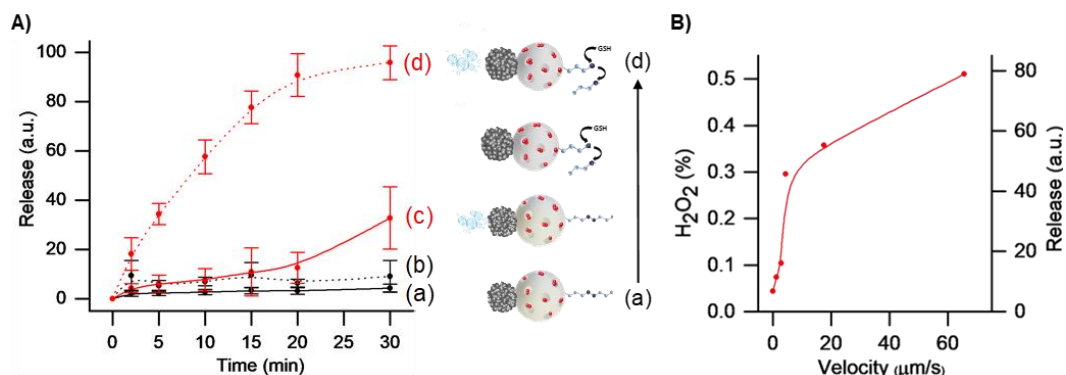


Figure 4. Normalized cargo release from S_1 nanomotors in static conditions determined by measuring $\text{Ru}(\text{bpy})_3\text{Cl}_2$ fluorescence (at 544 nm) vs time in aqueous solution (50 mM PBS pH 7.5), using: (a) nanomotors without GSH and without H_2O_2 addition, (b) 0.1% H_2O_2 -propelled nanomotors without GSH addition, (c) nanomotors with 10 mM GSH addition and without H_2O_2 , and (d) 0.1% H_2O_2 -propelled nanomotors with 10 mM GSH addition (A). Values from three independent experiments. Relation between H_2O_2 (%), velocities, and normalized cargo release (%) from S_1 nanomotors (B).

This is supported by additional experiments that demonstrated that under stirring conditions cargo delivery from S_1 in the presence of GSH and GSH + H_2O_2 was almost the same (Figure SI-10A). Besides, the influence of nanomotors velocity on cargo release was studied. For that, a dye delivery assay using S_1 at a fixed time of 30 minutes, static conditions, and variable concentrations of fuel was performed. As observed in Figure 4B, an increase in nanomotors movement, as consequence of higher fuel concentrations, turns out in an increment of cargo release to the medium. Finally, cargo release from nanomotor S_2 (loaded with the cytotoxic drug Doxorubicin) was also evaluated. A similar delivery behavior under static and stirring conditions in the presence of GSH and H_2O_2 to that found for S_1 was observed (Figure SI-10B). The total amount of Doxorubicin released was calculated spectroscopically and amounted 0.7 μmol per gram of solid S_2 .

In summary, these experiments demonstrated that our Janus Pt-MSNs nanomotors display high self-propulsion capabilities at relatively low concentrations of H_2O_2 *via* catalytic fuel decomposition. Moreover, the nanobots remain capped and only deliver their payload upon recognition of the reducing agent GSH, due to the cleavage of the gatekeepers. Thus, the nanodevice displays desired features for nanomotors in terms of biomedical applications: (i) autonomous motion and (ii) the ability to sense the environment and deliver the drug only in the presence of a stimulus (*i.e.* GSH).

3.4. Self-propel and drug release capabilities in cells

Nanomotors for biomedical applications should propel in the presence of low fuel concentration with no premature cargo leakage, and deliver the payload once target cells or tissues are reached. Taking into account these concepts and encouraged by the above results (*i.e.*, self-propulsion and controlled release capabilities), we studied Doxorubicin delivery in THP-1 cancer cells by confocal fluorescence microscopy. In this experiment, THP-1 cells were incubated with a suspension of $50 \mu\text{g ml}^{-1}$ of S_2 in the presence and absence of H_2O_2 (0.02%) at 37°C for 30 min. Subsequently, uninternalized nanoparticles were removed by washing and cells were further incubated for 1, 4 and 6 h in a fresh medium. Before acquiring the confocal fluorescence image, the THP-1 cell nucleus and membrane were stained with Hoechst 3342 and WGA, respectively.

As shown in Figure 5A, an intracellular Doxorubicin-associated fluorescence was observed indicating S_2 internalization and the cleavage of the gatekeeper by intracellular GSH in both cases (absence or presence of fuel). Moreover, a larger intracellular Doxorubicin release was observed for nanobots incubated with H_2O_2 after 4 and 6 h. This suggests that the enhanced diffusion of the nanobots in the presence of fuel results in an enhanced cell internalization and a larger intracellular cargo release. These results demonstrate the ability of the nanomotor to sense the redox environment in the cell and to specifically trigger the release of the cytotoxic drug. In addition, an improvement in

cells uptake attributed to the autonomous movement of nanomotors was confirmed at very low fuel concentrations. Larger amounts of fuel are toxic for THP-1 and therefore were not studied.

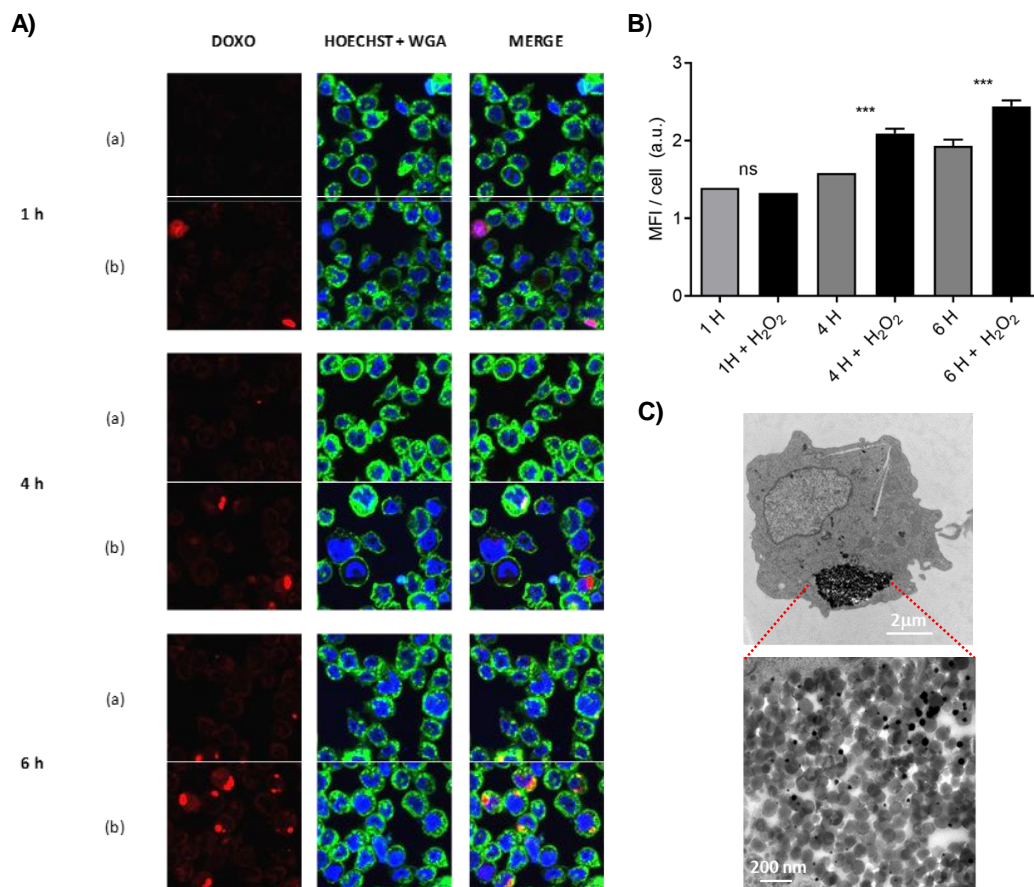


Figure 5. A) Confocal microscopy images of internalization and controlled Doxorubicin release of S_2 nanodevice in THP-1 cells at different times. THP-1 cells treated with $50 \mu\text{g ml}^{-1}$ of S_2 nanomotors in the absence of fuel (a); THP-1 cells treated with $50 \mu\text{g ml}^{-1}$ of S_2 in a medium containing 0.02% of H_2O_2 (b). From left to right: Doxorubicin fluorescence, DNA, and membrane fluorescence marker (Hoechst 3342 and WGA, respectively) and combined (merge). B) Mean fluorescence intensity quantification in cells from confocal images at different times and with or without the addition of fuel. Values from at least three independent experiments. C) TEM image of S_2 nanomotors ($100 \mu\text{g ml}^{-1}$) internalization in THP-1 cells after 6 h.

Nanomotors internalization in cancer cells was also confirmed by TEM. Figure 5C shows the uptake of nanoparticles and, as the image is zoomed, Janus-like nanomotor structures are clearly perceived. The results were completed with the WST-1 cell viability

tests after 24 h, confirming that the concentration of S_2 and fuel selected for the treatment carried out, did not significantly affect THP-1 cells (Figure SI-11). Furthermore, a reduction in the amount of drug necessary to induce cell death by apoptosis was observed, noting that $200 \mu\text{g} \cdot \text{ml}^{-1}$ of S_2 (corresponding to $0.14 \mu\text{M}$ of drug released) displayed the same cellular toxicity as $1.5 \mu\text{M}$ of free Doxorubicin, which demonstrates the effective strategy of using fuelled nanomotors to enhance drug delivery in cells for therapeutic applications.

Finally, as proof of concept, the capacities of nanomotors mentioned above to perform autonomous movement and release therapeutic payloads in THP-1 cells were examined using a microchip device aiming to reproduce channels and fluids of living systems, such as blood vessels. Nanomotor testing on microfluidic platforms are the pre-application stage in more complex organ-on-a-chip devices to achieve the future implementation in real therapies⁶¹. Previous studies demonstrated how the use of this type of device with physical limits confines the space where nanomotors “swim”, controlling their speed and directionality without using external sources^{62,63}.

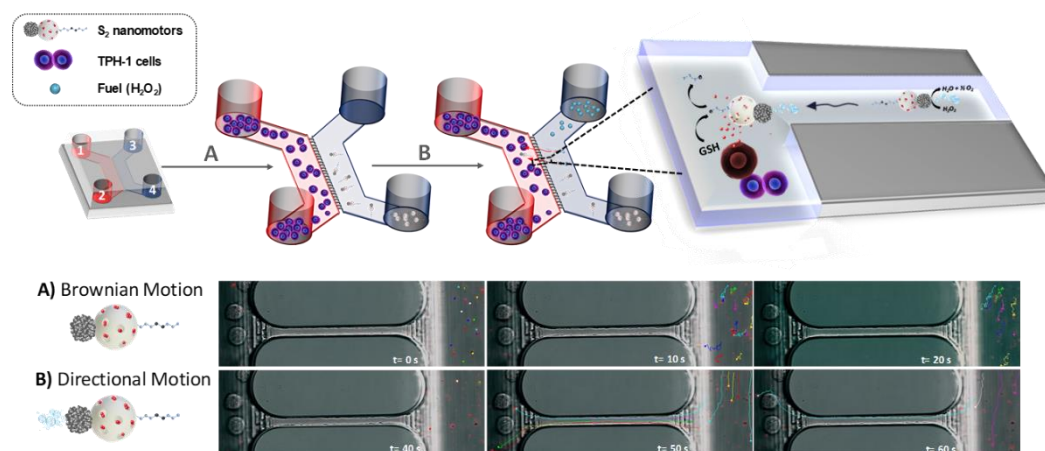


Figure 6. Three-dimensional scheme depicting the assay followed to study self-propulsion and drug release capabilities of S_2 nanomotors in THP-1 cells using a microchip device and time-lapse optical images taken from SI-1 and SI-2 videos of confocal microscopy showing the nanomotors motion behavior, which includes the trajectories analyzed by Manual Tracking plug-in of the FIJI program, before (A) and after the addition of 0.02% H_2O_2 at 40 s of the experiment (B). (Experimental conditions: $108 \text{ THP-1 cells} \cdot \text{ml}^{-1}$ in wells 1 and 2, 0.02% H_2O_2 in well 3 and $100 \mu\text{g} \cdot \text{ml}^{-1}$ of S_2 nanomotors in well 4).

For the assay, a 4-compartment microchip (from XonaChips®) was used, which allowed the compartmentalization of THP-1 cells, nanomotors and fuel. The 4 wells are connected two by two 1-2 (red part) and 3-4 (blue part) and these were additionally connected to each other by micrometric channels (Figure 6). The experiment was performed in a cell culture media (RPMI-1640 buffer) depositing 10^8 THP-1 cells in wells 1 and 2, while $100 \mu\text{g} \cdot \text{ml}^{-1}$ of S_2 nanomotors were added to position 3 (see Methods section for more details). Then 2 min videos were recorded by confocal microscopy (SI-1 video). Without fuel and after the addition of S_2 , the nanomotors diffused through the cuvette (blue part) and once stabilized, a Brownian motion behavior was observed, as shown in the trajectories recorded in time-lapse images taken from SI-2 video (A).

At 40 s of assay time, the fuel (0.02% H_2O_2) was added to the well 3 and then a clear directional movement was observed. Interestingly, this propelled some nanomotors through the microchannels towards the cells area (red part), as can be seen in the trajectories recorded from SI-3 video at different times (B). Activated nanomotors swam to the opposite side of fuel addition in a confined flow, movement denominated as negative rheotaxis. Velocities of S_2 observed in that experiment seemed higher than the speed recorded by the NTA, when the cross section of the channel decrease from $100 \mu\text{m}$ to $4 \mu\text{m}$ (microchannels). This effect could be due to the bubble creation in a confined area and also to the enhanced flow velocity by a Venturi effect⁶⁴. The movement of the nanomotors through the microchannels to a wider area would mimic the effect suffered by circulating cells when moving from capillary to post-capillary vessels, with larger diameters, reducing their speed and moving towards the vessel walls. This process facilitates blood cells interaction with the endothelium and extravasation to tissues⁶⁵.

Regarding controlled release of the drug, a similar experiment by confocal microscopy but extending the assay time until 30 min was carried out. Figure 7 shows the fluorescence intensities along the profile of several regions of interest analyzed, corresponding with different experiments (with and without the fuel). When H_2O_2 -powered nanomotors

reached cells through the microchannels, there was an increase in cell fluorescence over time, demonstrating the Doxorubicin delivery mediated by intracellular GSH. In the absence of H_2O_2 , the fluorescence intensity was low and similar in both times analyzed, suggesting the inability of non-powered nanomotors to cross microchannels and reach target cells, remaining in the channel between wells 3 and 4 (as observed in the SI-1 video). Note that nanomotors **S₂** remained capped and only delivered the cargo when internalized in cells.

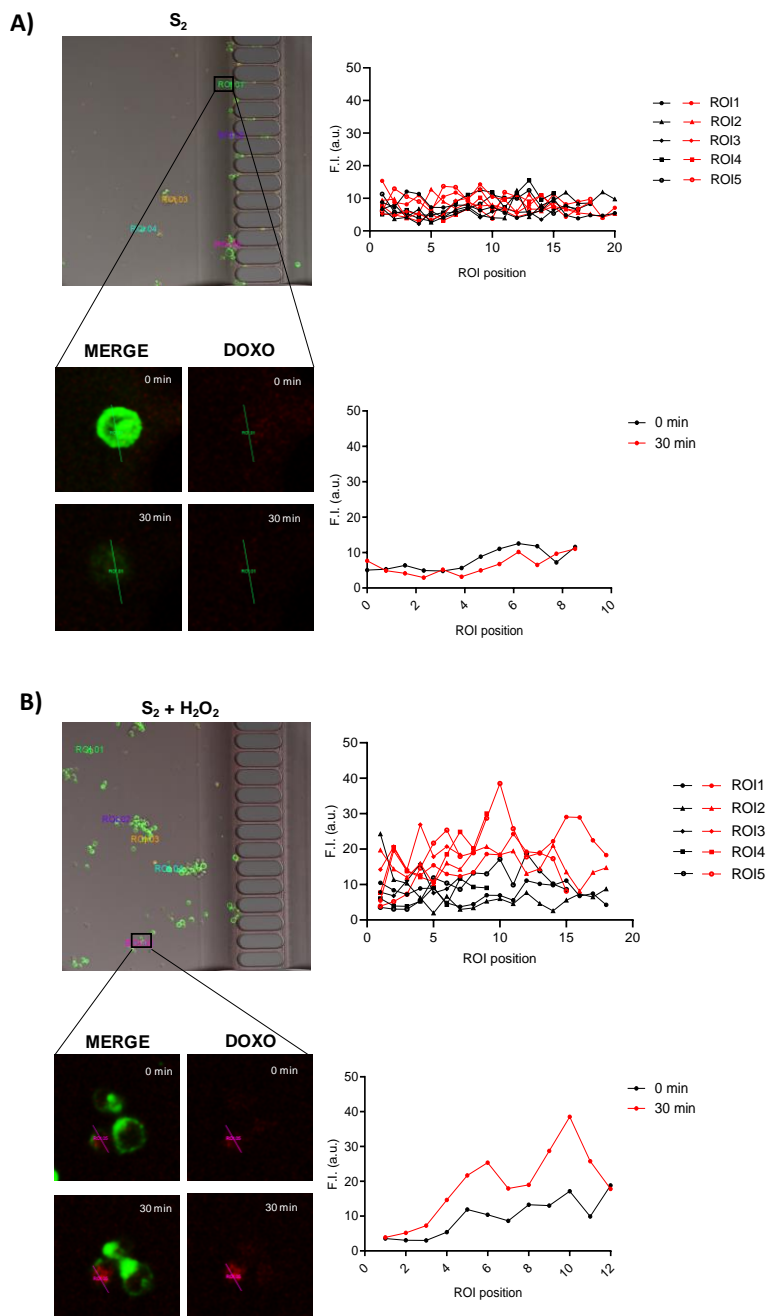


Figure 7. Image of THP-1 cells and S_2 nanomotors ($100 \mu\text{g} \cdot \text{ml}^{-1}$) in the microchip device in the absence (A) and the presence (B) of H_2O_2 solution (0.02%). Analysis of Doxorubicin fluorescence intensity in 5 defined linear regions of interest (ROI 1-5), corresponding to different THP-1 cells at 0 (black) and 30 (red) minutes of test time (ROI 1 from S_2 and ROI 5 from $S_2 + H_2O_2$ zoomed).

4. Conclusions

In summary, we report here the design, synthesis, and characterization of ultrafast and directional Janus Pt-MSNs nanomotors with stimuli-responsive drug release capabilities. They are based on the anisotropic conjunction of two individual nanoparticles with different and complementary functions, i) a PtNds face, responsible for the autonomous self-propulsion via catalytic decomposition of H_2O_2 into water and oxygen bubbles and, ii) a redox sensitive (S-S-PEG) gated-MSNs face, as nanocontainer for the loading of Doxorubicin cytotoxic drug. The main advantage of PtNds nanoparticles used as propelling element, lies in their major roughness and high active surface catalytic area. PtNds endow improved propulsion capacity to the nanomotors at very low concentration of fuel, which was demonstrated by the elevated relative velocities registered ($426 \text{ bl}\cdot\text{s}^{-1}\cdot\%^{-1}$). These values are far superior to the speeds reported by previous chemically-powered nano/micromotors reported, including Pt-catalytic motors made using sputtering technology, as well as by some mobile microorganisms. Moreover, the nanobots remain capped and only deliver their payload upon recognition of the reducing agent GSH, due to the cleavage of the gatekeepers. We also observed that an increase in nanomotors movement, as consequence of higher fuel concentrations, turns out in an increment of cargo release to the medium. We also found that the nanorobot S_2 is able to internalize in THP-1 cancer cells. THP-1 were selected as model cells to evaluate the selective drug release capacity of our nanomotors mediated by the reducing environment present in them. Moreover, a larger intracellular Doxorubicin release was observed for nanobots incubated with H_2O_2 after 4 and 6 hours. Finally, the use of nanorobots to target THP-1 cells was also studied using a microchip device with physical boundaries (microchannels), mimicking the transport along capillary vessels. The fast displacement of the propelled nanodevices facilitated nanomotors to pass through the microchannels towards the cells area where are internalized in THP-1 cells. However, non-fueled

nanomotors were not able to reach target cells and delivery its cargo, revealing the advantage of using self-propelled nanoparticles.

Overall, our nanomotors gather highly desired properties for nanobots for biomedical applications such as autonomous motion, biocompatibility, efficient cargo transport and stimulus-responsive controlled drug release in cancer cells. In future works, it is expected to delve into a more selective delivery of therapeutic payloads to target destinations, including specific cellular markers in the nanomotor design, as well as, in other therapeutic strategies based on the elimination of hydrogen peroxide by their catalytic decomposition. It is widely reported that H_2O_2 produced by both cancer cells and associated fibroblasts, causes DNA damage and inflammation, resulting in cell proliferation and metastasis. Besides, some resistance to tumor drugs is also associated with the presence of hydrogen peroxide. In accordance to this, our Janus Pt-MSN nanomotors would be a useful antioxidant therapeutic tool to prevent development and recurrence tumor and overcome drug resistance. We envision that combining the versatility of stimuli-responsive gatekeepers and catalytic nanomotors can lead to promising advances in nanorobotics and biomedicine in the near future.

5. Materials and methods

5.1. Chemicals

Dihydrogen hexachloroplatinate (H_2PtCl_6), polyvinylpyrrolidone (PVP), ascorbic acid, 3-mercaptopropionic acid, tetraethyl orthosilicate (TEOS), (3-mercaptopropyl)-trimethoxysilane, n-cetyltrimethylammonium bromide (CTABr), paraffin wax, tris(2,2'-bipyridyl)dichlororuthenium(II) hexahydrate ($\text{Ru}(\text{bpy})_3\text{Cl}_2$), 2,2'-dipyridyl disulfide, O-(2-mercuptoethyl)-O'-methyl-hexa(ethylene glycol) (PEG-SH), Doxorubicin ($\text{C}_{27}\text{H}_{29}\text{NO}_{11}$), 2,2'-azino-bis(3-ethylbenzothiazoline)-6-sulfonic acid (ABTS), fetal bovine serum (FBS), RPMI-1640 medium, L-glutathione reduced (GSH), Hoechst 33342 and WGA were purchased by Sigma-Aldrich. Sodium hydroxide (NaOH), hydrogen peroxide (30%), sodium hydrogen

phosphate monohydrate, disodium hydrogen phosphate heptahydrate, absolute ethanol, toluene, chloroform, and acetonitrile were provided by Scharlau.

5.2. General methods

Transmission electron microscopy (TEM) images were achieved using a JEOL TEM-2100F Electron microscope and TEM images of cells were acquired using a microscope FEI Tecnai Spirit G2. Scanning transmission electron microscopy coupled with electronic energy dispersive x-ray spectroscopy (STEM-EDX) was performed using a JEM 2100F instrument. Powder X-ray diffraction (PXRD) measurements were carried out using a Seifert 3000TT diffractometer using $\text{CuK}\alpha$ radiation. Dynamic light scattering (DLS) experiments were performed using a ZetaSizer Nano ZS (Malvern). N_2 adsorption-desorption isotherms were recorded using a Micromeritics TriStar II Plus automated analyzer. Thermal analysis was performed with a TA Instruments SDTQ600 apparatus (USA). Nanoparticle tracking experiments were carried out using a Nanosight NS300 (Malvern). UV-visible measurements were recorded with a JASCO V-650 Spectrophotometer. Confocal microscopy imaging was recorded with a Leica TCS SP8 AOBS inverted laser scanning confocal and a microfluidic device XC450 of XonaChip®.

5.3. Synthesis of mesoporous silica nanoparticles (MSNs)

To synthesize mesoporous silica nanoparticles, CTAB (1.00 g, 2.74 mmol), was first dissolved in deionized water (480 ml) and the solution was magnetically stirred. Then, to increase the pH, NaOH (3.5 ml, 2 M) was added, followed by an adjustment in the temperature to 80°C. TEOS, used as inorganic silica precursor, was added dropwise to the surfactant solution. The mixture was stirred for 2 h at 80°C giving a white precipitate. Finally, the solid was isolated by centrifugation, washed with deionized water until reaching neutral pH and dried overnight at 70°C. The nanomaterial, named “as made”, was calcined at 550 °C using an oxidant atmosphere for 5 h in order to remove the template phase, obtaining the final mesoporous nanomaterial (MSNs).

5.4. Synthesis of platinum nanodendrites (PtNdS)

For the preparation of platinum nanodendrites, H_2PtCl_6 (164 mg) and PVP (20 mg) were dissolved in deionized water (20 mL). Then, a solution of ascorbic acid in water (350 mg in 10 mL) was added drop by drop to the H_2PtCl_6 solution. The reaction was heated at 45°C for 1 h under magnetic stirring. The initially pale-yellow color change to black when the platinum nanoparticles are synthesized^{66,67}.

5.5. Synthesis of Janus Pt-MSN nanoparticles (S_0)

Janus Pt-MSN were synthesized following an adapted method previously reported by Villalonga et al⁴⁵. Mesoporous silica nanoparticles (180 mg) were dispersed in an aqueous solution (10 ml, 6.7 % ethanol) and CTAB was added (208 μl , 1 μM). The temperature of the mixture was increased at 75°C and 1 g of paraffin wax was added. When the paraffin was melted, the mixture was homogenized using an Ultra-Turrax T-8 (IKA, Germany) for 10 minutes. Then, the reaction was further magnetically stirred at 75°C for 1 h, to form a Pickering emulsion. The result was cooled to room temperature, diluted with methanol (10 ml) and treated with (3-mercaptopropyl)trimethoxysilane (200 μl). The reaction was magnetically stirred for 3 h and the resultant solid, was isolated by centrifugation and washed with methanol two times. Afterward, the partially mercapto-functionalized mesoporous silica nanoparticles were dispersed into the platinum nanoparticles (30 ml). The reaction was stirred overnight at room temperature. Lastly, the solid was filtered, washed with chloroform, and dried. This process yielded the Janus Pt-MSN nanoparticles (S_0).

5.6. Synthesis of Janus Pt-MSN (Ru)-PEG (S_1)

The platinum face was functionalized with 3-mercaptopropionic acid in order to protect it, 50 mg of S_0 reacted with 70 μl of this molecule for 1 h, using ethanol as solvent. After 1 h, the solid was washed with ethanol for 3 times. The next step was loading the pores

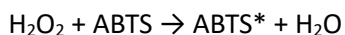
with the dye, the nanoparticles were resuspended in 3 ml of a concentrated solution of $[\text{Ru}(\text{bpy})_3]\text{Cl}_2 \cdot 6\text{H}_2\text{O}$ (30 mg) in anhydrous acetonitrile and stirred for 24 h. Next, we proceeded to functionalize the mesoporous face. First, the solid reacted with 93 μl (3-mercaptopropyl)-trimethoxysilane for 5.5 h. Second, 110 mg of 4,4'-dipyridyl disulfide were added to the mixture and the reaction was magnetically stirred 24 h. Third, the thiolated-solid reacted overnight with 50 μl of PEG-SH after being washed with acetonitrile and resuspended in 3 ml of acetonitrile. Finally, the suspension was centrifugated, washed with acetonitrile and dried under vacuum, yielding the final solid **S₁**.

5.7. Synthesis of Janus Pt-MSN (Doxorubicin)-PEG (**S₂**)

To synthesize this solid, the same procedure used for the preparation of **S₁** was followed. However, in this case the pores were loaded with the anticancer drug Doxorubicin. For 50 mg of **S₀** we added 24 mg (0.044 mmol) of Doxorubicin diluted in 50 mM sodium phosphate buffer pH 7.5. The filling process was carried out in darkness, under magnetic stirring for 24 h. Lastly, once the “molecular gate” was formed, the solid was further washed with 50 mM sodium phosphate buffer pH 7.5. The resulting nanoparticles (**S₂**) was stored in buffer solution at 4°C.

5.8. Peroxidase-like activity assay

To confirm the catalytic activity of our nanomotors, peroxidase activity assays were performed⁶⁸. The method employed is based on the platinum capability to oxidize ABTS in the presence of H_2O_2 , mimicking the peroxidase catalytic action. The result is a blue-green product (ABTS*) that can be detected by UV-visible spectrophotometry ($\lambda_{\text{abs}} = 405 \text{ nm}$). This reaction is resumed in the next equation:



For this assay, dissolutions of ABTS (9 mM) and H_2O_2 (from 0 to 30 mM) were prepared in 100 mM PBS pH 5. Afterwards, 2.9 mL of ABTS and 0.1 mL H_2O_2 were mixed in a cuvette at 25 °C and 0.05 mL of S_1 ($0.5 \text{ mg} \cdot \text{ml}^{-1}$) were added to them. Finally, the variation in the absorbance was recorded for 3 minutes.

5.9. Motion analysis by MSD calculation

To evaluate the nanomotors movement we analyzed the trajectories of single nanoparticles by NTA using a Nanosight NS300 device. This technique is based on the tracking of the light scattered by the nanoparticles when a laser beam falls upon them. The device is formed by a sCMOS camera coupled to an optical microscope and a single mode laser diode with 55 mW blue light illumination.

The samples were diluted in sodium phosphate buffer at a concentration of $0.002 \text{ mg} \cdot \text{ml}^{-1}$, ultrasonicated and introduced into the Nanosight chamber at 25°C using a 1 mL syringe. Nanomotors motion was registered in 5 videos of 30 seconds with a speed of 30 frames $\cdot \text{s}^{-1}$. The x-y coordinates of 20 nanoparticles throughout that time (selected size between 100–200 nm to avoid aggregates) were extracted by the NTA 3.0 software. That allows the estimation of the mean square displacement (MSD) for each nanoparticle, obtained applying the equation 1 (assuming the motion to be two-dimensional)¹⁶.

Equation 1:
$$\text{MSD} \equiv \langle (x_t - x_0)^2 \rangle = \frac{1}{N} \sum_{i=0}^N \left(x^i(t) - x^t(0) \right)^2$$

(N: number of averaged nanoparticles; x^i and x^t vector positions of particles at different times).

For the nanoparticles with Brownian motion, the rotational diffusion coefficient was gotten from the plot of MSD vs Δt , through the Stokes-Einstein equation ($\text{MSD} = 4D_r \Delta t$). Whereas, for the nanoparticles that follows a directional motion, the parabolic

component of the Stokes-Einstein equation ($MSD = 4D_t \Delta t + (v \Delta t)^2$) is applied to obtain the velocity and translational diffusion coefficient.

The time interval used in this study was set below the rotational diffusion time (τ_r) where propulsion movement dominates, theoretically calculated using the following equation:

Equation 2:
$$\tau_r = \frac{8\pi\eta R^3}{k_B \cdot T}$$

where η is the viscosity (10^{-3} Pa · s), k_B is the Boltzmann constant, T is the temperature (25°C) and R is the radius of the particle (145 nm, assuming a spherical morphology). Under these conditions a value of 0.8s was obtained for τ_r .

To calculate the propulsion force (F_{Prop}) or the drag force (F_{drag}) applied on activated nanomotors we employed the drag law of Stokes in fluids, assuming nanomotors morphology as spherical.

Equation 3:
$$F_{\text{drag}} = 6\pi\eta R V$$

where η is the viscosity (10^{-3} Pa) and R is the radius of the particle (145 nm). Calculated F_{drag} were 5.6, 8.5, 16 and 53 fN for 0.02, 0.7, 0.2 and 0.35% of fuel concentration, respectively.

5.10. Control release studies

Release of $\text{Ru}(\text{bpy})_3\text{Cl}_2$ from \mathbf{S}_1 was carried out under static and stirring conditions, to study the effect of the nanomotor self-propulsion on the delivery of the cargo. In a typical stirring experiment, 4 different suspensions of 0.5 mg of \mathbf{S}_1 in 1 ml of 50 mM PBS (pH 7.5) were prepared. Solutions were placed in a shaker (Thermo-shaker HC24N Grant Instruments PCMT) 30 minutes at 14000 rpm. After this period, H_2O_2 , GSH or both were

added at final concentrations of 1% and 10 mM, respectively (registered as zero release time). At scheduled times (2, 5, 10, 15, 20 and 30 minutes), 200 μl aliquots were taken and centrifugated (3 minutes, 125000 rpm) to isolate the $\text{Ru}(\text{bpy})_3\text{Cl}_2$ released in the supernatant from the nanoparticles. Then, fluorescence emission of the dye was monitored at 595 nm with a JASCO spectrofluorometer FP-8300. The results of three independent experiments are shown in Figure 5.A. In the static experiment, the four samples were prepared as previously described ($0.5 \text{ mg} \cdot \text{ml}^{-1}$ in 50 mM PBS, pH 7.5) but remained without external stirring. After 30 minutes, the inputs (H_2O_2 , GSH or both, at final concentrations of 0.1% and 10 mM, respectively) were carefully added through the wall of the tubes containing the samples. Afterwards, 200 μl aliquots were taken at different times (2, 5, 10, 15, 20 and 30 minutes) and centrifuged (3 minutes, 125000 rpm) to sediment the nanodevices. Fluorescence of $\text{Ru}(\text{bpy})_3\text{Cl}_2$ delivered to the media was measured at 595 nm ($\lambda_{\text{exc}} = 453 \text{ nm}$), Figure 4.A. The Doxorubicin release from S_2 assay was further performed in static conditions, following the same procedure than for S_1 . In this case, the Doxorubicin fluorescence emission was monitored at 555 nm ($\lambda_{\text{exc}} = 470 \text{ nm}$). The kinetic curves of four independent experiments are shown in Figure SI-10B.

5.11. Cell culture conditions

THP-1, human monocytic cell line derived from an acute monocytic leukemia patient, were purchased from ATCC and were grown in RPMI-1640 supplemented with 10% FBS. Cells were incubated at 37°C in an atmosphere of 5 % carbon dioxide.

5.12. Viability Assay

THP-1 cells were seeded in 96-well plates at 80,000 cells/well and incubated at 37°C for 24 h. Then, cells were treated with different reagents concentrations to evaluate their toxicity to cells. The reagents analyzed were H_2O_2 , S_2 nanomotors and free Doxorubicin. Finally, cell viability was evaluated by incubation with the cell proliferation WST-1 reagent for 1 hour and measuring the absorbance at 595 nm.

5.13. Cell uptake of nanomotors by confocal microscopy

THP-1 were seeded at 10^6 cells \cdot ml $^{-1}$ in a 6-well plate and incubated with **S₂** nanomotors ($50 \mu\text{g} \cdot \text{ml}^{-1}$) in RPMI-1640 buffer supplemented with 10% FBS at 37°C for 30 min in the presence and absence of 0.02% (8.5 mM) H₂O₂. Afterward, uninternalized nanoparticles were removed from cells by a washing step and further incubated for 1, 4 and 6 h in a fresh media. Next, cells were seeded on glass coverslips and DNA and membrane marker, Hoechst 33342, and WGA respectively, were added. Finally, slides were visualized under a Leica TCS SP2 AOBS inverted laser scanning confocal microscope (Leica Microsystems Heidelberg GmbH, Mannheim, Germany). The images were acquired with an excitation wavelength of 405 nm for Hoescht, 480 nm for Doxorubicin and 650 nm for WGA (Wheat germ agglutinin). The distribution of fluorescence inside the cells was analyzed using ImageJ Software (Figure 6A).

5.14. Cell uptake of nanomotors by TEM

THP-1 cells were seeded in a 6-well plate at 800,000 cells/well and incubated at 37°C for 24 h. Then, cells were treated with Janus nanomotors ($100 \mu\text{g} \cdot \text{ml}^{-1}$) at 37°C for 6 h. After this period, cells were washed with phosphate buffer 0.1 M (pH 7.4) and fixed in a 2.5 % glutaraldehyde + 2% paraformaldehyde solution for 1 h at room temperature and 72 hours more at 4°C. Fixed cells were washed with phosphate buffer, dehydrated in ethanol and stained with uranyl acetate (1%) and osmium tetroxide (1%). Finally, samples were included in epoxy resin (Araldite) and sectioned for TEM analysis. TEM images were acquired using a microscope FEI Tecnai Spirit G2 operating at 80 kV with a digital camera (Soft Image System, Morada), Figure 6C.

5.15. Self-propel and drug release capabilities of S₂ in microchip device

Movement and delivery abilities of nanomotors were performed by recording confocal microscopy videos using a 4-compartment microchip device (acquired from XonaChips®)

with a 150 μm microgroove barrier and a 75 x 25 mm size. This device has 4 wells connected two by two (1-2; 3-4) and these were connected to each other by micrometric channels (Figure 6). The experiment was carried out by depositing 10^6 THP-1 cells/ml in 1 and 2 wells dyed with WGA, $100 \mu\text{g} \cdot \text{ml}^{-1}$ of S_2 nanomotors in position 4 and completing the volume with RPMI-1640 buffer in well 3, (final volume 150 μl per well). At this point, it was waited few minutes to start the video, in order to eliminate the diffusive movement of the nanomotors after their addition to the well. Brownian motion of nanodevices was then recorded using a Leica TCS SP2 AOBS confocal microscope during 5 min. Then, the same methodology was repeated adding the fuel (H_2O_2) in position 3 to a total concentration of 0.02% in the cuvette (fuel volume added was previously removed from the well 3 to maintain a constant total volume). Furthermore, to study the controlled Doxorubicin release from S_2 in the cells, previous experimental procedure was also followed but for a prolonged time of 30 minutes. In recorded videos, assemblies nanomotors (up to 350 nm) can be observed through the excitation of the Doxorubicin loaded in the silica nanopores because of the confocal microscopy resolution⁶⁹. Finally, nanomotors trajectories were drawn with the plugin Manual Tracking from Image J software⁷⁰ and the intensity of cellular fluorescence was also analyzed using LAS X software and the "Line Profile" tool. This tool measures the fluorescence intensity along the linear regions of interest (ROI) defined by us and are shown graphically as a curve. Five regions of interest were defined (ROI 01-05), and the fluorescence intensity associated with Doxorubicin was analyzed in each condition. Line profiles were placed through the cells and the peak currents were evaluated simultaneously at time 0 and 30 minutes (Figure 7).

6. References

1. Esteban-Fernández de Avila, B.; Martín, A.; Soto, F.; Lopez-Ramirez, M. L.; Campuzano, S.; Vásquez-Machado, G. M.; Gao, W.; Zhang, L.; Wang, J. Single Cell Real-Time miRNAs Sensing Based on Nanomotors. *ACS Nano*, **9**, 6756–6764 (2015).

2. De Luis, B.; Llopis-Lorente, A.; Rincón, P.; Gadea, J.; Sancenón, F.; Aznar, E.; Villalonga, R.; Murguía, R. M.; Martínez-Mañez, R. An Interactive Model of Communication between Abiotic Nanodevices and Microorganisms. *Angew. Chem.*, **131**, 15128–15132 (2019).
3. Liang, C.; Zhan, C.; Zeng, F.; Xu, D.; Wang, Y.; Zhao, W.; Zhang, J.; Guo, J.; Feng, H.; Ma, X. Bilayer Tubular Micromotors for Simultaneous Environmental Monitoring and Remediation. *ACS Appl. Mater. Interfaces*, **10**, 35099–35107 (2018).
4. Pijpers, I. A. B.; Cao, S.; Llopis-Lorente, A.; Zhu, J.; Song, S.; Joosten, R. R. M.; Meng, F.; Friedrich, H.; Williams, D. S.; Sanchez, S.; van Hest, J. C. M.; Abdelmohsen, L. K. E. A. Hybrid Biodegradable Nanomotors through Compartmentalized Synthesis. *Nano. Lett.*, **20**, 4472–4480 (2020).
5. Tu, Y.; Peng, F.; Sui, X.; Men, Y.; White, P. B.; van Hest, J. C. M.; Wilson, D. A. Self-Propelled Supramolecular Nanomotors with Temperature-Responsive Speed Regulation. *Nat. Chem.*, **9**, 480–486 (2016).
6. Wang, H.; Moo, J. G.; Pumera, M. From Nanomotors to Micromotors: The Influence of the Size of an Autonomous Bubble-Propelled Device upon Its Motion. *ACS Nano*, **10**, 5041–5050 (2016).
7. Hu, N.; Zhang, B.; Gai, M.; Zheng, C.; Frueh, J.; He, Q. Forecastable and Guidable Bubble-Propelled Microplate Motors for Cell Transport. *Macromol. Rapid Commun.*, **38**, 1-6 (2017)

8. Paxton, W. F.; Sen, A.; Mallouk, T. E. Motility of Catalytic Nanoparticles through Self-Generated Forces. *Chemistry*, **11**, 6462–6470 (2005).
9. Hong, Y.; Blackman, N. M.; Kopp, N. D.; Sen, A.; Velegol, D. Chemotaxis of Nonbiological Colloidal Rods. *Phys. Rev. Lett.*, **99**, 1-4 (2007)
10. Golestanian, R.; Liverpool, T. B.; Ajdari, A. Propulsion of a Molecular Machine by Asymmetric Distribution of Reaction Products. *Phys. Rev. Lett.*, **94**, 1-4 (2005).
11. Valadares, L. F.; Tao, Y. G.; Zacharia, N. S.; Kitaev, V.; Galembeck, F.; Kapral, R.; Ozin, G. A. Catalytic Nanomotors: Self-Propelled Sphere Dimers. *Small*, **6**, 565–572 (2010)
12. Howse, J. R.; Jones, R. A.; Ryan, A. J.; Gough, T.; Vafabakhsh, R.; Golestanian, R. Self-Motile Colloidal Particles: From Directed Propulsion to Random Walk. *Phys. Rev. Lett.*, **99**, 1-4 (2007).
13. Kagan, D.; Laocharoensuk, R.; Zimmerman, M.; Clawson, C.; Balasubramanian, S.; Kang, D.; Bishop, D.; Sattayasamitsathit, S.; Zhang, L.; Wang, J. Rapid Delivery of Drug Carriers Propelled and Navigated by Catalytic Nanoshuttles. *Small.*, **6**, 2741–2747 (2010).
14. Van Nguyen, K.; Minteer, S. D. DNA-Functionalized Pt Nanoparticles as Catalysts for Chemically Powered Micromotors: Toward Signal-On Motion-Based DNA Biosensor. *Chem. Commun.*, **51**, 4782–4784 (2015).
15. Sanchez, S.; Soler, L.; Katuri, J. Chemically Powered Micro- and Nanomotors. *Angew. Chem.*, **54**, 1414–1444 (2015).

16. Ma, X.; Jang, S.; Popescu, M. N.; Uspal, W. E.; Miguel-Lopez, A.; Hahn, K.; Kim, D. P.; Sanchez, S. Reversed Janus Micro/Nanomotors with Internal Chemical Engine. *ACS Nano*, **10**, 8751–8759 (2016).
17. Kim, K.; Guo, J.; Liang, Z. X.; Zhu, F. Q.; Fan, D. L. Man-Made Rotary Nanomotors: A Review of Recent Development. *Nanoscale*, **8**, 10471–10490 (2016).
18. Parmar, J.; Vilela, D.; Villa, K.; Wang, J.; Sánchez, S. Micro- and Nanomotors as Active Environmental Microcleaners and Sensors. *JACS*, **140**, 9317–9331 (2018).
19. Jinqiang Wang, J.; Zhang, Y.; Archibong, E.; Ligler, F.S.; Gu, Z. Leveraging H₂O₂ Levels for Biomedical Applications. *Adv. Biosys.*, **1**, 1-15 (2017).
20. Abdelmohsen, L. K. E. A.; Peng, F.; Tu, Y.; Wilson, D. A. Micro- and Nanomotors for Biomedical Applications. *J. Mater. Chem. B*, **2**, 2395–2408 (2014).
21. Gao, W.; Wang, J. Synthetic Micro/Nanomotors in Drug Delivery. *Nanoscale*, **6**, 10486–10494 (2014).
22. Tu, Y.; Peng, F.; André, A.A.; Men, Y.; Srinivas, M.; Wilson, D.A. Biodegradable Hybrid Stomatocyte Nanomotors for Drug Delivery. *ACS Nano*, **11**, 1957–1963 (2017).
23. Lv, H.; Xing, Y.; Du, X.; Xu, T.; Zhang, X. Construction of Dendritic Janus Nanomotors with H₂O₂ and NIR Light Dual-Propulsion via a Pickering Emulsion. *Soft Matter*, **16**, 4961–4968 (2020).

24. Aznar, E.; Oroval, M.; Pascual, L.; Murguía, J. R.; Martínez-Máñez, R.; Sancenón, F. Gated Materials for On-Command Release of Guest Molecules. *Chem. Rev.*, **116**, 561–718 (2016).
25. Bernardos, A.; Piacenza, E.; Sancenón, F.; Hamidi, M.; Maleki, Turner, R.J.; Martínez-Máñez, R. Mesoporous Silica-Based Materials with Bactericidal Properties. *Small*, **15**, 1-34 (2019).
26. Hu, S.; Shao, S.; Chen, H.; Sun, J.; Zhai, J.; Zheng, H.; Wan, M.; Liu, Y.; Mao, C.; Zhao, J. Preparation and Properties of Janus Heparin-Loaded Ammoniated-Hollow Mesoporous Silica Nanomotors. *J. Phys. Chem. C.*, **122**, 9680-9687 (2018)
27. Xuan, M.; Shao, J.; Lin, X.; Dai, L.; He, Q. Self-Propelled Janus Mesoporous Silica Nanomotors with Sub-100 nm Diameters for Drug Encapsulation and Delivery. *Chem. Phys. Chem.*, **15**, 2255-2260 (2014).
28. Ma, X.; Hahn, K.; Sanchez, S. Catalytic Mesoporous Janus Nanomotors for Active Cargo Delivery. *J. Am. Chem. Soc.*, **137**, 15, 4976-4979 (2015).
29. Baraban, L.; Makarov, D.; Streubel, R.; Mönch, I.; Grimm, D.; Sánchez, S.; Schmidt, O.G. Catalytic Janus Motors on Microfluidic Chip: Deterministic Motion for Targeted Cargo Delivery. *ACS Nano*, **6**, 3383-3389 (2012).
30. Maggi, C.; Simmchen, J.; Saglimbeni, F.; Katuri, J.; Dipalo, M.; De Angelis, F.; Sanchez, S.; Di Leonardo, R. Self-Assembly of Micromachining Systems Powered by Janus Micromotors. *Small*, **12**, 446-451 (2016).

31. Yu, H. L.; Kopach, A.; Misko, V. R.; Vasylenko, A. A.; Makarov, D.; Marchesoni, F.; Nori, F.; Baraban, L.; Cuniberti, G. Confined Catalytic Janus Swimmers in a Crowded Channel: Geometry-Driven Rectification Transients and Directional Locking. *Small*, **12**, 5882-5890 (2016).
32. Gibbs, J. G.; Fragnito, N. A.; Zhao, Y. Asymmetric Pt/Au Coated Catalytic Micromotors Fabricated by Dynamic Shadowing Growth. *Appl. Phys. Lett.*, **97**, 1-3 (2010).
33. Katuri, J.; Caballero, D.; Voituriez, R.; Samitier, J.; Sanchez, S. Directed Flow of Micromotors through Alignment Interactions with Micropatterned Ratchets. *ACS Nano*, **12**, 7282-7291 (2018).
34. Solovev, A. A.; Xi, W.; Gracias, D. H.; Harazim, S. M.; Deneke, C.; Sanchez, S.; Schmidt, O. G. Self-Propelled Nanotools. *ACS Nano*, **6**, 1751-1756 (2012).
35. Wilson, D.A.; Nolte, R.J.M.; van Hest, J.C.M. Autonomous Movement of Platinum-Loaded Stomatocytes. *Nature Chem.*, **4**, 268-274 (2012).
36. Draz, M. S.; Lakshminaraasimulu, N. K.; Krishnakumar, S.; Battalapalli, D.; Vasan, A.; Kanakasabapathy, M. K.; Sreeram, A.; Kallakuri, S.; Thirumalaraju, P.; Li, Y.; Hua, S. Yu, X. G.; Kuritzkes, D.R.; Shafiee, H. Motion-Based Immunological Detection of Zika Virus Using Pt-Nanomotors and a Cellphone. *ACS Nano*, **12**, 5709–5718 (2018).
37. Vazquez-Duhalt, R.; Tejeda-Rodriguez, J. A.; Núñez, A.; Soto, F.; Gracia-Gradilla, V.; Cadena-Nava, R.; Wang, J. Virus-Based Nanomotors for Cargo Delivery. *J. Chem. Nano. Mat.*, **5**, 194-200 (2018).

38. Peng, F.; Men, Y.; Tu, Y.; Chen, Y.; Wilson, D. A. Nanomotor-Based Strategy for Enhanced Penetration across Vasculature Model. *Adv. Funct. Mater.*, **28**, 1-8 (2018).
39. Hortelão, A. C.; Patiño, T.; Perez-Jiménez, A.; Blanco, À.; Sánchez, S. Enzyme-Powered Nanobots Enhance Anticancer Drug Delivery. *Adv. Funct. Mater.*, **28**, 1-10 (2018).
40. Llopis-Lorente, A.; Garcia-Fernandez, A.; Murillo-Cremaes, N.; Hortelao, A. C.; Patino, T.; Villalonga, R.; Sancenon, F.; Martínez-Máñez, R.; Sanchez, S. Enzyme-Powered Gated Mesoporous Silica Nanomotors for On-Command Intracellular Payload Delivery. *ACS Nano*, **13**, 12171–12183 (2019).
41. Hortelão, A. C.; Carrascosa, R.; Murillo-Cremaes, N.; Patiño, T.; Sánchez, S. Targeting 3D Bladder Cancer Spheroids with Urease-Powered Nanomotors. *ACS Nano*, **13**, 429–439 (2019).
42. Sun, J.; Mathesh, M.; Li, W.; Wilson, D. A., Enzyme-Powered Nanomotors with Controlled Size for Biomedical Applications. *ACS Nano*, **13**, 10191–10200 (2019).
43. Chen, Z.; Xia, T.; Zhang, Z.; Xie, S.; Wang, T.; Li, X. Enzyme-Powered Janus Nanomotors Launched from Intratumoral Depots to Address Drug Delivery Barriers. *Chem. Eng. Trans.*, **375**, 1-12 (2019).
44. Luo, M.; Li, S.; Wan, J.; Yang, C.; Chen, B.; Guan, J. Enhanced Propulsion of Urease-Powered Micromotors by Multilayered Assembly of Ureasases on Janus Magnetic Microparticles. *Langmuir*, **36**, 7005–7013 (2020).

45. Villalonga, R.; Diez, P.; Sanchez, A.; Aznar, E.; Martínez-Máñez, R.; Pingarrón, J. M. Enzyme-Controlled Sensing-Actuating Nanomachine Based on Janus Au-Mesoporous Silica Nanoparticles. *Chemistry*, **19**, 7889–7894 (2013).
46. Diez, P.; Sanchez, A.; Gamella, M.; Martinez-Ruiz, P.; Aznar, E.; de la Torre, C.; Murguía, J. R.; Martínez-Máñez, R.; Villalonga, R.; Pingarrón, J. M. Toward the Design of Smart Delivery Systems Controlled by Integrated Enzyme-Based Biocomputing Ensembles. *J. Am. Chem. Soc.*, **136**, 9116–9123 (2014).
47. Llopis-Lorente, A.; Diez, P.; Sanchez, A.; Marcos, M. D.; Sancenón, F.; Martinez-Ruiz, P.; Villalonga, R.; Martínez-Máñez, R. Interactive Models of Communication at the Nanoscale Using Nanoparticles That Talk to One Another. *Nat. Commun.*, **8**, 1-7 (2017).
48. Innocenzi, P.; Kozuka, H.; Yoko, T. Fluorescence Properties of the Ru(bpy)₃²⁺ Complex Incorporated in Sol–Gel-Derived Silica Coating Films. *J. Phys. Chem. B.*, **101**, 2285-2291 (1997).
49. Llopis-Lorente, A.; de Luis, B.; Garcia-Fernandez, A.; Diez, P.; Sanchez, A.; Dolores Marcos, M.; Villalonga, R.; Martínez-Máñez, R.; Sancenón, F. Au-Mesoporous Silica Nanoparticles Gated With Disulfide-Linked Oligo(ethylene Glycol) Chains for Tunable Cargo Delivery Mediated by an Integrated Enzymatic Control Unit. *J. Mater. Chem. B.*, **5**, 6734–6739 (2017).
50. Choudhury, U.; Soler, L.; Gibbs, J. G.; Sanchez, S.; Fischer, P. Surface Roughness-Induced Speed Increase for Active Janus Micromotors. *Chem. Commun.*, **51**, 8660–8663 (2015).

51. Long, N. V.; Ohtaki, M.; Uchida, M.; Jalem, R.; Hirata, H.; Chien, N. D.; Nogami, M. Synthesis and Characterization of Polyhedral Pt Nanoparticles: Their Catalytic Property, Surface Attachment, Self-Aggregation and Assembly. *J. Colloid Interface Sci.*, **359**, 339–350 (2011).
52. Lim, B.; Jiang, M.; Camargo, P. H. C.; Cho, E. C.; Tao, J.; Lu, X.; Zhu, Y.; Xia, Y. Pd-Pt Bimetallic Nanodendrites with High Activity for Oxygen Reduction. *Science*, **324**, 1302–1305 (2009).
53. Fan, J.; Yin, J. J.; Ning, B.; Wu, X.; Hu, Y.; Ferrari, M.; Anderson, G. J.; Wei, J.; Zhao, Y.; Nie, G. Direct Evidence for Catalase and Peroxidase Activities of Ferritin-Platinum Nanoparticles. *Biomaterials*, **32**, 1611–1618 (2011).
54. Duan, W.; Ibele, M.; Liu, R; Sen, A. Motion analysis of light-powered autonomous silver chloride nanomotors. *Eur. Phys. J. E.*, **35**, 1-8 (2012).
55. Wang, S.; Wu, N. Selecting the Swimming Mechanisms of Colloidal Particles: Bubble Propulsion versus Self-Diffusiophoresis. *Langmuir*, **30**, 3477–3486 (2014).
56. Maeda, K.; Imae, Y.; Shioi, J.I.; Oosawa, F. Effect of Temperature on Motility and ChemoTaxis of Escherichia Coli. *J. Bacteriol.*, **127**, 1039–1046 (1976).
57. Ma, X.; Hortelao, A. C.; Miguel-Lopez, A.; Sanchez, S. Bubble-Free Propulsion of Ultrasmall Tubular Nanojets Powered by Biocatalytic Reactions. *J. Am. Chem. Soc.*, **138**, 13782–13785 (2016)

58. Archer, R. A.; Howse, J. R.; Fujii, S.; Kawashima, J.; Buxton, G. A.; Ebbens, S. J. pH-Responsive Catalytic Janus Motors with Autonomous Navigation and Cargo-Release Functions. *Adv. Funct. Mater.*, **30**, 1-9 (2020)
59. Ebbens, S.; Jones, R. A. L.; Ryan, A. J.; Golestanian, R.; Howse, J. R. Self-Assembled Autonomous Runners and Tumblers. *Phys. Rev. E.*, **82**, 1-4 (2010).
60. Saito, G. S.; J. A.; Lee, K.-D. Drug Delivery Strategy Utilizing Conjugation Via Reversible Disulfide Linkages: Role and Site of Cellular Reducing Activities. *Adv. Drug Deliv. Rev.*, **55**, 199–215 (2003).
61. Kimura, H.; Sakai, Y.; Fujii, T. Organ/Body-on-a-Chip Based on Microfluidic Technology for Drug Discovery. *Drug Metab. Pharmacokinet.*, **33**, 43–48 (2018).
62. Restrepo-Perez, L.; Soler, L.; Martinez-Cisneros, C.; Sanchez, S.; Schmidt, O. G. Biofunctionalized Self-Propelled Micromotors as an Alternative On-Chip Concentrating System. *Lab Chip*, **14**, 2914-2917 (2014).
63. Restrepo-Perez, L.; Soler, L.; Martinez-Cisneros, C. S.; Sanchez, S.; Schmidt, O. G. Trapping Self-Propelled Micromotors with Microfabricated Chevron and Heart-Shaped Chips. *Lab Chip*, **14**, 1515–1518 (2014).
64. Rubio, L. D.; Potomkin, M.; Baker, R. D.; Sen, A.; Berlyand, L.; Aranson, I. S. Self-Propulsion and Shear Flow Align Active Particles in Nozzles and Channels. *Adv. Intell. Syst.*, **3**, 1-10 (2020).

65. Schmid-Schönbein, G. W., Usami, S., Skalak, R., & Chien, S. The Interaction of Leukocytes and Erythrocytes in Capillary and Postcapillary Vessels. *Microvascular Research*, **19**, 45–70 (1980).
66. Peng, F.; Tu, Y.; van Hest, J. C. M.; Wilson, D. A. Self-Guided Supramolecular Cargo-Loaded Nanomotors with Chemotactic Behavior towards Cells. *Angew. Chem.*, **127**, 11828–11831 (2015).
67. Long, N.V.; Chien, N.D.; Hayakawa, T.; Hirata, H.; Lakshminarayana, G.; Nogami, M. The Synthesis and Characterization of Platinum Nanoparticles: A Method of Controlling the Size and Morphology. *Nanotechnology*, **21**, 1-16 (2010).
68. Jiang, S.; Penner, M. H. Selective Oxidation of Enzyme Extracts for Improved Quantification of Peroxidase Activity. *Anal. Biochem.*, **476**, 20–25 (2015).
69. Schattling, P. S.; Ramos-Docampo, M. A.; Salgueirino, V.; Stadler, B. Double-Fueled Janus Swimmers with Magnetotactic Behavior. *ACS Nano*, **11**, 3973–3983 (2017).
70. Sbalzarini, I. F.; Koumoutsakos, P. Feature Point Tracking and Trajectory Analysis for Video Imaging in Cell Biology. *J. Struct. Biol.*, **151**, 182–195 (2005).

Acknowledgments

The authors want to thank the Spanish Government for RTI2018-100910-B-C41 (MCIU/AEI/FEDER, UE) and CTQ2017-87954-P projects and the Generalitat Valenciana for support by project PROMETEO/2018/024. P. Díez thanks the Spanish government for her Juan de la Cierva postdoctoral fellowship. E. Lucena-Sánchez thanks MINECO for her FPU fellowship. A. Escudero is also gratefully for her PhD. grant by the Generalitat Valenciana.

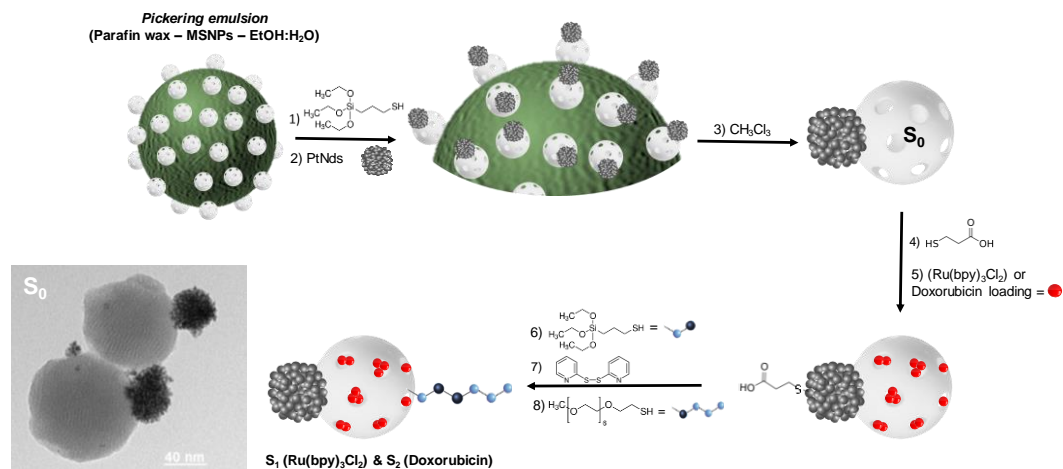
Author contributions

Paula Díez: Experimental design, nanoparticle development and characterization, data analysis, discussion, and writing. Elena Lucena-Sánchez: Experimental design, performing biological experiments, data analysis, discussion, and writing. Andrea Escudero: Contributed to nanoparticle development and characterization analysis, discussion, and writing. Antoni Llopis-Lorente: Conceptualization, Writing – review & editing. Reynaldo Villalonga: Conceptualization, Writing – review & editing, Supervision. Ramón Martínez-Mañez: Conceptualization, Project administration, Writing – review & editing, Supervision. All authors have approved the final version of the manuscript.

Conflicts of interest

There are no conflicts to declare.

7. Supporting information



SI-Scheme 1. Schematic Illustration of the steps in the preparation of Janus Pt-MSN nanomotors. TEM image of representative Janus Pt-MSN nanomotors (S_0).

Table SI-1. Representative published H_2O_2 -fueled nano- and micro-motors. i) Janus Pt-MSN nano and micromotors. ii) nanomotors with other designs. Most of the described motors need high amounts of fuel and does not achieve directional movement.

Motor type	Size	$[\text{H}_2\text{O}_2]$ (%)	Velocity	Reference
i) Janus Pt-MSN				
NANOMOTORS				
Pt-MSN	145 nm	0.3	$19.4 \mu\text{m s}^{-1}$ $461 \text{ body length s}^{-1} \%^{-1}$	(Present work)
Pt/Cr-MSN	75 nm	30	6 mm s^{-1} $8 \text{ body length s}^{-1} \%^{-1}$	27
Heparin-Pt -HMS	250 nm	15	212 mm s^{-1} $56.5 \text{ body length s}^{-1} \%^{-1}$	26
Pt-SiO ₂	480 nm	15	5.6 mm s^{-1} $0.8 \text{ body length s}^{-1} \%^{-1}$	11
Pt- HMS	500 nm	1.5	$D = 1.49 \mu\text{m}^2 \text{ s}^{-1}$ (diffusion coefficient)	16
Pt-MSN	<100 nm	2.5	$D = 9.20 \mu\text{m}^2 \text{ s}^{-1}$	28

MICROMOTORS				
Colloid Co/Pt-SiO ₂	5 mm	15	9 mm s ⁻¹ 0.9 body length s ⁻¹ % ⁻¹	29
Pt- SiO ₂	5 mm	5	2.5° μm ⁻¹ (angular speed)	30
Pt-SiO ₂ beads	3 mm	5	0.41 mm s ⁻¹ 0.027 body length s ⁻¹ % ⁻¹	31
Pt/Au-SiO ₂	2 mm	5	D = 0.88 μm ² s ⁻¹	32
Pt-SiO ₂	2.5 mm	3	6 mm s ⁻¹ 1.33 body length s ⁻¹ % ⁻¹	33
ii) Other designs				
InGaAs/ GaAs/(Cr)Pt nanotubes	280-600 nm	20	110 mm s ⁻¹ 18.3 body length s ⁻¹ % ⁻¹	34
Pt Nanoparticle - Antibody	20 nm	10	1.2 mm s ⁻¹ 5.99 body length s ⁻¹ % ⁻¹	35
Janus Pt-VLP NM viral	25-30 nm	1.5	4.15 mm s ⁻¹ 110.67 body length s ⁻¹ % ⁻¹	36
(PEG-PS) polymersome - based Janus	100-300 nm	1	D = 3.7 μm ² s ⁻¹	37
Polymer stomatocytes - Pt NP	316 nm	0.3	23 mm s ⁻¹ 242.6 body length s ⁻¹ % ⁻¹	38

Table SI-2. Main features and innovation points of the presented nanomotors in comparison to previously reported Janus Pt-MSN nanomotors.

Feature	Previous works	Present work	Provided advantages
Catalytic component	Metallic layer	Pt <u>nanodendrites</u>	Higher catalytic surface
Architecture	Half-coated Janus	Snowman-like Janus	Minimal reduction of effective silica surface, catalytic component location
Fabrication method	Electron beam <u>evaporation/sputtering</u>	Pickering emulsion	Higher yield, no need of expensive equipment
Controlled release	No	Yes	Reading information from the environment and controlled cargo release
Fuel concentration	1-10%	0.02-0.35%	Lower concentrations
Biological studies	None/cell culture	Directional motion through capillary and internalization	Demonstration of advanced functionality

7.1. Nanomaterial characterization

The nanodevices S_0 , S_1 and S_2 were characterized using standard procedures.

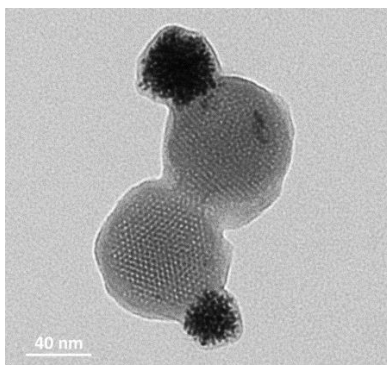


Figure SI-1. TEM image of Janus Pt-MSN nanomotors (S_0) after catalytic reaction in a 30% of H_2O_2 solution for 24 h.

7.1.1. Powder X-ray diffraction analysis

In the Figure SI-3 are represented the PDRX patterns of the calcined MSNs S_0 and S_1 at low ($1.5 < 2\theta < 7$) and at high angles ($35 < 2\theta < 80$). S_0 presents a main peak around 2.4° , which is typical of mesoporous materials with MCM-41 structure. This low angle reflection was preserved in S_1 , revealing that the processes of cargo loading, and chemical functionalization did not transform the mesoporous structure. In addition, at high angles S_1 shows several diffraction patterns indexed as (111), (200), (220) and (311) Bragg peaks of a Pt cubic structure.

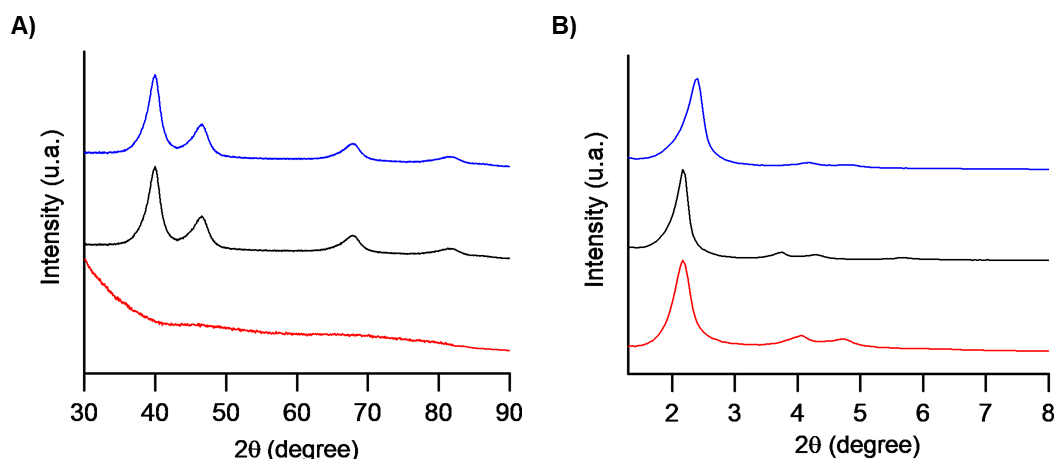


Figure SI-2. PDRX pattern at high-angles (A) and low-angles (B) of calcined MSNs (red curve), S_0 (black curve) and S_1 (blue curve).

7.1.2. N_2 adsorption-desorption isotherms

The N_2 adsorption-desorption isotherms of S_0 and S_1 are shown in Figure SI-4. S_0 presents two principal adsorption steps. Between 0.2 and 0.4 P/P_0 value shows the first step, which is due to the nitrogen condensation inside the mesopores by capillarity and reveals the emptiness of the pores. Besides, the lack of hysteresis loop suggest that the pores are cylindrical and uniform. The second step at P/P_0 value around 0.9 shows a typical H1 hysteresis loop. It is considered as textural-like porosity and correspond to the space among nanoparticles. In contrast, the N_2 adsorption-desorption isotherm of S_1 lacks the sharp step at low-medium relative pressure, exhibiting an important decrease in the

N_2 volume adsorbed, which indicates that the loading and capping processes have been successful.

Total pore volume and pore size were estimated by using the Barret, Joyner and Halenda (BJH) model on the adsorption branch of the isotherm, for $P/P_0 < 0.4$, which is associated to the surfactant generated mesopores. Brunauer, Emmett and Teller (BET) specific values are calculated from N_2 adsorption-desorption isotherms and show an important reduction in MSN ($1068 \text{ m}^2 \cdot \text{g}^{-1}$) compared to S_0 ($432 \text{ m}^2 \cdot \text{g}^{-1}$), which is due to the attachment of non-porous platinum nanoparticles. Moreover, the surface reduction is even superior in S_1 upon cargo loading and functionalization with the gating system ($25 \text{ m}^2 \cdot \text{g}^{-1}$) Both, BJH and BET values are shown in Table SI-1.

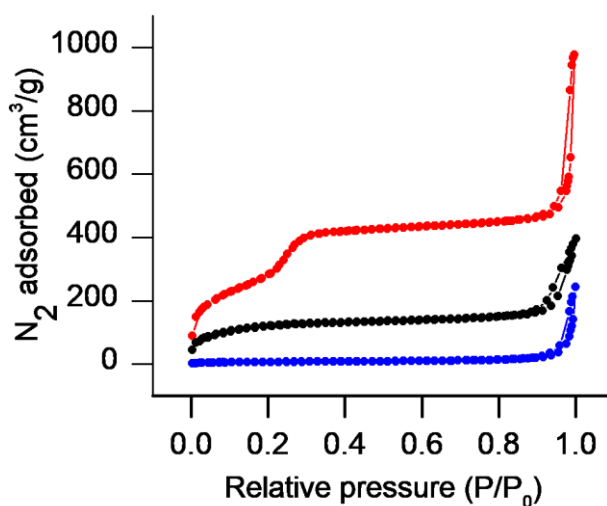


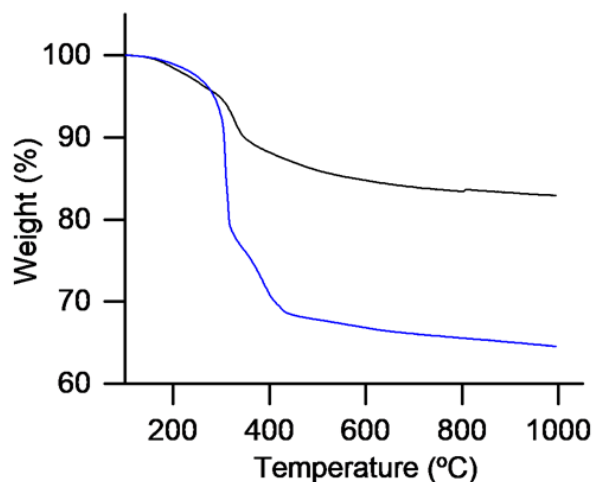
Figure SI-3. N_2 adsorption-desorption isotherms for calcined MSNs (red curve), starting Janus Pt-MSNs S_0 (black curve) and final Janus Pt-MSNs S_1 (blue curve).

Table SI-3. Pore diameters, pore volumes and BET specific surface values calculated from the N₂ adsorption-desorption isotherms for prepared nanomaterials.

	BJH pore ($P/P_0 < 0.4$) (nm)	Total pore volume ($\text{cm}^3 \cdot \text{g}^{-1}$)	S_{BET} ($\text{m}^2 \cdot \text{g}^{-1}$)
MSNs	1.96	0.96	1068
S ₀	1.97	0.38	432
S ₁	-	-	25

7.1.3. Thermogravimetric assay

Thermogravimetric studies of S₀ and S₁ are shown in **Figure SI-4** reveal the organic content corresponding to the capping system (S-S-PEG) and the organic content of the loaded Ru(bpy)₃Cl₂. The first thermal decomposition above ~245 °C corresponds to the gatekeeper, while the second one at ~ 320 °C is attributed to the loaded dye.

**Figure SI-4.** Thermogravimetric analysis of S₀ (black curve) and S₁ (blue curve).

7.1.4. DLS analysis

The hydrodynamic size and zeta potential of S_0 and S_1 were determined by dynamic light scattering studies. To that purpose, the solids were suspended in distilled water at a concentration of $0.01 \text{ mg} \cdot \text{ml}^{-1}$. The results, shown in Figure SI-5, reveal a decrease in negative surface charge as well as an increment in the hydrodynamic diameter, both as a consequence of molecular gate (S-S-PEG) attachment and cargo loading in the mesoporous face of the nanomotor.

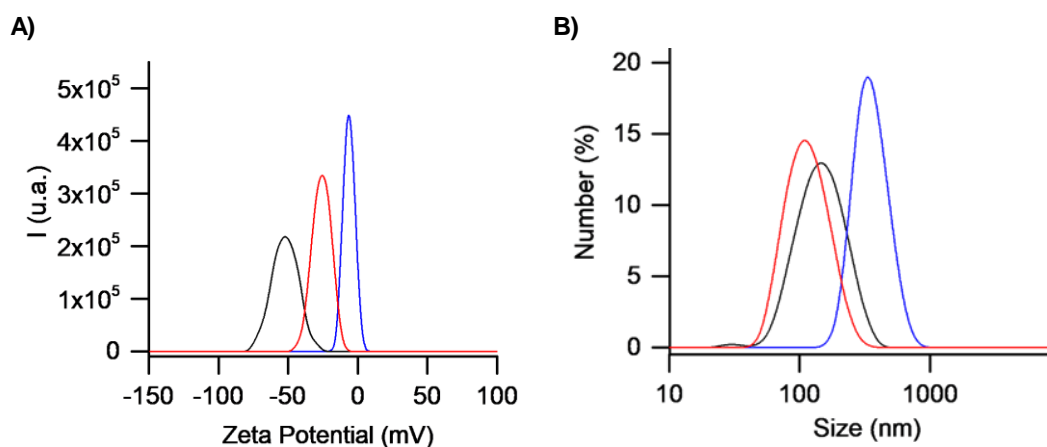


Figure SI-5. DLS analysis showing the zeta potential (A) and hydrodynamic diameter (B) of calcinated MCM-41 (red curve), S_0 (black curve) and S_1 (blue curve) nanomaterials.

7.2. Motion analysis

7.2.1. Peroxidase-like activity assay

The nanomotors present a typical Michaelis-Menten kinetic. The values of the Michaelis constant (K_M) and the maximum velocity (V_{max}), defined as the maximum rate at which an enzyme can catalyze a reaction, were estimated from the Lineweaver-Burk graphs. Data show that the nanomotor owns an intrinsic peroxidase activity. For a variable concentration of H_2O_2 , K_M was 2.3 mM and V_{max} was $0.32 \mu\text{M} \cdot \text{min}^{-1}$.

Equation SI-1:

$$\frac{1}{v} = \frac{K_M}{v_{max}} \cdot \frac{1}{[S]} + \frac{1}{v_{max}}$$

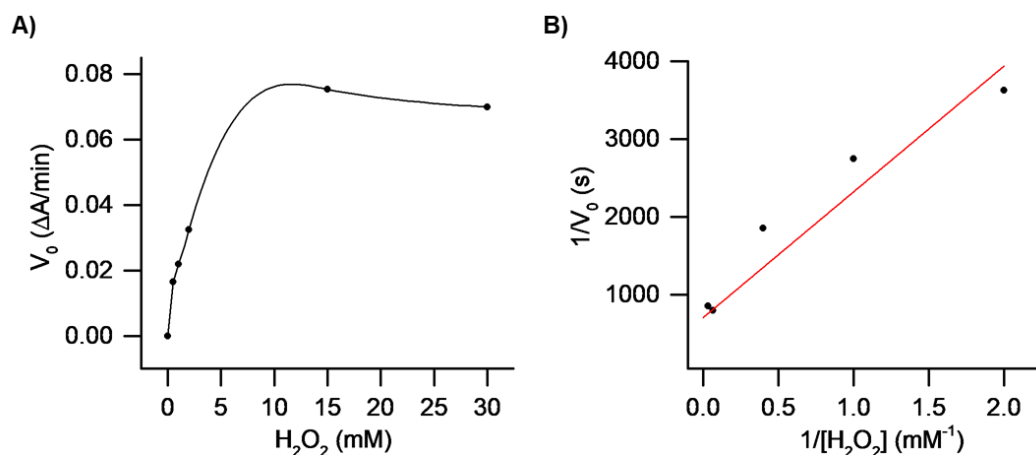


Figure SI-6. Peroxidase-like activity assay: effect of H_2O_2 concentration on the nanomotor catalyzed reaction rate at fixed ABTS dye concentration in 9 mM and temperature at 25°C (A). Lineweaver-Burk plot of H_2O_2 -catalysed decomposition used to determinate K_M applying the equation SI-1 (B).

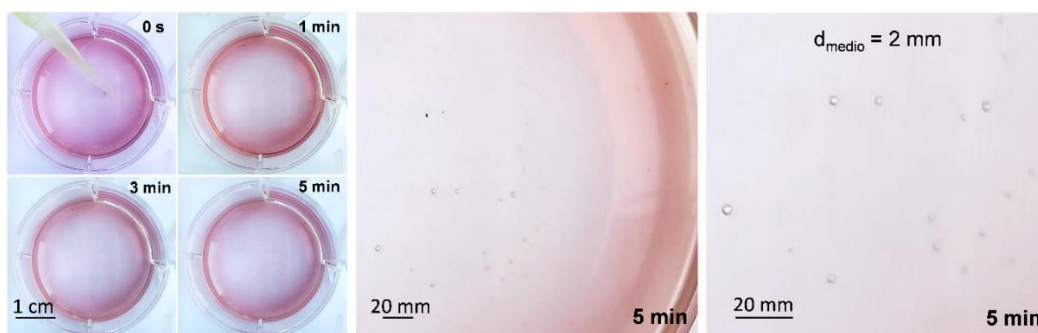


Figure SI-7. Time-lapse images of bubble growth by H_2O_2 -propelled S_1 nanomotors solutions. Bubble generation (average diameter: 2 mm) by the catalytic decomposition of H_2O_2 can be observed after 5 min of fuel addition.

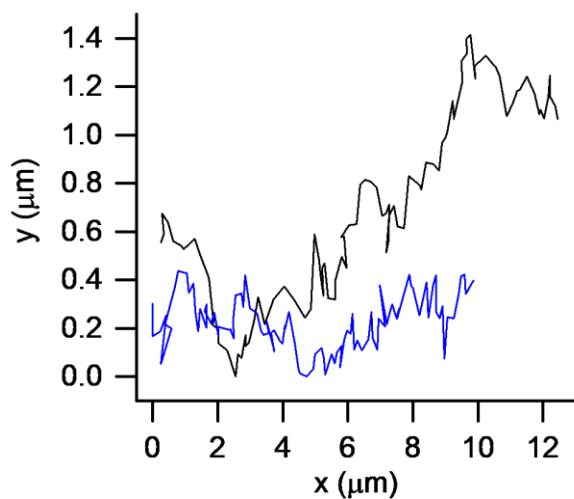


Figure SI-8. Zoomed trajectories (on y-positions) for two Janus Pt-MSN S_1 nanomotors at maximum fuel concentration tested (0.35%), where the random reorientations suffered by nanomotors are observed.

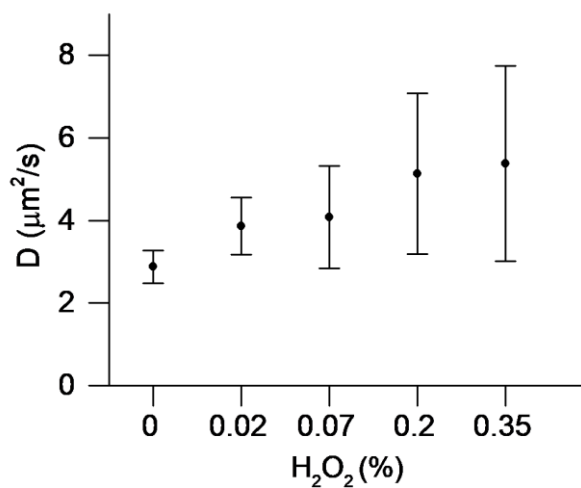


Figure SI-9. Diffusion coefficients determined from the MSD vs Δt equations (lineal and parabolic form) for the nanomotors at different fuel concentrations ($n=6$).

7.3. Control release studies

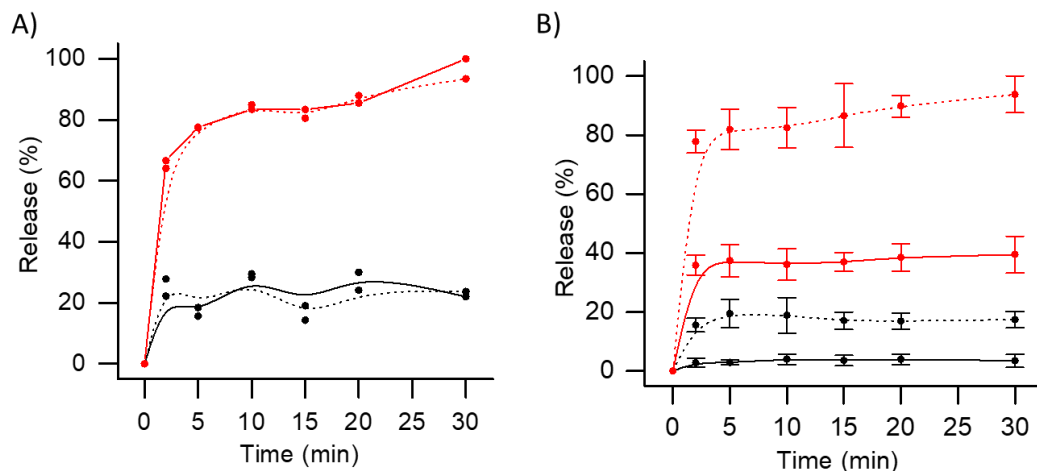


Figure SI-10. Normalized cargo release from Janus Pt-MSN nanomotors **S₁** under stirring conditions determined by measuring Ru(bpy)₃Cl₂ fluorescence (at 595 nm) (A) and normalized cargo release from nanomotors **S₂** in static conditions determined by measuring Doxorubicin fluorescence (at 555 nm) (B) vs time in aqueous solution (50 mM PBS pH 7.5), using: (a) nanomotors without GSH and without H₂O₂ addition, (b) 0.1% H₂O₂-propelled nanomotors without GSH addition, (c) nanomotors with 10 mM GSH addition and without H₂O₂, and (d) 0.1% H₂O₂-propelled nanomotors with 10 mM GSH addition. Values from four independent experiments.

7.4. Cell assays

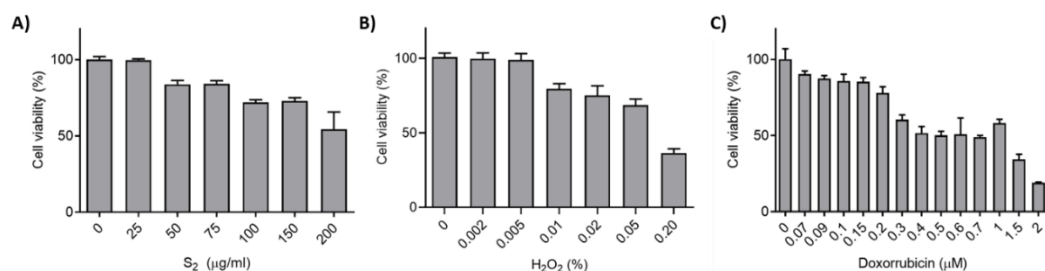


Figure SI-11. Viability of THP-1 cells after 24 h of incubation with **S₂** nanomotors (A), different concentrations of H₂O₂ (from 0 to 0.2%) (B), free Doxorubicin (C). Values from at least three independent experiments.

**Chapter III | Nanoparticle-mediated tumor
microenvironment remodeling favors the
communication with the immune cells for tumor killing**

Nanoparticle-mediated tumor microenvironment remodeling favors the communication with the immune cells for tumor killing

Elena Lucena-Sánchez^{a,b}, Francisco J. Hicke^a, Sandra Clara-Trujillo^{a,b}, Alba García-Fernández^{*a,b,c}, Ramón Martínez-Mañez^{*a,b,c,d}

^aInstituto Interuniversitario de Investigación de Reconocimiento Molecular y Desarrollo Tecnológico (IDM) Universitat de València–Universitat Politècnica de València, Camino de Vera s/n, 46022, Valencia, Spain.

^bUnidad Mixta UPV-CIPF de Investigación en Mecanismos de Enfermedades y Nanomedicina, Valencia, Universitat Politècnica de València, Centro de Investigación Príncipe Felipe, Valencia Spain

^cCIBER de Bioingeniería, Biomateriales y Nanomedicina, Instituto de Salud Carlos III

^dUnidad Mixta de Investigación en Nanomedicina y Sensores. Universitat Politècnica e València, Instituto de Investigación Sanitaria La Fe (IIS La Fe), Valencia Spain.

*Corresponding authors: algarfe4@upvnet.upv.es; rmaez@qim.upv.es

Published: February 23, 2024

(Reprinted with permission from Advanced Therapeutics, 2024, Feb 23. © Wiley-VCH GmbH 2021)

1. Abstract

Melanoma is one of the most common types of skin cancer with a bad prognosis and limited treatment options, especially in advanced stages. Recently, immunotherapy has changed the landscape of oncology. Cancer cells can activate various mechanisms to suppress immune responses, such as the immunological checkpoint PD-1/PD-L1, whose blockage reactivates immune-killing of melanoma cells. Moreover, exposure to inhibitory cytokines such as TGF- β induces T regulatory cell differentiation, which promotes cancer immunosuppression. Current advances in this area have provided exciting outcomes in the clinical treatment of melanoma, however, there are still limitations, and a combination of several treatments is usually needed. Based on the above, inhibition of the TGF- β production and the PD-1/PD-L1 checkpoint might be a feasible strategy to increase T cell infiltration and cytotoxicity and thus overcome tumor immune escape. In this work, mesoporous silica nanoparticles (MSN) loaded with a PD-L1 inhibitor (JQ1) and capped with polyethyleneimine (PEI) and a siRNA targeting TGF- β (TGF- β siRNA) are reported. An efficient PD-L1 downregulation and TGF- β silencing are achieved using the nanoparticles, along with the promotion of cancer death in pre-treated cells. This system demonstrates to be a specific and innovative therapeutic approach for the treatment of melanoma.

KEYWORDS: immunotherapy, melanoma, PD-L1, TGF- β , nanoparticles

2. Introduction

Melanoma is a malignancy of melanocytes and one of the most common types of skin cancer. It has been rated as one of the most aggressive cancers, due to its rapid metastasizes, frequently associated with poor clinical outcomes at late stages^{1,2}. Patients presenting the most disseminated form of this disease have very low survival rates (15%)

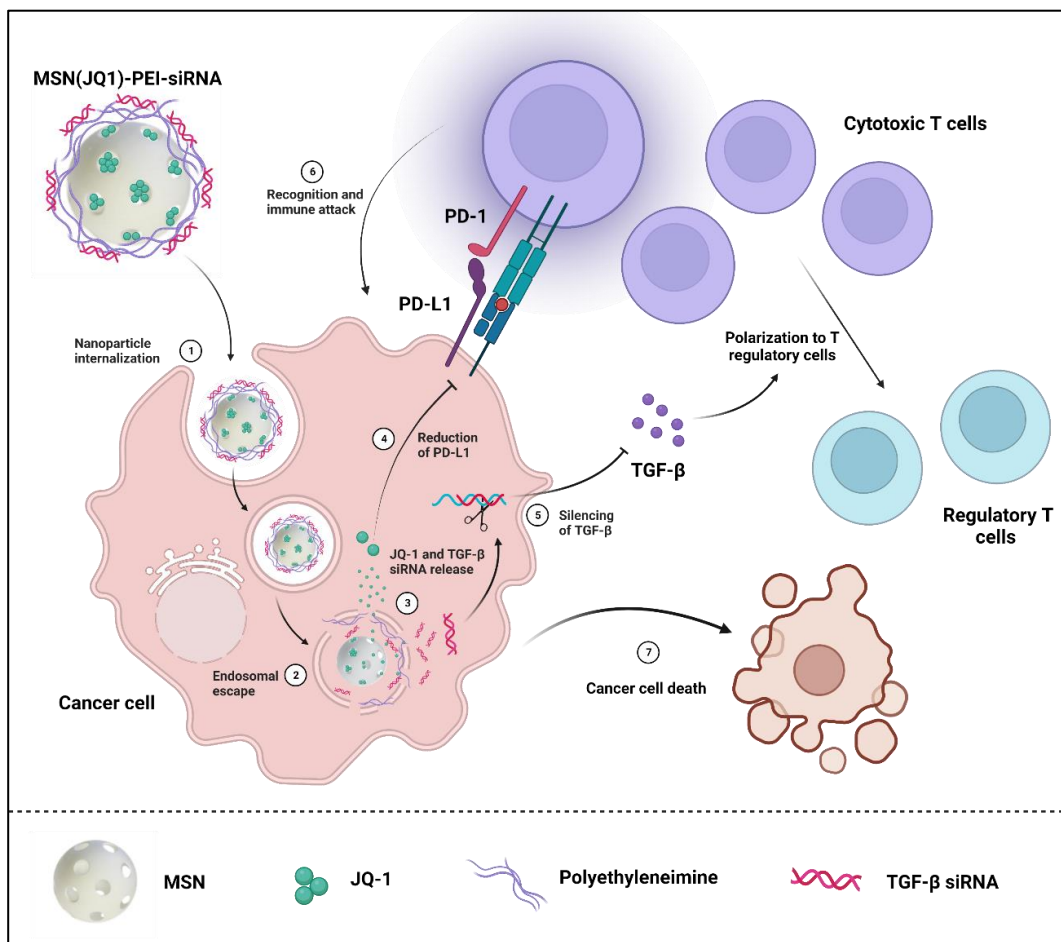
and highly restricted therapeutic alternatives. The treatment for advanced melanoma includes the use of chemotherapeutic drugs and resistance to antitumoral therapies is usually observed^{2,3}. In this scenario, targeted therapies and immunotherapy have arisen as promising approaches for the treatment of metastatic melanoma^{2,4}. In comparison with traditional therapies, these strategies improve the quality of life of the patient, increase the survival rate, and overcome dose-associated toxicity⁵. Especially, immunotherapy has gained tremendous attention as a powerful approach to cancer treatment, with a high potential for late-stage melanoma^{2,6-8}. Immunotherapy is based on the interaction between the immune system and cancer cells, mainly through surface molecules, to promote tumor cell death^{4,9}. Some of these molecules are immune checkpoints, which prevent autoimmunity and become essential to control immune system activity, especially that of the cytotoxic T cells¹⁰. In contrast, the activation of these immune checkpoints in cancer triggers the inhibition of immune responses against cancer and tumor escape from immunosurveillance barriers, thus favoring cancer progression^{2,10}. One of the most clinically relevant checkpoints is the programmed cell death ligand 1 (PD-L1). Several specific antibodies have been approved and widely used in clinics for patients with melanoma¹¹⁻¹⁴. Despite their ability to reactivate anti-tumor immunity, they have some disadvantages, such as a high price, instability in the bloodstream, low bioavailability, and the need for frequent injections¹⁵⁻¹⁷. Hence, small drugs inhibiting PD-L1 become promising candidates for cancer immunotherapy as well as overcoming antibodies-associated instability. One of these molecules is JQ1, a freshly discovered specific inhibitor for BET bromodomains, causing a dramatic decline in PD-L1 expression (Scheme 1)¹⁸⁻²⁰.

Even though the advantages of immunotherapy, not all patients respond to these therapies, and most immune treatments involve the combination of different strategies². In the case of melanoma, given its complexity, the influence of the tumor microenvironment on both cancer and immune cells must be considered. Melanoma cells have been adapted to secrete cytokines and growth factors, favoring an active tumor

microenvironment that plays a crucial role in cancer cell survival and immune evasion^{21,22}. Under normal conditions, the transforming growth factor beta, TGF- β , is important to control T cell homeostasis by inhibiting cell proliferation and activation. However, large amounts of TGF- β are produced during tumor progression and act as an immunosuppressive cytokine, driving T cell polarization to T regulatory subtypes, which contributes to tumor immune escape²²⁻²⁴. The most common strategy to prevent TGF- β suppression is the blockage of TGF- β receptors in T cells. However, this could deregulate immune homeostasis and have detrimental effects, such as inflammatory complications, due to its importance in T-cell development and survival^{25,26}. Bearing all this in mind, the downregulation of TGF- β production in tumor cells can be a safer strategy, may restore anti-tumor immunity and reduce undesired side effects²³. Small interfering RNAs (siRNA) have been assessed in clinical trials and seem to be an effective tool for the suppression of TGF- β (Scheme 1)²².

Here, we propose a combined strategy for modulating the communication between tumor cells and their metabolic and immune microenvironment to restore anti-tumor immunity through nanomedicine (*vide infra*). In this context, nanotechnology offers a variety of tools capable of transporting different therapeutic agents, both alone and in combination, and breaking with the immunotherapy limitations related to poor bioavailability, dose-limiting toxicity, and immune-mediated side effects^{2,5,27-29}. In this scenario, a large variety of delivery systems have been developed from liposomes³⁰, polymeric nanoparticles³¹, inorganic nanoparticles³², and metal-organic frameworks³³ to achieve cancer elimination by the immune system. Among them, mesoporous silica nanoparticles (MSNs) have been extensively explored as a multiplatform and have been applied in cancer immunotherapy^{5,34}. MSNs are good candidates for immunotherapy considering their unique features, such as stability, large and easily modifiable surface area, high porosity, high loading capacity, good biocompatibility, and self-adjuvanticity^{27,35,36}. Remarkably, MSNs can hold inside a variety of molecules of different polarities and

sizes and their surface can be modified with a range of (bio)molecular ensembles (known as gatekeepers or molecular gates) to control drug transport and achieve sustained control release^{35,37–39}. Besides, mesoporous gated materials preserve the cargo overcoming issues such as poor solubility, instability, frequent injections required, or undesired side effects^{17,40}, and its release can be triggered on command and spatiotemporally, by chemical⁴¹, physical¹⁹, and biochemical stimuli⁴².



Scheme 4. Design of MSN(JQ1)-PEI-siRNA nanodevice to overcome tumor escape from immune system. MSNs were loaded with JQ1 and capped with PEI and TGF- β siRNA. JQ1 is a specific inhibitor that blocks PD-L1 expression and TGF- β siRNA induces the degradation of TGF- β mRNA. It allows tumor recognition and cancer cell death by T cells.

From another point of view, MSNs are a versatile platform that can be also coated with different molecules to incorporate additional functionalities, such as enhancing selectivity to target cells or accomplishing an efficient cargo delivery inside the cells^{37,43}. This occurs especially with nucleic acids, such as siRNAs, which are prevented from entering cells due to their negative charge and present very poor stability in biofluids²¹. The functionalization of MSNs with positively charged polymers, like polyethyleneimine (PEI), has been widely described as an efficient strategy for acid nucleic delivery^{44–47}. Further, PEI-coated nanoparticles possess the capability of initiating endosomal escape before the degradation of the genetic molecules in endolysosomes, thus achieving cytosolic delivery of the nucleic acids^{46,48}.

Based on the above, we envisioned MSNs as excellent candidates for the synergistic delivery of therapeutic agents, necessary to enhance anti-tumor immunity in melanoma. In particular, we have developed a mesoporous silica nanodevice capable of simultaneously delivering the JQ-1 drug and TGF- β siRNA to restore tumor elimination from the immune system. High drug loading and siRNA protection are both achieved with nanoparticles while allowing a controlled codelivery in tumor cells. Cell treated with the nanoparticles exhibited a PD-L1 expression downregulation, as well as depletion in TGF- β production. The combined strategy effectively modulates the tumor microenvironment resulting in the defeat of tumor hideout and thus the restoration of anti-tumor immunity, evidenced by melanoma/T cell cocultures. Taken together, our findings demonstrate the potential of this combined strategy for reversing the immunosuppressive microenvironment in melanoma. Besides, this research evidences the use of MSNs as a powerful multiplatform for cancer immunotherapy by allowing expression-modifiable elements and drug-therapy combinations to overcome common limitations of immunotherapy.

3. Results and discussion

3.1. Design, synthesis, and characterization of nanodevices

MSNs were used as an inorganic scaffold due to their singular properties, including a high loading capacity, large surface area, and easily functionalizable surface. The pores of nanoparticles were loaded with the JQ1 drug, which is a BET bromodomain inhibitor that downregulates PD-L1 expression at the transcriptional level. Then nanoparticles were capped with a polyethyleneimine (PEI) layer through electrostatic interactions, yielding MSN-PEI and MSN(JQ1)-PEI. PEI is a positive polymer composed of repeating units with an amine and two carbon aliphatic spacers that interacts with the negatively charged surface of the nanoparticles. Finally, a second layer of a pre-designed TGF- β siRNA was included on the MSN(JQ1)-PEI surface to obtain the final nanoparticles MSN(JQ1)-PEI-siRNA (Figure 1A). PEI polymer was used because (1) it is known to provide a suitable strong positive layer to coordinate negative nucleic acids, including RNAs, and (2) in cells leads to endosomal rupture and release of RNAs to the cytoplasm⁴⁹. Similar nanoparticles containing a fluorescent siRNA not binding to any known gene, BlockiT, were also prepared as a control (MSN(JQ1)-PEI-BlockiT) as well as unloaded nanoparticles containing the TGF- β siRNA (MSN-PEI-siRNA). A scheme showing the structure of the nanodevices synthesized is represented in Table S1 in the Supplementary Information.

Nanoparticles were characterized by standard procedures, powder X-ray diffraction (PXRD), TEM, N₂ adsorption-desorption curves, DLS, and zeta potential. PXRD patterns of as-made MSNs show four low angles reflections of typical Bragg peaks of mesoporous materials with a hexagonal arrangement of pores, indexed as (100), (110), (200), and (210). As a result of calcination and surfactant elimination, a displacement and widening of the peaks owing to silanol groups' condensation and unit cell contraction can be appreciated (Figure S1). TEM images (Figure 1B) show the presence of spherical nanoparticles with an average size of ca. 100 nm containing mesopores as white channels.

The porous structure was also confirmed by N₂ adsorption-desorption isotherms of empty MSNs and JQ1-loaded and capped MSNs (MSN(JQ1)-PEI) (Figure S2). For the starting calcined MSNs, type IV isotherms with a BET-specific surface area of 906.68 m²/g, pore volume of 0.65 cm³/g, and pore size of 2.86 nm, typical of mesoporous silica materials, was determined. In contrast, no absorption step was observed for MSN(JQ1)-PEI, that showed a BET-specific surface area of 27.71 m²/g, which confirmed that the mesopores were filled and capped. The JQ1 content was determined by HPLC studies in four independent experiments, resulting in a loading amount of 53.09 ± 7.59 µg JQ-1/mg MSNs (loading efficiency of 42.8%).

Subsequently, the siRNA binding capacity of the nanoparticles was studied. Hence, TGF-β siRNA was incubated with PEI-coated MSNs and the supernatants of the reaction were subjected to an electrophoretic assay. The most optimal ratio turned out to be 1:25 (siRNA/PEI-coated MSNs) since no siRNA was detected in the gel, supporting that all siRNA molecules had been attached to MSNs (Figure 1. C). The proper assembly of TGF-β siRNA in the final nanodevices MSN-PEI-siRNA and MSN(JQ1)-PEI-siRNA, was also confirmed by the same method. Figure 1.D shows an electrophoretic assay in which free TGF-β siRNA is detectable in lane 1, while it is practically undetectable in the supernatants from mixtures of TGF-β siRNA with MSN-PEI and MSN(JQ1)-PEI (Figure 1.D).

In addition, the different steps in the synthesis of the final nanoparticles were monitored by DLS and zeta potential (Figure 1). The presence of a distinct peak in the size distribution curves, as well as values of polydispersity index (PDI) ranging from 0.1-0.3, confirmed the monodispersity of our nanoparticles in aqueous solutions (Figure 1.E). The hydrodynamic diameter of MSNs started in 146.73 ± 0.55 nm and increased by 30-40 nm after PEI assembly. The siRNA attachment also expanded the diameter, up to 285.9 ± 4.78 nm in the case of MSN(JQ1)-PEI-siRNA. Zeta potential changed from a negative value of -

41.12 ± 1.54 mV, characteristic of MSNs, to 39.58 ± 1.76 mV for MSN(JQ1)-PEI and to 30.67 ± 0.92 for MSN(JQ1)-PEI-siRNA (Figure 1. F).

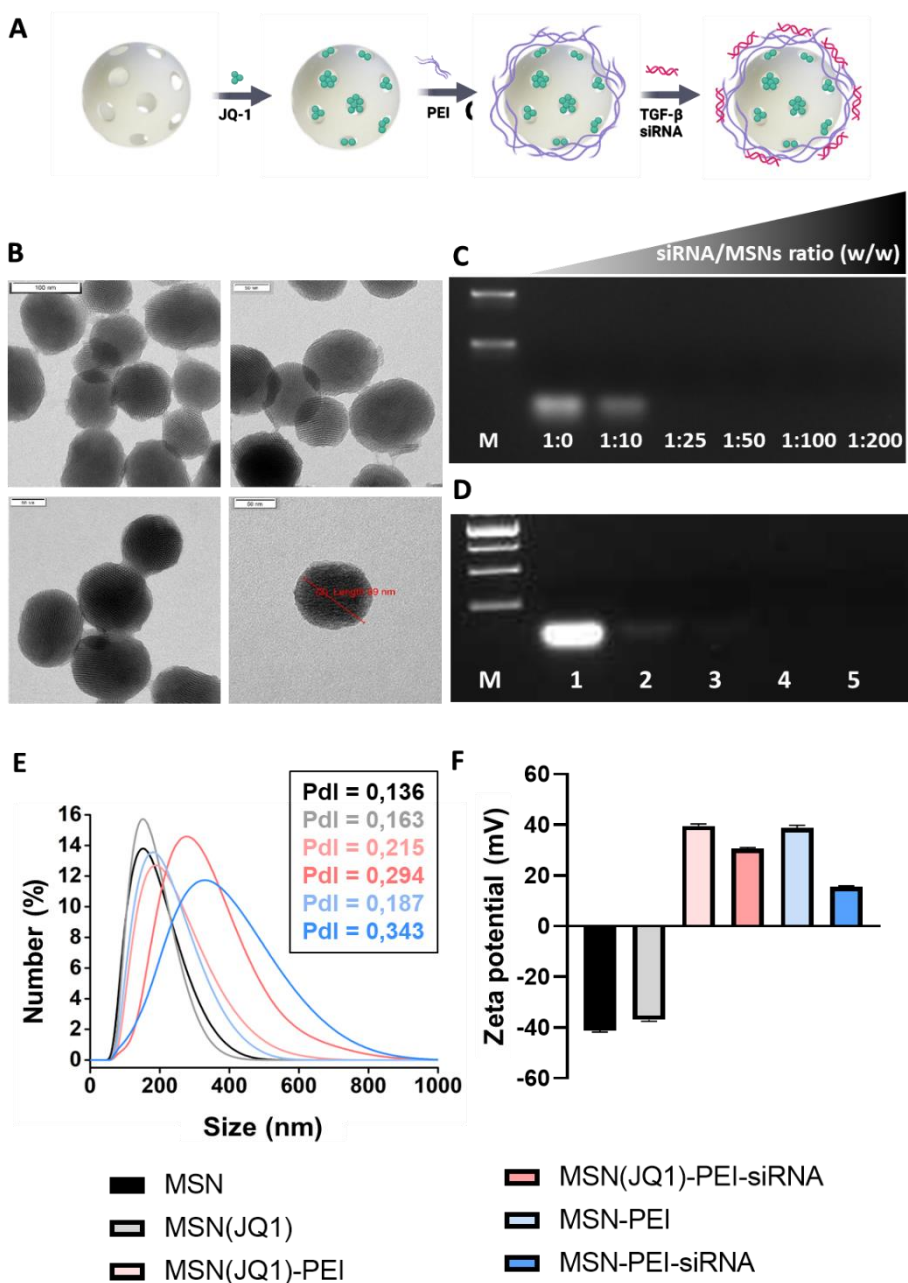


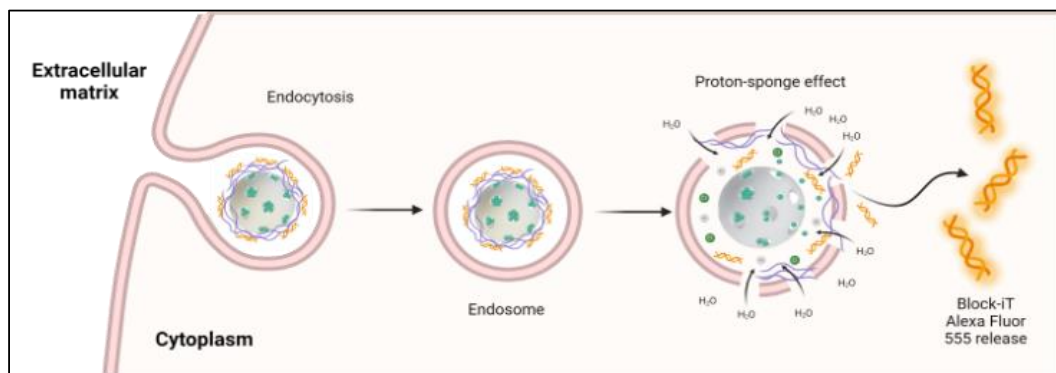
Figure 1. A) Schematic representation of MSN(JQ1)-PEI-siRNA synthesis. B) TEM images of MCM-41 type calcined nanoparticles (MSN). The dispersion of the particles along with their typical hexagonal porosity and pore arrangement is displayed. The size of MCM-41 can also be appreciated, which is around 100 nm. C) Gel electrophoresis assay of supernatant from siRNA/MSN-PEI reaction optimization at different siRNA/MSN-PEI

ratios. D) Gel electrophoresis assay of supernatant from different solids and siRNA reaction at 25:1 ratio (lane 1: free TGF- β siRNA, lane 2: MSN(JQ1)-PEI-siRNA, lane 3: MSN-PEI-siRNA, lane 4: MSN(JQ1)-PEI, lane 5: MSN-PEI). E) Hydrodynamic size distribution and Pdl values determined by dynamic light scattering. F) Zeta potential of different solids. Values are expressed as mean \pm SEM (n=3). (Figure 1.A. was created by the authors on Biorender).

3.2. MSN(JQ1)-PEI-siRNA nanoparticles are efficiently internalized with the subsequent siRNA delivery

It is widely described that MSNs are internalized by cells through endocytosis being the clathrin-mediated endocytosis the main pathway. This process involves the formation of clathrin-coated vesicles able to fuse with endosomes that are finally transferred into lysosomes^{50,51}. Moreover, to achieve siRNA delivery to the cytosol the nanoparticles must scape from the endosomes. To achieve endosomal escape, the nanoparticles were coated with PEI, which is known to acts as a “proton sponge” due to protonation at acidic pH resulting in endosome breakdown and siRNA delivery into the cytosol (Figure 2. A). To demonstrate the endosomal escape and thus siRNA delivery, MSN(JQ1)-PEI nanoparticles were linked to BlockiT, an Alexa red fluorescent RNA molecule that is not homologous to any known gene (to give MSN(JQ1)-PEI-BlockiT). Then, cells were treated with MSN(JQ1)-PEI-BlockiT at 15 μ g/ml for 48 h and with a lysosomal marker (LysoTracker Green DND-26) for 1 h. A red fluorescent signal (associated with RNA BlockiT) near the lysosomes (in green) was only observed in cells treated with the nanoparticles. The confocal microscopy images barely showed overlapping signals between lysosomes and the red fluorescent RNA, which is preferentially situated in the cytoplasm (white arrows) (Figure 2. B), with Pearson’s correlation coefficients (Rr) of 0.4863 ± 0.0464 . The results confirmed the proper uptake of the nanoparticles by melanoma cells, PEI-mediated endosomal escape, and siRNA delivery into the cytoplasm.

A



B

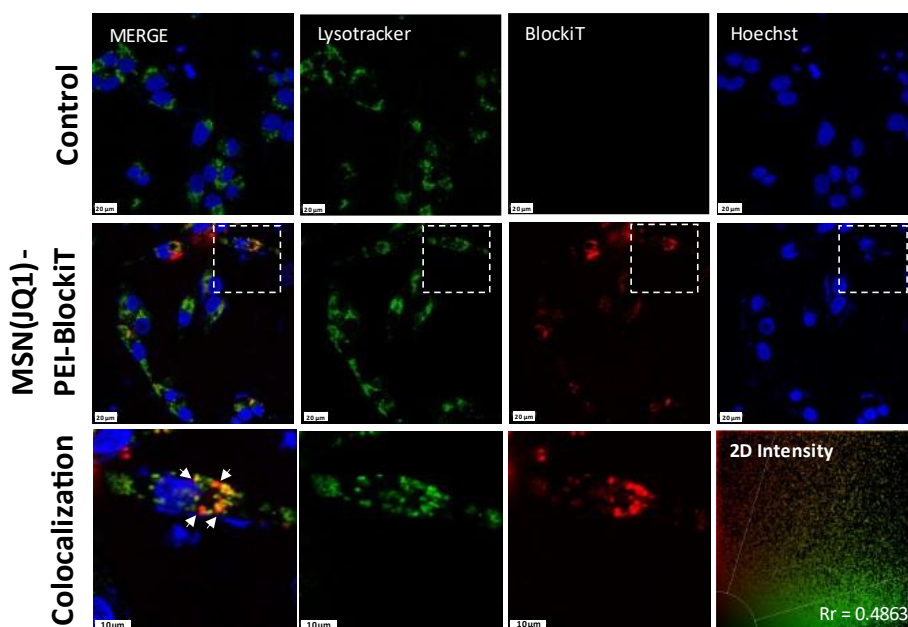


Figure 2. A) Scheme of fluorescent Block-iT Alexa Fluor Red release by MSN(JQ1)-PEI-Block-iT. B) Representative confocal images of control vs. intracellular MSN(JQ1)-PEI-Block-iT localization and endosomal escape after 48h (top images). Enlargement of inset area from M(JQ1)-PEI-Block-iT treated cells in the different channels showing the colocalization (bottom images). Pearson's colocalization coefficient (Rr), provided in the column of two-dimensional intensity, represents a correlation between pixel intensities between trimers and tracker channels in the close-up image. Nanoparticles in red, Lysosomes marker (Lysotracker Green DND-26) in green, and nuclei marker (Hoechst) in blue. Nanoparticles inside the cells in which endosomal escape occurred were pointed by white arrows. Scale bar: 20 μm ; enlargements 10 μm . (Figure 2. A was created by the authors on BioRender.com).

3.3. MSNs as a versatile nanosystem for the codelivery of JQ-1 and TGF- β siRNA

Several works reported the range of JQ-1 concentration which achieves a significant reduction in PD-L1^{19,20,52–54}. In order to prove it, two concentrations of JQ-1 (1 and 2 μ M) were tested in A375, and PD-L1 expression was evaluated by western blot (Figure S3). The results were as expected; a significant decrease in PD-L1 with both concentrations. Then, to assess the ability of nanoparticles containing JQ1 to reduce PD-L1 expression, A375 cells were treated for 48h with 1 μ M free JQ1 or JQ1 encapsulated in MSN(JQ1)-PEI or MSN(JQ1)-PEI-siRNA at an equivalent JQ1 concentration (8.62 μ g/mL of nanoparticles) and PD-L1 expression was evaluated (Figure 3). Western blot results showed that PD-L1 expression is significantly reduced (4-fold) in cells when they were treated with JQ1, both alone and encapsulated on MSNs (Figure 3. A, and 3. B). Further, the reduction was similar in MSN(JQ1)-PEI and MSN(JQ1)-PEI-siRNA, which demonstrates that TGF- β siRNA has no effect in PD-L1 expression and confirms that the responsible for PD-L1 reduction is JQ1. Besides, these findings were confirmed by flow cytometry, which shows 30% fewer positive PD-L1 cells upon treatment with JQ-1 (Figure 3. C) and a decrease in fluorescence intensity (corresponding to PD-L1 expression per cell) (Figure 3.D). No significant differences were observed when cells were treated with nanoparticles without JQ1 (MSN-PEI and MSN-PEI-siRNA) compared to control group. Overall, the results confirmed that JQ-1 drug is responsible of PD-L1 decreased expression and otherwise, levels of PD-L1 are maintained at the same order when it is absent.

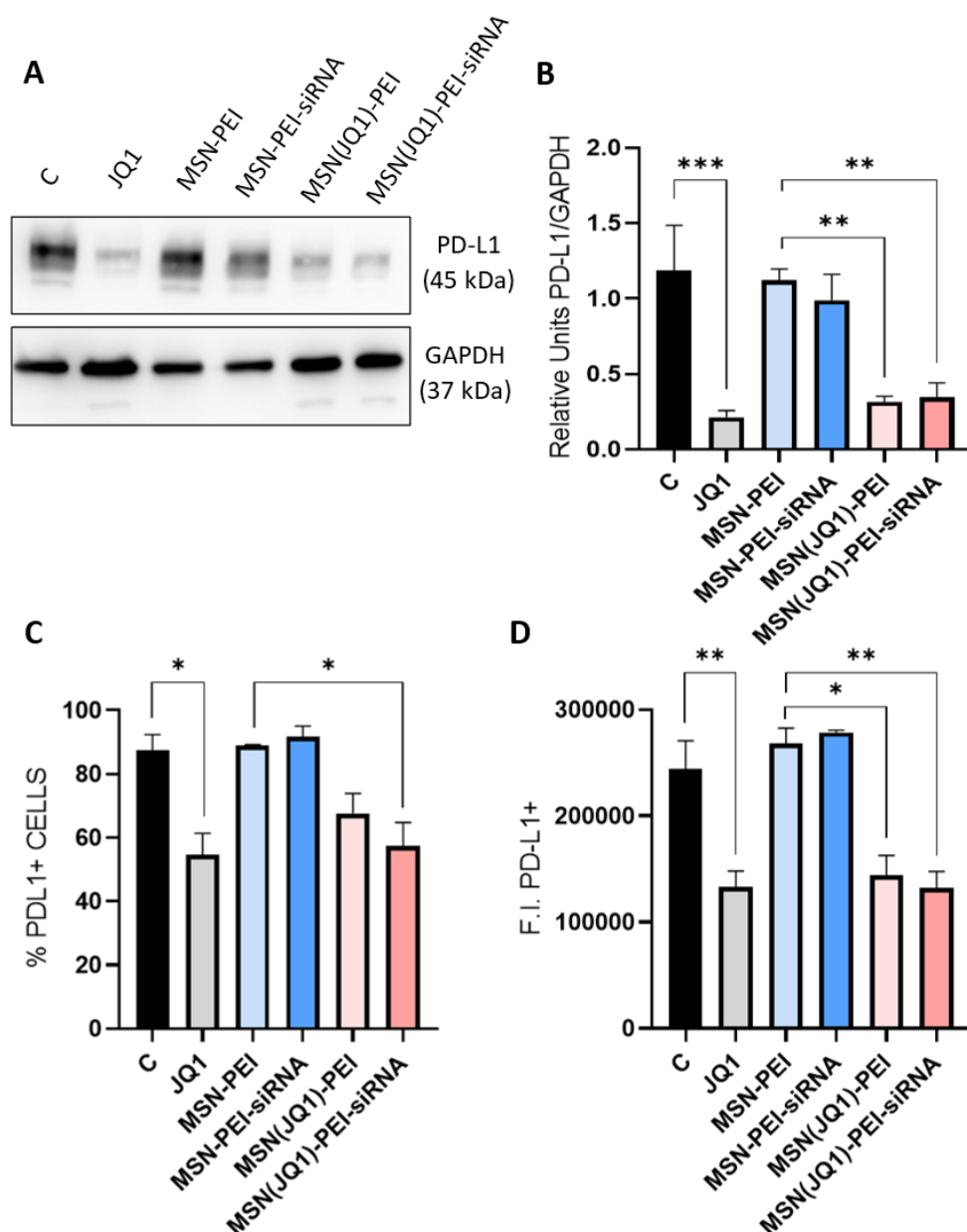


Figure 5. A) Western Blot analysis of PD-L1 expression in A375 cells with different treatments for 48h (expected band 45 kDa). GAPDH (37 kDa) was included as a loading control. B) Quantification of ratio protein expression versus internal reference (GAPDH). The results show a decrease in PD-L1 expression only with free JQ1 and solids loaded with JQ1 (MSN(JQ1)-PEI and MSN(JQ1)-PEI-siRNA). C) Percentage of PD-L1 positive cells after a 48h treatment determined by flow cytometry. D) Fluorescence intensity of PD-L1 positive cells. Decreased PD-L1 expression induced by JQ1 was confirmed. Values are expressed as mean \pm SEM ($n \geq 3$), and statistical significance was assessed by One-way ANOVA followed by Tukey's post-tests were performed to calculate the statistical significance of the results: * $p < 0.05$; ** $p < 0.01$; *** $p < 0.001$ ($n \geq 3$).

On the other hand, the ability of siRNA-bearing nanoparticles to silence TGF- β in A375 was also studied. Cells were incubated with three different concentrations of MSN-PEI-siRNA and MSN(JQ1)-PEI-siRNA nanoparticles (4.31, 8.62, and 17.24 $\mu\text{g}/\text{mL}$) corresponding to different TGF- β siRNA concentrations (12.96, 25.92, and 51.84 nM respectively) for 48 h and TGF- β production was analyzed in the supernatant by ELISA. Besides, TGF- β siRNA transfection was carried out with lipofectamine, widely used for the in vitro delivery of nucleic acids, as a control (named TGF- β siRNA). The results show a significant reduction of TGF- β levels with all the tested concentrations of MSN-PEI-siRNA or MSN(JQ1)-PEI-siRNA nanoparticles (Figure 4). In addition, we confirmed a remarkable knockdown in TGF- β expression (up to 50%) with nanoparticles at the previously tested JQ-1 concentration of 1 μM (corresponding to condition 1 in Figure 4)^{19,20}. Thereby, MSN(JQ1)-PEI-siRNA is an effective nanocarrier to achieve siRNA transport and effectively achieving cytoplasm delivery to develop its function.

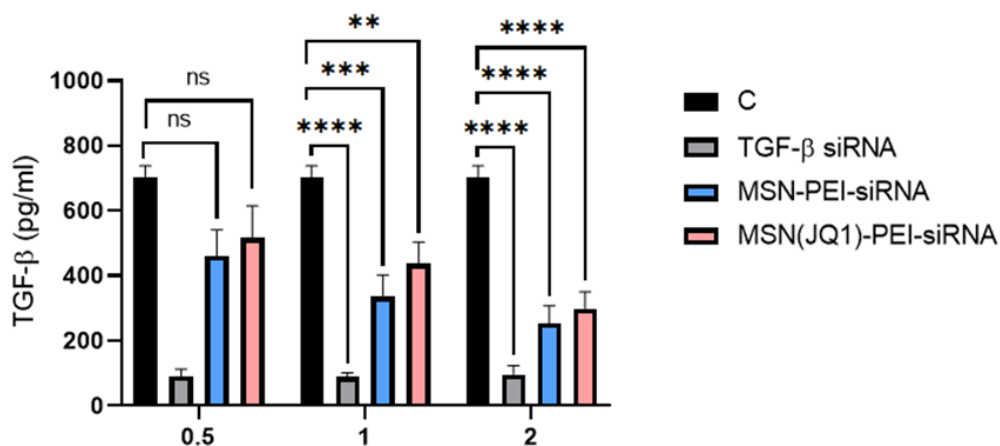


Figure 6. TGF- β levels (pg/ml) in A375 cells supernatant after transfection with free siRNA (concentrations 12.96 nM (0.5), 25.92 nM (1) and 52.84 nM (2)) or treatment with MSN-PEI-siRNA or MSN(JQ1)-PEI-siRNA at equivalent concentrations of nanoparticles (4.31 $\mu\text{g}/\text{ml}$, 8.62 $\mu\text{g}/\text{ml}$ and 17.24 $\mu\text{g}/\text{ml}$ respectively). These concentrations correspond to 0.5, 1 and 2 μM of JQ1 encapsulated respectively. Values are expressed as mean \pm SEM from at least three independent experiments, and statistical significance was assessed by Two-way ANOVA followed by Tukey's post-tests were performed to calculate the statistical significance of the results: ** $p < 0.01$; *** $p < 0.001$; **** $p > 0.0001$ ($n \geq 3$).

3.4. The codelivery of JQ-1 and TGF- β restores cancer cell death

Before moving to study the effect of the final nanoparticles MSN(JQ1)-PEI-siRNA, we tested the possible toxic effect of the combined therapy and nanoparticles in melanoma cells. The A375 cells were treated with free JQ1 at 1 μ M, MSN-PEI or MSN(JQ1)-PEI-siRNA at 8.62 μ g/mL (equivalent to 1 μ M of JQ1 and 25.92 nM of siRNA). After 48 h, cell viability was studied by WST-1 (Figure 7. B) or by the CellTiter assay (Figure S4). In all cases cell viability remained at 100%, thus discarding any toxic effect of the treatments and confirming the suitability of the proposed combined therapy using MSNs.

In a second step, considering the well-known role of PD-L1 expression and TGF- β production in immune evasion of tumor cells and the effective modulation of both by MSN(JQ1)-PEI-siRNA, we attempted to discover how this nanodevice would affect T-cell-triggered tumor cell death. For this purpose, a co-culture assay was carried out using A375 melanoma cells and Jurkat T cells as a model of T lymphocytes. Cultured A375 cells were treated with free or encapsulated JQ-1 and TGF- β siRNA, before being co-cultured with activated Jurkat T cells (15-fold excess in A375 cell number) and cell viability was assessed by Cell proliferating reagent WST-1. As Figure 7. C reveals, when Jurkat T cells were incubated with untreated melanoma cells any cytotoxic effect was observed, which can be ascribed to the immunosuppressive environment developed by cancer cells. Similarly, no effect was found when cells were treated with TGF- β siRNA or MSN-PEI. In the case of JQ1 administered free a slight reduction of cancer cell viability (75%) was observed. In addition, this effect was reinforced with the use of MSN(JQ1)-PEI-siRNA which reduces cell viability to values lower than 50%. This suggests that efficient PD-L1 downregulation and TGF- β silencing by using MSN(JQ1)-PEI-siRNA restores tumor cell recognition by T cells along with the promotion of cancer death. The observations support the potential of MSN as a scaffold for carrying and delivering TGF- β siRNA and JQ1 drug as a combined therapy. Further, this combination has been demonstrated to be the most effective in promoting efficient T-cell killing of melanoma cells.

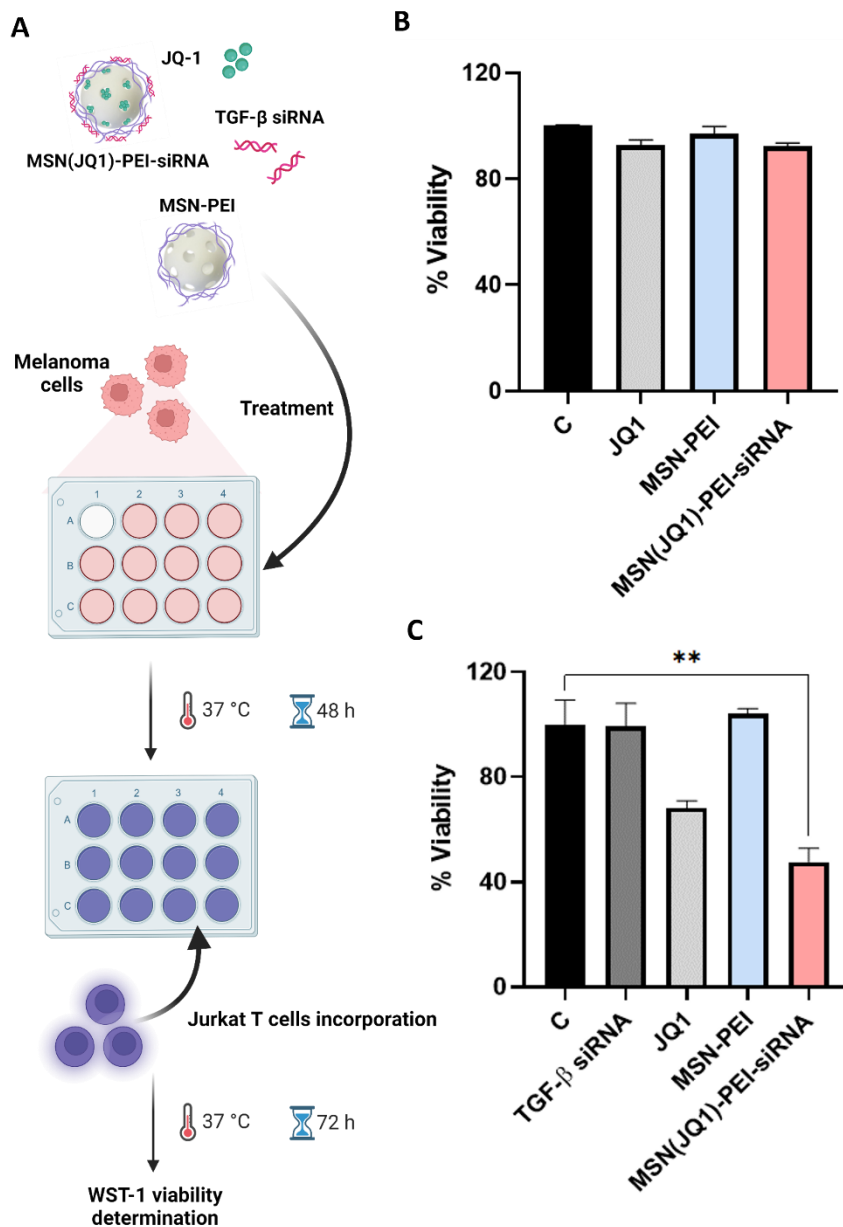


Figure 7. A) Schematic representation of coculture experiment to evaluate cancer immunogenic cell death. B) Cytotoxicity profile of free JQ1 (1 μ M) and equivalent concentration of different solids (8,62 μ g/ml) in A375 cells at 48h using WST-1 cell viability assay. The data represent the mean \pm SEM. C) Cell viability assay in A375 cells pretreated with free siRNA (25.92 nM), JQ1 (1 μ M) or different solids (8.62 μ g/ml) for 48h and then, cocultured with Jurkat cells at a ratio 1:15 for 72h. Data show the mean \pm SEM (n=3). The statistical significance was studied by One-way ANOVA followed by Tukey's post-tests to calculate the statistical significance of the results: *p<0.05; **p<0.01 (n \geq 3). (Figure 7.A.. was created by the authors on Biorender).

4. Conclusions

In summary, we report herein a mesoporous silica-based nanodevice for efficiently co-delivering a payload and a siRNA in cells as a novel immunotherapeutic approach in melanoma. In particular, the nanodevice consists of MSNs loaded with the PD-L1 inhibitor JQ1 and capped with the polymer PEI and TGF- β siRNA (MSN(JQ1)-PEI-siRNA). The nanoparticles are characterized using well-known standard techniques. PEI in the nanoparticles induces endosomal escape and effective siRNA delivery in melanoma cells. Besides, MSN(JQ1)-PEI-siRNA effectively achieves a reduction in PD-L1 expression and TGF- β production in melanoma cells. Finally, T-cell-mediated killing assays reveal the potential of the combined strategy to eliminate melanoma cells. The effective modulation in tumor plasticity allows to avoid immune escape mechanisms as well as to restore the recognition and attack by T-cells, which finally elicits tumor cell death.

Considering the need for combined therapeutic strategies to overcome tumor escape mechanisms from immunosurveillance, MSNs are a potential platform for a one-shot treatment capable of protecting siRNAs, increasing bioavailability, and generating self-adjuvant. Despite the complex tumor microenvironment, the combination of two therapeutic agents in a single nanoparticle enables the reactivation of the anti-tumor immune response and is a boost for cancer immunotherapy^{55,56}. The field of cancer immunotherapy is still in the early stage and there are still many challenges and questions to elucidate. It is expected that nanotechnology will provide insight into the development of new advanced cancer immunotherapy in a near future with the potential for clinical application^{5,56}.

5. Materials and methods

5.1. General methods

For materials characterization, we used transmission electron microscopy (TEM), powder X-ray diffraction (PXRD), N₂ adsorption-desorption isotherms, Zeta potential, dynamic light scattering (DLS), and 1/MSD Triple Quadrupole system (Agilent Technologies, USA). PXRD measurements were performed on a Seifert 3000TT diffractometer using Cu K α radiation. TEM images were acquired using an FEI Tecnai Spirit G2 microscope operating at 80 kV with a digital camera. The N₂ adsorption-desorption isotherms were captured using an automated analyzer Micromeritics TriStar II Plus. A Zetasizer Nano ZS device (Malvern Instruments, Malvern) was employed to measure the zeta potential and it was calculated from the particle mobility values by applying the Smoluchowski model. Dynamic light scattering (DLS) studies to assess particle size were performed in a Malvern Zetasizer Nano ZS instrument. Cell viability and ELISA measurements were taken with a Wallac 1420 workstation. Confocal microscopy imaging was performed with a Leica TCS SP8 HyVolution II (Leica Microsystems Heidelberg GmbH, Heidelberg, Germany) inverted laser scanning confocal microscope.

5.2. Synthesis of MSNs MCM-41 type

Mesoporous silica nanoparticles were synthesized using CTAB as a templating agent⁵⁷. 2.74 mmol of CTAB (Sigma) dissolved in deionized water (480 ml) was magnetically stirred and mixed with 3.5 ml of NaOH (Scharlab) 2M. The temperature was increased to 80 °C and 5 ml of the silica precursor, tetraethylorthosilicate, TEOS (Sigma), was added drop by drop. This solution was maintained under agitation for 2h at 80 °C. After that, centrifugation at 10,000 rpm for 20 min was used to isolate the white solid, and the pH solution was neutralized by washing it with deionized water. Finally, the white solid was dried overnight, referred to as MSNs “as made”, and then, to obtain the final

mesoporous nanoparticles (MSNs), the CTAB was removed by calcining the material at 550 °C under an oxidant atmosphere for 5 h.

5.3. Preparation of MSN(JQ1)-PEI and MSN-PEI nanoparticles

To load the pores with the JQ1 drug (Eurodiagnostico), an impregnation method was employed^{19,58}. First, JQ1 was dissolved in ethanol (Scharlab) (12.4 mg in 1 ml) and then, added to calcined nanoparticles. The MSNs (100 mg) were spread out on a plate and 500 µL of JQ-1 solution was added dropwise. The plate was placed in the heater and MSNs dried at 37 °C. Once dried, the protocol of impregnation was repeated with the rest of the JQ-1 solution. Afterward, JQ1-loaded MSNs (MSN(JQ1)) or empty MSNs (MSN) were suspended in PBS (1 ml) and 50 mg of polyethyleneimine (PEI) dissolved in PBS (4 ml) (Sigma) was added. The mixture was stirred at room temperature for 3 h and then, the nanoparticles were separated by centrifugation and rinsed twice with PBS. Finally, the solid MSN(JQ1)-PEI or MSN-PEI was dried at 37 °C.

5.4. Quantification of JQ1 delivered

To quantify the encapsulated drug, 5 mg of MSN(JQ1)-PEI were suspended in 0.5 mL of 100 mM PBS at pH 4. Mixtures were stirred in a shaker at 30 °C and 900 rpm for 1 h. Then, the samples were centrifuged to remove the unanchored molecular gate in the supernatant. Afterward, 0.5 ml of acetonitrile were added and incubated for 1 h at 900 rpm. The supernatant was collected and diluted 1:100 in acetonitrile. LC/MSD analysis was carried out with a mobile phase of acetonitrile:water (70:30) at a flow rate of 0.3 ml/min. Linearity was obtained from 0.5 to 10 µg/ml with a limit of detection of 0.149 µg/ml and a limit of quantification of 0.453 µg/ml.

5.5. Assembly optimization of TGF- β siRNA to PEI-coated MSNs

To assess the optimal ratio of siRNA binding to MSNs, TGF- β siRNA (Sigma, NM_000660) and MSN-PEI at different ratios (1:0, 1:10, 1:25, 1:50, 1:100, 1:200) were mixed in DNase free H₂O (Invitrogen, 11538646) and stirring for 30 min at 37 °C. Next, nanoparticles were centrifuged, and supernatants were collected and loaded in agarose gel to assess the binding efficiency. The siRNA was detected via ethidium bromide staining. The TGF- β siRNA was created using the proprietary Rosetta Inpharmatics siRNA Design algorithm (Seq.5'-3': GCAACAAUCCUGGCGAUA).

5.6. Synthesis of MSN(JQ1)-PEI-siRNA, MSN-PEI-siRNA, and MSN(JQ1)-PEI-BlockiT

Once the optimal ratio has been determined, we proceed to obtain the final MSN(JQ1)-PEI-siRNA. Besides, empty nanoparticles (without JQ1 cargo), MSN-PEI-siRNA, and nanoparticles containing a fluorescent siRNA not homologous to any known gene, MSN(JQ1)-PEI-BlockiT, were also prepared. In all cases, 1 mg of PEI-coated nanoparticles were dispersed into DNase-free H₂O (1 ml) and 30 μ L of TGF- β siRNA stock (100 μ M) or BlockiT Alexa Fluor Red (Sigma, 14750100) stock were added. The mixtures were incubated at 12,000 rpm and 37 °C for 30 min. Last, siRNA-bearing nanoparticles were collected via centrifugation, and supernatants were saved to confirm the absence of siRNA and the correct binding to nanoparticles.

5.7. Cell culture conditions

The A375 malignant melanoma cell line was purchased from ATCC. Cells were maintained in DMEM (Sigma, D6429), supplemented with 10% FBS (Sigma), and incubated in 5% CO₂ at 37 °C. The human Jurkat T lymphocyte cell line was acquired from ATCC. Cells

were maintained in RPMI (Sigma, R8758), supplemented with 10% FBS, and incubated in 5% CO₂ at 37 °C.

5.8. Toxicity studies

A375 cells were seeded at a cellular density of 30,000 cells/well in a 96-well plate and subjected to various treatments, free JQ1 at 1µM, MSN-PEI and MSN(JQ1)-PEI-siRNA at 8.62 µg/ml (equivalent to 1µM of free JQ1). These concentrations correspond to those used in the rest of the experiments. After 48h of incubation, the cell viability was determined using the cell proliferation reagent WST-1 (Sigma, 11644807001) for 1 h and measuring the absorbance at 595 nm in a Wallac 1420 workstation. In parallel, the same experiment was performed, and the viability was determined by measuring ATP using the CellTiter-Glo Cell (Promega, G7571) Viability Assay. The substrate was added and incubated for 10 min and the cell viability signal was determined by luminescence.

5.9. Endosomal escape

To verify PEI-induced endosomal escape, the A375 cells were harvested on glass coverslips in 6-well plates and allowed to attach for 24h at 37 °C. Then, MSN(JQ1)-PEI-BlockiT were added and incubated for 48h. After that, cells were incubated in the presence of a green lysotracker (LysoTracker Green DND-26 from Thermo Fisher, L7256) for 1h and in the presence of the DNA marker Hoechst 34580 (Fisher, 11584876) for 20 min before being analyzed. siRNA delivery inside the cells was followed through BlockiT-associated fluorescence (Alexa Fluor Red) in a confocal Leica TCS SP8 HyVolution II microscope. The images, Pearson's co-localization coefficient (Rr) and 2D scatterplot of colocalization were acquired and analyzed with Leica Application Suite X software.

5.10. Evaluation of PD-L1 expression by Western Blot

First, A375 cells were cultured in a 6-well plate at a cellular density of 500,000 cells/well in the presence of IFN- γ (20 ng/ml) (Sigma, SRP3058) for 24h to attach to the plate. The next day, the medium was removed, and cells were incubated with free JQ1 at 1 μ M and 2 μ M for 48h in to determine the optimal drug concentration to reduce PD-L1 expression. To generate whole-cell extracts, cells were lysed in a buffer containing 25 mM Tris-HCl, pH 7.4, 1mM EGTA, 1% SDS and protease and phosphatase inhibitors. The protein concentration was quantified by using the Pierce BCA Protein Assay Kit (Thermo Fisher, 10741395). SDS-Page was used to separate the proteins in the cell lysates were, they were transferred to nitrocellulose membranes, blocked with 5% non-fat milk, washed with 0.1% Tween/PBS, and incubated overnight with the specific primary antibody. Membranes were washed and incubated with the secondary antibody conjugated to horseradish peroxidase for 1h. The primary antibodies, anti-PD-L1 antibody (Cell Signaling, 13684) and anti-GAPDH antibody (Fisher, 11335232), were prepared at 1:1000 dilutions in 5% non-fat milk. The secondary antibodies, anti-rabbit IgG antibody (Abcam, ab205718) and anti-mouse IgG antibody (Sigma, A4416) were prepared at 1:3000 dilutions in 5% non-fat milk. Chemiluminescence was detected after Lumi-Light Western Blotting Substrate (Amersham Pharmacia Biotech) incubation. The procedure was repeated with the rest of the treatments, MSN-PEI, MSN-PEI-siRNA, MSN(JQ1)-PEI, and MSN(JQ1)-PEI-siRNA at 8,62 μ g/ml which corresponds to the optimal concentration previously reported.

5.11. Flow cytometric determination of PD-L1 expression

Cells were seeded at 500,000 cells/well in a 6-well plate in the presence of IFN- γ (20ng/ml) for 24h. Subsequently, the medium was changed, and the treatments were added, free JQ1 at 1 μ M or MSN-PEI, MSN-PEI-siRNA, MSN(JQ1)-PEI, and MSN(JQ1)-PEI-siRNA at 8.62 μ g/ml. After 48h, cells were washed with PBS and detached from the plate

using 0.5% Trypsin-EDTA (Gibco). They were transferred into an eppendorf and washed twice with PBS 2% BSA. Cells were incubated for 1h with anti-PD-L1-PE (Thermo Fisher, 12-5983-41) according to manufacturer's instructions in PBS 2% BSA at 4 °C. After that, cells were washed three times with PBS 2% BSA and resuspended in 200 µl of PBS 2% BSA. Finally, PE-positive cells were assessed by flow cytometry on a CytoFlex S device (Beckman Coulter) followed by data analysis with CytoExpert software.

5.12. Silencing assay

To determine the effectiveness of TGF- β siRNA-loaded nanoparticles, A375 cells were seeded in a 12-well plate at 80,000 cells per well in DMEM supplemented with 10% FBS and incubated for 24h. After that, the medium was removed and a new medium with the appropriate treatment was added to the wells. Cells were treated with 12.96, 25.92, and 51.84 nM of free siRNA and Lipofectamine 2000 (Thermo Fisher, 11668019) in a reduced serum Opti-MEM medium, or with different amounts of MSN(JQ1)-PEI-siRNA or MSN-PEI-siRNA (4.31, 8.62 and 17.24 µg/ml respectively), equivalent to free siRNA concentration in DMEM 1%FBS. After 6 hours, lipofectamine was removed and the medium was replaced by DMEM 1%FBS. The plate was incubated for 48 h and then, the supernatants were collected and TGF- β expression was assessed by a Quantikine ELISA test (Biogen, RND-DB100C) following the instructions of the provider.

5.13. Evaluation of T-cell-mediated killing of melanoma cells

A375 cells were plated in a 12-well plate at 250,000 cells/well and incubated for 24h for achieving cell adherence. Cells were treated with free JQ1 (1µM) and TGF- β siRNA (25.92 nM) (same as silencing assay), and with nanoparticles, MSN-PEI, and MSN(JQ1)-PEI-siRNA (8.62 µg/ml) in DMEM 1% FBS for 48h. In parallel, Jurkat cells were activated with anti-CD3 and anti-CD28 antibodies (Palex Medical, 480684 and 452103 respectively). For Jurkat T cell activation, a 6-well plate was coated with 1 µg/ml of anti-CD3 antibody in PBS at 37 °C for 2h. Then PBS was removed and Jurkat cells were seeded into the wells at

a density of 700,000 cell/well in RPMI 10% FBS plus anti-CD28 antibody (5 μ g/ml). Jurkat cells were incubated in the presence of antibodies for 72 h. Once T cells were activated, the medium of A375 cells was replaced by RPMI 10% FBS containing Jurkat cells at 1:15 and incubated for 72 h. After that, medium with Jurkat cells was removed, and the plate was washed to remove cells in suspension. Finally, cell viability was assessed by the cell proliferation reagent WST-1 by absorbance measure at 595 nm in a Wallac 1420 Workstation. Absorbance values were normalized, and viability percentages calculated establishing control wells values as 100%.

5.14. Statistical analysis

The values represent the mean \pm SEM of at least three separate experiments. Significance was determined by one-way or two-way ANOVA followed by a Tukey test using GraphPad Prism software. $p < 0.05$ was considered statistically significant.

6. References

1. Xu, L. et al. Apigenin suppresses PD-L1 expression in melanoma and host dendritic cells to elicit synergistic therapeutic effects. *Journal of Experimental and Clinical Cancer Research*, **37**, 1-15 (2018).
2. Carreira, B. et al. Nanomedicines as Multifunctional Modulators of Melanoma Immune Microenvironment. *Advanced Therapeutics*, **4**, 1-39 (2021).
3. Huang, F., Santinon, F., Flores González, R. E. & del Rincón, S. v. Melanoma Plasticity: Promoter of Metastasis and Resistance to Therapy. *Frontiers in Oncology*, **11**, 1-21 (2021).

4. Ferrucci, P. F. & Cocorocchio, E. Novel Biomarkers and Druggable Targets in Advanced Melanoma. *Cancers*, **14** (81), 1-17 (2021)
5. Escriche-Navarro, B. et al. Mesoporous Silica Materials as an Emerging Tool for Cancer Immunotherapy. *Advanced Science*, **9**, 1-24 (2022).
6. Pelster, M. S. & Amaria, R. N. Combined targeted therapy and immunotherapy in melanoma: a review of the impact on the tumor microenvironment and outcomes of early clinical trials. *Ther. Adv. Med. Oncol.* **11**, 1–11 (2019).
7. Sadozai, H., Gruber, T., Hunger, R. E. & Schenk, M. Recent successes and future directions in immunotherapy of cutaneous melanoma. *Frontiers in Immunology*, **8**, 1-25 (2017).
8. Kuryk, L. et al. From Conventional Therapies to Immunotherapy: Melanoma Treatment in Review. *Cancers (Basel)*, **12**, 1-20 (2020).
9. Chen, D. S. & Mellman, I. Oncology meets immunology: The cancer-immunity cycle. *Immunity*, **39**, 1–10 (2013).
10. Sa, H. S., Daniel, C. C. & Esmaeli, B. Update on Immune Checkpoint Inhibitors for Conjunctival Melanoma. *J Ophthalmic Vis Res*, **17**, 405–412 (2022).
11. de Azevedo, S. J. et al. First-line atezolizumab monotherapy in patients with advanced BRAFV600 wild-type melanoma. *Pigment Cell Melanoma Res*, **34**, 973–977 (2021).
12. Carbognin, L. et al. Differential Activity of Nivolumab, Pembrolizumab and MPDL3280A according to the Tumor Expression of Programmed Death-Ligand-1 (PD-

- L1): Sensitivity Analysis of Trials in Melanoma, Lung and Genitourinary Cancers. *Plos One*, **10** (6), 1-16 (2015).
13. Hu, Z., Ye, L., Xing, Y., Hu, J. & Xi, T. Combined SEP and anti-PD-L1 antibody produces a synergistic antitumor effect in B16-F10 melanoma-bearing mice. *Sci Rep*, **8**, 1-13 (2018).
14. Sullivan, R. J. & Flaherty, K. T. Major therapeutic developments and current challenges in advanced melanoma. *British Journal of Dermatology*, **170**, 36-44 (2013).
15. Lee, J. Y. et al. Structural basis of checkpoint blockade by monoclonal antibodies in cancer immunotherapy. *Nat Commun*, **7**, 1-10 (2016).
16. Zhan, M. M. et al. From monoclonal antibodies to small molecules: The development of inhibitors targeting the PD-1/PD-L1 pathway. *Drug Discovery Today*, **21**, 1027–1036, (2016).
17. Pan, C. et al. Recent advance of peptide-based molecules and nonpeptidic small-molecules modulating PD-1/PD-L1 protein-protein interaction or targeting PD-L1 protein degradation. *European Journal of Medicinal Chemistry*, **213**, 1-16 (2021).
18. Xue, J. et al. Nanoparticles with rough surface improve the therapeutic effect of photothermal immunotherapy against melanoma. *Acta Pharm Sin B*, **12**, 2934–2949 (2022).
19. Zhu, H. et al. BET Bromodomain Inhibition Promotes Anti-tumor Immunity by Suppressing PD-L1 Expression. *Cell Rep*, **16**, 2829–2837 (2016).

20. Erkes, D. A. et al. The next-generation BET inhibitor, PLX51107, delays melanoma growth in a CD8-mediated manner. *Pigment Cell Melanoma Res*, **32**, 687–696 (2019).
21. Varrone, F., Mandrich, L., Caputo, E. & Baroudjian, B. Melanoma Immunotherapy and Precision Medicine in the Era of Tumor Micro-Tissue Engineering: Where Are We Now and Where Are We Going? *Cancers*, **13**, 1-22 (2021).
22. Conroy, H., Galvin, K. C., Higgins, S. C. & Mills, K. H. G. Gene silencing of TGF- β 1 enhances antitumor immunity induced with a dendritic cell vaccine by reducing tumor-associated regulatory T cells. *Cancer Immunology, Immunotherapy* **61**, 425–431 (2012).
23. Thomas, D. A. & Massagué, J. TGF- β directly targets cytotoxic T cell functions during tumor evasion of immune surveillance. *Cancer Cell* **8**, 369–380 (2005).
24. Wang, Y. et al. Co-inhibition of the TGF- β pathway and the PD-L1 checkpoint by pH-responsive clustered nanoparticles for pancreatic cancer microenvironment regulation and anti-tumor immunotherapy. *Biomater Sci* **8**, 5121–5132 (2020).
25. Li, S. et al. Cancer immunotherapy via targeted TGF- β signalling blockade in T_H cells. *Nature*, **587**, 1-33 (2020).
26. Saunier, E. F. & Akhurst, R. J. TGF Beta Inhibition for Cancer Therapy. *Current Cancer Drug Targets*, **6**, 565 - 578 (2006).
27. Argyo, C., Weiss, V., Bräuchle, C. & Bein, T. Multifunctional mesoporous silica nanoparticles as a universal platform for drug delivery. *Chemistry of Materials*, **26**, 435–451 (2014).

28. Nguyen, T. L., Choi, Y. & Kim, J. Mesoporous Silica as a Versatile Platform for Cancer Immunotherapy. *Advanced Materials*, **31**, 1-17 (2019).
29. Wang, X. et al. Comprehensive Mechanism Analysis of Mesoporous-Silica-Nanoparticle-Induced Cancer Immunotherapy. *Adv Healthc Mater*, **5**, 1169–1176 (2016).
30. Gu, Z., da Silva, C. G., van der Maaden, K., Ossendorp, F. & Cruz, L. J. Liposome-based drug delivery systems in cancer immunotherapy. *Pharmaceutics*, **12**, 1–25 (2020).
31. Karabasz, A., Bzowska, M. & Szczepanowicz, K. Biomedical applications of multifunctional polymeric nanocarriers: A review of current literature. *Int J Nanomedicine*, **15**, 8673–8696 (2020).
32. Evans, E. R., Bugga, P., Asthana, V. & Drezek, R. Metallic nanoparticles for cancer immunotherapy. *Materials Today*, **21**, 673–685 (2018).
33. Ni, K., Luo, T., Nash, G. T. & Lin, W. Nanoscale metal-organic frameworks for cancer immunotherapy. *Acc Chem Res*, **53**, 1739–1748 (2020).
34. García-Fernández, A., Aznar, E., Martínez-Mañez, R. & Sancenón, F. New Advances in In Vivo Applications of Gated Mesoporous Silica as Drug Delivery Nanocarriers. *Small*, **16** 1-62 (2020).
35. Tang, F., Li, L. & Chen, D. Mesoporous silica nanoparticles: Synthesis, biocompatibility and drug delivery. *Advanced Materials*, **24**, 1504–1534 (2012).

36. Garrido-Cano, I. et al. Biocompatibility and internalization assessment of bare and functionalised mesoporous silica nanoparticles. *Microporous and Mesoporous Materials*, **310**, 1-12 (2021).
37. Aznar, E. et al. Gated Materials for On-Command Release of Guest Molecules. *Chemical Reviews*, **116**, 561–718 (2016).
38. Mal, N. K., Fujiwara, M. & Tanaka, Y. Photocontrolled reversible release of guest molecules from coumarin-modified mesoporous silica. *Nature*, **421**, 350–353 (2003).
39. Vivo-Llorca, G. et al. MUC1 Aptamer-Capped Mesoporous Silica Nanoparticles for Navitoclax Resistance Overcoming in Triple-Negative Breast Cancer. *Chemistry - A European Journal*, **26**, 16318–16327 (2020).
40. García-Fernández, A. et al. Targeting inflammasome by the inhibition of caspase-1 activity using capped mesoporous silica nanoparticles. *Journal of Controlled Release*, **248**, 60–70 (2017).
41. Park, C., Oh, K., Lee, S. C. & Kim, C. Controlled Release of Guest Molecules from Mesoporous Silica Particles Based on a pH-Responsive Polypseudorotaxane Motif. *Angew Chem Int Ed Engl*, **119**, 1477–1479 (2007).
42. Agostini, A. et al. Design of enzyme-mediated controlled release systems based on silica mesoporous supports capped with ester-glycol groups. *Langmuir*, **28**, 14766–14776 (2012).

43. Descalzo, A. B., Martínez-Máñez, R., Sancenón, F., Hoffmann, K. & Rurack, K. The supramolecular chemistry of organic-inorganic hybrid materials. *Angewandte Chemie - International Edition*, **45**, 5924–5948 (2006).
44. Keasberry, N. A., Yapp, C. W. & Idris, A. Mesoporous silica nanoparticles as a carrier platform for intracellular delivery of nucleic acids. *Biochemistry (Moscow)*, **82**, 655–662 (2017).
45. Xia, T. et al. Polyethyleneimine coating enhances the cellular uptake of mesoporous silica nanoparticles and allows safe delivery of siRNA and DNA constructs. *ACS Nano*, **3**, 3273–3286 (2009).
46. García-Fernández, A. et al. Nanodevices for the Efficient Codelivery of CRISPR-Cas9 Editing Machinery and an Entrapped Cargo: A Proposal for Dual Anti-Inflammatory Therapy. *Pharmaceutics*, **14**, 1-20 (2022).
47. Garrido-Cano, I. et al. miR-99a-5p modulates doxorubicin resistance via the COX-2/ABCG2 axis in triple-negative breast cancer: from the discovery to in vivo studies. *Cancer Communications*, **42**, 1412–1416 (2022).
48. Wang, M., Li, X., Ma, Y. & Gu, H. Endosomal escape kinetics of mesoporous silica-based system for efficient siRNA delivery. *Int J Pharm*, **448**, 51–57 (2013).
49. Boussif, O. et al. A versatile vector for gene and oligonucleotide transfer into cells in culture and in vivo: Polyethylenimine. *Proc Natl Acad Sci USA*, **92**, 7297–7301 (1995).

50. Garrido-Cano, I. *et al.* Biocompatibility and internalization assessment of bare and functionalised mesoporous silica nanoparticles. *Microporous and Mesoporous Materials* **310**, 1-12 (2021).
51. Vivero-Escoto, J. L., Slowing, I. I., Lin, V. S. Y. & Trewyn, B. G. Mesoporous silica nanoparticles for intracellular controlled drug delivery. *Small* **6**, 1952–1967 (2010)
52. Melaiu, O. *et al.* PD-L1 is a therapeutic target of the bromodomain inhibitor JQ1 and, combined with HLA class I, a promising prognostic biomarker in neuroblastoma. *Clinical Cancer Research*, **23**, 4462–4472 (2017).
53. Zhu, H. *et al.* BET Bromodomain Inhibition Promotes Anti-tumor Immunity by Suppressing PD-L1 Expression. *Cell Rep*, **16**, 2829–2837 (2016).
54. Jing, X. *et al.* BRD4 inhibition suppresses PD-L1 expression in triple-negative breast cancer. *Exp Cell Res*, **392**, 1-10 (2020).
55. Makuku, R., Khalili, N., Razi, S., Keshavarz-Fathi, M. & Rezaei, N. Current and Future Perspectives of PD-1/PDL-1 Blockade in Cancer Immunotherapy. *Journal of Immunology Research*, **2021**, 1-15 (2021).
56. Yan, S., Zhao, P., Yu, T. & Gu, N. Current applications and future prospects of nanotechnology in cancer immunotherapy. *Cancer Biology and Medicine*, **16**, 486–497 (2019).
57. Giménez, C. *et al.* Gated mesoporous silica nanoparticles for the controlled delivery of drugs in cancer cells. *Langmuir*, **31**, 3753–3762 (2015).

58. García-Fernández, A. et al. Targeted-lung delivery of dexamethasone using gated mesoporous silica nanoparticles. A new therapeutic approach for acute lung injury treatment. *Journal of Controlled Release*, **337**, 14–26 (2021).

Acknowledgements


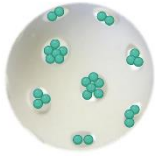
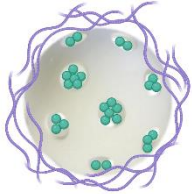
The authors thank the Spanish Government (project PID2021-126304OB-C41, (MCUI/FEDER, EU)) and the Generalitat Valenciana (project PROMETEO CIPROM/2021/007). This work was also supported by CIBER -Consortio Centro de Investigación Biomédica en Red- (CB06/01/2012), Instituto de Salud Carlos III, Ministerio de Ciencia e Innovación. E.L-S is grateful for her FPU fellowship funded by MINECO (FPU18/06539). F.J.H thanks MIU for his FPU grant (FPU20/06021). Graphical images and schemes were created with BioRender.com.

Author contributions

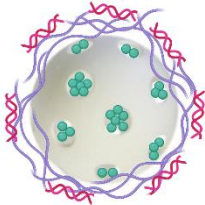
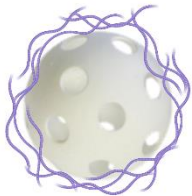
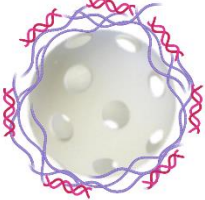
Elena Lucena-Sánchez: Experimental design, nanoparticle development, performing biological experiments, data analysis, discussion, and writing. Francisco J. Hicke: Contributed to nanoparticle characterization analysis. Sandra Clara-Trujillo: Contributed to nanoparticle characterization analysis. Alba García-Fernández: Experimental design, analysis, experiments discussion, Conceptualization, Writing – review & editing, Supervision. Ramón Martínez-Máñez: Conceptualization, Project administration, Writing – review & editing, Supervision. All authors have approved the final version of the manuscript.

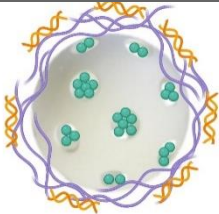
7. Supporting Information

Table S1. Schematic representation of nanodevices' structure. (Schemes were created by the authors on Biorender)

Abbreviation	Description	Scheme
MSN	calcined MSNs	
MSN(JQ1)	MSNs loaded with JQ-1 drug	 JQ-1
MSN(JQ1)-PEI	MSNs loaded with JQ-1 drug and capped in the external surface with polyethyleneimine molecules	 Polyethyleneimine JQ-1

Nanoparticle-mediated tumor microenvironment remodeling favors the communication with the immune cells for tumor killing

Abbreviation	Description	Scheme
MSN(JQ1)-PEI-siRNA	MSNs loaded with JQ-1 drug, capped in the external surface with polyethyleneimine molecules and finally coated with a siRNA targeting TGF- β	 <p data-bbox="891 548 1159 580">Polyethyleneimine</p> <p data-bbox="974 618 1077 651">JQ-1</p> <p data-bbox="946 685 1104 717">siTGF-β</p>
MSN-PEI	MSNs capped in the external surface with polyethyleneimine molecules	 <p data-bbox="891 1024 1159 1056">Polyethyleneimine</p>
MSN-PEI-siRNA	MSNs capped in the external surface with polyethyleneimine molecules and finally coated with a siRNA targeting TGF- β	 <p data-bbox="891 1374 1159 1407">Polyethyleneimine</p> <p data-bbox="946 1441 1104 1473">siTGF-β</p>

Abbreviation	Description	Scheme
MSN(JQ1)-PEI-BlockiT	MSNs loaded with JQ-1 drug, capped in the external surface with polyethyleneimine molecules and finally coated with BlockiT siRNA	 <p data-bbox="893 515 1160 687">Polyethyleneimine JQ-1 BlockiT</p>

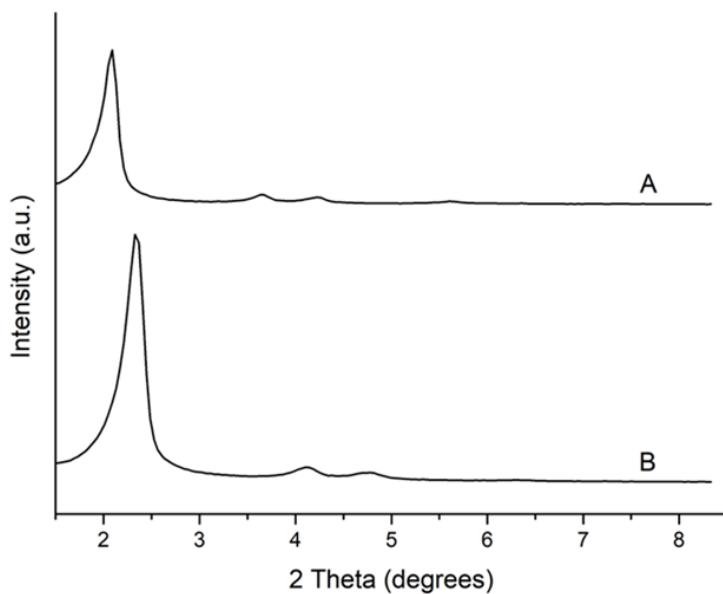


Figure S1. Powder X-ray patterns of A. MCM-41 nanoparticles as made and B. calcined MSNs (MSN), showing the typical reflections of MCM-41 hexagonal structure.

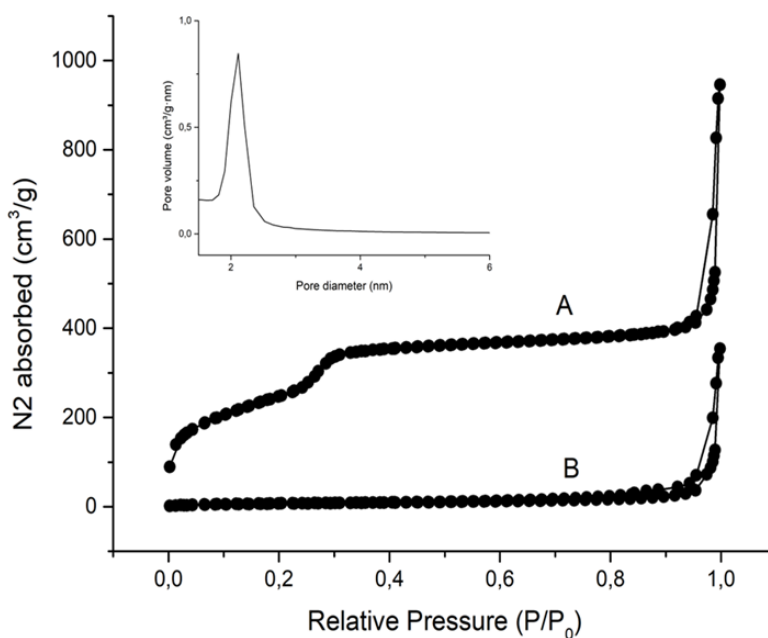


Figure S2. Nitrogen adsorption-desorption isotherm for A. calcined MSNs (MSN) and B. MSN(JQ1)-PEI (inset: pore size distribution for calcined MSNs).

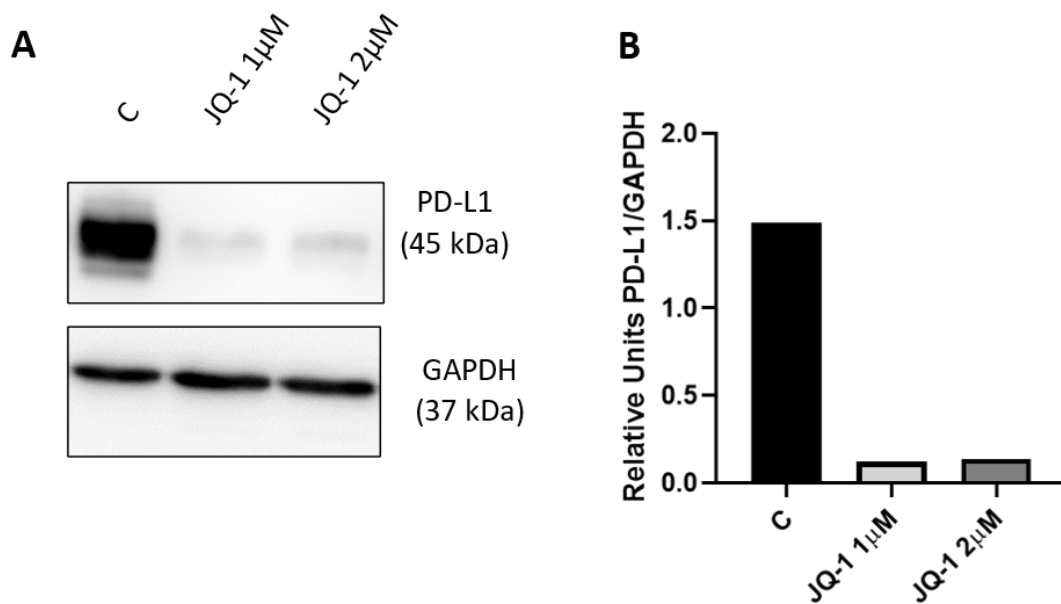


Figure S3. A. Western Blot analysis of PD-L1 expression in A375 cells with different concentrations of JQ-1 for 48h (expected band 45 kDa). GAPDH (37 kDa) was included as a loading control. B. Quantification of ratio protein expression versus internal reference (GAPDH). The results show a decrease in PD-L1 expression with the smallest concentration, 1 μ M of JQ1.

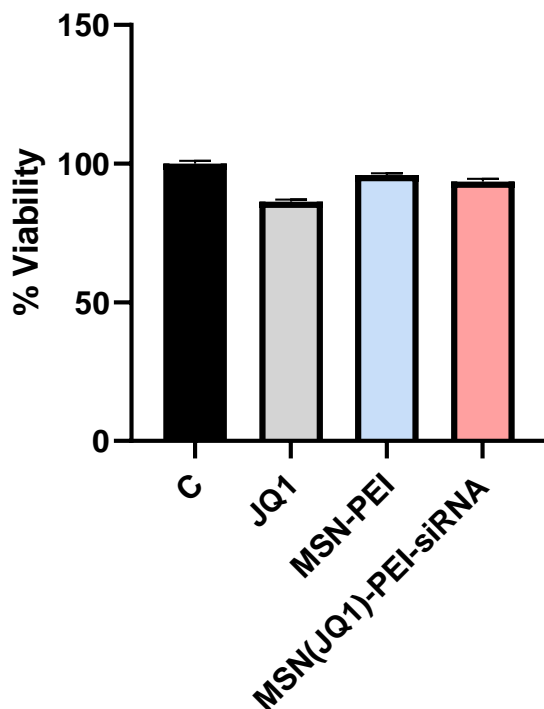


Figure S4. Cytotoxicity profile of free JQ1 (1 μ M) and different solids at 8,62 μ g/ml (equivalent to JQ1 concentration) in A375 cells at 48 h using ATP CellTiter-Glo viability assay. The data represent the mean \pm SEM (n=3).

**Chapter IV | Nanoparticles to re-establish
communication between cancer and immune cells as a
new immunotherapeutic strategy**

Nanoparticles to re-establish communication between cancer and immune cells as a new immunotherapeutic strategy

Elena Lucena-Sánchez^{a,c}, Francisco J. Hicke^{a,b}, Alba Ortuño-Bernal^{a,c}, Andrea Escudero^{a,c},
Nelia Jiménez-Alduan^{a,c}, Paula Díez^{a,b,d}, Alba García-Fernández^{*a,b,c}, Ramón Martínez-
Máñez^{*a,b,c,d}

^aInstituto Interuniversitario de Investigación de Reconocimiento Molecular y Desarrollo Tecnológico (IDM) Universitat de València–Universitat Politècnica de València, Camino de Vera s/n, 46022, Valencia, Spain.

^bCIBER de Bioingeniería, Biomateriales y Nanomedicina, Instituto de Salud Carlos III

^cUnidad Mixta UPV-CIPF de Investigación en Mecanismos de Enfermedades y Nanomedicina, Valencia, Universitat Politècnica de València, Centro de Investigación Príncipe Felipe, Valencia Spain

^dUnidad Mixta de Investigación en Nanomedicina y Sensores. Universitat Politècnica e València, Instituto de Investigación Sanitaria La Fe (IIS La Fe), Valencia Spain.

*Corresponding authors: algarfe4@upvnet.upv.es, rmaez@qim.upv.es

Project in progress: 2024

1. Abstract

Recently, cancer immunotherapy has emerged as a promising alternative treatment approach, enabling the body's immune system to fight cancer. Cytotoxic T cells play a pivotal role in recognizing and eliminating tumor cells and their effectiveness relies on establishing a physical interaction (immunological synapse) and developing efficient communication. This required communication is often disrupted by immune escape mechanisms developed by tumors, allowing cancer progression. In this scenario, we envisioned the development of a versatile nanoplatfrom able to restore compromised immunological synapses, restoring cellular connection and communication between cancer cells and cytotoxic T cells. Here, we report a Janus mesoporous silica-Au nanoparticle (J-pHLIP-PD1) including specific binding sites in opposite faces for simultaneous binding cancer cells and T cells. The gold face is functionalized with the PD-1 antibody that interacts with PD-1 receptor in T-cells, while the silica face carries the pHLIP peptide which undergoes specific insertion into the tumor cell membrane. J-pHLIP-PD1 nanoparticles effectively decorate the surface of tumour cells and capture T-lymphocytes via the PD-1 antibody, resulting in reduced cancer cell viability. Treatment with J-pHLIP-PD1 produces a significant decrease in metastatic burden accompanied by an increased presence of cytotoxic lymphocytes in a melanoma metastatic mouse model. Overall, our nanosystem represents an attractive platform to artificially link T-cells and tumor cells restoring cell-cell communication with the goal of cancer elimination.

KEYWORDS. Immunotherapy, communication, pHLIP, PD-1, nanoparticles

2. Introduction

The immune system's primary task is to distinguish the antigens that belong to the body from those of foreign or damaged cells, to eliminate them¹. One example is

tumorigenic mutant cells whose elimination involves several types of immune cells that coordinate their actions and prevent cancer development. However, this process is sometimes defective, and the immune system fails in the removal, allowing the tumor to progress^{2,3}. Recently, cancer immunotherapy has become a potent strategy to take advantage of the immune system's ability to identify and eliminate cancer cells. Compared to conventional therapies (such as chemotherapy, radiotherapy, and surgery), these treatments have significantly improved patients' quality of life and survival rates^{4,5}. However, despite the progress with cancer nanovaccines⁶, checkpoint therapies⁷ and T-cell therapy (i.e. CAR-T)⁸, the translation into patients remains challenging and raises concerns related to low response and adverse effects⁹⁻¹¹. In most cases, tumors escape from the immune system due to disrupting immune cell-tumor cell connections, which are not restored by the current methods described above^{10,12}.

The immune cells responsible for tumor cell recognition and elimination are mainly cytotoxic T cells and their activity against tumor cells requires physical interaction through the formation of immunological synapses¹²⁻¹⁴. These synapses are specialized structures formed when the plasma membrane of two cells comes into close contact to facilitate communication¹³⁻¹⁵. In fact, synapse disruption has been related to abnormalities that compromise anti-tumor immunity and let cancers bypass the immune system¹¹⁻¹³. Therefore, recognition between cancer and cytotoxic T cells must happen to develop an immunological response against cancer cells¹⁵⁻¹⁸. In this scenario, we envisioned the development of a versatile nanoplatform capable of restore cell-cell communication by creating an artificial link between T-cells and tumor cells with the objective of cancer cell elimination.

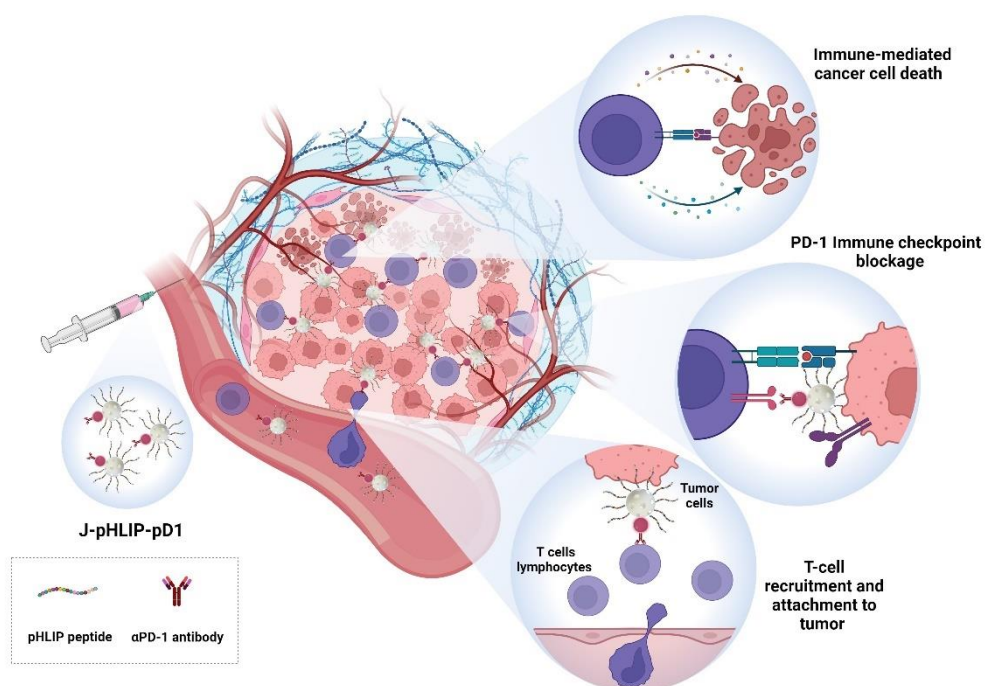
From another point of view, nanotechnology has undergone important growth in recent years and has demonstrated unlimited applications in different areas such as cancer therapy¹⁹. Since a few years ago, nano-immunotherapies have been incorporated into the field using liposomes, polymer conjugates, solid NPs, and other

nanomaterials^{20,21}. These NPs are often employed to protect immunotherapeutic drugs (antibodies²², antigens²³, cytokines²⁴, small molecules²⁵, etc.) and enhance their targeted delivery to generate a more regulated immune response, hence lowering the possibility of immunological overreaction or systemic side effects^{26,27}. In contrast, our approach follows a different concept based on designing nanoparticles including specific binding sites in opposite faces enabling the simultaneous binding of T-cell and cancer cells to induce the activation of the cytotoxic T lymphocytes with the subsequent tumor cell lysis.

Particularly, nanoparticles with two different chemical faces, called Janus nanoparticles, are good candidates for the construction of nanodevices through the stable immobilization of diverse biological molecules in their different surfaces^{19,28-30}, and we focused on the use of Janus Au-mesoporous silica (Janus Au-MS) nanoparticles. To drive the NPs to the tumor cells, the mesoporous face is decorated with the pHLIP peptide. This peptide has been used for tumor-targeted therapy due to its ability to insert into the tumor cell membrane at the characteristic acidic pH of the tumor cell environment^{19,31-33}. On the other hand, the gold face is functionalized with the PD-1 antibody to attach T-cells and overcome immune evasion. PD-1 is expressed on tumor-infiltrating lymphocytes and appears to be concentrated in immunological synapses^{34,35}. When PD-1 interacts with its ligand in tumor cells, PD-L1, delivers an inhibitory signal responsible for defective synapse and immune escape^{14,36-38}. Many blocking antibodies against PD-1 or its ligands have been developed and they have revolutionized cancer immunotherapy^{13,38}.

Considering the importance of optimal synapse formation combined with communication at both levels to accomplish T cell recognition and killing of tumor cells, we report herein a new immunotherapeutic approach based on nanoparticles for cellular synapse and communication restoration between cancer cells and the immune system. Although new nanodevices are reported every year, engineering NPs to reestablish communication in living systems is a barely studied field that can expand the capabilities

of nanoparticles^{39,40}. The pHLIP peptide inserts specifically into the tumor cell membrane, decorating cells' surface with nanoparticles and allowing PD-1 antibody to retain circulating lymphocytes and trigger tumor cell death (Scheme 1). The strategy results in a highly effective restoration of immune-triggered cancer cell death both in vitro in melanoma cells and in vivo in a metastatic mouse model. Overall, our nanosystem provides an appealing platform for restoring cell-cell communication between tumor cells and T-cells to eradicate cancer.



Scheme 1. A nanodevice able of restoring cell-cell contact with the goal of cancer elimination was developed. A Janus nanoparticle functionalized with pHLIP peptide and α PD-1 antibody has been designed to act as a linker between tumor cells and T-lymphocytes. This allows PD-1 checkpoint blockage and immune-mediated cancer cell death.

3. Results and discussion

3.1. Design, synthesis, and characterization of nanoparticles

Given our objective, we employed Janus Au-MSNs (J) that contain two different surfaces having different functionalization chemistries. Additionally, these nanoparticles

have aroused special attention because of their unique features such as stability, good biocompatibility, self-adjuvanticity, and large and easily modifiable surface area, among others⁴¹⁻⁴³. Janus Au-MSNs were synthesized by the toposelective combination of gold nanoparticles and MSNs (see experimental section for details) providing specific surfaces in opposite faces. The gold face acts as scaffold for the immobilization of the antibody α PD1 that should interact with PD-1 receptor in lymphocytes as well as overcome immune suppression from tumor cells. On the opposite side, MSN face is used for grafting the peptide pHLIP able to interact with cancer cell membranes. pHLIPs are moderately hydrophobic with a special behavior depending on the pH. Whereas at physiological pH the peptide is in equilibrium between soluble and membrane-bound unstructured forms, at acidic pH (characteristic of tumor cell environment) pHLIP inserts across the lipid bilayer forming a stable transmembrane helix and is not taken up by endocytosis^{31,32}.

For this purpose, the pHLIP peptide was covalently anchored to MSN functionalised with 3-(triethoxysilyl)propyl isocyanate. Moreover, the MSN face was also labelled with fluorophore rhodamine B modified with APTES for imaging purposes. In addition, the α PD1 antibody was reacted with the Traut's reagent to introduce sulfhydryl groups that were attached to gold face by the formation Au-S bonds (Figure 1.A). We also prepared different control nanoparticles, in which one of the essential components was eliminated: (i) control nanoparticles lacking the α PD1 antibody unable to link T-cells (J-pHLIP); and (ii) control nanoparticles lacking the pHLIP peptide unable to target tumor cells (J-PD1). The labelled nanoparticles were referred as (J-pHLIP*-PD1). All the prepared nanoparticles are summarized in Table S1 (Supporting Information).

J-pHLIP-PD1 was characterized using standard procedures; TEM, dynamic light scattering, zeta potential, energy dispersive X-ray spectroscopy (STEM-EDX), powder X-ray diffraction (PXRD) and reducing SDS-Page. The crystalline structure and morphology of nanoparticles were confirmed by transmission electron microscopy (TEM), Figure 1.B

shows the hybrid anisotropic nanostructure of Janus nanoparticles (J), with Au nanoparticles (diameter of ca. 20 nm), and MSNs (diameter of ca. 100 nm) on opposite faces. The crystalline structure was confirmed by PXRD (Figure S.1). At low-angles the characteristic Bragg peaks of the hexagonal mesoporous silica matrix, indexed as planes (100), (110), (200) and (210), was observed. Moreover, the Janus nanoparticles also displayed four gold characteristic Bragg peaks, planes (111), (200), (220) and (311), at high angles. Additionally, STEM-EDX analysis allowed the construction of a map showing the atomic composition (wt %) of J-pHLIP-PD1 (Figure 1C). The figure exhibits the presence of Si, O and Au atoms corresponding to the scaffold along with N atoms assigned to peptide and antibody immobilization, S atoms (assigned to disulfide-linked chains from the anchored antibody) and P atoms (attributed to the peptide pHLIP and the antibody α PD1) were also detected (Figure S.2). Finally, to complete the characterization, the nanoparticles were evaluated by dynamic light scattering analysis (DLS) and zeta potential. The average hydrodynamic diameter increased from 172.4 ± 11.6 nm to 288.4 ± 5.3 nm and the zeta potential decreased from -37.6 ± 0.7 mV to -26.8 ± 0.2 mV for J and J-pHLIP-PD1, respectively (Figure 1.E and 1.F). Similar values were also observed for J-pHLIP and J-PD1 nanoparticles. These changes from J to J-pHLIP-PD1 are in agreement with the proper immobilization of the peptide and/or the antibody on the nanoparticles' surface.

Besides, the proper immobilization of the antibody and peptide was corroborated in all prepared nanoparticles. The nanoparticles were incubated in lysis buffer for 10 min at 95 °C to separate the antibody and the peptide and the supernatants were evaluated in SDS-Page gel (Figure 1.D). The gel revealed four lanes for the J-pHLIP-PD1 sample at 150 kDa, 50 kDa and 25 kDa attributed to the antibody PD-1 and to the heavy (HC) and light chain (LC) of the antibody, respectively. Besides a broad line at 4-5 kDa corresponds to the pHLIP peptide. In the J-pHLIP and J-PD1 samples, only lanes of the peptide and of the PD-1 antibody were observed, respectively. Different concentrations of pHLIP or PD-1 were loaded into the SDS-Page gel to obtain a standard curve together with the antibody

and peptide from J-pHLIP-PD1 (Figure S3). Coomassie images were quantified with ImageJ and loading values of 16.44 μg of pHLIP/mg J-pHLIP-PD1 and 7.42 μg of PD-1/mg J-pHLIP-PD1 were found by extrapolation.

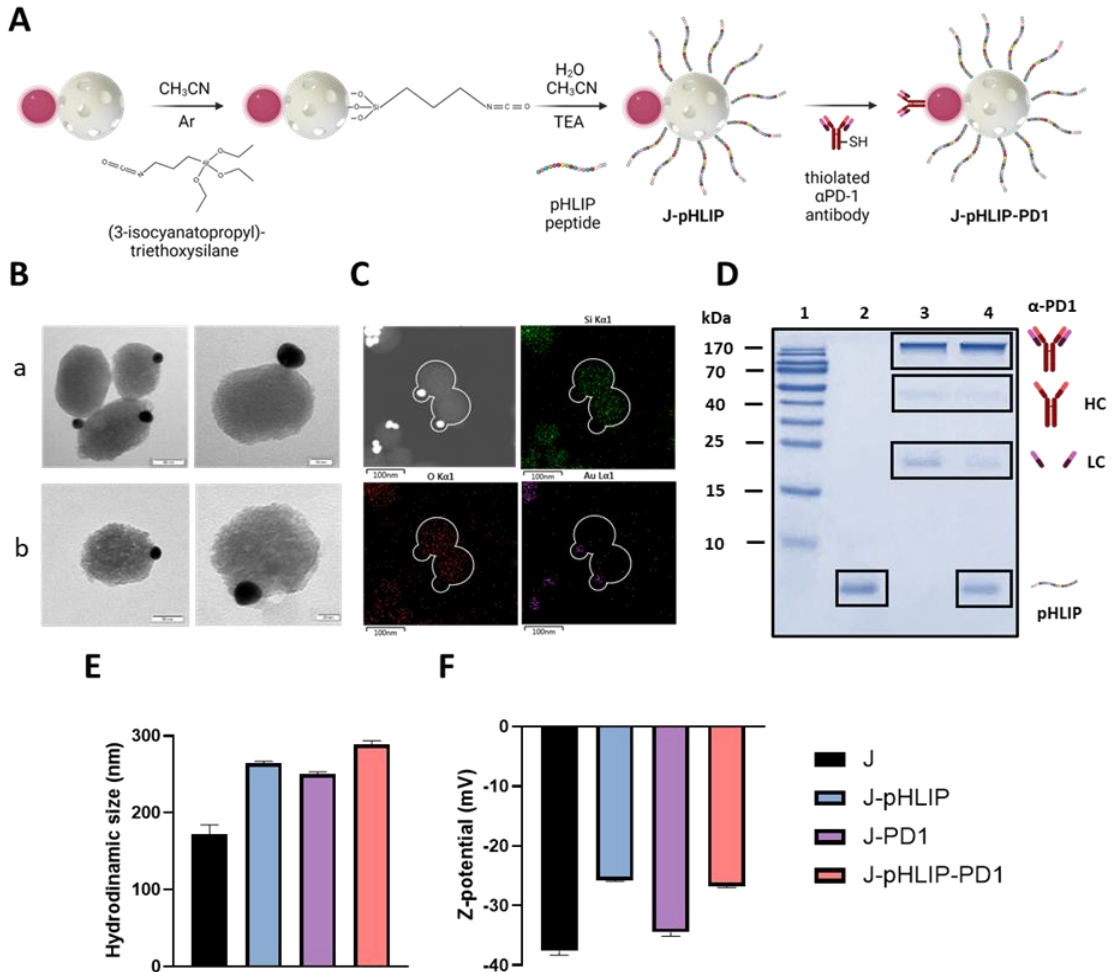


Figure 1. A. Schematic representation of J-pHLIP-PD1 synthesis. B. TEM images of Janus MSN-Au nanoparticles (J) (a) and the final device J-pHLIP-PD1 (b). C. STEM-EDX elemental mapping of Si atoms, O atoms and Au atoms. D. SDS-Page gel electrophoresis assay of the different nanoparticles: protein ladder (1), J-pHLIP (2), J-PD1 (3) and J-pHLIP-PD1 (4). E. Hydrodynamic size distribution and. F. Zeta potential of different solids. Values are expressed as mean \pm SEM (n=3). (Figure 1.A was created by the authors on Biorender).

3.2. J-pHLIP-PD1 nanoparticles attach to cancer cell membrane and capture of T-lymphocytes

The next step was to confirm the preferential attachment of the nanoparticles on the cancer cell membrane versus internalization. The proposed cancer cell membrane retention strategy is based on the fact that tumor cells regulate the acidity and stabilize their cytoplasmic pH which translates into an extracellular pH significantly lower than physiological pH. Taking advantage of this phenomenon, the pHLIP peptide (derived from the bacteriorhodopsin C helix) changes its conformation and inserts itself into the cell membrane through the C-terminal extreme with the amine terminus outward when the pH is acidic (Figure 2.A). This is due to the protonation of negatively charged residues which enhances peptide hydrophobicity^{31,32}. To study nanoparticles behaviour, Sk-Mel-103 melanoma cells were treated with the fluorescent-labelled nanoparticles J*-pHLIP at pH 6.5 or 7.5 for 30 min and after 1 hour, nanoparticles localization was evaluated by confocal and electronic microscopy. Figure 2. B. shows representative Z-stacks images from treated cells obtained by confocal microscopy. It can be appreciated that J*-pHLIP (shown in red) is located through cell membrane (displayed in green) and colocalize with it at pH 6.5, but the nanoparticles are inside the cell, and surrounded by membrane at physiological pH. Furthermore, TEM images of cell sections confirm these results (Figure 2.C). Images of cells treated with J*-pHLIP at pH 6.5 show that most of the nanoparticles are not internalized and are located close to or in contact with the external part of the cell membrane. In contrast, TEM images at pH 7.5 show the presence of nanoparticles inside the cell, while virtually no non-internalised nanoparticles are visible. Our results confirm that the pHLIP peptide-functionalised nanoparticles avoid being endocytosed at pH 6.5, yet they remain mainly on the outside of the cell membrane.

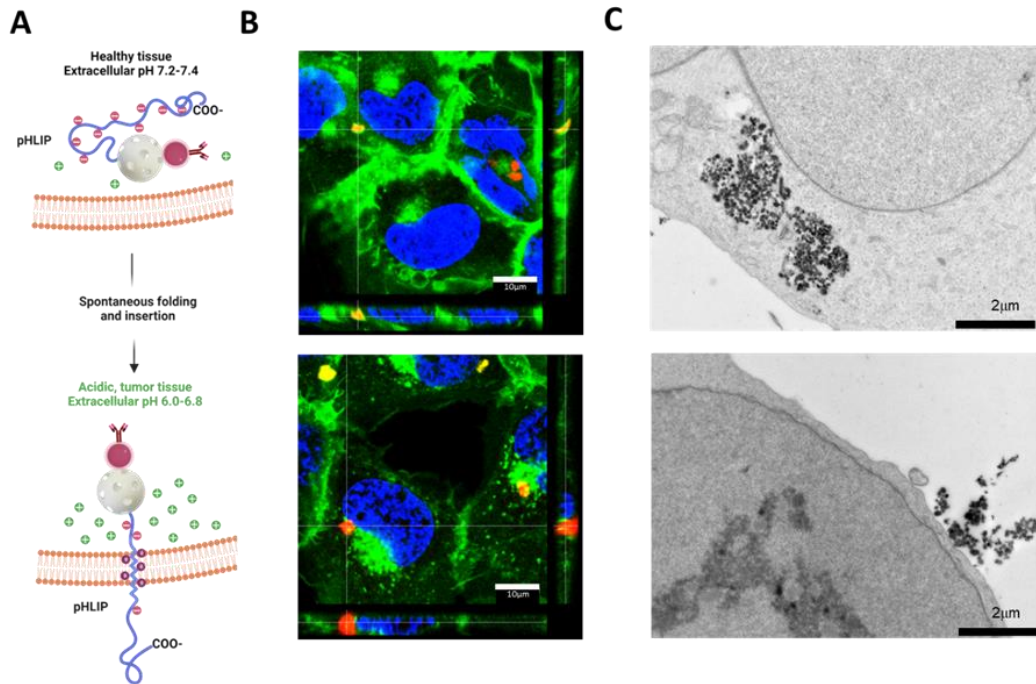


Figure 2. A) Schematic representation of pHLIP peptide behavior attached to the prepared nanoparticles depending on the pH of the microenvironment. B) Z-stack confocal microscopy images and C) electronic microscopy images of melanoma cells pretreated with 50 μg of J*-pHLIP nanoparticles for 30 minutes and incubation for 1h in DMEM pH 7.5 (above) and 6.5 (below) respectively.

In a second step, the ability of J*-pHLIP-PD1 to capture T-lymphocytes was evaluated. First, PD-1 expression was confirmed in our model based on Jurkat T-cells. PD-1 expression was corroborated in Jurkat cells, in activated Jurkat cells ($\alpha\text{CD3}/\alpha\text{CD28}$) (therapeutic purpose) and in Jurkat green cells (imaging purposes) by western blot and flow cytometry (Figure S4). Finally, the ability of J*-pHLIP-PD1 to capture and bind T-lymphocytes to tumor cells was evaluated in co-culture system (Figure 3.A). Tumor cells were seeded on the bottom of the transwell and pretreated with J*-pHLIP-PD1 or J*-pHLIP at acidic pH to simulate the tumor or metastasis microenvironment. Then, Jurkat T cells were incorporated into the top of the system and let them migrate. The bottom of the transwell was then observed in a fluorescence confocal microscope. As can be appreciated in the Figure 3.B, a significant number of Jurkat T cells (green cells) are

retained in the tumor cell layer on the bottom of the transwell when tumor cells (in blue) were pretreated with J*-pHLIP-PD1 (in red). In contrast, the lymphocytes migrate and pass through the transwell insert when tumor cells were pretreated with J*-pHLIP (lacking the PD-1 antibody). The number of Jurkat T cells per field was quantified and represented in Figure 3.C. Moreover, Figure 3.D display a representative image showing nanoparticles acting as “linkers” between tumor (in blue) and lymphocyte (in green) cells.

Nanoparticles to re-establish communication between cancer and immune cells as a new immunotherapeutic strategy

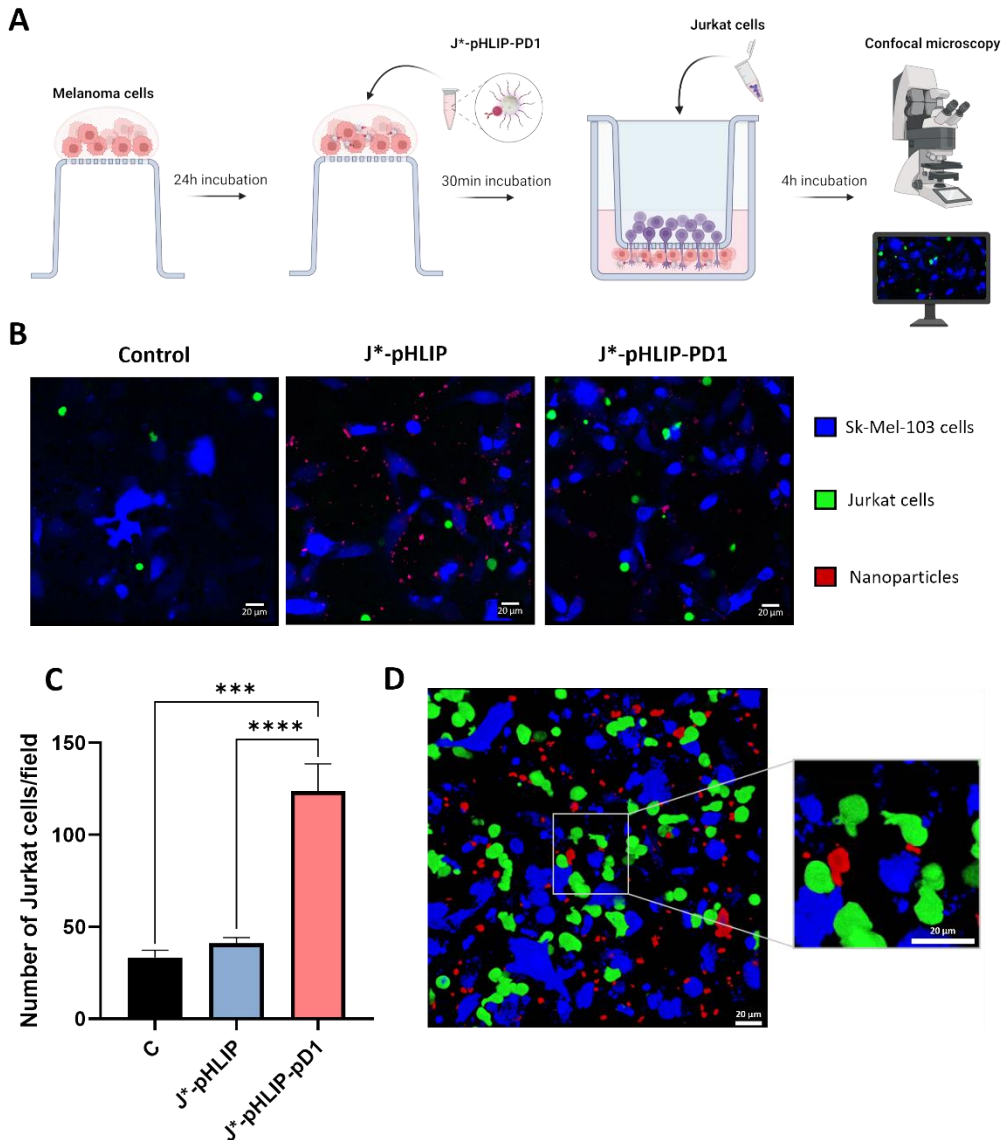


Figure 3. A) Schematic representation of Jurkat cells (T-lymphocytes) migration assay. Sk-Mel-103 were seeded in a drop on the bottom of the insert. After 24h, the drop was aspirated, and a new drop with 50 $\mu\text{g}/\text{mL}$ of J*-pHLIP-PD1 was added to the insert for 30 minutes. After that, Jurkat cells were seeded on the top of the insert and let migrate for 4h. Jurkat migration was analyzed by confocal microscopy. B) Confocal microscopy images of Jurkat (green) migration and retention in transwell seeded with melanoma cells (blue), pretreated with nanoparticles (in red). C) Quantification of the number of Jurkat cells retained per field. Data represents mean \pm SEM (n=3). Statistical analysis was carried out by one-way ANOVA test (***p<0.001; ****p<0.0001). D) 3D enlargement showing how J*-pHLIP-pD1 acts as a link between tumor and T-cells.

3.3. Cellular communication and therapeutic effect of J-pHLIP-PD1

The final objective of restoring communication between tumor cells and T-cells is to achieve cancer cell death. To demonstrate this, tumor cells were seeded and treated with J-pHLIP or J-pHLIP-PD1, then Jurkat T cells were added, and viability was measured after 72 hours (Figure 4.A). A significant reduction in cell viability was only observed for tumor cells pretreated with J-pHLIP-PD1 in the presence of Jurkat cells. In contrast, no significant reduction in cell viability was found for control nanoparticles. Further, no effect in cell viability was observed from nanoparticles in T-cells or melanoma cells, individually (Figure 4.B). Obtained results manifest the nanosystem's ability to bring tumor cells and lymphocytes closer and develop anti-tumor immune response.

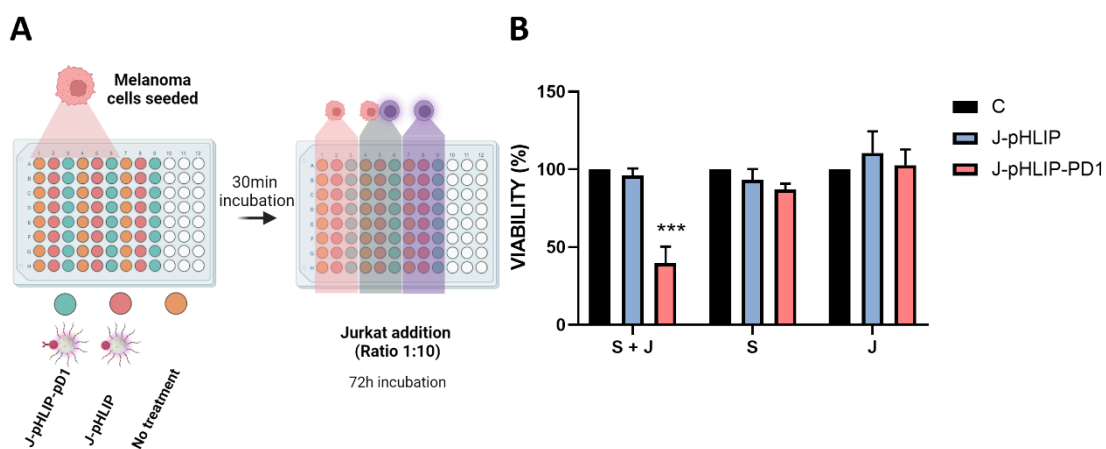


Figure 4. A) Co-culture cell viability assay diagram. Sk-Mel-103 cells were seeded in a 96-Wells plate. After 24h, cells were treated with J-pHLIP and J-pHLIP-pD1 nanoparticles at pH 6.5 for 30 min. Finally, medium was changed to pH 7.5 and Jurkat cells were added to the plate at a 1:10 ratio and incubated for 72h. B) WST-1 cell viability assay (S:Sk-Mel-103cells, J:Jurkatcells). Data represents mean±SEM (n=3). Statistical analysis was carried out using GraphPad Prism 8, and results were compared by two-way ANOVA test (**p<0.01).

3.4. J-pHLIP-PD1 reduces metastatic clusters in a B16-F10-Luc mouse metastatic model

To assess and compare the cytotoxic effects *in vivo* with our previous results *in vitro*, we selected a metastatic melanoma model to evaluate the therapeutic impact of J-pHLIP-PD1 to capture circulating cancer cells and communicate with immune cells⁴⁴⁻⁴⁶. For that purpose, healthy BALB/cOlaHsd mice were first intravenously injected via the tail vein with $5 \cdot 10^5$ B16-F10-Luc cells and after 30 minutes with J-pHLIP, J-PD1, J-pHLIP-PD1 or vehicle (25 mg/Kg in PBS) (Figure 5.A). The metastatic spread of cancer cells was monitored *in vivo* by IVIS measuring luminescence. As expected, luminescence associated with metastases was developed in the lungs in all the animals after tail vein injection of the B16-F10-Luc melanoma cell line (Figure 5C and S5). While lung luminescence (metastatic burden) increased along time in the animals treated with the vehicle and control nanoparticles (J-pHLIP and J-PD1), the treatment with J-pHLIP-PD1 resulted in a drastic mitigation of lung metastases progression. The metastatic burden at the end point was significantly reduced (5.8-fold) compared to vehicle group (Figure 5B). As expected, J-pHLIP did not exhibit any effect and similar luminescence values to that of the vehicle group were obtained. A moderate effect at the endpoint with the J-PD1 treatment, attributed to the therapeutic effect described for PD-1 antibody, was found. Nevertheless, the superiority of the J-pHLIP-PD1 system was also demonstrated compared to J-PD1 treatment. (Figure 5.B and C). These findings were in accordance with the *in vitro* results shown above. Additionally, systemic administration of J-pHLIP-PD1 did not show apparent toxicity. No significant differences were observed in mice body weight after the nanoparticle treatment. Hemograms and biochemistry blood analysis showed values in the expected interval with no significant differences compared to vehicle group. Besides, histological analysis of major organs did not reveal pathological alterations. (Figure S6).

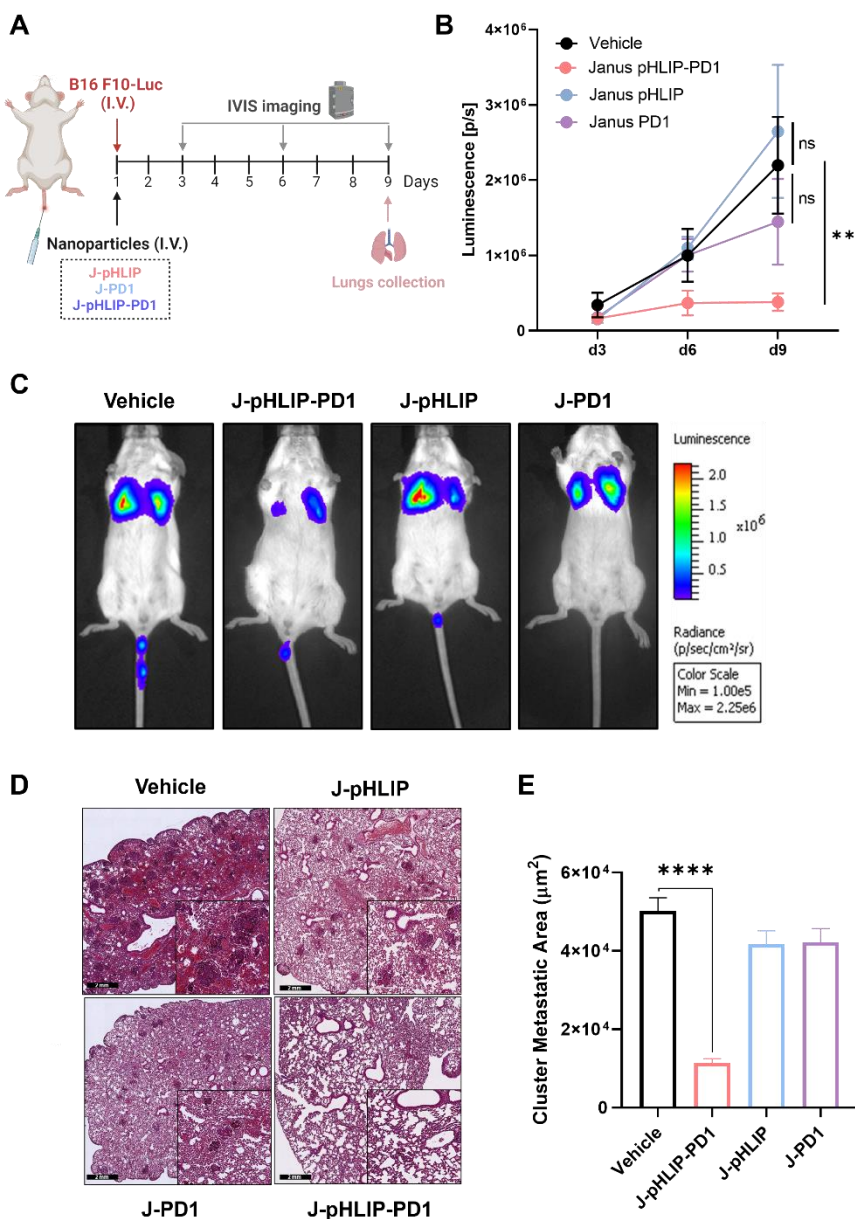


Figure 5. A) Schematic representation of the in vivo B16-F10-Luc Metastatic Model. Balb/c mice intravenously injected with B116-F10-Luc melanoma cancer cells. Then, NPs were intravenously administered (25 mg/Kg in PBS). The luminescence from melanoma cells was monitored for 9 days ($n = 5$ mice/group). B) Quantification of luminescence by IVIS in mice for 9 days. C) Representative IVIS images at endpoint (day 9). Data represents as mean \pm SEM. Statistical analysis determined by two-way ANOVA with post Tukey test for multiple comparisons (** $p < 0.01$). D) Representative H&E-stained lung sections. Scale bar: 2 mm. E) Quantification of cluster metastatic area at day 9. Values are expressed as mean \pm SEM. Statistical significance determined by two-way ANOVA followed by Tukey's post-tests (**** $p < 0.0001$).

Additionally, the analyses of histological hematoxylin and eosin (H&E) stained lung sections were performed. Histological sections clearly revealed much fewer metastatic nodules in the animals treated with J-pHLIP-PD1 in comparison with the control groups (Figure 5.D). The metastatic areas were measured in representative histological sections, showing a wide significant difference between groups (Figure 5.E). Only after treatment with J-pHLIP-PD1, the size of metastatic lesions decreased versus those found in the vehicle (4.5-fold higher), and J-pHLIP or J-PD1 (3.7-fold higher) groups. These differences support those observed in B16-F10-Luc associated luminescence. Remarkably, J-pHLIP-PD1 was found to be the most efficacious with significant metastasis suppression and reduction, indicating the importance of the combination of the peptide pHLIP and the antibody PD-1 in the same particle to facilitate cellular connection between tumor and immune system. All data together show a significant therapeutic effect of the bifunctionalised J-pHLIP-PD1.

Since the treatment aims to restore the immune antitumor response by capturing cytotoxic lymphocytes through PD-1 antibody, we additionally evaluated the presence of cytotoxic CD8+ and helper CD4+ T lymphocytes in the metastatic areas (lungs in this case). Figure 7.A. shows the procedure developed; plasma cells from lungs were isolated and immunophenotyping by flow cytometry and cells were stained with anti-CD3 lymphocyte marker, anti-CD4 and/or anti-CD8. An enhanced percentage of CD4+ and CD8+ T cells were found in the group treated with J-pHLIP-PD1 (Figure 7.B and 7.C), being higher in the case of cytotoxic CD8+ lymphocytes. As expected, CD8+/CD4+ ratio was greater with the complete nanoparticle (J-pHLIP-PD1) in comparison with other groups (Vehicle, J-pHLIP, and J-PD1), which is related with antitumoral (more cytotoxic) activity. These results suggest the implication of cytotoxic lymphocytes in cancer cell elimination when animals were treated with J-pHLIP-PD1.

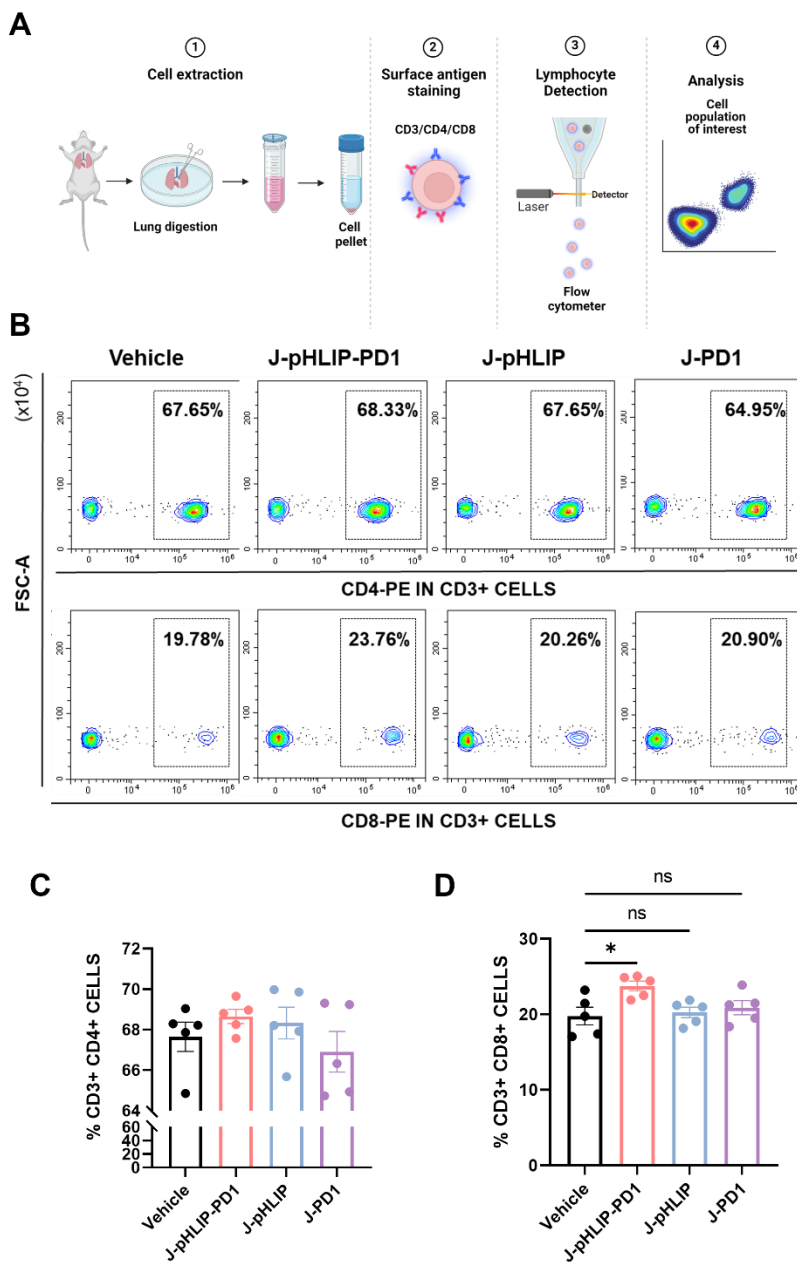


Figure 6. A) Representation of immunophenotyping assay of lymphocyte infiltration in lungs. B) Representative flow cytometry contour plots of mice samples to identify CD4 (up) and CD8 T cells (below). C) Percentage of CD3/CD4 positive cells and D) CD3/CD8 positive cells detected by flow cytometry. Values are expressed as mean \pm SEM. Each data point represents one mouse (n=5). Statistical significance determined by one-way ANOVA followed by Tukey's post-tests (*p<0.05).

4. Conclusions

We report herein an efficient platform (J-pHLIP-PD1) as an immunotherapeutic treatment by (1) promoting the retention of cytotoxic T cell at close proximity to tumor cells, (2) restoring the communication between the tumor and immune system by PD-1 antibody, (3) triggering a significant decline in cancer cell viability, resulting in a reduction of the spread of cancer cells limiting metastasis. The proposed concept is new compared to traditional NPs which usually use a single ligand to target tumor cells or are aimed to improve current immunotherapeutic agents' therapeutic profile. The J-pHLIP-PD1 platform uses nanotechnology to favour tumor cell recognition by facilitating cellular connection between tumor and immune system¹⁹. This solution takes advantage of the well-established PD-1 checkpoint immunotherapy and circumvents the major limitations of the current immunotherapy technologies. A metastatic model has been used for validation as a particularly challenging application scenario. Cancer metastasis causes more than 90% of cancer-related fatalities being most of the treatments ineffective due to the difficult to specifically target these tiny, delocalized tumors. Our system also holds promise as an effective means to neutralize circulating tumor cells with the potential to form new metastases. Lung metastatic clusters suffered a significant reduction when mice were treated with J-pHLIP-PD1 accompanied with the increase of CD8+/CD4+ ratio in metastatic lungs. These results successfully stand the proof-of-concept of redirecting T cells to cancer cells and restoring communication between them using double topospecific functionalized nanoparticles.

Despite the progress, immunotherapies, including cytokines, immune checkpoint therapies, and CAR-T cell treatments, often lead to significant autoimmunity and side effects, needing frequent high-dose. These treatments also face challenges like antigen loss on tumor cells, poor T-cell infiltration, and resistance in the tumor microenvironment. Cancer nanovaccines encounter difficulties in crossing physiological barriers and achieving

adequate antigen targeting, limiting their effectiveness by reducing immune cell infiltration into tumors. The successful demonstration of the proposed strategy paves the way for a new class of immunotherapies based in nanoparticles and engineered to improve the proximity of distinct cell populations with key roles in complex patterns of progression of various types of cancer. In this instance, it would not be difficult to develop new tumor-immune cells binding nanosystems. Our technology is easily adaptable to each cell type and situation and thus overcoming tumor heterogeneity and possible acquired resistance expecting stronger responses than the one caused by current therapies or nanotherapies. This endows the nanoparticle based immune-engaging technology with a great versatility and flexibility and it provides a general platform with groundbreaking translational potential of developing easy-to-make, specific and efficacious immunotherapy for cancers treatment⁴⁷⁻⁴⁸.

5. Materials and methods

5.1. General Techniques

For nanoparticles characterization, we used transmission electron microscopy (TEM), dynamic light scattering (DLS), zeta potential, scanning transmission electron microscopy coupled with electronic energy dispersive x-ray spectroscopy (STEM-EDX) and powder X-ray diffraction (PXRD). TEM images were acquired with a FEI Tecnai Spirit G2 microscope operating at 80 kV. Dynamic light scattering (DLS) studies was performed to determine particle size in a Malvern Zetasizer Nano ZS instrument. Zeta potential was calculated by Smoluchowski model. STEM-EDX was performed using a JEM 2100F instrument. PXRD measurements were performed on a Seifert 3000TT diffractometer using Cu K α radiation.

To ascertain the correct binding of pHLP and PD-1 to the nanoparticle, a reducing SDS-Page gel was performed. 200 μ g of synthesized nanoparticles were suspended in lysis

buffer (1M TrisHCl, 0,5M EDTA, 0,5M EGTA and 10% SDS) (40 μ L) and boiled at 95 $^{\circ}$ C for 10 minutes. The supernatant was recovered after centrifugating 6 minutes at 17000 g, resuspended in 1X sample buffer (62.5 mM Tris-HCl, 10% Glycerol, 2% SDS, 0.3 M β -mercaptoethanol and 0.1% Bromophenol blue) (45 μ L), and boiled at 95 $^{\circ}$ C for 10 minutes. Samples were loaded into an acrylamide gel and subjected to electrophoresis. Finally, acrylamide gels were stained with Coomassie Blue. Similarly, the pHLIP and PD-1 binding quantification was accomplished by the same procedure. Different quantities of peptide (100, 50, 25, 12.5 and 6.25 μ g) or antibody (12.5, 6.25, 3.13 and 1.56 μ g) were prepared in sample buffer and subjected to electrophoresis in parallel with 500 μ g of the corresponding nanoparticles. Finally, gel images were analyzed using Image J software.

5.2. Synthesis of mesoporous silica nanoparticles

To prepare MSNs (type MCM-41), 1.0 g of CTAB was dissolved in 0.48 L of deionized water under sonication and mix with 3.5 ml of 2.0 M NaOH solution. The temperature of the mixture was adjusted to 80 $^{\circ}$ C and then, 5 ml of silica precursor, Tetraethyl orthosilicate (TEOS), was added dropwise under vigorous stirring. This blend was agitated for 2 hours at a constant temperature, and the obtained white solid was washed with water through centrifugation and dried. The final solid was calcined at 550 $^{\circ}$ C for 5 hours under an oxidant atmosphere.

5.3. Synthesis of gold nanoparticles

Gold nanoparticles (20 nm) were prepared according to the Frens method⁴⁹. 100 ml of 0.3 mM HAuCl₄ solution were boiled and then, 5 ml of 39 mM trisodium citrate solution were added. The reaction mixture was heated for 10 min and cooled to room temperature. This procedure was repeated 4 times.

5.4. Synthesis of Janus MSN-Au nanoparticles

Janus MSN-Au nanoparticles (J) were prepared according to the previously reported method⁴⁹. 200 mg of MSN were dispersed in 10 ml of CTAB (1 μ M in 6.7% ethanol aqueous solution) and heated at 75 °C. Then, one gram of paraffin wax was added and melted. After melting the paraffin wax, the blend was stirred at 25000 rpm for 10 min using an Ultra Turrax T-10 homogenizer (IKA, Germany). After that, the resulting Pickering emulsion was stirred at 4000 rpm and 75 °C for 1 hour, and finally, cooled to room temperature and mixed with 10 ml of methanol. To introduce thiol groups on the MSNs, 200 μ l of (3-mercaptopropyl)trimethoxysilane (MPTS) were added and incubated for 3 hours at room temperature under magnetic stirring. The thiolated emulsion was filtered, washed with methanol, and dispersed in 400 ml of freshly prepared gold nanoparticles aqueous solution. The reaction was stirred overnight, then filtered and washed two-times with methanol and three-times with chloroform until the complete removal of the paraffin wax. After drying at 70 °C overnight, Janus nanoparticles were kept in desiccator until use.

5.5. Synthesis of RBITC-APTES dye derivative

RBITC dye functionalized with a triethoxysilane anchor group synthesis was slightly modified from a reported procedure⁵⁰. A solution of 25.4 mg of RBITC (0.047 mmol, 1.1 eq.) in 6 ml of ethanol were mixed with 10.18 μ l of (3-aminopropyl)triethoxysilane (APTES) (0.043 mmol, 1.0 eq) and 3.03 μ l Triethylamine (TEA) (0.022 mmol, 0.5 eq). The reaction vessel was purged with argon and the mixture was stirred in the dark at room temperature overnight. The solvent was removed under reduced pressure to obtain RBITC-APTES as a dark pink solid (33,4 mg, 0.046 mmol) and it was stored in a freezer for later usage.

5.6. Synthesis of J*-pHLIP and J-pHLIP

First, a mixture of 15 mg of Janus MSN-Au nanoparticles and 15.64 μl of (3-isocyanatopropyl)-triethoxysilane (0.06 mmol, 4 mmol/g Janus) were suspended in 2 ml of anhydrous CH_3CN and purged with argon. The suspension was stirred at room temperature for 5.5 h to partially functionalize the mesoporous side with isocyanate groups, and the solid was isolated by centrifugation and washed with CH_3CN , EtOH, and distilled water (1 x 2 ml). Then, the modified Janus MSN-Au nanoparticles were suspended in 1 ml of CH_3CN , and 15 mg of pHLIP peptide (Seq. ACEQNPIYWARYADWLFTPLLLLDLALLVDADEGT) dissolved in distilled water added to the mixture. Then 30 μL of triethylamine (TEA) were added. The mixture was stirred at room temperature 2h to form the covalent urea bond between the isocyanate group and the N-terminal amine group of the peptide. After that, the solid was washed with distilled water several times. The suspension was stirred at room temperature for 5.5 h, and the solid was isolated by centrifugation and washed with DMSO and distilled water several times to obtain J-pHLIP. On the other hand, to attach the RBITC to the surface, the nanoparticles were suspended in 2 ml of anhydrous CH_3CN and 11.4 mg of RBITC-APTES (0.015 mmol, 1 mmol/g Janus MSN-Au) was added. The suspension was stirred at room temperature for 5.5 h, and the solid was isolated by centrifugation and washed with DMSO and distilled water several times to obtain J*-pHLIP.

5.7. Preparation of J-PD1, J*-pHLIP-PD1 and J-pHLIP-PD1 nanoparticles

To synthesize the different nanoparticles with the antibody, αPD1 (CD279 (PD-1) Monoclonal Antibody eBioJ105 (J105) (14-2799-37) from Life technologies or InVivoMab anti-mouse PD-1 RMP1-14 (BE0273) from Abyntek) was thiolated using the Traut's reagent, which reacts with primary amines to introduce sulfhydryl groups. First, 50 μg of αPD1 was mixed with 50 μl of PB 0.1M pH 8 EDTA 2mM and 0.5 μl of Traut's Reagent (14 mM in PB 0.1M pH 8 EDTA 2mM) was added to the antibody solution. The solution was

incubated for 1 hour at 300 rpm and room temperature. Next, to separate the thiolated antibody from excess Traut's reagent, a desalting column was used. The thiolated antibody was incubated with J, J*-pHLIP or J-pHLIP nanoparticles in a ratio 25 µg/mg respectively for 1h at 1200 rpm. Finally, J-PD1, J*-pHLIP-PD1 or J-pHLIP-PD1 were washed with PBS and stored with PBS at 4 °C.

5.8. Cell culture conditions

The Sk-Mel-103 human melanoma and Jurkat cell line was obtained from ATCC. Cells were maintained in DMEM and RPMI respectively, supplemented with 10% FBS. Green fluorescent Jurkat cell line were purchased from Innoprot and maintained in RPMI supplemented with 10% heat-inactivated FBS and 250µg/ml of G-418. All cell lines were incubated in 5% CO₂ at 37 °C.

5.9. Evaluation of PD-1 expression by Western Blot

For Jurkat and Jurkat green, cells were cultured in a 6-well plate at a cellular density of 700,000 cel/well for 24 hours. In the case of activated Jurkat T cells, a 6-well plate was coated with αCD3 (1 µg/ml) in PBS for 2h. Afterwards, 700,000 cel/ml of Jurkat cells and αCD28 (5µg/ml) were incorporated in RPMI 10% FBS. The plate was incubated 72h. To generate whole-cell extracts, cells were lysed in a buffer containing 25 mM Tris-HCl, pH 7.4, 1mM EGTA, 1% SDS and protease and phosphatase inhibitors. The protein concentration was quantified by using the Pierce BCA Protein Assay Kit (Thermo Fisher, 10741395). SDS-Page was used to separate the proteins in the cell lysates, they were transferred to nitrocellulose membranes, blocked with 5% non-fat milk, washed with 0.1% Tween/PBS, and incubated overnight with the specific primary antibody. Membranes were washed and incubated with the secondary antibody conjugated to horseradish peroxidase for 1h. The primary antibodies, anti-PD-1 antibody and anti-GAPDH antibody, were prepared at 1:1000 dilutions in 5% non-fat milk. The secondary antibodies, anti-mouse IgG antibody (Sigma, A4416) and anti-rabbit IgG antibody were prepared at 1:3000

dilutions in 5% non-fat milk. Chemiluminescence was detected after Lumi-Light Western Blotting Substrate (Amersham Pharmacia Biotech) incubation.

5.10. Flow cytometric determination of PD-1 expression

Cells were counted and transferred into an eppendorf at density of 300,000 cells/eppendorf. They were wash twice with PBS 2% BSA and incubated for 1h with anti-PD1-APC according to the manufacturer's instructions in PBS 2% BSA at 4°C. After that, cells were washed three times with PBS 2% BSA and resuspended in 200 µl of PBS 2% BSA. Finally, APC-positive cells were assessed by flow cytometry on a CytoFlex S device (Beckman Coulter) followed by data analysis with CytoExpert software.

5.11. Evaluation of nanoparticle attachment to cell membrane

To evaluate cellular localization of J*-pHLIP, we employed fluorescence confocal microscopy and transmission electronic microscopy. In the case of fluorescence, Sk-Mel-103 were seeded on glass coverslip in a 6-well plate at density of 300,000 cel/ml and allowed to attach overnight. Next day, cells were treated with 50 µg/ml of J*-pHLIP in DMEM pH 7.5 and 6.5 for 30 min. Then, the corresponding medium was changed and incubated for another 30 min. Cells were incubated in the presence of the DNA marker Hoechst 34580 for 20 min and in the presence of membrane marker WGA 647 conjugate for 5 min before being analyzed in Z-stacks by a confocal Leica TCS SP8 HyVolution II microscope.

For transmission electronic microscopy, Sk-Mel-103 were seeded in a chamber slide at 20,000 cel/well and incubated overnight. Then, 50 ug/mL of J*-pHLIP were incorporated to the wells in DMEM pH 7.5 and 6.5 for 30 min and after, medium was changed and plates incubates for a total of 1h. Chamber slides were washed and fixed with 3% of glutaraldehyde in phosphate buffer 0.1 M, dehydrated in ethanol and stained

with uranyl acetate (1%) and osmium tetroxide (1%). Samples were included in epoxy resin (Araldite), sectioned, and analyzed using a microscope FEI Tecnai Spirit G2 operating at 80 kV with a digital camera (Soft Image System, Morada).

5.12. Lymphocytes migration and retention assay

First, 8µm pore PET permeable inserts (GBO, 662638) were coated with 10µg/cm³ of fibronectin diluted in PBS at 37 °C to allow the adhesion of suspension Jurkat cells. After 1h, inserts were washed and dried in the hood. In parallel, Sk-Mel-103 melanoma cells were stained using the Cell tracker deep red (Fisher, C34565) and DragQ5 (Thermo Fisher, 62251) for 40 min. Then, cells were seeded at a confluency of 100,000 cel/insert in a drop on the bottom of the insert and incubated overnight for attachment. After, the drop was aspirated and a new drop containing 50µg/ml of J*-pHLIP or J*-pHLIP-PD1 in DMEM pH 6.5 was incorporated, using parafilm on the top of the insert to prevent liquid filtration. This was incubated at 37 °C for 30 min and after that, inserts were washed with medium and Jurkat Green was incorporated at a density of 150,000 cell/insert on the top and let them migrate for 4h. Jurkat migration and retention were analyzed by confocal microscopy and images were quantified using Image J.

5.13. Evaluation of therapeutic effect in cocultures

First, Jurkat cells should be stimulated. For this purpose, a 6-well plate was coated with αCD3 (1 µg/ml) in PBS for 2h. Afterwards, 700,000 cells/ml of Jurkat cells and αCD28 (5µg/ml) were incorporated in RPMI 10% FBS and the plate was incubated 72h. Then, to evaluate the effect in cocultures, Sk-Mel-103 were seeded at density of 10,000 cells/well in 96-well plate and incubated overnight. Cells were treated with 50µg/ml of J-pHLIP or J-pHLIP-PD1 in DMEM pH 6.5 for 30 min. Then, medium was removed and stimulated Jurkat cells were added in RPMI (pH 7.5) at 1:10 ratio. After a 72h incubation, medium with Jurkat cells was removed, and the plate was washed to remove cells in suspension. Finally, viability was determined using WST-1 viability reagent by absorbance measure at 595 nm

in a Wallac 1420 Workstation. Absorbance values were normalized, and viability percentages calculated establishing control wells values as 100%.

5.14. B16-F10-Luc Metastatic Model

Animal procedures were approved by Ethical Committee for Research and Animal Welfare Generalitat Valenciana, Conselleria d'Àgricultura, Medi ambient, Canvi climàtic i Desenvolupament Rural (license number 2022 VSC PEA 280). Female Balb/cOlaHsd wild type mice (37 days old) (Envigo) were intravenously injected in the tail with $5 \cdot 10^5$ B16-F10-Luc cells (melanoma cell line that express constitutively the luciferase gene) in a volume of 100 μ l. After 30 minutes, 0.5 mg of J-pHLIP, J-PD1 or J-pHLIP-PD1 were intravenously injected in the tail of each mouse (100 μ l, PBS) (25 mg/Kg). Mice were monitored on an IVIS spectrum imaging system. D-luciferin (15 mg/ml, 200 μ l) was administered via subcutaneous injection, 10 min prior to image acquisition and bioluminescence signal was analyzed by using the Living Imaging software from Caliper Life Sciences. Mice were sacrificed at day 9 and organs were obtained for ex vivo evaluation.

5.15. Histological analysis of lungs for metastasis evaluation

To evaluate the presence of metastatic nodules, one lung from each mouse was fixed in 4% PFA. After that, lungs were embedded in paraffin for tissue sections (5 μ m) and hematoxylin-eosin staining (H&E). Stained sections were scanned in Leica Aperio Versa at 20x magnification. Metastatic B16-F10 cell clusters were microscopically counted, and metastatic areas quantified in different lung sections from three animals per group using ImageScope.

5.16. Isolation and immunophenotyping of plasma cells from ex vivo lungs of mice

The other lung of each mouse was disintegrated and suspended in RPMI-1640 medium (1.5 ml) and digestion buffer (2 mg Collagenase type IV (MERK C5138), 50 units type IV DNase I from bovine pancreas (DN25 SIGMA-ALDRICH) and 2 ml of RPMI- 1640 medium) (1.5 ml) and incubate for 45 min at 37 °C (200 rpm). Then 2 ml of RPMI-1640 were added and the mixture transferred to a 50 ml conical tube through a 70 µm cell strainer followed by a second filtration through 40 µm cell strainer. The samples were centrifuged at 300 g for 5 minutes, resuspended in erythrocyte lysis buffer 1X and incubated at room temperature for 1 minute to remove erythrocytes. Then 10 ml of PBS were added, and cells were isolated by centrifugation at 300 g for 5 minutes and counted. To proceed to immunophenotyping, $3 \cdot 10^5$ cells were stained with 2 µg/ml of anti-CD3-APC-Cy7 in combination with 2 µg/ml of anti-CD8-PE or anti-CD4-PE in PBS 5% FBS at room temperature. After 20 minutes, samples were washed three times with PBS 5% FBS and resuspended in 200 µl of PBS. Finally, positive cells were assessed by flow cytometry on a CytoFlex S device (Beckman Coulter) followed by data analysis with CytoExpert software.

5.17. Statistical analysis

All of the values represent the mean \pm SEM of at least three independent experiments. In the case of animal studies (n=5 mice/group), mice were randomly assigned to treatment groups. Significance from the different experiments was mainly determined by one-way or two-way ANOVA followed by Tukey post-tests for multiple comparisons as indicated in the figures using GraphPad 8 software. A p-value below 0.05 was considered statistically significant and indicated with asterisk: *p < 0.05, **p < 0.01, and ***p < 0.001 and ****p < 0.0001).

6. References

1. Daneshpour, H. & Youk, H. Modeling cell–cell communication for immune systems across space and time. *Curr Opin Syst Biol* **18**, 44–52 (2019).
2. Escriche-Navarro, B. et al. Mesoporous Silica Materials as an Emerging Tool for Cancer Immunotherapy. *Advanced Science* **9**, 1-24 (2022).
3. Vinay, D. S. et al. Immune evasion in cancer: Mechanistic basis and therapeutic strategies. *Semin Cancer Biol* **35**, S185–S198 (2015).
4. Schuster, M., Nechansky, A., Loibner, H. & Kircheis, R. *Cancer immunotherapy. Biotechnol J* **1**, 138–147 (2006).
5. Dillman, R. O. Cancer immunotherapy. *Cancer Biother Radiopharm* **26**, 1–64 (2011).
6. Ahmad, M. Z. et al. Emerging advances in synthetic cancer nano-vaccines: opportunities and challenges. *Expert Rev Vaccines* **19**, 1053–1071 (2020).
7. Marin-Acevedo, J. A. et al. Next generation of immune checkpoint therapy in cancer: New developments and challenges. *J Hematol Oncol* **11** (39), 1-20 (2018).
8. Ahmed, M. M. E. Car-T Cell Therapy: Current Advances and Future Research Possibilities. *Journal of Scientific Research in Medical and Biological Sciences* **2**, 86–116 (2021).

9. Yu, M., Yang, W., Yue, W. & Chen, Y. Targeted Cancer Immunotherapy: Nanoformulation Engineering and Clinical Translation. *Advanced Science* **9**, 1-37 (2022).
10. Guo, Q., Huang, F., Goncalves, C., del Rincón, S. V. & Miller, W. H. Translation of cancer immunotherapy from the bench to the bedside in *Advances in Cancer Research. Elsevier* **143**, 1–62 (2019).
11. Shi, Y. Clinical Translation of Nanomedicine and Biomaterials for Cancer Immunotherapy: Progress and Perspectives. *Adv Ther* **3**, 1-9 (2020).
12. Rivoltini, L. et al. Immunity to cancer: Attack and escape in T lymphocyte-tumor cell interaction. *Immunol Rev*, **188**, 97–113 (2002).
13. Díaz, L. R. et al. Imbalance of immunological synapse-kinapse states reflects tumor escape to immunity in glioblastoma. *JCI Insight* **3**, 1-17 (2018).
14. Kearney, C. J., Brennan, A. J., Darcy, P. K. & Oliaro, J. The Role of the Immunological Synapse Formed by Cytotoxic Lymphocytes in Immunodeficiency and Anti-Tumor Immunity. *Crit Rev Immunol* **35**, 325–347 (2015).
15. Stephan, M. T., Stephan, S. B., Bak, P., Chen, J. & Irvine, D. J. Synapse-directed delivery of immunomodulators using T-cell-conjugated nanoparticles. *Biomaterials* **33**, 5776–5787 (2012).
16. González, P. A. et al. Modulation of tumor immunity by soluble and membrane-bound molecules at the immunological synapse. *Clin Dev Immunol*, **2013**, 1-19 (2013).

17. Stephan, M. T., Stephan, S. B., Bak, P., Chen, J. & Irvine, D. J. Synapse-directed delivery of immunomodulators using T-cell-conjugated nanoparticles. *Biomaterials* **33**, 5776–5787 (2012).
18. Im, S. et al. Harnessing the Formation of Natural Killer–Tumor Cell Immunological Synapses for Enhanced Therapeutic Effect in Solid Tumors. *Advanced Materials* **32**, 1–8 (2020).
19. Llopis-Lorente, A. et al. Interactive models of communication at the nanoscale using nanoparticles that talk to one another. *Nat Commun* **8**, 1–7 (2017).
20. Goldberg, M. S. Improving cancer immunotherapy through nanotechnology. *Nat Rev Cancer* **19**, 587–602 (2019).
21. Yang, Z., Ma, Y., Zhao, H., Yuan, Y. & Kim, B. Y. S. Nanotechnology platforms for cancer immunotherapy. *Wiley Interdiscip Rev Nanomed Nanobiotechnol* **12**, 1–28 (2020).
22. Francis, D. M. et al. Drug-eluting immune checkpoint blockade antibody-nanoparticle conjugate enhances locoregional and systemic combination cancer immunotherapy through T lymphocyte targeting. *Biomaterials* **279**, 1–27 (2021).
23. Fang, R. H., Kroll, A. V. & Zhang, L. Nanoparticle-Based Manipulation of Antigen-Presenting Cells for Cancer Immunotherapy. *Small* **11**, 5483–5496 (2015).
24. Zhuang, J. et al. Nanoparticle delivery of immunostimulatory agents for cancer immunotherapy. *Theranostics* **9**, 7826–7848 (2019).

25. Yang, Y. S. S. et al. Targeting small molecule drugs to T cells with antibody-directed cell-penetrating gold nanoparticles. *Biomater Sci* **7**, 113–124 (2019).
26. Riley, R. S., June, C. H., Langer, R. & Mitchell, M. J. Delivery technologies for cancer immunotherapy. *Nat Rev Drug Discov* **18**, 175–196 (2019).
27. Le, Q. V., Choi, J. & Oh, Y. K. Nano delivery systems and cancer immunotherapy. *J Pharm Investig* **48**, 527–539 (2018).
28. Pérez-Calabuig, A. M. et al. An enzyme-controlled Janus nanomachine for on-command dual and sequential release. *Chemical Communications* **56**, 6440–6443 (2020).
29. Llopis-Lorente, A. et al. Stimulus-responsive nanomotors based on gated enzyme-powered Janus Au-mesoporous silica nanoparticles for enhanced cargo delivery. *Chemical Communications* **55**, 13164–13167 (2019).
30. Villalonga, R. et al. Enzyme-controlled sensing-actuating nanomachine based on janus au-mesoporous silica nanoparticles. *Chemistry - A European Journal* **19**, 7889–7894 (2013).
31. Wyatt, L. C. et al. Peptides of pHLIP family for targeted intracellular and extracellular delivery of cargo molecules to tumors. *Proc Natl Acad Sci U S A* **115**, E2811–E2818 (2018).
32. Yao, L. et al. pHLIP peptide targets nanogold particles to tumors. *Proc Natl Acad Sci U S A* **110**, 465–470 (2013).

33. Andreev, O. A., Engelman, D. M. & Reshetnyak, Y. K. PH-sensitive membrane peptides (pHLIPs) as a novel class of delivery agents. *Mol Membr Biol* **27**, 341–352 (2010).
34. Pentcheva-Hoang, T., Chen, L., Pardoll, D. M. & Allison, J. P. Programmed death-1 concentration at the immunological synapse is determined by ligand affinity and availability. *Proc Natl Acad Sci U S A* **104**, 17765–17770 (2007).
35. Jang, J. H. et al. Imaging of Cell–Cell Communication in a Vertical Orientation Reveals High-Resolution Structure of Immunological Synapse and Novel PD-1 Dynamics. *The Journal of Immunology* **195**, 1320–1330 (2015).
36. Ribas, A. Tumor Immunotherapy Directed at PD-1. *New England Journal of Medicine* **366**, 2517–2519 (2012).
37. Salmaninejad, A. et al. PD-1/PD-L1 pathway: Basic biology and role in cancer immunotherapy. *J Cell Physiol* **234**, 16824–16837 (2019).
38. Wolchok, J. D. PD-1 Blockers. *Cell* **162**, 937 (2015).
39. De Luis, B., Llopis-Lorente, A., Sancenón, F. & Martínez-Máñez, R. Engineering chemical communication between micro/nanosystems. *Chem Soc Rev* **50**, 8829–8856 (2021).
40. de Luis, B. et al. Nanoprogrammed Cross-Kingdom Communication Between Living Microorganisms. *Nano Lett* **22**, 1836–1844 (2022).
41. Zhang, X., Fu, Q., Duan, H., Song, J. & Yang, H. Janus Nanoparticles: From Fabrication to (Bio)Applications. *ACS Nano* **15**, 6147–6191 (2021).

42. Khoei, S. & Nouri, A. Preparation of Janus nanoparticles and its application in drug delivery in Design and Development of New Nanocarriers. *Elsevier Inc.* **2018**, 145–180 (2018).
43. Agrawal, G. & Agrawal, R. Janus Nanoparticles: Recent Advances in Their Interfacial and Biomedical Applications. *ACS Appl Nano Mater* **2**, 1738–1757 (2019).
44. Mitchell, M. J., Wayne, E., Rana, K., Schaffer, C. B. & King, M. R. Trail-coated leukocytes that kill cancer cells in the circulation. *Proc Natl Acad Sci USA* **111**, 930–935 (2014).
45. Mitchell, M. J., Wayne, E. C., Rana, K., Schaffer, C. B. & King, M. R. Unnatural killer cells: TRAIL-coated leukocytes that kill cancer cells in the circulation. in IEEE Annual Northeast Bioengineering Conference, NEBEC vol. 306 1–6 (2014).
46. Wayne, E. C. et al. TRAIL-coated leukocytes that prevent the bloodborne metastasis of prostate cancer. *Journal of Controlled Release* **223**, 215–223 (2016).
47. Zhang, L. et al. Programmable Bispecific Nano-immunoengager That Captures T Cells and Reprograms Tumor Microenvironment. *Nano Lett* **22**, 6866–6876 (2022).
48. Alhallak, K. et al. Nanoparticle T-cell engagers as a modular platform for cancer immunotherapy. *Leukemia* **35**, 2346–2357 (2021).
49. Frens, G. Controlled Nucleation for the Regulation of the Particle Size in Monodisperse Gold Suspensions. *Nature Physical Science* **241**, 20–22 (1973).

50. Klippel, N., Jung, G. & Kickelbick, G. Hybrid inorganic-organic fluorescent silica nanoparticles—influence of dye binding modes on dye leaching. *J Solgel Sci Technol* **107**, 2-19 (2023).

Acknowledgements

This work was supported by the European Research Council (ERC) via Advanced Grant (101052997, EDISON). The authors thank the Spanish Government (project PID2021-126304OB-C41 by MCIN/ AEI /10.13039/501100011033/ and by European Regional Development Fund - A way of doing Europe. This study was also supported by the Generalitat Valenciana (project PROMETEO CIPROM/2021/007). This study forms part of the Advanced Materials program (MFA/2022/049) and was supported by MCIN with funding from European Union NextGenerationEU (PRTR-C17.I1) and by Generalitat Valenciana. This work was supported by the European Research Council (ERC) via Advanced Grant (101052997, EDISON) and by CIBER -Consortio Centro de Investigación Biomédica en Red- (CB06/01/2012), Instituto de Salud Carlos III, Ministerio de Ciencia e Innovación. E.L-S is grateful for her FPU fellowship funded by MINECO (FPU18/06539). F.J.H thanks MIU for his FPU grant (FPU20/06021). Graphical images and schemes were created with BioRender.com.

Author contributions

E.L.-S.: Experimental design, performing *in vitro* experiments, data analysis, discussion, and writing. F.J.H.: Nanoparticle development and characterization. A. O.-B: Contributed to *in vitro* experiments and *ex vivo* sample processing. A. E.: Contributed to *in vivo* experiments and *ex vivo* sample processing. N.J.-A.: Contributed to *in vivo* experiments. P. D-S. Nanoparticle development and characterization. A.G.-F.: Experimental design, *in vivo* experiments, analysis, experiments discussion, Conceptualization, Writing – review & editing, Supervision. R.M.-M.: Conceptualization,



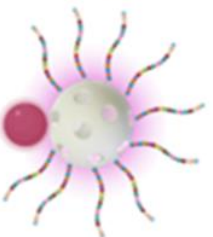
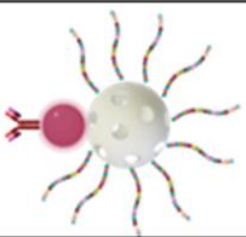
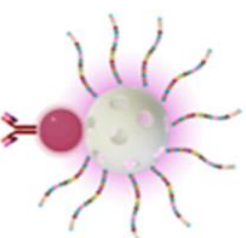

Project administration, Writing – review & editing, Supervision. All authors have approved the final version of the manuscript.

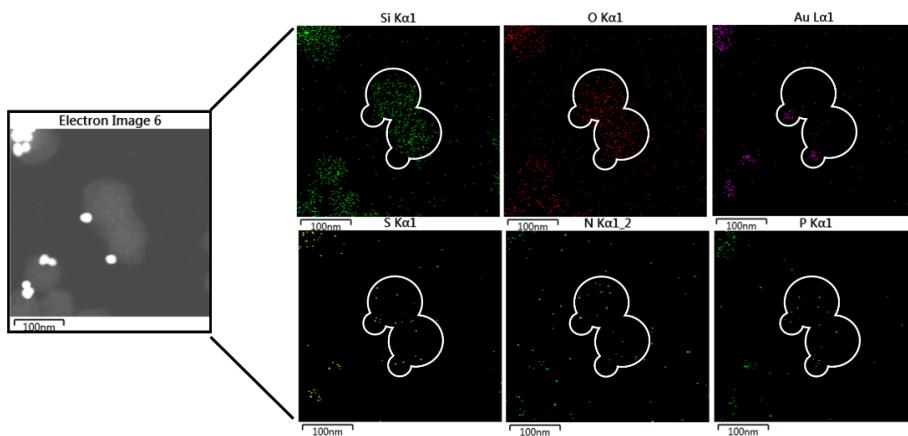
Competing interests

The authors declare no competing financial interests.

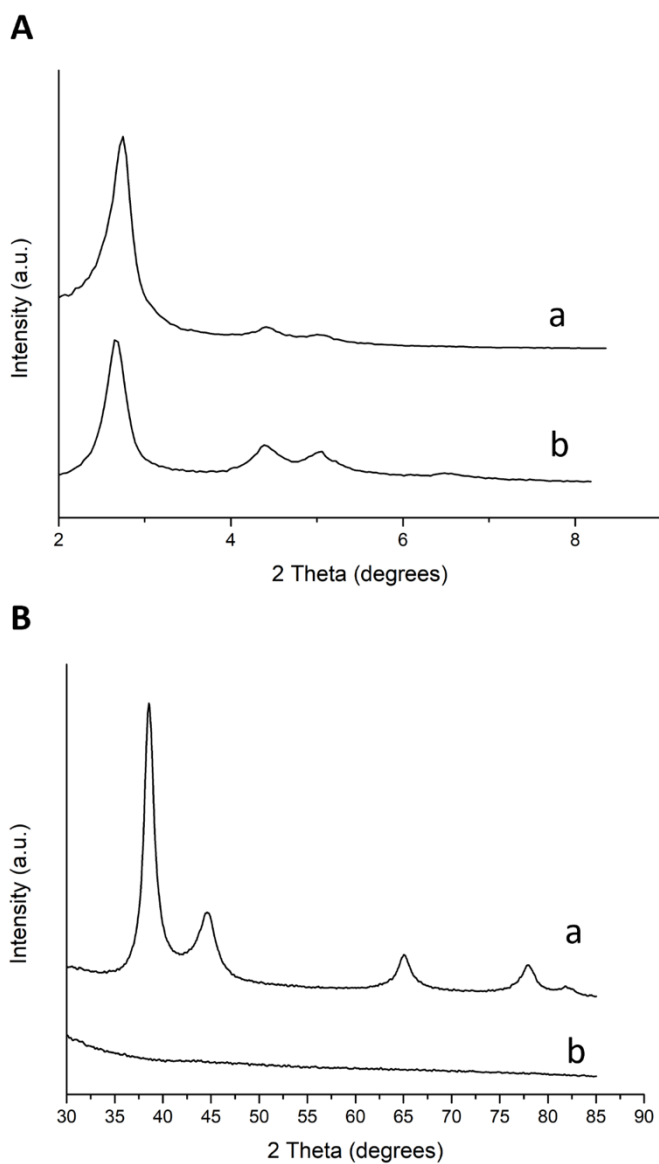
7. Supporting information

Supplementary Table 1. Schematic representation of nanodevices' structure. (Schemes were created by the authors on Biorender)

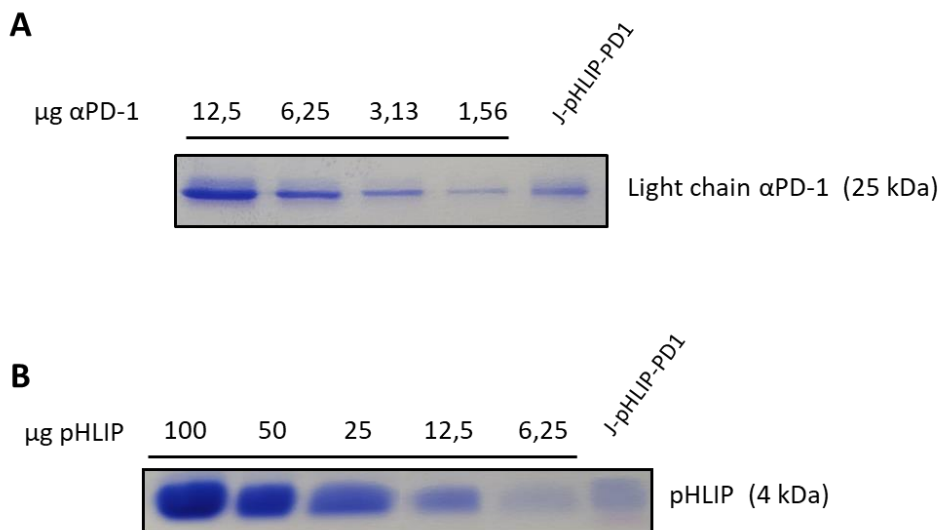
Abbreviation	Description	Scheme
J	Janus nanoparticle	
J-pHLIP	Janus nanoparticle functionalized in the silica surface with pHLIP peptide	
J*-pHLIP	Janus nanoparticle functionalized in the silica surface with Rhodamine B and pHLIP peptide	
J-pHLIP-PD1	Janus nanoparticle functionalized in the silica surface with pHLIP peptide, and in the gold surface with α PD-1 antibody	
J*-pHLIP-PD1	Janus nanoparticle functionalized in the silica surface with Rhodamine B and pHLIP peptide, and in the gold surface with α PD-1 antibody	
J-PD1	Janus nanoparticle functionalized in the gold surface with α PD-1 antibody	



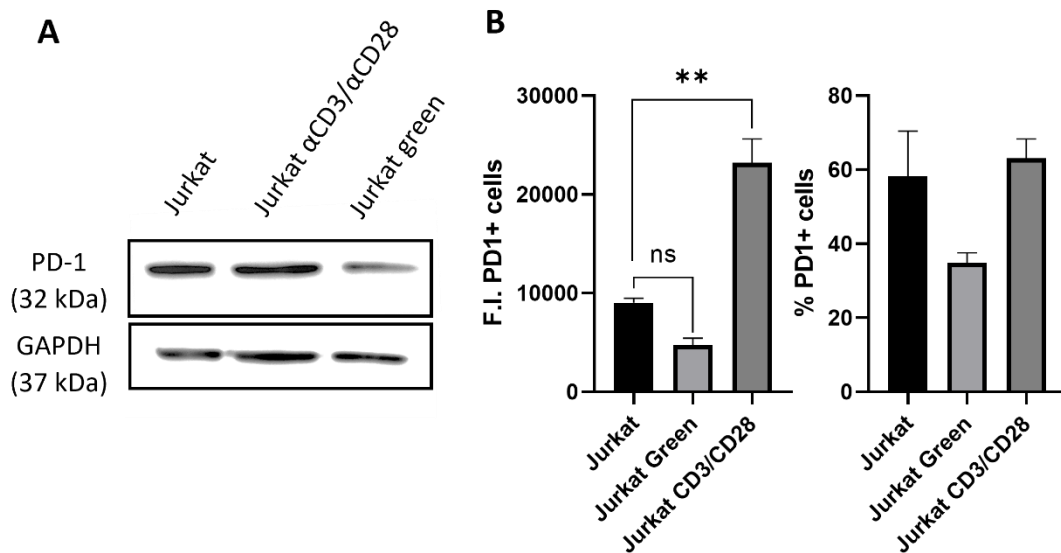
kSupplementary Figure 2. STEM image and STEM-EDX elemental mapping of Si atoms, O atoms, Au atoms, S atoms (attributed to the disulfide bonds functionalized to gold surface and the peptide), N and P atoms (attributed to antibody and peptide) in J-pHLIP-PD1.



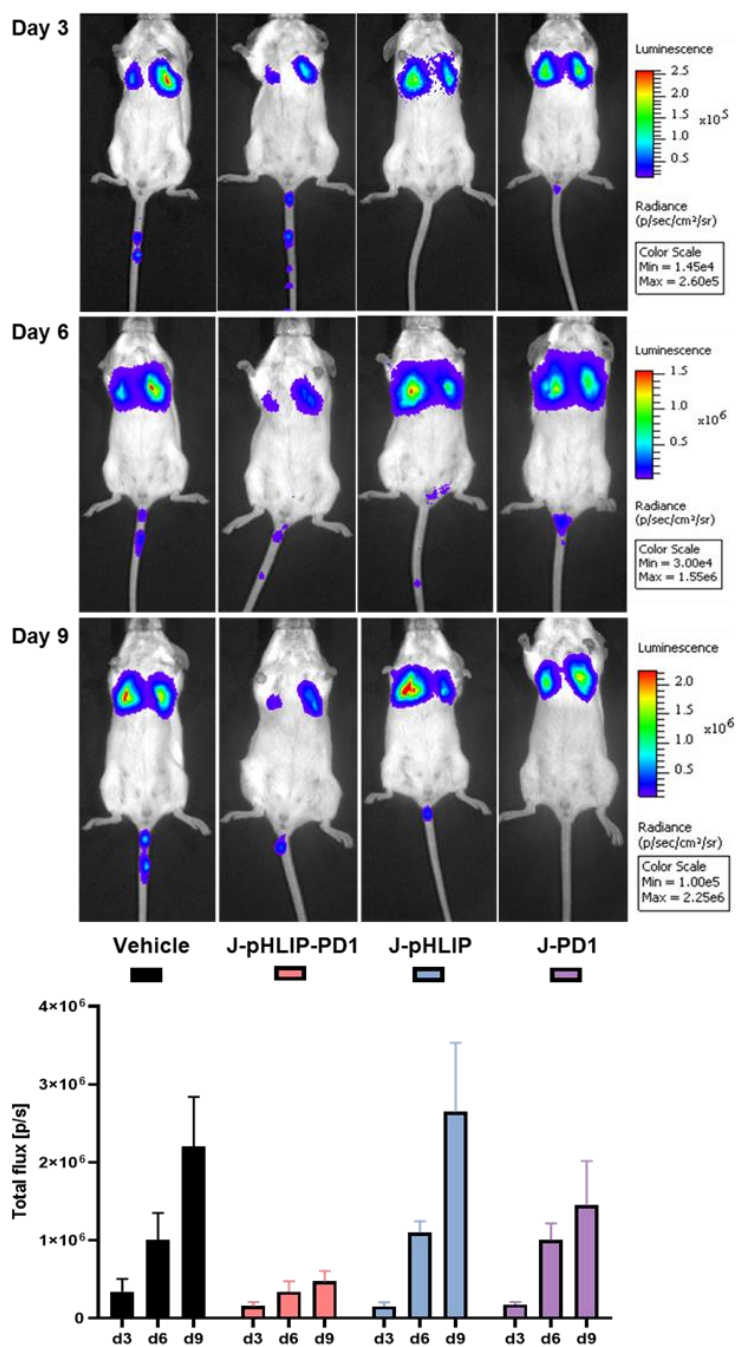
Supplementary Figure 3. Powder X-ray patterns at A. low angles and B. high angles of MSNs (A) and Janus MSN-Au nanoparticles (B).



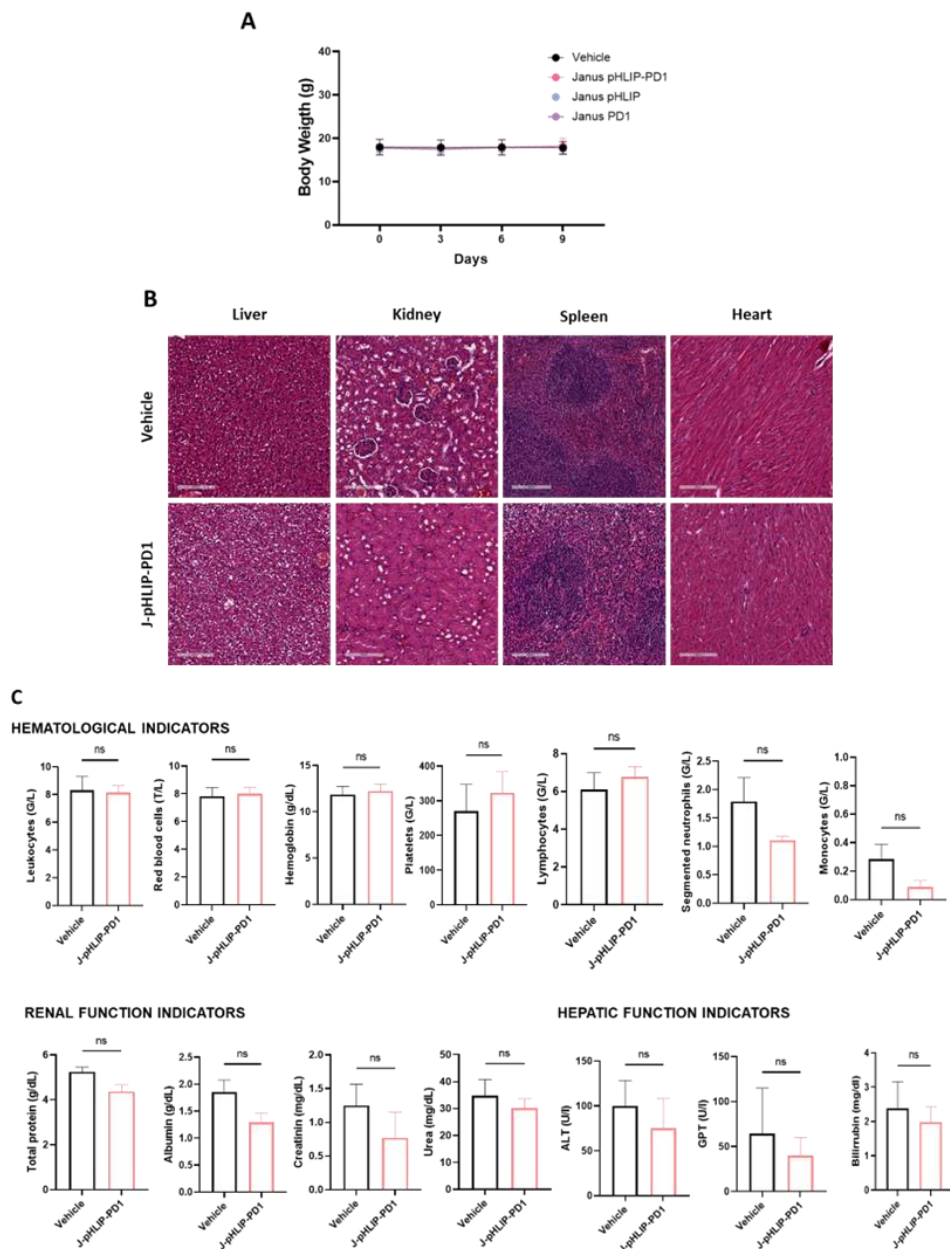
Supplementary Figure 4. SDS-Page gel electrophoresis assay. A. Quantification of αPD-1 and B. pHLIP peptide.



Supplementary Figure 5. A. Western Blot analysis of PD-1 expression in Jurkat cells, unstimulated or stimulated with anti-CD3 and anti-CD28 for 72h and in Jurkat green cells (expected band 32 kDa). GAPDH (37 kDa) was included as a loading control. B. Percentage of PD-1 positive cells (left) and fluorescence intensity of PD-1 positive cells (right) determined by flow cytometry. Data represent means ± SEM (n=3). Statistical analysis was carried out using GraphPad Prism 8, and results were compared by One-Way ANOVA tests (**p<0.01).



Supplementary Figure 6. A. Representative IVIS images of luminescence monitoring at day 3, 6 and 9 (luminescence intensity is represented according to the min-max. range detected each day). B. Quantification of photon flux (photons per second) from IVIS images. Data represent means \pm SEM (n=5 mice/group).



Supplementary Figure 7. A) Weight changes from each group of mice treated with the different nanoparticles and the B16-F10-Luc cells. Data represents means \pm SEM ($n=5$). B) H&E-staining of main organs from metastatic mice model. Main organs from vehicle groups and mice treated with the complete nanoparticle (J-pHLP-PD1). Scale Bar, 200 μ m. C) Hemogram and biochemistry blood analyses of B16-F10-Luc cells injected mice treated with vehicle or the complete nanoparticle. Data represents means \pm SEM ($n=5$ mice/group). Statistically significant determined by t-test.

Discussion

The research performed in this PhD thesis has aimed the development of new versatile and innovative advanced nanodevices for anti-tumor therapy. All described systems share a general characteristic in their structure; they are based on mesoporous support accurately functionalized with other inorganic materials and/or with biological structures. We decided to use mesoporous silica according to its versatility and intrinsic characteristics, such as high stability, biocompatibility, or the possibility to be functionalized, making it an appealing material for biomedical applications.

The purpose of the design of these systems is to get over the current limitations of traditional and new modalities of cancer treatments. In the last years, nanomedicine has undergone growth in the number of nanodevices applied to cancer treatment. This area is under continuous research because of the ineffectiveness of the actual treatments. Many of the nanodevices developed allow surpassing limitations like drug resistance or associated off-target toxicity and are currently in the market or in clinical trials. However, despite the improvements in this area, there are still challenges to overcome, thus limiting the nanomedicine-based tumor therapies translation to clinics. Between the traditional treatment obstacles found in clinics, there is a reduced penetrability in tumor tissue due to transvascular pressure gradient which can be solved by using recently designed self-moving nanoparticles. We have contributed to this field in this thesis by designing two systems based on “two-face” Janus nanoparticles that convert chemical energy into mechanical movement. Besides, the silica face can act as a drug container and deliver the cargo via specific stimulus.

In a first example, Janus Au-MSNs have been designed as nanomotors, with self-propulsion provided by the enzyme catalase in the gold face and drug release capabilities in the mesoporous face controlled in response to GSH (high levels of GSH are found in cells). To date, there are not too many reports of gated materials combined with chemical-powered nanomotors. Besides, this system employs catalase as strategy to achieve self-movement, which is commonly present in living organisms¹. Movement only in the

presence of fuel (H_2O_2) was proved along with the effect of movement on drug delivery efficiency; Doxorubicin delivery suffers a significant upturn when the nanobot is being propelled. Cargo release occurs only when the GSH is present (as inside the cells) via the reduction of the disulfide bonds in the gatekeeper. Moreover, propelled nanoparticles improved drug release in cells. Despite this, a high amount of fuel was required to propel the nanoparticles which limits its biomedical application. Thereby, new designs are required to improve fuel catalysis and driving efficiency, thus increasing biocompatibility. Despite obtaining promising results in tumor cell culture, this design is still a proof of concept and further investigations are necessary to validate its behavior, for example in microfluidic devices, simulating penetration in capillary vessels, as well as in more realistic scenarios such as spheroids or in vivo conditions.

Following with the interest in the use of propelled nanodevices for enhanced drug delivery, an innovative platinum-mesoporous silica nanomotor has been described in chapter 2. In this case, the nanomotor is composed of MSN anchored to a platinum nanodendrite. Janus Pt-MSNs were prepared by the conjugation of two different nanoparticles in a single nanodevice by the described Pickering emulsion method, instead of chemical or physical deposition of Pt onto the silica support reported in most reported designs². This synthesis procedure provides a feasible and novel way to obtain Janus Pt-MSNs. Moreover, the mesoporous silica nanoparticle face was loaded with a drug and a disulfide-containing oligo(ethylene glycol) chains was used as a gating system. These Janus-type nanomotors present an ultra-fast self-propelled motion. Likewise, nanomotors exhibited a directional movement and enhanced internalization and cargo delivery in THP-1 cells, as demonstrated using a microchip device that mimics penetration from capillary to post-capillary vessels. The nanosystem shows many suitable characteristics for biomedical applications, such as rapid autonomous motion, versatility, and stimuli-responsive controlled drug release. Given the number of stimuli-responsive gatekeepers available that can be tested in combination with different materials and enzymes, this is a promising and versatile strategy that can be applied to cancer cells to overcome therapy

limitations. Future improvements in nanomotor design should involve the use of more selective drug delivery, the use of more biocompatible fuels as well as the validation of enhanced penetrability and thus therapeutic activity in 3D and in vivo models. Nevertheless our system represents a powerful tool in the field, with superior capabilities compared to conventional nanocarriers, making possible an easier transport of drugs to specific targeted organs to provide maximum therapeutic efficacy.

Analogous to traditional treatments, novel approaches, such as immunotherapy, can be favored by the use of nanotechnology. In this regard, some aspects to be improved with the use of nanoparticles include the combination of several therapeutic strategies in a single treatment and the recruitment of a significant number of effective cytotoxic T cells responsible for triggering tumor cell death.

Based on the above, we designed MSN loaded with a PD-L1 inhibitor (JQ1) and capped with polyethyleneimine (PEI) and a siRNA targeting TGF- β (TGF- β siRNA). We believed that inhibition of the TGF- β production and the PD-1/PD-L1 checkpoint might be a feasible strategy to increase T cell infiltration and cytotoxicity and thus overcome tumor immune escape. Our aim was to create a novel platform for integrating two established immune-based anti-tumor approaches to improve their effectiveness. Although these approaches, PD-L1 checkpoint and TGF- β inhibition, have been extensively exploited alone and in combination³, our system offers a unique aspect of novelty. The unique characteristics of MSN allow the design of millions of combined synergistic therapies in a unique nanodevice. On the other hand, PD-L1 blockage is usually accomplished using antibodies that are unstable in the fluids, have low bioavailability, and require multiple doses. Instead of antibodies we have used the newly discovered JQ-1 PD-L1 inhibitor that acts at the transcriptional level, is still under research having promising preliminary results, yet its use limited by its very short half-life and its poor water solubility^{4,5}. Besides, TGF- β effect is mostly controlled by acting on its receptor. In contrast, we attempted to inhibit TGF- β production by using siRNA targeting TGF- β . For this, we incorporated into

the nanoparticle the positively charged polymer PEI for efficient endosomal escape and siRNA delivery. According to the results, PD-L1 and TGF- β are dramatically dismissed using the designed system, thus achieving in combination efficient immunogenic tumor cell death. While the objective of this work was accomplished, there are still some crucial aspects that can be improved. For instance, there is a need to enhance transfection efficiency, and significant efforts are currently underway to address this issue. Furthermore, the reduction in viability observed in the co-culture system provides a representative approximation, but it still falls short of accurately replicating what occurs in a biological system. For this reason, more advanced assays such as co-culture systems utilizing real blood lymphocytes or validation in living animals. A higher response in animal models according to drug and siRNA protection by MSNs, increased bioavailability, and self-adjuvantivity would be expected.

One important limitation of immunotherapies is the fact that many tumors are characterized by an immunosuppressive microenvironment where there are no sufficient tumor-infiltration of lymphocytes to ensure the effectiveness of the treatment. Cytotoxic T cells play a principal role in recognizing tumor cells; however their effectiveness relies on establishing a physical interaction with the cancer cells and developing efficient communication. This required communication is often disrupted by immune escape mechanisms developed by tumors, allowing cancer progression. In this scenario, in chapter 4 we developed nanoparticles able to restore cellular connection and communication between cancer cells and cytotoxic T cells by using a Janus mesoporous silica-Au nanoparticle including specific binding sites (a pHLP peptide and PD-1 antibody) in opposite faces for simultaneous binding cancer cells and T cells. The pHLP peptide allows decorate tumor cells with the nanoparticles without internalization, whereas the PD-1 antibody is used to attach lymphocytes to tumor cells and to restore the communication disrupted. The efficacy of this new approach has been tested in a metastatic mouse model with promising results. The successful demonstration of this proof-of-concept strategy paves the way for a new class of immunotherapies based in

nanoparticles. The immune system is very complex, and more efforts are needed for further applications of tumor-immune cells binding nanosystems. Further testing with our nanoparticles in other cancer models will be developed in due course.

In summary, the work presented in this thesis is the result of a multidisciplinary project that covers aspects of material science, chemistry and biology. The nanosystems developed aim to provide new ideas to the complex issue of cancer treatment, settling down alternatives to solve some of the narrow limitations and endowing nanoparticles with new and promising functionalities. It is expected that the performance and feasibility of our designs could be validated in other tumors and that these or similar nanomaterials will advance towards reaching the bedside to improve the outcomes of cancer patients in the near future. Nevertheless, as stated before, more validation studies are needed to ensure effectiveness and to avoid potential side effects, and to assess their benefit-to-risk ratio and impacts on the organisms. Future research should focus on improving our understanding of the biodistribution, pharmacokinetics, persistence, and clearance in living organisms. It is hoped that the results derived from this doctoral thesis may inspire new research projects that combine nanotechnology and medicine with the aim of advancing towards clinical translation.

References

1. Mahomoodally, M. F., Désiré A.-L., D. & Rosette M. A.-L., E. Catalase. in *Antioxidants Effects in Health: The Bright and the Dark Side* 81–90 (Elsevier, 2022).
2. Ye, S. & Carroll, R. L. Design and fabrication of bimetallic colloidal ‘janus’ particles. *ACS Appl Mater Interfaces* **2**, 616–620 (2010).
3. Gulley, J. L. et al. Dual inhibition of TGF- β and PD-L1: a novel approach to cancer treatment. *Molecular Oncology*, **16**, 2117–2134 (2022).

4. Tian, Y. et al. JQ1-Loaded Polydopamine Nanoplatfrom Inhibits c-MYC/Programmed Cell Death Ligand 1 to Enhance Photothermal Therapy for Triple-Negative Breast Cancer. *ACS Appl Mater Interfaces* **11**, 46626–46636 (2019).
5. Li, Y. et al. Lipid-mediated delivery of CD47 siRNA aids JQ1 in ensuring simultaneous downregulation of PD-L1 and CD47 and improves antitumor immunotherapy efficacy. *Biomater Sci* **10**, 6755–6767 (2022).

Conclusions

This Ph.D. thesis has contributed to the biomedical field by designing new hybrid nanodevices to overcome some of the main limitations in cancer treatment. Specifically, the conclusions acquired from this work are:

1. Enzyme-powered Janus Au-mesoporous silica nanoparticles have been developed with an enhanced stimulus-responsive doxorubicin delivery and improved cellular internalization.
2. Ultra-fast Janus Pt-mesoporous silica nanodevices are able to pass through physical barriers and reach cells, obtaining a higher drug delivery at reduced fuel concentrations.
3. MSNs-based nanosystems for combined delivery of JQ-1 drug and TGF- β siRNA efficiently reverse immunosuppressive microenvironment in melanoma and promote cancer immunogenic cell death.
4. The lymphocyte recruitment and recovery of cytotoxic synapse with tumor cells by a pHLIP and α PD-1 modified Janus Au-mesoporous silica nanoparticle achieve an efficient tumor cell death and reduced metastatic burden in a murine melanoma cancer model.

Taken together, the results evidence the potential of using nanotherapies to address unmet medical needs, such as overcoming biological barriers and immune stimulation, in cancer therapy.

